

Exploring behavioral circuits with holographic  
optogenetics and network imaging

by

Joseph Donovan

DISSERTATION

Submitted in partial satisfaction of the requirements for the degree of

DOCTOR OF PHILOSOPHY

in

Neuroscience

in the

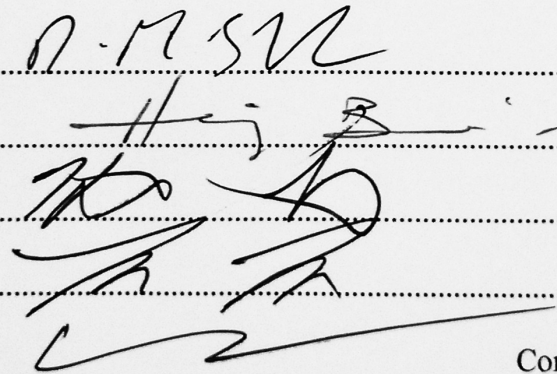
GRADUATE DIVISION

of the

UNIVERSITY OF CALIFORNIA, SAN FRANCISCO

Approved:

Chair

  
The signature block contains four horizontal dotted lines. The first line has a signature that appears to be 'D. M. S. V. L.'. The second line has a signature that appears to be 'H. J. S.'. The third line has a signature that appears to be 'K. S.'. The fourth line has a signature that appears to be 'L. S.'. The signature 'Committee in Charge' is written at the end of the fourth line.

Committee in Charge

Copyright 2016

by

Joseph Donovan

## Acknowledgements

I would like to thank all the members of the lab - who make sure I always have interesting technical questions to answer and create an enjoyable scientific environment. Special thanks to Herwig Baier for his support and scientific guidance. I'd like to thank Marco, Inci, Julie, and Tod for their collaboration on several very interesting projects which furthered my scientific understanding. And of course the lab managers - Enrico in Germany and Wendy in SF - who kept the lab running.

I would like to thank all my thesis committee members, current and former, for their time and guidance, despite the great distance.

I'm deeply appreciative to my family and my nui nui for their continued enthusiasm and support.

I would like to thank Alison Barker and Marco dal Maschio for critical reading of this thesis.

## Included works

This thesis contains three previously published works:

Semmelhack, **Donovan**, et al.; eLife 2014

Temizer, **Donovan**, et al.; Current Biology 2015

Thiele, **Donovan**, Baier; Neuron 2014

And one full manuscript, soon to be in the second round of review:

Dal Maschio\*, **Donovan**\*, et al.

\*(Equal contributions)

The work presented in these manuscripts is equivalent to a standard thesis.



# Exploring behavioral circuits with holographic optogenetics and network imaging

Joseph C. Donovan

## Abstract

Understanding how individual neurons within a circuit process sensory information and influence broader network dynamics to drive behavior is a longstanding goal of neuroscience. The larval zebrafish, *Danio rerio*, is an excellent model organism for behavioral circuit investigation, providing genetic and optical access and a variety of visually evoked behaviors. Psychophysics can investigate features of visual stimuli crucial for behavior. Together with two-photon calcium imaging this approach can locate brain regions involved in processing these stimuli, for example retinorecipient areas such as the optic tectum. These sensory processing regions send information downstream towards motor related areas, including the nucleus of the medial longitudinal fasciculus (nMLF). The nMLF is a midbrain nucleus, shown to be active during visually evoked behavior. Optogenetics is a powerful technique for exploring circuit function, especially in motor areas. Light from an optic fiber can be used to activate a population of neurons in the nMLF, inducing behavior, and together with ablations shows a crucial role for this area in postural control. These approaches can find the role of a population of neurons, however understanding the functional impact of individual neurons within a circuit is a greater challenge. To increase the resolution of circuit investigation, we have designed a holographic light-shaping system that enables activation with single neuron precision. A protocol was developed that combines this approach with simultaneous imaging and behavior, to relate behavioral output to functional properties of the circuit. This system creates a combined approach that can extract functional information from individual neurons in behavioral circuits.

# Table of contents

Introduction.....	1
Investigating behavioral circuits: motivation and approaches .....	1
Limits and challenges .....	4
The larval zebrafish is an excellent model for circuit investigation .....	5
Section 1 – Circuits supporting visually evoked behavior.....	7
A dedicated visual channel for prey detection .....	8
A visual pathway for looming-evoked escape in larval zebrafish .....	42
Section 2 – Introduction to optogenetics and a motor control circuit.....	75
Descending control of swim posture by a midbrain nucleus in zebrafish.....	76
Section 3 – Optical circuit exploration using shaped three-dimensional light fields.....	115
Linking neural circuits to behavior by 3D cell resolution optogenetics and multiplane network imaging .....	117
Section 4 – Conclusion and outlook .....	176
References.....	178

## Table of Figures

Figure 1 - Semmelhack Fig. 1 .....	12
Figure 2 - Semmelhack Fig. 2 .....	14
Figure 3 - Semmelhack Fig. 3 .....	17
Figure 4 - Semmelhack Fig. 4 .....	19
Figure 5 - Semmelhack Fig. 5 .....	21
Figure 6 - Semmelhack Fig. 6 .....	23
Figure 7 - Semmelhack Fig. 7 .....	25
Figure 8 - Semmelhack Fig. 8 .....	26
Figure 9 - Temizer Fig. 1 .....	57
Figure 10 - Temizer Fig. 2 .....	59
Figure 11 - Temizer Fig. 3 .....	60
Figure 12 - Temizer Fig. 4 .....	62
Figure 13 - Temizer Fig. 5 .....	63
Figure 14 - Temizer Fig. 6 .....	64
Figure 15 - Temizer Fig. 7 .....	66
Figure 16 - Thiele Fig. 1 .....	91
Figure 17 - Thiele Fig. 2 .....	92
Figure 18 - Thiele Fig. 3 .....	93
Figure 19 - Thiele Fig. 4 .....	94
Figure 20 - Thiele Fig. 5 .....	95
Figure 21 - Thiele Fig. 6 .....	96
Figure 22 - Thiele Fig. 7 .....	97
Figure 23 - Thiele Fig. 8 .....	99

Figure 24 - Dal Maschio Fig. 1 .....	131
Figure 25 - Dal Maschio Fig. 2 .....	133
Figure 26 - Dal Maschio Fig. 3 .....	135
Figure 27 - Dal Maschio Fig. 4 .....	137
Figure 28 - Dal Maschio Fig. 5 .....	139
Figure 29 - Dal Maschio Fig. 6 .....	141

# Introduction

## Investigating behavioral circuits: motivation and approaches

A central goal of neuroscience is to understand how neuronal circuits process sensory inputs leading to the generation of motor behaviors. This is a deep challenge that will require many more decades to solve and must be approached on multiple fronts simultaneously. Advancements in experimental methods have been critical in improving the ability to relate sensory and motor parameters to properties of a functional circuit, particularly in terms of observing network-scale dynamics (calcium imaging), and also direct mapping of function (optogenetics).

A fundamental and classical approach towards understanding such circuits is psychophysics, which entails studying the quantitative relationship between stimuli input parameters and the perceptions they evoke. For model organisms, which are unable to directly describe their sensory percepts, behavior can be tracked and parameterized to provide a readout of internally processed stimuli state. Thus experimental psychophysics can be thought of as uncovering a mapping, from sensory inputs to behavioral outputs. This approach is useful and has uncovered several interesting circuit properties – for instance classical work in toads uncovered feature detectors selective to visual features of prey <sup>1</sup>. A challenge is that for most sensory modalities, an experimentally intractable number of possible stimuli exist. For instance, considering vision, mixing different spatial, luminance, color, and movement features results in billions of possible stimuli. This necessitates finding a simplified description of the ‘parameter space’.

Psychophysics provides a crucial base for further experimentation, as understanding the important input parameters gives hints to the functional processing aspects of a circuit. Alone psychophysics cannot directly address what is in between the sensory inputs and motor outputs – that is the neuronal circuitry, and the functional details of how stimuli are processed. Modeling using simplified assumptions can make

guesses about internal representations and state, but just as many equations can describe the same curve, there are many possible circuit mechanics that could produce the same behavioral responses, especially when viewed through the lens of behavioral variability.

Electrophysiology is a powerful tool for investigating neuronal activity related to sensory stimuli or motor behaviors, and allows for high-fidelity activity readout in a small number of cells. However this approach is limited by low throughput and only recording in one or two neurons simultaneously is quite constraining. With repeated and reliable events, and well-defined cell types, this approach can be effectively applied. However when responses are variable or cell types are numerous or poorly defined these limitations are problematic. A related challenge is that mapping a certain neuron or functional unit accurately across multiple specimens can be extremely difficult. Even for cells of a defined type, there can be significant variations within the type or across individuals. Furthermore, the concept of well-defined cell types begins to break down when looking at sufficiently specialized subtypes<sup>2,3</sup>. Thus narrowly focused investigation only provides a small piece of the puzzle in each specimen, making it hard to piece together.

With the advent of calcium imaging, the circuit investigation can operate on a broader scope. Hundreds of neurons can be imaged simultaneously, and emerging technologies are improving the ability to rapidly image volumes or in deeper structures. The large number of neurons imaged can challenge simple analysis approaches, though techniques for analyzing large populations of neurons are being developed<sup>4-6</sup>. One downside to calcium imaging approaches is the indirect measurement of neuronal activity through intracellular calcium levels, which reduces accuracy and places limits on temporal resolution. Voltage sensors are being actively developed that offer significant improvements in temporal resolution and measurement of subthreshold activity. Current voltage sensors produce weak signals, though further development will address this issue - just as the GCaMP sensory family has been improved over several generations<sup>7</sup>. However faster sensors will be difficult to use with large volumetric imaging, as microscopy involves a fundamental tradeoff between speed, volume, and signal quality.

Calcium imaging and all other recording techniques are fundamentally limited to collecting correlations between circuit parameters and sensory inputs or behavioral outputs – the relationship between the two is assumed and not casually demonstrated. Fortunately, imaging can be combined with other techniques that can directly influence circuit activity.

Optogenetics allows remote control of neuronal activity, through the use of genetically-encoded light sensitive channels. Different families of optogenetics actuators enable excitatory and inhibitory modulation with a range of different colors and temporal properties <sup>8</sup>.

A key aspect of optogenetics is selectivity – increased precision in activating neurons allows for more focused circuit investigation. This specificity can be provided genetically through expression control systems, which allow neurons of selected types or in certain areas to be targeted even with unfocused stimulation. Unfortunately, the desired expression pattern is not always available or clean. When using a genetic targeting approach with broad stimulation, the population of neurons activated is fixed within each specimen. Genetic control can be extended through the spatial control of stimulation light. Spatial control is generally harder to implement, but has the strong advantage that it can be used to select targets for which a clean genetic line does not exist, and additionally allows different sets of neurons to be activated within the same specimen, resulting in better internally controlled experiments than activating different patterns in different specimens. Optimal spatial control would entail shaping light patterns in three-dimensions to target any desired neurons within a volume, regardless of their positions.

Selecting targets for optogenetic activation can be difficult, as there are often many genetic lines with expression in a desired brain region. Spatially selective activation also runs into numerical limitations that scale as the resolution of the activation increases. However, optogenetics does not have to be applied alone. Combining optogenetics with other approaches, such as imaging - which so far have been infrequently used together in the same specimen due to technical challenges - allows them to

enhance each other. Imaging provides a view of the circuit state (which can help interpret the outcome of stimulation) and could facilitate target selection for stimulation. Optogenetics enable a degree of direct and precise circuit manipulation that imaging alone cannot achieve. This combination could be used across different specimens, but when investigating circuits at high-resolution, it is superior to combine multiple approaches within each individual. As mentioned previously, mapping functional cell types across different individuals can be quite difficult, especially when trying to uncover the detailed functional role of each neuron. Combining behavior, imaging, and optogenetics simultaneously allows them to complement each other, enabling the maximal amount of information to be extracted during experimentation.

## Limits and challenges

Outfitted with these powerful tools, dissecting circuits is still a formidable challenge. For instance in the worm *C. elegans*, the entire set of neurons are known and uniquely labeled, and their connectivity has been mapped through electron microscopy<sup>9</sup>. However a comprehensive understanding of how this connectivity drives functional behavior has proven elusive. Progress is being made through functional analysis of network properties, and more advanced analysis approaches, such as dimensionality reduction, are proving useful<sup>10</sup>.

This challenge is quite difficult, so let us take a brief step back and rather consider ‘where’ in the circuit is easiest to approach first. An obvious place to start is the sensory input side. Early sensory processing is fairly well understood, easy to directly access and can be repeatedly subjected to stimuli that are reliably processed. Circuit representations here are related to sensory parameters, and can be more feasibly recorded and understood through modeling. Another option is to approach from the direction of the circuit outputs – motor areas driving behavior. In these areas the representations are again physically connected to reality and easier to understand – behavior is easily quantified, unlike higher-order sensory perceptions. In this domain, optogenetics is at its zenith, since patterns activated in the circuit can directly



influence behavior, which can be used as a readout of circuit state. Whereas optogenetics activations targeted ‘earlier’ in the circuit are less likely to produce quantifiable changes in behavioral parameters, and tend to be more stochastic.

Understanding the circuit components between sensory input and behavioral output is a critical part of the challenge, and the ultimate goal - but just like solving a maze, it is easier to start from either end than from the middle. Considering the previously discussed aspects of circuit complexity, existing tools, and input/output accessibility, model organization selection is an important aspect of any attempt to investigate circuits.

## **The larval zebrafish is an excellent model for circuit investigation**

The ideal model organism is accessible – both genetically and optically, behaviorally interesting, and at the ‘right’ level of complexity. The larval zebrafish is an excellent candidate, particularly for aspects of fine-scale circuit investigation. It develops rapidly, has several sensory modalities, including vision, which allows for easy control of stimuli, and crucially is transparent. Transparency affords excellent optical access which is a sizable advantage, since optical methods can provide volumetric recording access, and also sophisticated optogenetic control. Optical techniques are also some of the fastest improving technologies and will only become more powerful.

Zebrafish also have well developed expression control systems, which are crucial for use with genetically-encoded calcium sensors and optogenetic actuators. The Gal4/UAS expression control system is currently the best developed, and several libraries of expression patterns are available, including two from our lab - an enhancer trap screen and a gene trap screen<sup>11–13</sup>. The specificity of genetic control in zebrafish is not without limitations and there are plenty of cell types for which there is not a specific line, or lines that can be quite variegated – with substantially different expression patterns in each individual. This problem can be overcome by spatial selectivity, which will be explored in the last chapter of this thesis.

Zebrafish are vertebrates, which can be an advantage over simpler model organisms also suited to circuit investigation such as *Drosophila*. More complex organisms, such as mice, can support higher level cognitive and learning processes, however the challenge of untangling a circuit scales supralinearly with network size, making investigation at the single neuron level extremely challenging. The behavioral circuits in zebrafish are excellent targets for detailed circuit investigation – complex enough to be interesting, but small enough to feasible approach at a single-neuron resolution.

Zebrafish also have a rich behavioral repertoire, including a variety of visual behaviors. Simpler behaviors, such as the optokinetic reflex (OKR) or optomotor response (OMR), are driven by moving gratings and quite robust<sup>14</sup>. Other behaviors, such as prey capture and escape behaviors, have a strong survival relevance and require more advanced processing<sup>15</sup>. This range of visual behaviors has a mix of different stimuli selectivities and brain regions involved, and the motor outputs of these behaviors are quantifiable, making them interesting targets for investigation.

## **Section 1 – Circuits supporting visually evoked behavior**

Why explore visual circuits? Vision is a crucial sense for many of our behaviors, and provides a high-throughput depiction of the surrounding world. Visual inputs can be effectively controlled in experiments through the use of monitors and projectors. Our initial experimentation used small OLED-based screens, later switching to modified projectors for adjustable screen size and better color control for integration with two-photon imaging. Two-photon imaging is an approach that uses two half-power photons for molecular excitation, which allows for increased axial resolution, deeper tissue penetration, and less interference with visual experiments, since the imaging beam is infrared<sup>16</sup>. Two works covering investigation of visual circuits using two-photon imaging follow.

# A dedicated visual channel for prey detection

Julia L. Semmelhack, **Joseph C. Donovan**, Tod R. Thiele, Enrico Kuehn, Eva Laurell, and Herwig Baier

Max Planck Institute of Neurobiology, Am Klopferspitz 18, 82152 Martinsried, Germany.

## Abstract

Zebrafish larvae show characteristic prey capture behavior in response to small moving objects. The neural mechanism used to recognize objects as prey remains largely unknown. We devised a machine learning behavior classification system to quantify hunting kinematics in semi-restrained animals exposed to a range of virtual stimuli. Two-photon calcium imaging revealed a small visual area, AF7, which was activated specifically by the optimal prey stimulus. This pretectal region is innervated by two types of retinal ganglion cells, which also send collaterals to the optic tectum. Laser ablation of AF7 markedly reduced prey capture behavior. We identified neurons with arbors in AF7 and found that they projected to multiple sensory and premotor areas: the optic tectum, the nucleus of the medial longitudinal fasciculus (nMLF) and the hindbrain. These findings indicate that computations in the retina give rise to a visual stream which transforms sensory information into a directed prey capture response.

## Introduction

The visual systems of many species have an innate capacity to respond to features that denote either prey or predators<sup>17–20</sup>. However, the circuits underlying these responses are mostly unknown. Zebrafish larvae have an instinctive ability to hunt small moving prey objects, such as paramecia, as soon as they start to swim at five days post fertilization (5 dpf). Before initiating a prey capture swim, a larva must select the target from its surroundings, calculate its location, and make a decision as to whether the target is worth pursuing. It then initiates a multi-step motor routine involving bouts of turning and swimming toward the prey, culminating in a consummatory strike<sup>15,21–23</sup>. Precise maneuvers are required, and so prey capture tail movements are quite different from those observed during routine swims or escapes. To orient towards a paramecium on the left or right, larvae perform j-turns – unilateral bends where the tail is held in a J shape. If the prey is directly ahead, they slowly swim toward it, with back and forth undulations of the tail<sup>24</sup>. These movements appear to be triggered by small moving objects, but it is unclear how or where in the brain these objects are identified as prey.

Under the appropriate conditions, larvae can be induced to perform hunting swims when they are partially restrained in agarose. A head-fixed preparation facilitates automated tracking of tail movements, stimulus control, and functional imaging. Two recent studies have shown that a moving dot can evoke eye convergence and approach swims in head-fixed larvae<sup>25,26</sup>. However, these studies did not investigate the specific tail kinematics evoked by prey stimuli, or seek to categorize the tail movements as distinct from other types of swims. Here, we identified the distinctive features of prey capture swims in head fixed larvae, and developed a machine learning algorithm to quantify and distinguish these swims from other types of behavior. This allowed us to quantify the tail movements produced in response to a range of artificial prey stimuli, and determine the ideal stimulus to evoke the prey capture response.

To begin to identify the neural circuits for prey identification, we focused on the retinal ganglion cells (RGCs), the output neurons of the retina. There is a precedent for RGCs acting as prey detectors – a

classic study in the frog found RGCs that responded to small (1-3°) objects moving through the visual field <sup>27</sup>. In the mammalian visual system, certain RGC types act as feature detectors for one aspect of the visual scene, and the axons of these RGCs project to visual nuclei that mediate the response to that feature. For example, intrinsically photosensitive RGCs project to nuclei that control circadian rhythms and the pupillary light reflex <sup>28</sup>, and RGCs that respond to whole field motion innervate nuclei that drive compensatory eye movements <sup>29,30</sup>. In zebrafish, RGC axons terminate in ten retinorecipient areas called arborization fields (AFs) <sup>31</sup>, most of which have not been functionally characterized. We hypothesized that there could be a class of RGCs that respond specifically to prey-like visual stimuli and project to one or more of these AFs.

By imaging RGC axons in the AFs, we identified one visual area, AF7, which responds specifically to the optimal artificial prey stimulus, as well as to actual paramecia. Targeted laser ablation showed that this area is important for the behavior. Finally, we found that neurons with arbors in the AF7 neuropil innervate multiple areas known to be involved in prey capture behavior and locomotion in general - the optic tectum, nMLF, and hindbrain. These results identify AF7 as vital part of the prey capture pathway, and link a dedicated retinal output to an ecologically relevant behavior.

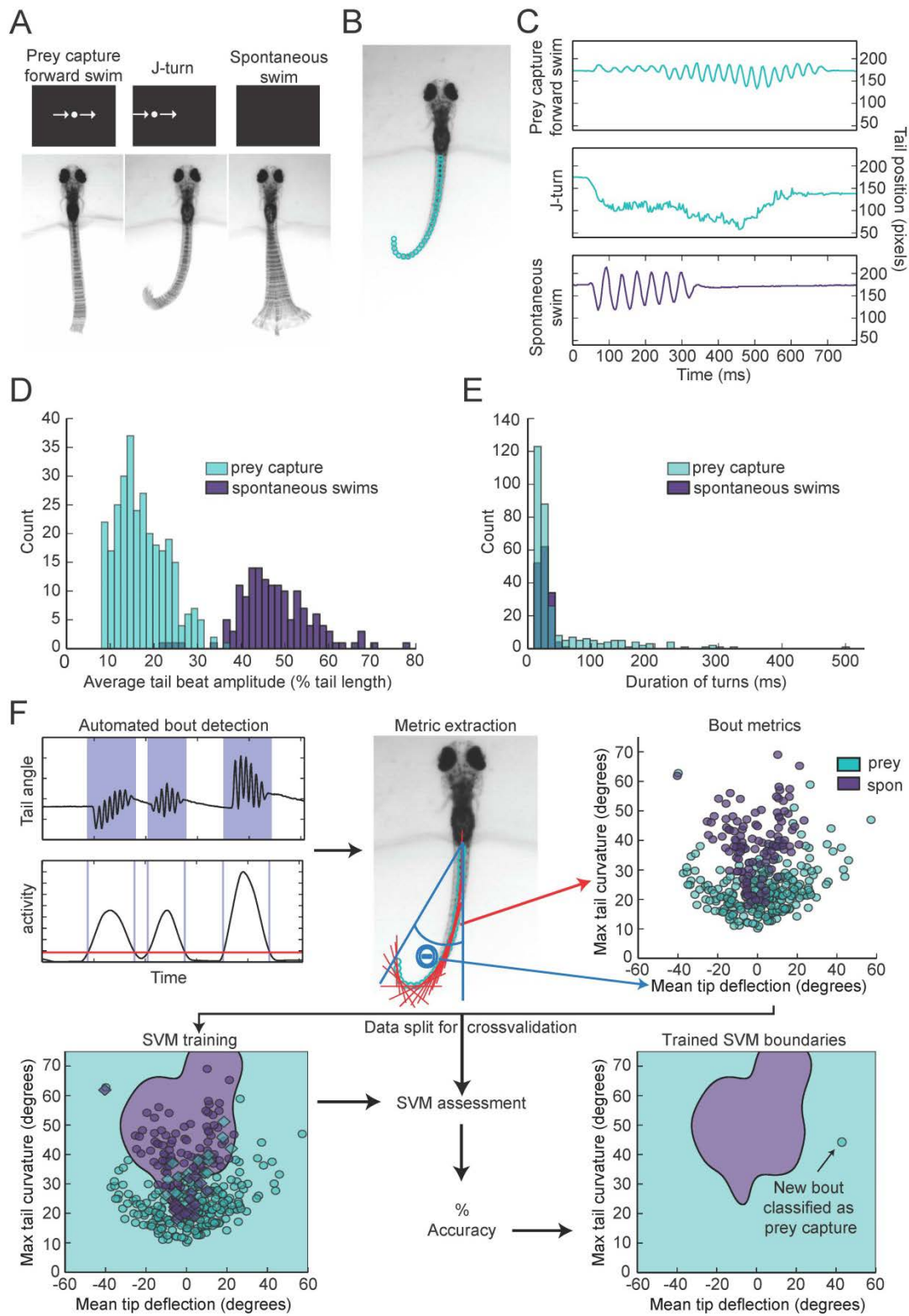
## **Results**

### **Analysis and classification of prey capture swims**

To investigate how prey objects are identified, we developed a head-fixed prey capture assay and automated behavioral classification system. Larvae were embedded in agarose at 6 dpf, and their tails were freed so that swimming movements could be recorded with a high speed camera. Visual stimulation was provided by a small OLED screen in front of the larva. In preliminary experiments, we found that a small (~3° of the visual field) white dot moving horizontally across a black screen was effective in evoking behavior. Larvae performed two types of behavior in response to this virtual prey: forward

swims, which consisted of low amplitude oscillations of the tail, and j-turns (Figure 1A)<sup>22</sup>. These swims were accompanied by eye convergence, which is another kinematic feature of prey capture<sup>24,25</sup>. Larvae also performed spontaneous swims in the absence of visual stimuli. To analyze tail movements, we digitized the tail, using a custom algorithm to assign ~40 points along its length in each frame (Figure 1B). Plotting the position of the tip of the tail during prey capture and spontaneous swims over time revealed several kinematic differences between the behaviors (Figure 1C). Prey capture forward swims and spontaneous swims both consist of back and forth movements of the tail, but the amplitude of the prey capture swim is much lower. In contrast, during a j-turn the tail is deflected to one side, often for hundreds of milliseconds.

**Figure 1** (on following page). **Head-fixed larvae respond to virtual prey with distinctive swimming movements.** (A) Overlay of 50 frames (167 ms) of high speed video showing examples of behavior in head fixed larvae. Larvae performed forward swims in response to a 3° dot. j-turns were observed when the same dot was to the right or left. Spontaneous swims were often observed in the absence of any stimulus. (B) Example video frame showing points assigned by the digitization algorithm. (C) The position of the tip of the tail over time for the videos in (A). (D) The distribution of tail beat amplitudes for each bout in expert-classified prey capture and spontaneous swim videos. (E) Duration of the longest bend greater than 20° during each bout. (F) Overview of support vector machine (SVM) based bout classification procedure, displaying only two parameters (maximum tail bend and mean tail tip deflection) for clarity. Bouts are extracted using a threshold on the normalized and smoothed first derivative of tail bend angles. Values for each parameter are calculated for all bouts and used to train an SVM. The SVM is then used to classify unlabeled bouts. See Figure 1-Figure Supplement 1 for plots of each of the five parameters, and accuracy of the SVM vs. number of parameters.





The apparent differences between spontaneous swims and prey capture were confirmed when we analyzed several hundred expert-classified prey capture and spontaneous swim videos. The average amplitude of the tail movements for prey capture bouts was 17% of tail length, while for spontaneous swims it was 48% of tail length (Figure 1D). We also observed the sustained tail deflections characteristic of j-turns. Plotting the duration of the longest tail deflection for each bout reveals a single peak at 27 ms for the spontaneous swims (Figure 1E). For prey capture swims, we also see a peak at this duration, representing the back and forth motion during forward swims, but in addition we see a long shoulder of turns of much longer duration, which consists of j-turns (Figure 1E). These stark differences suggest that prey detection triggers a specialized motor program.

In order to characterize the stimuli that evoke prey capture, we needed an objective method to quantify the behavior and distinguish it from spontaneous swims. We used a support vector machine (SVM), a supervised learning algorithm that allows for multi-dimensional classification, to train a classifier, which could then categorize new data. For this classification, prey capture forward swims and j-turns were not distinguished; both were included within the category of prey capture.

We trained the SVM on a set of 369 expert-labeled and digitized videos (Figure 1F). Bouts of swimming within the videos were identified using a thresholding operation on the smoothed derivative of the tail bend angle. For the dimensions of the SVM, we choose relatively simple parameters that allowed us to collapse a feature of the bout (e.g. tail curvature) into a single number. During training, each bout was assigned a position in 5-dimensional space corresponding to its values for the 5 parameters (Figure 1 – Figure Supplement 1), and decision boundaries were drawn in multidimensional space to separate the two types of behavior. The trained SVM could then be used to classify new videos. Using this approach, we were able to achieve a cross-validated accuracy of 96% (Figure 1 – Figure Supplement 1).

## Identifying the ideal prey stimulus

We next used the virtual prey assay and the SVM classifier to determine the ideal stimulus for evoking prey capture behavior. We presented head-fixed larvae with white dots ranging in size from 0.5-30° in diameter, while recording tail movements. To quantify the behavior, we used the trained SVM to identify swim bouts as prey capture or spontaneous swims. We calculated a prey capture score based on the percentage of time during each trial that the larva performed prey capture bouts. We found that a 3° dot was the optimal size to trigger prey capture (Video 1), and that the behavior was strikingly reduced when we increased the size to 10° (Figure 2A), which is consistent with data from free swimming and head-fixed larvae<sup>25,26</sup>. We also tested the response to dots traveling at a wide range of speeds, and found that 90°/s is the ideal speed for prey stimuli, and that larvae respond minimally to stimuli moving slower than 12°/s or faster than 360°/s (Figure 2B).

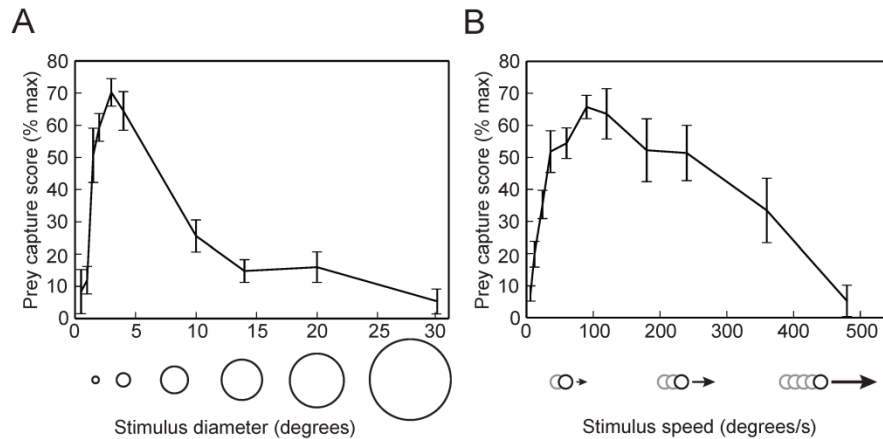


**Figure 2. Prey capture behavior is triggered by dots of a particular size and speed.** (A) Larvae were shown white dots of various sizes moving at 90°/s. Trials were scored by using the SVM to classify each bout and calculating the percentage of the trial that consisted of prey capture bouts. Scores are expressed as a percentage of the maximum for that larva.  $n = 16$  larvae. (B) Prey capture behavior in response to a 3° dot moving at 6 to 480°/s.  $n = 9$  larvae. Error bars =  $\pm$ SEM.

## Functional imaging of RGC axons

Given the highly selective nature of this innate behavioral response, we hypothesized that the preference for prey stimuli of a certain size and speed might arise in the retina. In that case, there should be a population of RGCs that responds specifically to prey. A recent functional imaging study reported responses to prey in the largest AF, the optic tectum<sup>32</sup>. However, the tectum receives input from many different types of RGCs, and responds to a wide variety of stimuli other than prey<sup>33,34</sup>, which makes it difficult to determine whether the tectal RGCs are responding selectively to prey. We thus focused our imaging experiments on AFs 1-9. We performed two-photon imaging of RGC axons in larvae with the calcium indicator GCaMP6 driven by an RGC-specific promoter. In these larvae, the ten AFs can be identified as distinct regions of fluorescent neuropil (Figure 3A and C). We asked whether the axons in any of these regions would respond to the ideal prey stimulus identified in our behavioral assay (3°, 90°/s). In our preparation, we could image all but the most ventral arborization field, AF1. We stimulated larvae with the prey stimulus while imaging RGC axons in AFs 2-9, and found one area, AF7, whose RGC axons responded robustly to the stimulus (Figure 3B), while seven other AFs did not respond to virtual prey. Some RGC axons in the optic tectum responded to the 3° stimulus, but the tectum response was much larger for stimuli of >10° (Figure 3 – Figure Supplement 1). We next varied the size of the stimulus while imaging in the AF7 plane, and found that AF7 RGC axons responded maximally to dots 2-3° in diameter, and much less to stimuli larger than 6° in diameter (Figure 3C-I). Interestingly, AF9, another AF in the same plane, did not respond to small dots but began to respond as the stimulus size was increased above 6° in diameter (Figure 3C-F). We also measured the response of AF7 to stimuli of varying speeds, and found that the optimal speed was 90°/s, and stimuli slower than 12°/s or faster than 360°/s evoked a much smaller response in these axons (Figure 3G). These tuning curves are strikingly similar to the behavioral tuning curves for size and speed (Figure 2A and B, grey trace in Figure 3F and G). At speeds above 360°/s the strong correlation between behavioral tuning and AF7 response degrades, since the behavioral response to extremely fast speeds is quite low. This could be caused by a threshold or

non-linearity in the neural circuit, such as the weak activation of the AF7 RGC axons being insufficient to drive the downstream neurons. We next tested the direction selectivity of the axons in AF7, and found that the area as a whole responded to prey stimuli moving in all four cardinal directions (Figure 3I), although the response was more robust to stimuli moving horizontally ( $p < .001$ ,  $t$  test).

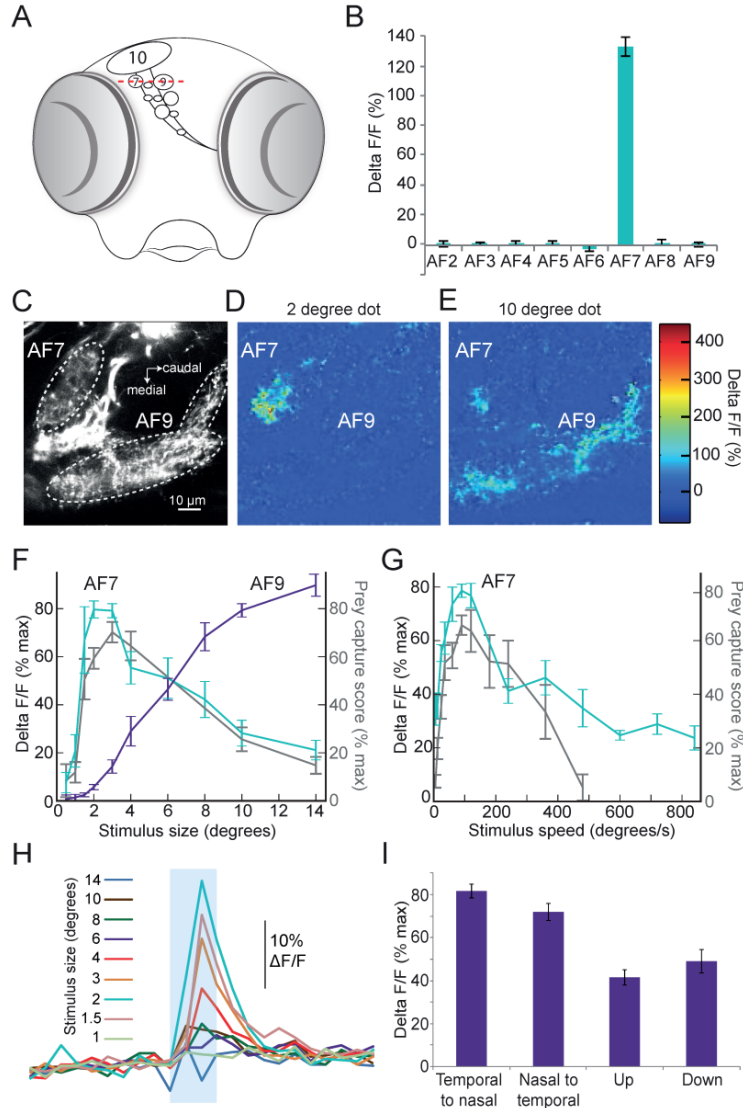


**Figure 3. Prey stimuli activate RGC axons that project to AF7.** (A) Schematic frontal view of the brain showing AFs. Red line indicates imaging plane for C-G. (B) Response to the ideal prey stimulus (3° dot, 90°/s) in other AFs in an *Isl2b:Gal4, UAS:GCaMP6s* transgenic larva. n = 9 larvae. (C) Baseline fluorescence of RGCs in an *Isl2b:Gal4, UAS:GCaMP3* larva. (D) Peak frame in the response to a 2° dot. (E) Peak frame in the response to a 10° dot. (F) Response of all larvae (n = 9) to stimuli 0.5-14 degrees in diameter. ROIs were defined anatomically as in (A). The  $\Delta F/F$  is plotted as a percentage of the maximum response for that larva. Grey lines represent the behavioral tuning curve from Figure 2A. (G) Response of AF7 RGC axons to a 3° dot travelling at a speed of 6 to 800 degrees/s. Grey lines represent the behavioral tuning curve from Figure 2B. (H) Responses of AF7 to a range of different size stimuli. Blue box represents the part of the trial when the stimulus was onscreen. (I) AF7 response to 3° dot moving in various directions. n = 10 larvae. Error bars =  $\pm$ SEM.

## Response to paramecia

If AF7-projecting RGCs are mediating behavioral responses to virtual prey, we reasoned that they should also respond to natural prey, such as paramecia. We found that head-fixed larvae will perform j-turns and forward swims when paramecia are added to the surrounding medium (Figure 4A). In the absence of paramecia, head-fixed larvae perform spontaneous swims but rarely prey capture (Figure 4B), while after paramecia were added to the dish we observed frequent prey capture bouts (Figure 4C). Like the behavior evoked by virtual prey, these swims could be reliably classified by an SVM. We next asked whether the paramecia were activating AF7 RGC axons. We recorded baseline activity for 30 seconds and then added a drop of a dense paramecia culture to the petri dish. We found that AF7 RGC axons were strongly activated during the paramecium trials, whereas AF9 axons were not (Figure 4D, Video 2). When we quantified the  $\Delta F/F$  in AF7 and AF9 for nine fish, we found that the peak response was significantly higher in AF7 during trials with paramecia (Figure 4E). The AF9 peak response in the same larvae was not significantly different in the presence of paramecia. The finding that AF7 axons respond to actual prey supports a role for this area in generating prey capture behavior.

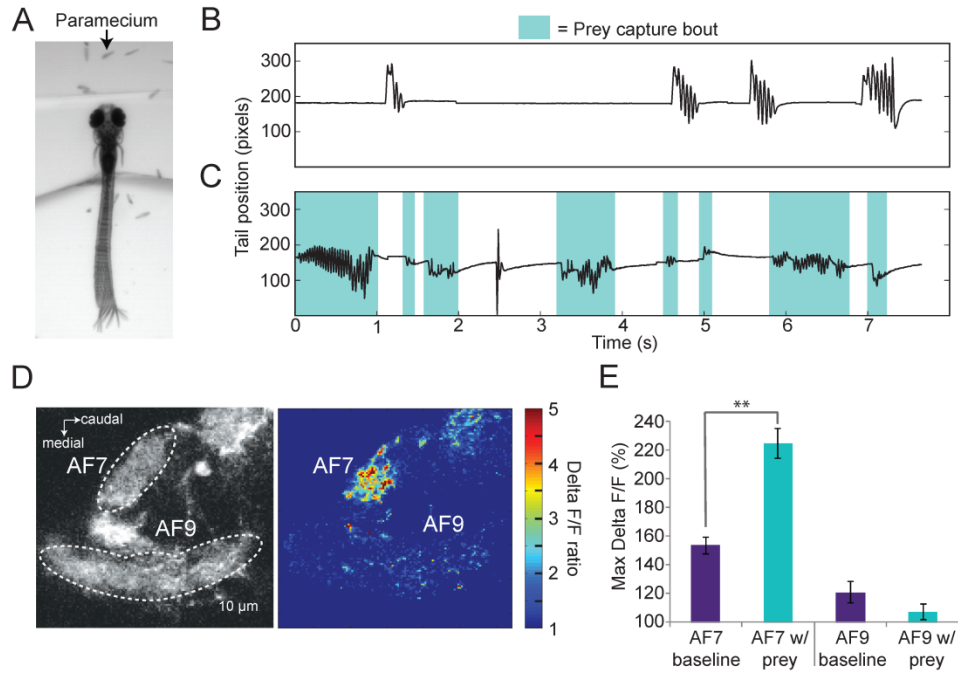


**Figure 4. Paramecia evoke prey capture behavior and the AF7 response.** (A) Overlay of 50 frames (167 ms) of high speed video showing a head fixed larva responding to paramecia. (B) The position of the tip of the tail of the larva in A without paramecia, showing spontaneous swims. (C) The same larva after paramecia were added to the dish. Bouts that were identified as prey capture by the SVM are colored blue. (D) *Ath5:Gal4, UAS:GCaMP6s* larvae were imaged before and after addition of paramecia. Pseudocolor represents the ratio of the  $\Delta F/F$  with paramecia to without. (E) AF7 and AF9 responses to paramecia in nine larvae. Maximum  $\Delta F/F$  is plotted for each trial. The AF7 response was significantly higher in trials with paramecia ( $p = 9.6 \times 10^{-5}$ , Wilcoxon rank sum test), whereas the AF9 response was not significantly different ( $p = 0.083$ ).  $n = 10$  larvae. Error bars =  $\pm$ SEM. See also Video 2.

### Anatomy of AF7-projecting RGCs

The activation of AF7 RGC axons specifically by small moving dots and paramecia suggests that there could be a specialized class of RGCs that project to this area. A subpopulation of RGCs has been previously shown to innervate AF7 and the *stratum opticum* (SO), the most superficial layer of the tectum<sup>35</sup>. However, little is known about their dendritic morphology, and it is unclear if these are the only inputs

to AF7. We set out to characterize the anatomy of the AF7-targeting RGCs using BGUG<sup>35</sup>, a highly variegated *UAS:mGFP* reporter that allows the visualization of individual neurons within a Gal4 line. By expressing mCherry and BGUG in RGCs, we labeled most RGCs red and <1% of them green. We could thus identify single RGCs with arbors in AF7 (Figure 5A) and trace the axon back to the retina to observe the cell's dendritic morphology. We identified 19 larvae with an arbor in AF7. All 19 RGCs exhibited the same axonal morphology, projecting to AF7 and the SO, but not to any other AFs (Figure 5A and B). Thus, a prey-specific information channel is routed to two distinct visual areas by each axon. Examining the dendritic morphology of these AF7-targeting RGCs revealed that AF7 receives inputs from two distinct RGC types. Thirteen cells (out of 19) had bistratified arbors with branches in ON and OFF layers of the IPL (Figure 5C), and the other six formed diffuse arbors spanning the entire IPL (Figure 5D). These dendritic morphologies correspond to two of the 14 RGC classes previously described in the zebrafish retina<sup>36</sup>, known as B2 and D1. These two types also project to other AFs, in much smaller numbers. However, the B2 and D1 neurons that project to AF7 only arborize in AF7 and the tectum. The responses to prey that we observe in RGC axons in AF7 could be due to B2 or D1 neurons, or both, as our gal4 line labels both types.



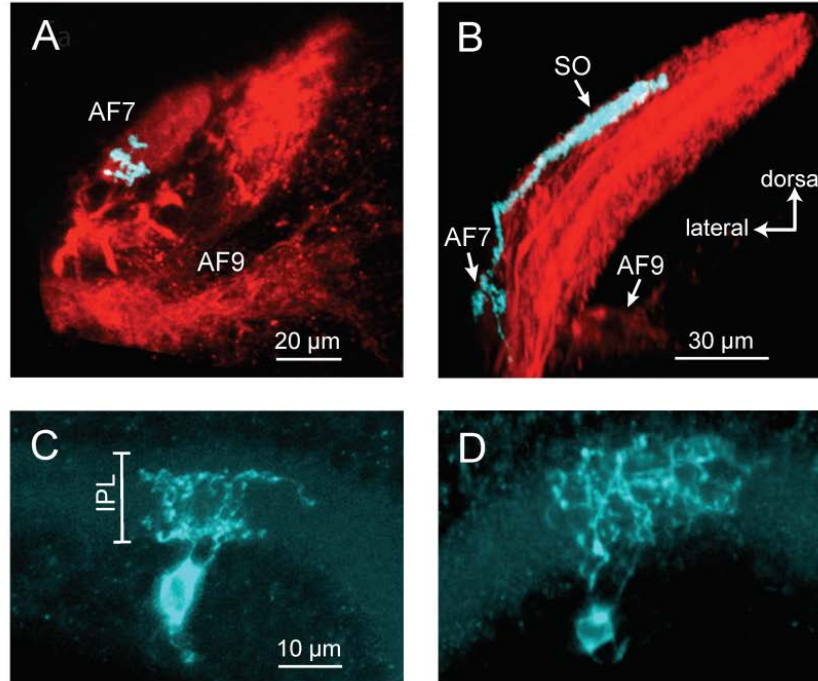


**Figure 5. Two types of RGCs project to AF7 and also arborize in the tectum.** (A) A single GFP-expressing RGC axon (cyan) arborizes in AF7 in an *Ath5:Gal4, UAS:mCherry, BGUG* larva. (B) The same axon also innervates the SO layer of the tectum. (C) Section of the retina showing dendritic morphology of a bistratified AF7-projecting RGC. Bracket indicates borders of the IPL (16  $\mu$ M). (D) Dendritic morphology of a diffuse bistratified AF7-projecting RGC.

### Ablation of AF7 neuropil

To test whether the AF7-projecting RGCs play a role in prey capture behavior, we performed two-photon laser ablations targeting the AF7 neuropil. Ablations were performed bilaterally in larvae expressing the fluorescent protein Dendra in RGCs (Figure 6A). Within three hours, degeneration of axons that project to AF7 could be observed (Figure 6B). Ablation of AF7 did not detectably change the projection of nearby RGC axons on their course to the tectum, nor did it decrease the intensity of RGC axon labeling in the SO (Figure 6 – Figure Supplement 1, A-D). We also observed that tectal neuron

responses to small stimuli remained intact after AF7 ablation (Figure 6 – Figure Supplement 1 E-H). These findings suggest that the ablation was restricted to the AF7 neuropil.

We recorded responses to swimming paramecia for five minutes before the ablation and again several hours afterwards, and used our SVM to categorize the bouts (Figure 6, C and D). As a control, we ablated a similarly sized region of AF9. We found that larvae with AF9 ablations spent as much time performing prey capture bouts as before ablation, whereas in AF7 ablated larvae prey capture time was significantly reduced (Figure 6E and F). On average, the AF7 ablated larvae spent 40% as much time performing prey capture bouts as they did before the ablation (Figure 6G). Although the effect was robust, ablated larvae did perform some prey capture bouts, which could reflect a failure to ablate all AF7 RGC axons, or a contribution from other retinal inputs to the behavior. To confirm that the AF7 ablation did not generally impair visual function, we tested the optomotor response (OMR) before and after ablations in AF7 or AF9. We found that, consistent with previous work<sup>37</sup> the OMR was not impaired in AF7-ablated larvae, but was reduced in AF9-ablated larvae (Figure 6H). These data suggest that AF7-projecting RGC axons are specifically required for prey capture behavior.

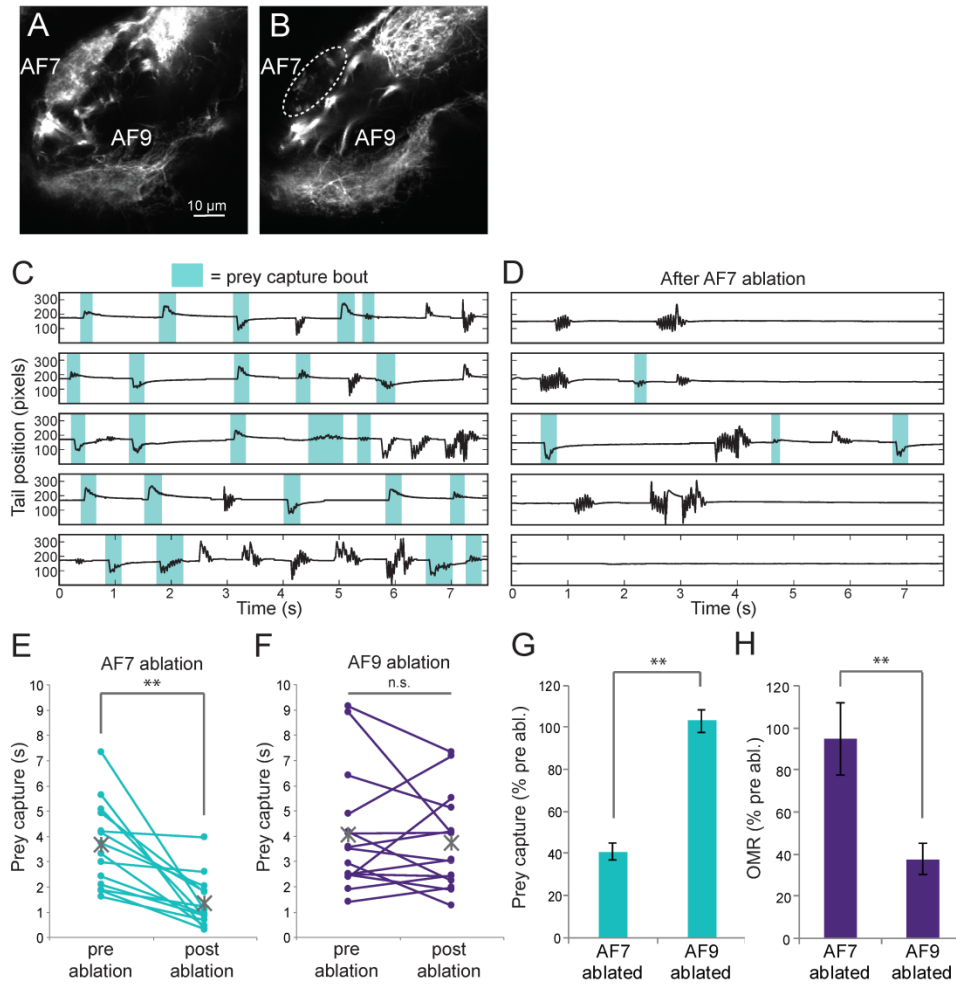


**Figure 6. Ablation of AF7 markedly reduces prey capture behavior.** (A) Intact *Ath5:Gal4, UAS:Dendra* larva at 8dpf. (B) *Ath5:Gal4, UAS:Dendra* larva after ablation of AF7 neuropil. (C) Pre-ablation response to paramecia in one example larva. Behavior was recorded for 5 minutes and the videos were edited to display all swim bouts. Each bout was classified by the same SVM as in Fig 4c. (D) The same larva after 2P laser ablation of AF7. (E) Total duration of prey capture bouts during the five 1 minute trials before and after AF7 ablations.  $n = 14$  larvae.  $p = 2.59 \times 10^{-4}$ , Wilcoxon rank sum test. (F) Prey capture time before and after AF9 ablations.  $n = 15$  larvae. (G) Duration of prey capture bouts after ablation as a percent of initial prey capture time.  $p = 2.68 \times 10^{-4}$ , Wilcoxon rank sum test. (H) Optomotor response to moving gratings after AF7 and AF9 ablation. AF7ablation  $n = 7$  larvae, AF9 ablation  $n = 9$  larvae.  $p = 5.2 \times 10^{-3}$ , Wilcoxon rank sum test. Error bars =  $\pm$ SEM. See Figure 6 – Figure Supplement 1 for AF7 and SO axon anatomy and periventricular neuron activity before and after ablation.

### **Pretectal neurons with arbors in AF7 project to the tectum, nMLF and hindbrain**

We used single cell electroporation to identify AF7's putative postsynaptic partners, by targeting cell bodies near AF7. We identified two classes of neurons with a proximal arbor located in the AF7 neuropil and distal arbors in other brain areas. The first class of neurons with processes in AF7, as well as the neighboring non-retinorecipient neuropil, formed a distinct projection to the tectum (Figure 7A and 7B). In all cases (n=12) the tectal branch was located in a region between the SO and SFGS layers that does not receive RGC axons. We also observed that all of these projections terminated in the anterior fifth of the tectum (Figure 7B, 7C, and Figure 7 – Figure Supplement 1).

A second type of neuron with dendrites in AF7 formed a projection to the nucleus of the medial longitudinal fasciculus (nMLF) and hindbrain (Figure 7D-F, and Figure 7 – Figure Supplement 1). The line *Gal4<sup>s117It</sup>*, which labels neurons in the midbrain tegumentum, including the nMLF<sup>38</sup>, was used as a landmark to identify the nMLF. These neurons (n=4) projected to the ipsi- and contralateral nMLF before terminating in the contralateral hindbrain. Thus, these AF7-innervating neurons could be directly involved in generating prey capture swims and j-turns.

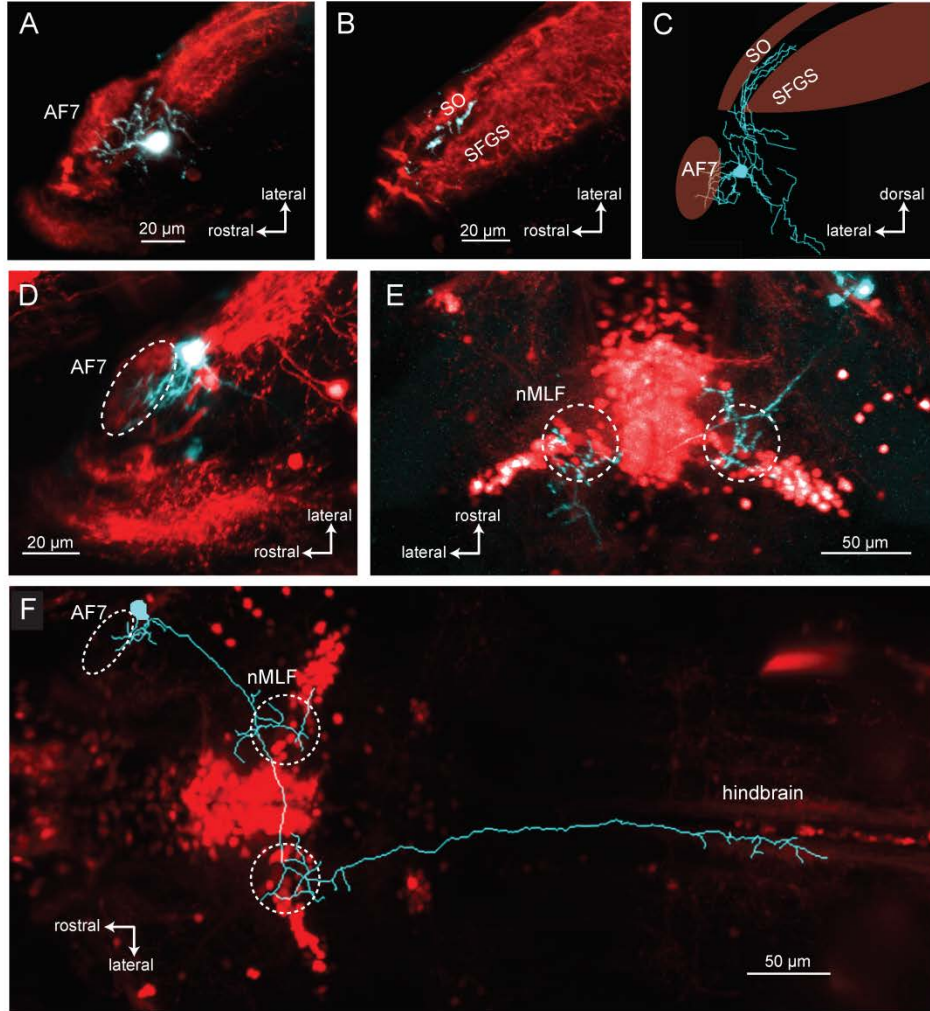


**Figure 7. Morphologies of pretectal AF7 neurons.** (A) Single cells were electroporated with tetramethylrhodamine (TMR) dextran (cyan) in an *Ath5:Gal4, UAS:GCaMP6s* larva (red). These neurons innervate AF7, as well as the adjacent non-retinorecipient neuropil in the same plane. (B) The cell imaged in (A) projects to the rostral tectum. (C) Tracing of the same cell, showing pretectal and tectal arbors. (D-E) Confocal images of a single electroporated cell in an *Ath5:Gal4, Gal4<sup>s117lt</sup> UAS:GCaMP6s* larva. (F) Tracing of the same cell as in (D) and (E) overlaid on a confocal image showing the *Gal4<sup>s117lt</sup>* labeling to identify the nMLF. See Figure 7 – Figure Supplement 1 for more examples.

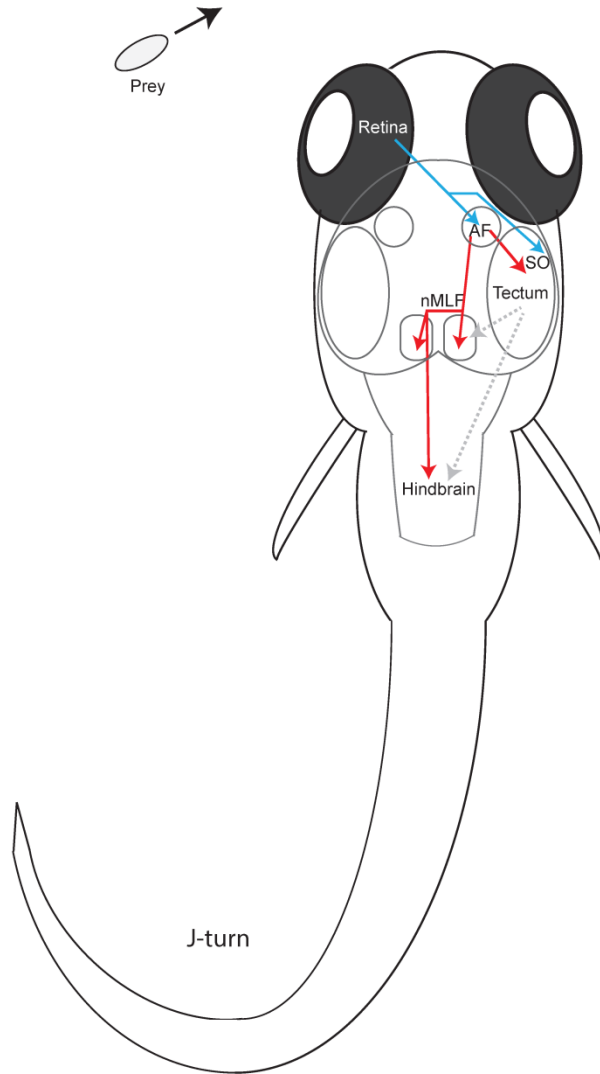


**Figure 8. Model for prey capture circuitry.** A prey stimulus on the left activates RGCs in the left eye (blue) which project to AF7 and the SO layer of the right tectum. Pretectal neurons (red) arborize in AF7 and send projections to the tectum or the nMLF and hindbrain. Activation of this circuitry produces a j-turn to the left, turning the larva in the direction of the prey. Previous studies have demonstrated connections between the tectum and nMLF (Gahtan et al., 2005) and between the tectum and hindbrain (Robles et al., 2011) (gray arrows).

## Discussion

While it was previously established that larvae respond to small moving stimuli<sup>25,26</sup>, little was known about where in the visual system this selectivity is generated. Our finding that a subset of RGC axons is tuned to prey stimuli suggests that the selectivity is generated early in the visual pathway, by circuits in the retina. There are examples of retinal circuits that generate a similar degree of stimulus selectivity. Experiments in the rabbit have identified local edge detectors –RGCs that respond only to slowly moving targets less than 1° in diameter<sup>39</sup>, and a similar type has been found in the mouse retina<sup>40</sup>. The unusually strong surround suppression in these cells is thought to be a consequence of amacrine cells acting presynaptically to inhibit bipolar cells as well as RGCs<sup>41,42</sup>. A similar mechanism could account for the size tuning of AF7-projecting RGCs.

In many cases, RGCs detect features that have a clear survival value for the animal. For example, *fast-OFF* RGCs in the salamander anticipate the location of a moving object<sup>43</sup>, a feature that could be used to predict the location of moving prey<sup>44</sup>. A classic study in the frog found RGCs that responded to small (1-3°) objects moving through the visual field; these cells were hypothesized to act as “bug detectors”<sup>27</sup>. These examples show that the retina can perform computations to detect ecologically important objects, allowing RGCs to transmit pre-processed information to the brain to coordinate behavior. Our data support a model in which retinal circuitry confers prey selectivity on a subset of RGCs, which transmit this information to two visual areas in the midbrain: AF7 and the SO layer of the optic tectum.

Based on the axonal branching pattern of its RGCs, we can identify AF7 as the parvocellular superficial pretectal nucleus (PSP). The PSP is a retinorecipient brain area innervated by RGC axons that also form an arbor in the most superficial retinorecipient layer of the tectum in goldfish<sup>45</sup>. PSP was one of the two possible adult brain areas suggested for AF7 based on its location in classical dye tracing work<sup>31</sup>. This nucleus was originally identified as the homologue of the lateral geniculate nucleus (LGN) in the

mammalian thalamus<sup>46</sup>, although this is controversial<sup>47</sup>. PSp has been anatomically described in several fish species, and is known to receive topographically organized retinal input<sup>45</sup>, although little functional information is available. Our group has recently demonstrated that AF7/PSp contains a retinotopic map. Most of the RGCs that project to this area reside in the temporal retina, creating a high-resolution representation of the anterior visual field<sup>36</sup>. This is the part of the visual environment in which the prey is usually located during prey capture behavior<sup>24</sup>.

Why might it be advantageous to route prey-responsive RGCs to both AF7 and the tectum? One possibility is that tectal neurons are responsible for directing the orienting movements towards a particular point in visual space, while AF7 neurons modulate or gate the tectal output, based on behavioral state (e.g. hunger, arousal). The tectum and its mammalian homologue, the superior colliculus, have been shown to be involved in the transformation of sensory information encoded in terms of visual space into the appropriate motor command<sup>48,49</sup>. The tectum has also been implicated in zebrafish prey capture in several recent studies. Ablation experiments have shown that the tectal neuropil and, more specifically, inhibitory tectal neurons in the most superficial layer play a role in prey capture<sup>23,50</sup>, and functional imaging experiments have found that tectal neurons are activated by moving paramecia<sup>32</sup>. Thus, the tectal circuits could translate a prey object's precise location in visual space into a swimming movement that results in pursuit of the prey.

We have identified a class of pretectal neurons that have dendrites in the AF7 neuropil and also project to the most rostral fifth of the tectum (Figure 7A-C, Figure 7 – Figure Supplement 1) which corresponds to the anterior visual field. If the motor map is roughly faithful to the visual map, tectal output neurons in this region could trigger prey capture forward swims. Within the pretectum, the AF7/tectum neurons also have processes in the non-retinorecipient neuropil next to AF7, which most likely corresponds to the magnocellular superficial pretectal nucleus (PSm). We hypothesize that these neurons could be integrating the retinal response to prey with information on behavioral state, and then providing excitatory input to the tectum when appropriate. These AF7 neurons project to a layer of the



tectum just ventral to SO, the tectal layer that receives prey-responsive RGC axons (Figure 5B, Figure 8). Tectal neurons with dendrites in these superficial layers could thus receive positional information from the raw retinal input in the SO, and excitatory input from the AF7 neurons that would release prey capture behavior only under certain conditions. However, at this point we do not know the response properties or type of neurotransmitter released by these neurons, so we can only speculate as to the input they provide to the tectum.

Modulation of the tectum by other visual areas is a common motif in vertebrate systems, and in many cases suppression or facilitation of tectal activity determines whether a behavioral response will occur. For example, a GABAergic projection from the basal ganglia to the superior colliculus is thought to act as a gate for the saccade-generating neurons of the superior colliculus, providing tonic inhibition whose cessation releases saccade movements<sup>51</sup>. Another example of tectal modulation is the local cholinergic and global GABAergic feedback to the tectum provided by the isthmus nuclei in birds<sup>52</sup>. The focal enhancement by cholinergic input has been shown to be necessary for the transmission of visual information to the area downstream of the tectum<sup>53</sup>. Finally, studies of prey capture in toads have identified a pretectal area that provides inhibitory input to the tectum, resulting in the preference for worm-like prey stimuli<sup>17</sup>. The sign of this modulation is opposite to that described in our model, but this might be explained by the different types of stimuli being selected by the two systems (i.e., elongated objects moving in the direction of their long axis, vs. small moving circles).

In addition to the class of AF7-innervating neurons that project to the tectum, we found another class which projects bilaterally to the nMLF and contralaterally to the caudal hindbrain (Figure 7D-F and Figure 7 – Figure Supplement 1). The nMLF is a cluster of reticulospinal neurons that are involved in controlling swim orientation<sup>38</sup>, as well as speed<sup>54</sup>. Two of the identified nMLF cells, MeLr and MeLc, have also been shown to be necessary for successful prey capture<sup>23</sup>. Projections from AF7 to the nMLF could therefore be involved in generating prey capture tail movements. The hindbrain also plays an important role in locomotion. Neurons in the hindbrain project to the spinal cord, and activation of the

caudal hindbrain has been shown to drive swimming behavior<sup>55,56</sup>. Thus far, the tectum has been considered the main output pathway to premotor centers in zebrafish. However, in other systems, multiple areas project to the premotor nuclei and may drive behavior independently or direct different aspects of a behavior; for example, in primates, both the frontal eye fields and the superior colliculus provide input to the brainstem regions controlling eye movements<sup>57</sup>. It remains to be seen what role the neurons projecting from AF7 to the nMLF and hindbrain might play in the various components of prey capture behavior.

Our results identify a specific pretectal, retinorecipient region as a key component of the prey detection circuit. They also point toward a series of parallel and interconnected pathways between multiple areas involved in this elementary form of object recognition. Finally, they identify potential anatomical links of the visual network to midbrain and hindbrain areas that serve to coordinate the locomotor maneuvers involved in capturing prey. Further studies should shed light on what role each area plays in the behavior and how they interact.

## Materials and methods

### Fish

Embryos were raised in Danieau's solution (17 mM NaCl, 2 mM KCl, 0.12 mM MgSO<sub>4</sub>, 1.8 mM Ca(NO<sub>3</sub>)<sub>2</sub>, 1.5 mM HEPES) at 27.5° C on a 14/10 light/dark cycle. Wild type TL larvae were used for behavioral experiments, and *nacre* mutants were used for imaging. Since gonadal differentiation has not occurred at this stage, males and females were used indiscriminately. All animal procedures conformed to the institutional guidelines of the Max Planck Society and the local government (Regierung von Oberbayern).

### Transgenic lines

The following transgenic lines were used: *Tg(Atoh7:Gal4-VP16)s1992t* (written as *Ath5:Gal4*), *Tg(UAS:Dendra-Kras)s1998t*, *Tg(UAS:mCherry)*, *Tg(pou4f3:Gal4, UAS:mGFP)* (a.k.a. *BGUG*), *Gal4<sup>s1171t</sup>*, *Tg(Isl2b.2:Gal4-VP16)* and *Tg(elavl3:GCaMP5G)*. To construct the *UAS:GCaMP6s* line, a fragment encoding GCaMP6s (Addgene) was cloned into a *14xUAS, pTol2* plasmid.

### Behavioral experiments

At 5 dpf, each dish of larvae was fed about 2 ml of a dense culture of paramecia. At 6 dpf, the larvae were embedded in 2.5% low melting point agarose (Invitrogen) in Danieau's solution and positioned 3 mm from the edge of a 35 mm Petri dish lid. After the agarose had set, the dish was filled with Danieau's solution and some of the agarose was cut away, leaving the tail caudal to the swim bladder free to move. After embedding, larvae were kept at 27.5° C for 48 hours. Behavioral experiments were conducted at 8 dpf in a 27.5° C chamber. For virtual prey experiments, larvae with a prey capture score (percent of the trial spent in prey capture bouts) of less than 30% for the 3° stimulus were excluded from the analysis.

Visual stimuli were designed using a custom program in the Python-based Vision Egg software<sup>58</sup>. The stimulus was a white dot on a black background, moving horizontally from left to right. Stimuli were presented on a 12 x 9 mm OLED Microdisplay (Emagin) covered with three magenta Wratten filters (Edmund Optics) and positioned 1 cm from the larva. Larvae were illuminated from below with an IR light source. We used a high speed camera (Photonfocus) to record tail movements at 300 frames/second (f/s), with a resolution of 300 x 300 pixels.

For behavioral experiments with paramecia, we embedded 6 dpf larvae in the center of a 35 mm Petri dish and cut away some of the agarose in front of the eyes by making an incision perpendicular to the body axis 1 mm from the head. The tail below the swim bladder was also freed. As we did for the virtual prey experiments, we waited 48 hours after embedding to test behavior. We added a few drops of paramecia (*Paramecium multimicronucleatum*, Carolina Biological Supply Company) to the dish and recorded at 300 f/s for five minutes. The procedure was repeated a few hours after laser ablations. For post-ablation behavioral experiments, the experimenter was blinded as to whether the animal was in the AF7 or AF9 ablation group.

To test the OMR, each embedded larva was positioned in an arena surrounded by three LED screens (5.5 x 7.5 cm). Gratings moving leftward at 20°/s were displayed on all three screens to produce turns. Stimulus presentation was controlled with a custom LabVIEW script, and tail movements were recorded at 250 f/s. The same procedure was repeated a few hours after laser ablations. To measure the number of swims, we digitized the tail as described below and used a thresholding operation on the smoothed derivative of the tail bend angle to identify swim bouts.

### **Tail digitization**

We developed a custom Python program that quantifies the tail position in each frame as a series of points, with approximately 40 points covering the tail. The program uses the OpenCV library to load videos. At the start of each video, the user is queried to select the base of the tail. From that point, the

program iterates through the tail in each frame, taking a slice through the image where the next tail midpoint is expected to be. This slice is smoothed, convolved with a tail-like kernel, and the maximum is taken to determine the midpoint of the tail. This sequence is repeated until the end of the tail, which is detected using a threshold for change in luminance across the slice. To improve accuracy, the width and contrast of the tail in the first frame of video are characterized and used to refine the tracking for the rest of video.

### **Support vector machine (SVM)**

The SVM code was written in Python. The SVM and cross-validation procedures were provided by the scikit-learn library <sup>59</sup>, which uses LIBSVM <sup>60</sup> for the SVM implementation. To avoid testing and training on the same dataset, we used five-fold stratified cross-validation for training <sup>61</sup>. For this validation, data are split into 5 groups of approximately equal mean. One group is reserved for testing while the others are used for training, and this procedure is repeated five times before the results are combined. We quantified 16 parameters for each bout. A radial basis function (RBF) kernel shape was used to draw the decision boundaries. A subset of the 16 parameters was selected by plotting the accuracy vs. number of parameters. The point that maximized performance while minimizing the number of parameters was selected. For the virtual prey SVM, 5 parameters were optimal (Figure 1 – Figure Supplement 1).

The virtual prey SVM was trained on 248 prey bouts and 121 spontaneous bouts. The paramecia SVM was trained on 273 prey bouts and 396 spontaneous bouts.

For the parameters described below, “tail angle” is the angle of deflection of tail center of mass, “tail tip” is defined as the last eight points of tail, and “tip angle” is the angle of a line down through the last eight points of the tail, with respect to vertical. Parameters 1-5 were used in the virtual prey SVM; parameters 1-6 were used in the paramecia SVM.

1. 'maximum tail curvature': maximum over the bout.

2. 'number of peaks in tail angle'
3. 'mean tip angle': absolute value of tip angle in each frame, averaged across the bout.
4. 'maximum tail angle': maximum of the bout
5. 'mean tip position': average position of last 8 points in the tail (horizontal deflection as a fraction of the tail length)
6. 'number of frames between peaks': mean (over bout) number of frames between peaks in the tail angle.
7. 'medium frequency power of tail angles': power of middle frequency band of fourier transform of tail angle.
8. 'low frequency power of tail angles': power of low frequency band of fourier transform of tail angle.
9. 'tail angle vs tip angle': mean (over bout) difference in angle of deflection between tail center of mass and tip center of mass.
10. 'tail angle vs. tip angle at frame of maximum tail angle': difference in angle of deflection between tail center of mass and tip center of mass in the frame with the maximum tail angle.
11. 'variance in tail angle': over entire bout.
12. 'mean tail curvature': mean curvature over entire bout.
13. 'mean tail tip angle': mean over entire bout
14. 'mean tail position': average position of tail from 12<sup>th</sup> point to end (horizontal deflection as a fraction of the tail)
15. 'mean tail curvature vs. tail angle': mean (over bout) difference between tail curvature and tail angle
16. 'maximum tip horizontal deviation'

## Two-photon Calcium imaging

Larvae were embedded as for behavioral experiments. Imaging experiments were performed at 7 or 8 dpf. Stimuli were presented on the same type of OLED screen as for behavior, also covered with three magenta wratten filters. Imaging was performed on a movable objective microscope (Sutter) using a 40x objective (Olympus). Excitation light was generated by a Ti: Sapphire laser (Coherent) tuned to 920 nm. Time series were recorded at 3.6 Hz with a resolution of 128x128 pixels. We used a red LED to provide some ambient light to the larva during imaging, and we heated the microscope box to 27° C.

## Confocal imaging

In order to record the response to paramecia in RGC axons, we embedded larvae in the center of a dish as for the paramecium behavior experiments and again cut away the agarose in front of the eyes and below the swim bladder. Since bright ambient light was required to allow the larvae to see the paramecia, we performed these imaging experiments on a confocal microscope (Zeiss 780) rather than a two-photon. Time series were acquired at a rate of 3.3 Hz and a resolution of 128x128 pixels. Experiments were performed with overhead lights on and a white LED illuminating the dish to enhance the visibility of the prey. Temporal series of the same field of view with and without paramecia were joined together. The resulting stack was registered with StackReg in Fiji to reduce motion artifacts and pixel misalignment between the two acquisitions. From the raw data,  $\Delta F/F$  was computed pixel-wise by a custom Matlab routine. Because we did not know when a paramecium was within the field of view, we calculated the baseline  $F$  for each pixel as the value of that pixel during a period of low activity. This was defined as the 8<sup>th</sup> percentile of the pixel's fluorescence over a sliding window of 25 frames. Maximum intensity projections of  $\Delta F/F$ , computed independently for the two segments of the stack (before and after addition of paramecia), were divided to give the  $\Delta F/F$  ratio between the two conditions for the pseudocolor image shown in Figure 4D. From the  $\Delta F/F$  maximum intensity projections, the average values over regions of interest corresponding to AF7 and AF9 were computed to compare the activity between the two

arborization fields. During the 30 second windows we imaged over, occasional responses were observed in AF7 and 9 in the absence of paramecia added to the bath. This could be the result of spontaneous activity, or small objects, e.g. bubbles or debris, floating in the solution.

## **RGC Anatomy**

*UAS:mCherry*, *BGUG*, *Islet2b:Gal4* (or *Ath5:Gal4*) larvae were treated with 0.2 mM 1-phenyl-2-thiocarbamide (PTU) from 1 dpf to reduce pigmentation of the retina. Larvae with sparse GFP in AF7 were identified, and confocal stacks of the axonal projections were acquired. To visualize dendritic arbors in the retina, vibratome sectioning was performed as previously described<sup>62</sup>. Briefly, 50  $\mu$ m vibratome sections were cut from larvae embedded in gelatin/albumin/sucrose and stained with a chick anti-GFP primary antibody (GeneTex, Catalog number GTX13970) and an Alexa 488 anti-chick secondary antibody (Invitrogen, Catalog number A-11039).

## **Two-photon laser ablation**

Ablations were performed in 8 dpf *Ath5:Gal4 UAS:Dendra*, *nacre* larvae, using the same two-photon microscope as for the imaging experiments. We found that treating the larvae with 0.1 mM PTU starting at 1 dpf was helpful in preventing tissue damage during ablation. Axons were killed by scanning an 850 nm beam for 750 ms over a 3 x 3  $\mu$ m area. Post-objective laser power was 80 mW/mm<sup>2</sup>. 4-5 scans were usually sufficient to ablate the AF7 neuropil. A Z stack of the area was taken 24 hours later to assess completeness of the ablation, and larvae with less than 80% of the volume ablated bilaterally were not used for the analysis. As a control, we ablated a similar volume of AF9 neuropil, with 4-5 scans.

## **Electroporations**

6 or 7 dpf larvae were embedded in agarose, immersed in extracellular solution and anesthetized with 0.02% tricane. Larvae with the transgenes *Ath5:Gal4*, *UAS:GCaMP6s*, and for some experiments *Gal4<sup>s117lt</sup>* were used. Patch pipettes (25-32 M $\Omega$ ) were filled with 15% tetramethylrhodamine dextran



(3000 MW) in intracellular saline. AF7 and 9 were used as landmarks to locate AF7 cells. Following contact with a cell, a voltage train was applied (1 s duration, 150 Hz, 1.4 ms pulse width, 2-6 V) by an Axon Axoprotector (Molecular Devices). Labeled cells were imaged on a Zeiss LSM780 confocal microscope.

### **Statistical analysis**

The Jarque–Bera test was used to determine whether data were normally distributed. The *t*-test was used to evaluate normally distributed data. For non-normally distributed data, we used the Wilcoxon rank sum test. Variance was tested and found to be similar between groups by Levene's test.

**Acknowledgments** We thank Estuardo Robles for help tracing neurons; Fumi Kubo for assistance with two-photon ablations; Marco Dal Maschio for help analyzing confocal data; and Cris Niell and members of the Baier lab for feedback on the manuscript.

## Supplementary Figures

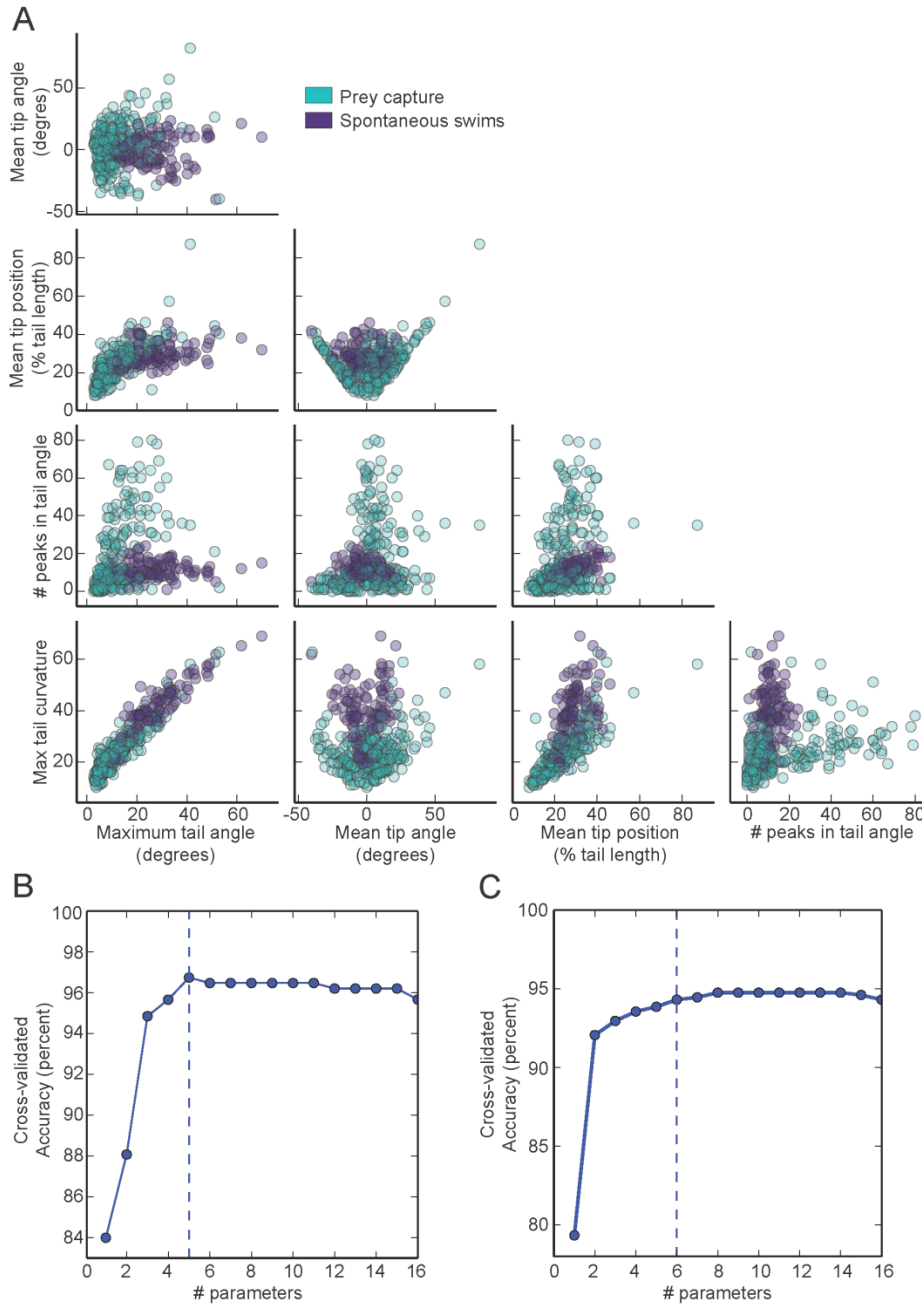


**Figure 1 – Figure Supplement 1. Prey capture and spontaneous behavior can be classified using five parameters.** (A) Each parameter used in the virtual prey SVM is plotted vs. the other four. (B) Accuracy of the virtual prey SVM as more parameters are used to classify the bouts as prey capture or spontaneous swims. The dotted line represents the number of parameters used in the final version. The parameters plotted were: 1. Maximum tail curvature, 2. Number of peaks in tail angle, 3. Mean tip angle, 4.

Maximum tail angle, 5. Mean tip position. (C). Accuracy of the parametric SVM plotted vs. number of parameters. The parameters shown here were 1. Mean tip angle, 2. Maximum tail curvature, 3. Number of peaks in tail angle, 4. Mean tip position, 5. Mean number of frames between peaks, 6. Maximum tail angle.

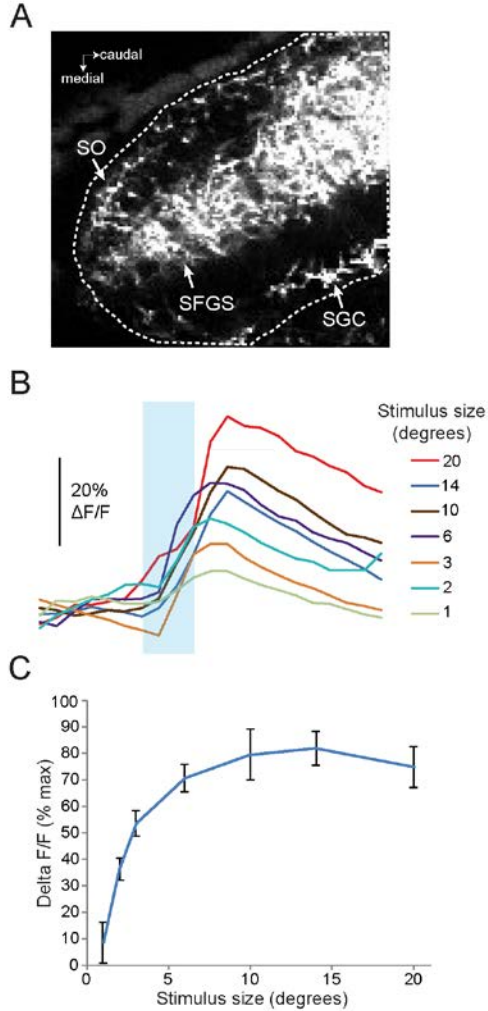


**Figure 3 – Figure Supplement 1. Response of RGC axons in the tectum to stimuli of varying sizes.**

(A) Baseline fluorescence of RGC axons in the anterior half of the tectum, 50  $\mu$ M below the dorsal surface of the tectum. Dotted line shows ROI, which includes the SO, SFGS, and SGC. (B) Traces showing responses to a range of different size stimuli in RGC axons in the anterior tectum of one larva.

*Ath5:Gal4, UAS:GCaMP6s* larvae were used for these experiments. (C) Average response of five larvae to stimuli 1-20 degrees in diameter.

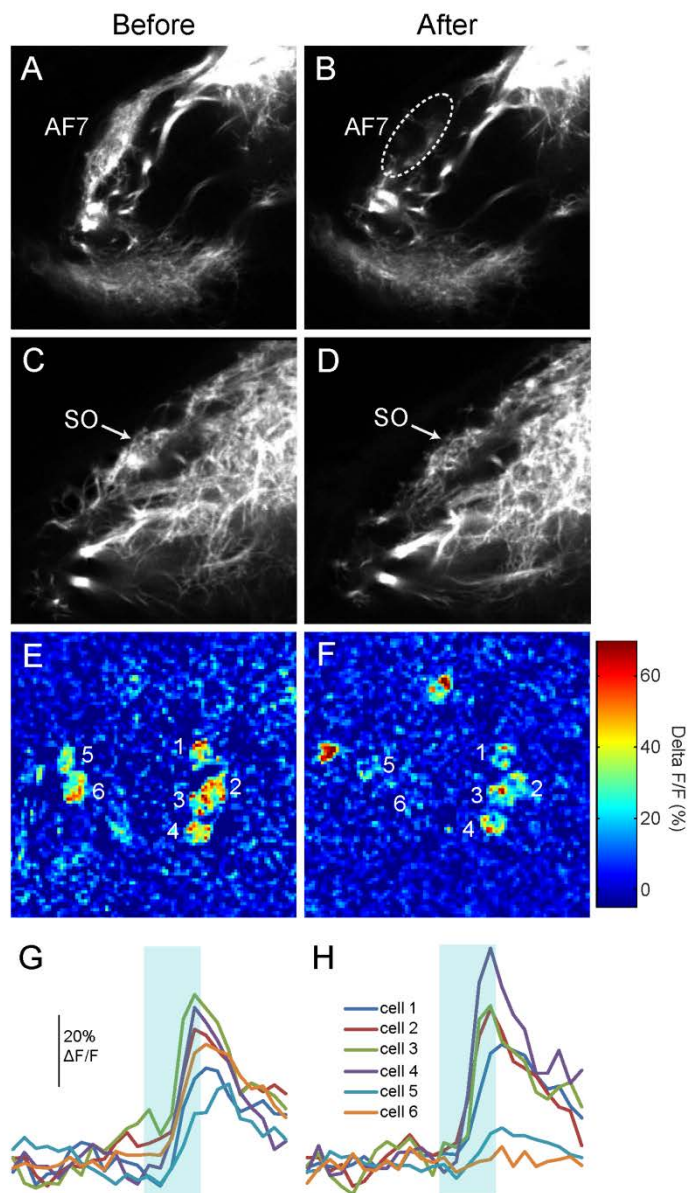


**Figure 6 – Figure Supplement 1. RGC axons in AF7 and the tectum after AF7 ablation. (A)**

*Ath5:Gal, UAS:Dendra* transgenes label RGC axons in AF7 and 9. **(B)** The same larva three hours after laser ablation of AF7. **(C)** RGC axons in the tectum in the same larva as above, before ablation. **(D)** SO axons three hours after AF7 ablation. **(E)** Responses of tectal neurons in the same larva as in A-D.

Periventricular neurons of the tectum labeled by *elavl3:GCaMP5G* responded to a prey stimulus (3° dot moving at 90°/s). **(F)** The same field of view after AF7 ablation. **(G)** Traces showing the responses of the individual cell bodies. **(H)** Responses in the same six cells after AF7 ablation.

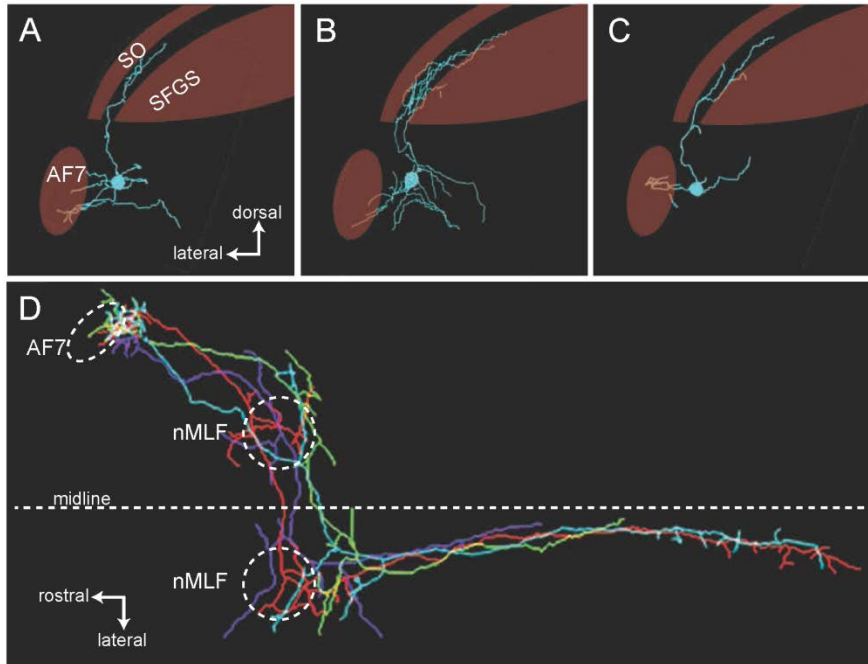


**Figure 7 – Figure Supplement 1. Examples of AF7 neurons. (A-C).** Tracings of example neurons with projections in AF7 and the tectum. **(D)** Overlay of tracings from four neurons with arbors in AF7 and the nMLF. In two cases, the projections toward the hindbrain became too faint to follow.

# **A visual pathway for looming-evoked escape in larval zebrafish**

Incinur Temizer<sup>1</sup>, **Joseph C. Donovan**<sup>1,2</sup>, Herwig Baier<sup>1\*</sup>, Julia L. Semmelhack<sup>1</sup>

<sup>1</sup>Max Planck Institute of Neurobiology, Am Klopferspitz 18, 82152 Martinsried, Germany

<sup>2</sup>Program in Neuroscience, University of California at San Francisco, San Francisco, CA 94143, USA

\*Contact: [hbaier@neuro.mpg.de](mailto:hbaier@neuro.mpg.de)

## SUMMARY

Avoiding the strike of an approaching predator requires rapid visual detection of a looming object, followed by a directed escape maneuver. While looming-sensitive neurons have been discovered in various animal species, the relative importance of stimulus features that are extracted by the visual system is still unclear. Furthermore, the neural mechanisms that compute object approach are largely unknown. We found that a virtual looming stimulus, i.e., a dark expanding disk on a bright background, reliably evoked rapid escape movements. Related stimuli, such as dimming, receding, or bright looming objects, were substantially less effective, and angular size was a critical determinant of escape initiation. Two-photon calcium imaging in retinal ganglion cell (RGC) axons revealed three retinorecipient areas that responded robustly to looming stimuli. One of these areas, the optic tectum is innervated by a subset of RGC axons that respond selectively to looming stimuli. Laser-induced lesions of the tectal neuropil impaired the behavior. Our findings demonstrate a visually mediated escape behavior in zebrafish larvae exposed to objects approaching on a collision course. This response is sensitive to spatiotemporal parameters of the looming stimulus. Our data indicate that a subset of RGC axons within the tectum responds selectively to features of looming stimuli, and that this input is necessary for visually-evoked escape.

## INTRODUCTION

A key function of the visual system is to extract ecologically relevant information from the environment in order to initiate appropriate behavior. A looming stimulus is a two dimensional representation of an object approaching on a collision course, which may represent a predator or an obstacle <sup>63</sup>. The behavioral response to looming stimuli is remarkably conserved across animal species <sup>63-68</sup> including humans <sup>69</sup>, and usually involves stereotyped defensive responses, such as freezing or escape. Given the importance of avoiding predation, we would expect that evolution has selected for a fast, hardwired neural pathway for the detection of looming. Indeed, specialized looming-sensitive neurons have been found in visual areas in locusts <sup>70,71</sup>, *Drosophila* <sup>72</sup>, amphibians <sup>73</sup>, and pigeons <sup>64</sup>. The visual parameters that are commonly used to detect looming threats include estimated time to collision <sup>64</sup> and a specific angular size of a looming object on the retina <sup>71,74,75</sup>.

Based on the rapidly expanding size of looming stimuli, a looming detector would require a large receptive field, in which inputs from an array of smaller units are pooled. The smaller units might be detectors of luminance change (e.g. dimming) or of sweeping edges. Their activation in a center-to-periphery sequence would mirror an expanding disk and thus signal looming. It is unclear where along the visual pathway the smaller units and the looming detectors reside. In mice, at least one type of RGC that is specialized for detecting approach motion has been described <sup>76</sup>, although it is not known how specific this cell type is for looming stimuli, and whether it is involved in defensive behavior <sup>77</sup>.

To begin to investigate the neural basis for visually-evoked escape in zebrafish larvae, we first explored the behavioral response to looming stimuli in semi-restrained zebrafish larvae. A head-restrained preparation facilitates stimulus control and tracking of tail kinematics. We found that specific parameters of the looming stimulus are critical to elicit escape maneuvers <sup>78-81</sup>. Furthermore, we demonstrated that larvae initiate escapes when the angular size of the looming stimulus surpasses 20°. To identify the retinorecipient areas responding to behaviorally relevant stimuli, we imaged Ca<sup>2+</sup> signals in RGC axon



terminals during stimulus presentation. We identified three brain areas in which RGC axons responded to looming stimuli. Pixelwise analysis allowed us to detect a subset of these inputs that selectively responded to behaviorally relevant stimuli. Through targeted laser ablations in the tectal neuropil, we showed that an intact tectum plays an important role in looming-triggered escapes. Together, our work has defined the visual stimulus parameters that trigger escape and established the retinotectal neuropil as the likely site of looming computation in the zebrafish brain.

## RESULTS

### An expanding disk triggers escape in zebrafish larvae

To investigate the escape behavior evoked by looming stimuli, we developed a head-restrained behavioral paradigm in which larvae were embedded in agarose and their tails were freed so that swimming behavior could be recorded with a high-speed camera (Figure 1A). Initial experiments showed that binocular presentation of a looming dark disk, which starts as a small dot and expands until it fills the whole screen, is an effective escape stimulus. In this stimulus configuration, we found that larvae performed the typical C-bend fast starts that were previously described in response to acoustic or head-tactile stimuli<sup>82,83</sup> (Figure 1B). The C-bend turns the larva away from the aversive looming stimulus, and is followed by an immediate fast forward swim, another kinematic feature of escape<sup>78</sup>, which propels the larva away from the looming object. The time from the onset of tail bending to the moment of maximum tail curvature varied between 9 ms and 18 ms (Figure 1B), similar to escapes evoked by tactile stimuli<sup>78</sup>. This C-bend and forward swim sequence was also observed in freely swimming larvae when presented with the looming stimulus (Supplemental Movie 1).

To verify that the visually evoked escape we observe involves the retina, rather than alternate pathways such as deep brain photoreceptors or the pineal organ<sup>84,85</sup>, we tested the escape response of *lakritz* mutants, which lack RGCs<sup>86</sup>. We observed that *lakritz* mutants did not perform any escapes in response to looming stimuli (Supplemental Figure 1), confirming that looming-triggered escapes require

the retina. Notably, *lakritz* mutants are still capable of escapes in response to tactile cues (Supplemental Movie 2).

### **Monocular stimulation evokes escapes away from the looming disk**

Next, we asked whether larvae are able to direct their escape swim away from an approaching object, by investigating the relationship between escape direction and stimulus position within the visual field (Figure 1C). Looming stimuli were presented in the center, left, and right of the larva's visual field. Moving looming stimuli, which started on the left and moved to the right while looming (or vice versa), were also presented (Figure 1C). Quantification of initial escape bend direction demonstrated a strong preference of the larvae to swim away from the looming stimulus. For example, both the stationary looming stimulus on the right and a left to right moving looming stimulus reliably evoked leftward escapes (Figure 1C). We observed an overall preference for leftward escape bends in these larvae. Behavioral laterality has been documented previously<sup>87</sup> and could be the explanation for this bias.

The responses to lateral stimuli suggested that purely monocular stimuli might be able to induce escape behavior. We presented looming stimuli on a screen visible to only one eye (Figure 1B), and found that the monocular stimulus evoked escape responses that were kinematically similar to those evoked by binocular stimuli (Supplemental Movie 3). When the right eye was presented with the looming stimulus, the larva typically performed an escape with the initial bend to the left. Monocularly triggered escapes tended to have a lower maximum bend angle than binocular escapes, perhaps because a monocular looming object is approaching from the side (as opposed to the front), meaning that the larva does not need to make as sharp a turn to swim away from the object. This experiment also showed that an increase in angular size detected by one eye gives sufficient information to the brain to trigger an escape. The use of monocular stimuli allows the contralateral side to be used as a within fish control for unilateral ablation experiments. Thus, for the remainder of this work we focus on monocularly induced escapes.

## **Escape swims are kinematically distinct from spontaneous swims**

In the absence of visual stimuli, larvae occasionally perform spontaneous swims. Comparison of the two types of behaviors showed that escape swims are characterized by movement of more rostral tail segments and a higher tail beat frequency than spontaneous swims, as revealed by dynamic bend angle plots (Figure 1D, Supplemental Movie 4). We used a quantitative thresholding approach to objectively distinguish spontaneous and escape swims. First, the tail was digitized as previously described<sup>88</sup>, and we extracted tail shape and kinematics from 350 swimming bouts performed in the presence (escape swims) or absence (spontaneous swims) of looming stimuli. The two parameters of maximum tail bend and average tail beat frequency revealed a clear separation between spontaneous and escape swims (Figure 1E). Escape swims had larger tail bend angles (escape: 61.0°, spontaneous: 38.3°, Mann-Whitney U test,  $p$ -value  $< 1.0 \times 10^{-5}$ ) and higher tail beat frequencies (escape: 45.5 Hz, spontaneous: 24.6 Hz, Mann-Whitney U test,  $p$ -value  $< 1.0 \times 10^{-5}$ ).

We classified as escape any swim bout that met the following three criteria: 1) initial escape bend direction away from the stimulus; 2) average tail beat frequency  $\geq 35$  Hz or maximum bend angle  $\geq 70^\circ$ ; 3) occurring before the collision with the approaching object (when angular size reaches  $180^\circ$ ). These conservative criteria allowed classification of escape swims with high accuracy (false positive rate 0%, false negative rate 7.2%). Looming-evoked escapes habituate after repeated display of the stimulus in many species<sup>67,74,75</sup>, and we also observed that zebrafish larvae would eventually habituate and cease responding. Thus we excluded trials including and following four consecutive unsuccessful trials.

## **Escape responses are most effectively elicited by a dark looming disk on a bright background**

Which parameters of the looming stimulus elicit escape behavior? We tested five different stimulus conditions; a looming dark disk on a bright background, a looming bright disk on a dark background, a receding bright disk on a dark background, a receding dark disk on a bright background and a uniformly dimming stimulus (Figure 2A).

A dark disk that expands from 2° to 48° of the visual field (hereafter referred to as dark looming) is the most effective stimulus, evoking escapes in more than 80% of the trials (Figure 2B). We asked whether the luminance change alone was sufficient to evoke an escape, and found that a 48° disk that was dimmed with identical temporal dynamics did not elicit escapes. The same was true for a disk that dimmed more slowly, with constant luminance decrements over time (linear dimming). Similarly, a bright receding disk (receding bright), with a luminance profile that matched the dark looming disk, was also ineffective, suggesting that dimming alone, or a combination of dimming and moving edges, are insufficient to induce escape behavior (Figure 2B). We next tested whether a looming bright disk on a dark background (bright looming) would trigger escapes. This stimulus evoked escapes in about 25% of the trials, suggesting that there are mechanisms that extract global expansion from a visual scene, regardless of the sign of stimulus contrast (Figure 2B). Finally, we tested a receding dark disk on a bright background (dark receding) to determine whether a decrease in the size of a dark spot would trigger the behavior. We did not observe any escapes in response to a receding dark disk (Figure 2B), suggesting that expansion is an important parameter of the looming stimulus.

### **Probability of escape is invariant over slow-to-moderate approach velocities**

Our looming stimulus models an object approaching at a constant velocity, which is fully described mathematically by the object's size-to-speed ratio ( $l/v$ ),  $l$  being the half-width of the object that is approaching at constant speed,  $v$ . Such constant velocity stimuli have been widely used to investigate escape responses in birds, fish and insects<sup>64,66,71,89</sup>. To further explore the behavioral correlates of the looming stimulus, we varied  $l/v$  (Figure 3A). We tested a range of  $l/v$  values: 30 ms, 60 ms, 90 ms, 120 ms and 150 ms, which correspond to approach speeds of 1, 0.5, 0.33, 0.25, 0.2 cm/s for an object with a radius of  $l = 3$  cm. We found that the probability of escapes was consistently high for  $l/v$  values above 30 ms. For the rapidly looming stimulus of  $l/v = 30$  ms, however, there was a decrease in escape probability (Figure 3B), suggesting that the expansion speed of this stimulus might exceed the detection limit of the escape circuitry.

### **Escape is evoked once the disk exceeds a threshold size of approximately 20°**

To dissect the stimulus parameters that are correlated with escape onset, we looked at the timing of responses for the range of  $l/v$  values. Strikingly, examining the remaining time to collision at the escape behavior onsets across  $l/v$  values (Figure 3C) revealed a strong linear relationship. This linear relationship suggests that escape is initiated when the stimulus reaches a threshold angular size on the retina, rather than at a fixed time before collision with the approaching object<sup>71</sup>. We computed this threshold angular size as  $21.7 \pm 2.5^\circ$  (mean  $\pm$  S.E.) based on the slope of the linear regression in Figure 3C. Similarly, a linear regression on the angular size at escape onset across  $l/v$  values (excluding  $l/v = 30$  ms, which does not reliably trigger escape) supports the concept of an angular size threshold of approximately 20° (Figure 3D).

To directly test this angular size threshold, we devised another set of experiments with truncated looming stimuli, which expand until a certain size is reached and then stop. Looming stimuli truncated to 15° or smaller were relatively ineffective at triggering the behavior, but did occasionally elicit an escape (Figure 3E). However, stimuli with final angular sizes above ~20° reliably induced escape. We fitted the data with a sigmoid, and confidence intervals placed the center of the sigmoid, (or point of maximum slope), between 17.5 and 20.7° (Figure 3E, dashed red lines). These data support the idea that the angular size of the stimulus is a critical parameter for computing approach.

For stimuli that approach with constant speed, angular size and speed are interrelated and thus difficult to disentangle. We generated a linearly expanding stimulus in which angular expansion was constant, unlike the constant approach speed stimuli (e.g. Figure 3A) in which the angular size expands exponentially. This stimulus expands more slowly than the constant approach speed looming object, particularly toward the end of the stimulus. We found that the 20°/s looming stimulus triggered more escape responses than the slower or faster stimuli (Figure 3F), indicating that the expansion speed of the looming stimulus is an important factor in evoking escape.

## Visual areas AF6 and AF8 respond to looming as well as dimming stimuli

Next we used functional imaging to determine whether there are RGCs that respond to looming stimuli. RGC axons innervate nine distinct arborization fields (AFs) in the larval brain, in addition to the optic tectum (Supplemental Figure 2) <sup>90,91</sup>. We performed two-photon calcium imaging of RGC axon terminals in larvae expressing the calcium indicator GCaMP6s under control of the RGC-specific promoter *Islet2b*. We presented a dark looming stimulus that was highly effective in triggering escapes ( $l/v = 60$  ms). While displaying the looming stimulus monocularly to the larvae and scanning through the contralateral AFs, we detected robust responses in only two extratectal areas, AF6 and AF8 (Figure 4A-C). To assess the stimulus selectivity of these areas, we presented the array of stimuli used for the behavior experiments. Additionally, to compare the responses to a looming stimulus with different kinematics, we tested a linearly looming stimulus (linear looming) which robustly triggered the escape behavior ( $20^\circ/\text{s}$  angular expansion; see Figure 3F). During each trial, there was first a blank screen, followed by the appearance of the stimulus (Figure 4B, "Stim on"), then the expansion, contraction, or dimming of the object ("Start") until the stimulus ceased changing ("End") and finally disappeared ("Stim off").

We found that AF6 RGC axons responded robustly to the dark looming stimulus (Figure 4A). AF6 RGCs were also activated by a linear looming stimulus (Figure 4A), which might be expected as this stimulus also evokes escape and is distinct from dark looming only in its temporal evolution. In addition, AF6 RGC axons responded to the dimming stimulus (Figure 4A). For these three decreasing luminance (OFF) stimuli, the peak AF6 response occurred during the expansion or darkening of the dark disk (Figure 4B). We also observed a slight response to the dark receding stimulus, but the plot of the time course of the response shows that the AF6 RGC axons were responding to the initial appearance of the dark stimulus, not its receding motion (Figure 4B). We also investigated the response of AF6 to a bright looming stimulus, which occasionally evoked escapes (Figure 2B), and found that AF6 was not responsive to this stimulus (Figure 4A).

We also observed responses to the looming stimulus in a more dorsal plane containing AFs 7, 8, and 9 (Figure 4C). Like AF6, AF8 axons responded to both looming dark and dimming (OFF) stimuli. Interestingly, AF9 RGCs responded vigorously to only looming bright and receding bright (ON) stimuli. For the receding bright stimulus, the time course of the response shows that the AF9 axons were activated by the appearance of the bright stimulus, not the receding motion (Figure 4D). Some AF9 axons were activated by dark looming and dimming stimuli, but this response was relatively weak. The third AF in this plane, AF7, was only weakly activated by bright looming stimuli and did not respond to any of the darkening stimuli (Figure 4C).

### **Pixelwise analysis reveals a generalized OFF response of RGCs innervating AF6 and AF8**

To determine whether individual RGC axons in these AFs are selective for any of the stimuli, we further analyzed the responses of single pixels within the imaging data. Each pixel corresponds to an area of 0.3 to 0.6  $\mu\text{m}^2$ , which is in the range of single presynaptic boutons of RGC axons<sup>92</sup>. We compared the pixel responses to dark vs. bright looming by subtracting each pixel's bright looming response from its dark looming response. This revealed that most AF6 and AF8 pixels responded to the dark looming stimulus, whereas AF9 pixels were activated by bright looming (Figure 5A). An analysis of the temporal dynamics of six example pixels (two from each AF) showed that responses to the dark looming and dimming stimuli occurred during the darkening (OFF) phase of the stimulus (Figure 5B), while the responses to the receding stimuli occurred at the initial appearance of the stimulus ("Stim on", Figure 5B).

We next plotted the individual pixel responses to dark looming vs. all other stimuli to assess whether this more fine-grained analysis would reveal selectivity for different stimulus features. Comparing the responses to dark looming and dimming for AF6 and AF8, we see that pixels that responded to looming dark also responded to dimming stimuli (Figure 5C, panel 1). We found that most AF6 pixels responded equally to looming and linear looming stimuli (Figure 5C, panel 4). Interestingly, the scatter plot of pixel responses in AF9 suggests two distinct populations; one that responded to

decreasing luminance stimuli, and a larger population that was activated by the increases in luminance that occurred during the looming and receding bright stimuli (Figure 5C, panels 11-15). Based on this analysis, AF6 and AF8 seem to be predominately innervated by RGCs that respond to decreases in luminance, rather than behaviorally relevant parameters such as the expansion of the looming object.

### **Functional imaging reveals looming-specific subsets of RGC axons in the tectal neuropil**

We expanded our analysis of looming-responsive RGCs by performing imaging experiments in the optic tectum. The tectum receives highly organized RGC input, with each axon arborizing in one of the ten layers of visual neuropil<sup>93</sup>. In response to the dark looming and linear looming stimuli, we saw robust activation in several layers of the stratum fibrosum et griseum (SFGS; Figure 6A) and often the stratum griseum centrale (SGC; Supplemental Figure 3). The dimming stimulus also activated some SFGS axons, but this response was confined to the deepest layer of SFGS, SFGS6 (Figure 6A). All of these stimuli primarily evoked responses in the central (rather than the more anterior or posterior) SFGS (Figure 6A). This confined response could be due to the fact that our screen spanned 62° of the monocular visual field. The looming stimulus therefore did not sweep across the most nasal and most temporal regions of the retina, which provide input to anterior and posterior tectum, respectively. In contrast, the two bright stimuli, bright receding and bright looming, both activated a larger swath of the tectum throughout the anterior/posterior axis (Figure 6A). This broad response could be due to the activation of RGCs that have very large receptive fields, or respond to overall luminance. Indeed, in the case of the receding bright stimulus, the response occurred at the appearance of the large bright object, not during the receding motion, indicating that these RGCs are likely activated by the increase in luminance (Figure 6B). In addition, we imaged the tectal neuropil responses to the dark receding stimulus and a dark flashed disk of 48° (Supplemental Figure 4), which induced similar activation patterns to the bright receding and dimming stimuli, respectively.



Pixelwise analysis of the tectal imaging data revealed populations of pixels that responded to decreasing or increasing luminance stimuli (Figure 6C), as in AF6, AF8 and AF9. However, unlike in the extratectal AFs, many dark looming-responsive pixels had a negligible response to dimming (e.g. Figure 6C, pixel #1). Indeed, the majority of looming-responsive pixels in the tectum had a weaker response to dimming than to looming (Figure 6D, panel 1). We calculated the ratio of the responses to looming over dimming for each pixel, and found that this ratio was significantly higher for tectal pixels compared to extratectal AF pixels (Mann-Whitney U test,  $p = 6.9 \times 10^{-4}$ ,  $< 1 \times 10^{-10}$ , and  $1 \times 10^{-10}$  for tectum vs. AF6, AF8 and AF9 respectively.)

Finally, we visualized the location of dark looming-selective pixels within the tectum by subtracting each pixel's dimming response from its dark-looming response (Figure 6E). This analysis confirmed that many of the pixels in the SFGS responded selectively to the expansion of the dark object, rather than to the change in luminance. When we plotted dark looming-selective pixels in the extratectal AFs with the same scale, we saw only a few pixels in AF6 with a slight preference for looming (Figure 6E). These results suggest that, unlike AF6 and AF8, the tectum receives substantial input from looming-specific RGCs.

### **Lesions of the tectal neuropil impair looming-evoked escapes**

Since our imaging experiments identified tectal RGC axons that responded specifically to the behaviorally relevant looming stimuli, we focused on the tectum as the potential neural substrate for escape behavior. To test the necessity of retinotectal projections for looming-evoked escape, we performed laser ablations of the tectal neuropil. Ablations were performed unilaterally in the left tectum of larvae expressing the fluorescent protein Dendra in RGCs. We selectively targeted the RGC axon bundles entering the tectum (Figure 7A). The contralateral tectum served as a control. Lesioning of axons subsequent to targeted ablations was immediately detectable (Figure 7A; post-ablation). All larvae were imaged 24h after the ablations to verify the persistence of the lesions. We confirmed that the ablations

were restricted to the tectum by assessing the integrity of other AFs with DiI injections to the eye to label RGC axons (Figure 7B).

We found that larvae with tectum lesions were significantly impaired in their ability to escape in response to a looming stimulus (Figure 7C). To confirm that the tectal neuropil ablations did not have a generally adverse effect on visual function or swimming behavior, we tested the optomotor response (OMR), before and after ablation, by presenting a moving grating to the ablated side. In line with previous work <sup>94</sup>, the OMR was unaffected by ablation of the tectum (Figure 7E). In a few experiments, we recorded the behavior of individual larvae before and after the ablation (Figure 7D). The lesions completely abolished escape responses on the ablated side, while behavior was unaltered on the control side (n=2 larvae). Together, these data indicate that the tectum plays an important role in looming-evoked escape behavior.

## DISCUSSION

We have established a behavioral paradigm to study escape behavior of zebrafish larvae in response to looming stimuli. We determined the specific parameters of the stimulus that triggered escape responses and used functional imaging to identify a subset of RGC axons that respond to looming. Two retinorecipient brain areas, AF6 and AF8, were shown to respond robustly, although not exclusively, to looming stimuli. RGCs innervating these two areas also responded to overall dimming. However, a looming-specific pattern of excitation within the retinorecipient layers of the optic tectum was detected, suggesting the existence of looming-selective RGCs that project only to the tectum. Ablation of RGC axons in the tectal neuropil markedly reduced the escape behavior, establishing the importance of this area for visually-evoked escapes.

Previously, studies in visual looming-mediated escape behaviors in locusts <sup>70</sup>, flies <sup>67,72</sup>, pigeons <sup>64</sup>, adult teleost fish <sup>66,95</sup>, amphibians <sup>73,96</sup>, mice <sup>77</sup> and primates <sup>63</sup> have shown that animals utilize similar neurobehavioral strategies to respond to the approach of a threatening stimulus. Electrophysiological and

behavioral studies in the locust have identified a looming-sensitive cell, the LGMD. The peak response timing of this cell varies linearly with the looming stimulus size-to-speed ( $l/v$ ) ratio<sup>70,71</sup>. This linear relationship means that the response peak of these cells occurs at a fixed delay after the stimulus reaches an angular size threshold on the retina. As a result, escapes in response to fast-looming stimuli (small  $l/v$ ) occur later than to slow-looming stimuli (large  $l/v$ ). Interestingly, our studies have found a similar linear relationship between the timing of escape onsets, the anticipated time of collision and the value of  $l/v$  (Figure 3C-D). Furthermore, the threshold angular size that was observed in our study (ca. 20°; Figure 3D) is remarkably similar to the angular size thresholds in other species<sup>71,73</sup>. The observation that this parameter matches quantitatively among phylogenetically distant species may reflect a convergence of the computational mechanisms that have evolved to signal approach of a threatening object.

Our lesioning experiments implicate the optic tectum in the looming-evoked escape response. The tectum and its mammalian homologue, the superior colliculus, contain a high-resolution map of visual space and are generally thought to be involved in localizing objects and directing appropriate orienting movements towards or away from salient objects, such as prey or predators<sup>97-99</sup>. We show that the direction of the escape behavior is dependent on the location of the stimulus within the visual field (Figure 1C). Thus, the location of looming-responsive neurons within the tectum could be read out to generate a directional motor response.

We found that RGCs in two retinorecipient areas, AF6 and AF8, as well as several layers of the tectum, were robustly activated by dark looming stimuli. It is worth noting that an expanding stimulus sweeps across a large part of the visual field and therefore activates a substantial population of neurons. This feature makes it inherently difficult to identify the neurons that are directly involved in encoding the escape-triggering stimulus. To identify the neural substrate of the behavior, we used a variety of stimuli that shared some parameters with the looming stimulus, but did not evoke the behavior. Using pixelwise analysis, we found that individual RGC axons in AF6 and AF8 responded generally to a decrease in luminance, rather than the behaviorally relevant parameter of expansion. These AFs have been shown to

receive input predominately from RGCs with dendrites in the OFF layer of the IPL <sup>91</sup>, which is consistent with their responses to dark looming and dimming. The functions of AF6 and AF8 remain unclear. They may “alert” the tectum to the presence of a shadow, thus facilitating a looming-evoked escape, or they may be involved in different luminance-sensitive behaviors, such as phototaxis.

Within the tectum, we observed responses to looming and dimming in the SFGS. RGC axons that arborize in AF6 and AF8 also innervate SFGS6, the deepest layer of the SFGS, and SGC <sup>91</sup>. Interestingly, several layers of the tectum, likely SFGS2-5, appear to respond more strongly to looming than to dimming. These SFGS layers are innervated by RGCs that do not arborize in any other AFs (projection classes 5-8 [28]). Thus, looming-selective RGCs, terminating in the SFGS, might underlie the stimulus selectivity of the behavior. It is possible, however, that additional RGC types are required for the behavior, and that the detection of the looming stimulus occurs in the downstream periventricular neurons of the tectum, perhaps via pooling of the inputs from an array of RGC dimming detectors. While the cellular composition of the looming circuit has yet to be revealed, the tectum is the likely site where spatiotemporal stimulus features are integrated. Once a critical angular size has been reached, a tectum-generated command then could then drive escape motor circuits in the hindbrain, such as the Mauthner neuron and its homologues <sup>100</sup>.

In summary, we have identified a new visual behavior in zebrafish larvae, which provides a powerful model for studying sensorimotor integration. Our results identify the essential features of the looming stimulus and indicate a key role for the tectum in the detection of approaching threats. Further studies should illuminate the neural basis of looming detection and the circuit components that underlie this vital behavior.

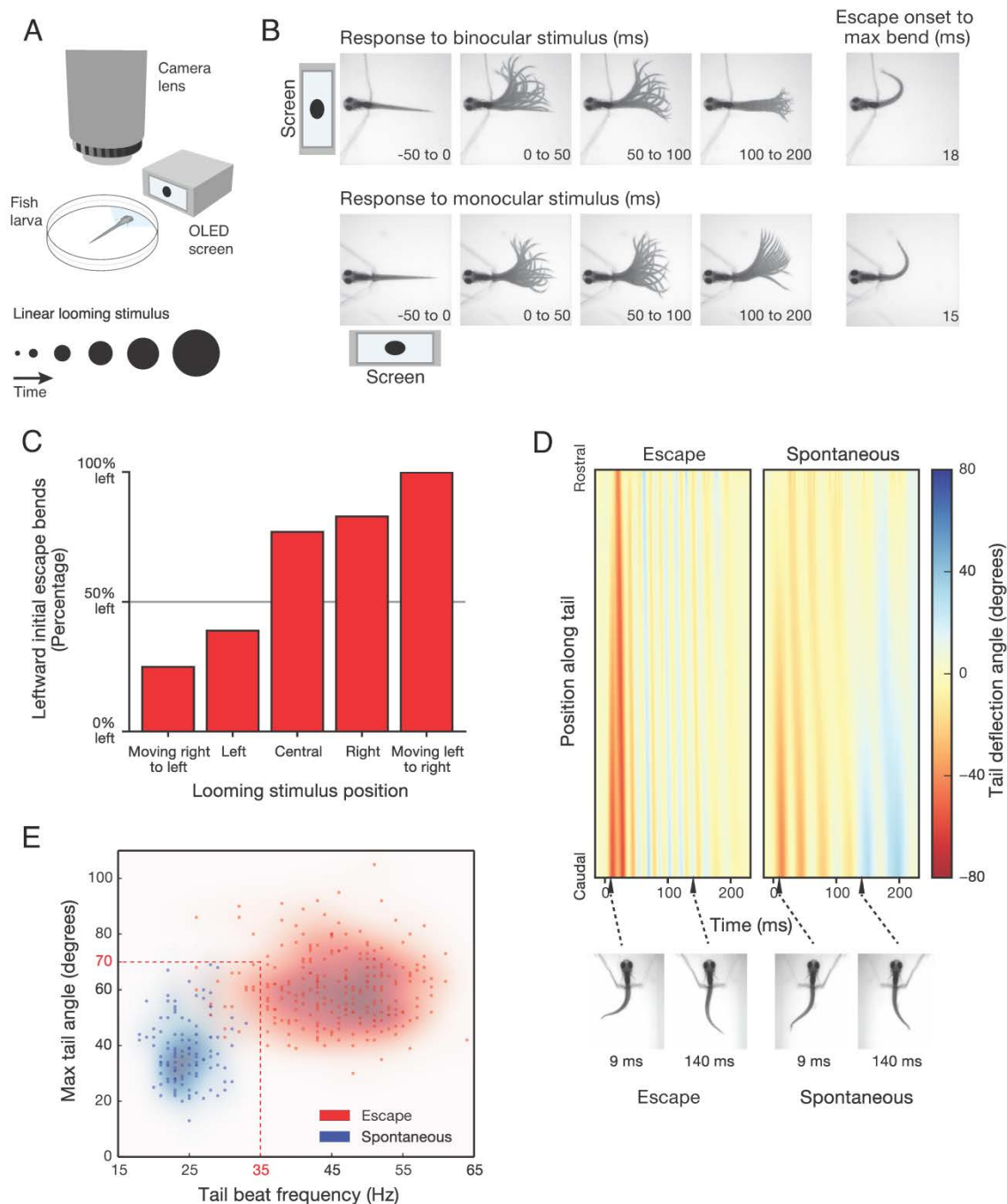


**Figure 1. Visual Display of an Expanding Disk Triggers Escape.** (A) Schematic of the behavioral setup showing a larva is embedded in agarose with its tail freed, with the screen positioned head-on (binocular orientation) or to the side (monocular orientation). (B) Examples of binocularly and monocularly evoked escape swims in 8 dpf TL larva. On the right, the frame showing the tail position at the point of maximum bending is displayed. (C) The direction of the initial bend of the escape response varies depending on the position of the binocularly presented looming stimulus. (n = 14 larvae) (D) Bend

angle plots showing the evolution of the tail shape during spontaneous and escape swims for a 7 dpf larva. Tail deflection angle, indicating overall bend angle from the baseline for each digitized tail points are color coded in each column. **(E)** Two tail metrics (maximum tail bend angle and average tail beat frequency) were extracted and used to identify escape swims. Data were pooled from 114 spontaneous swim bouts and 236 escape swim bouts,  $n = 36$  larvae. Intensity of shading depicts the mean value of each group.

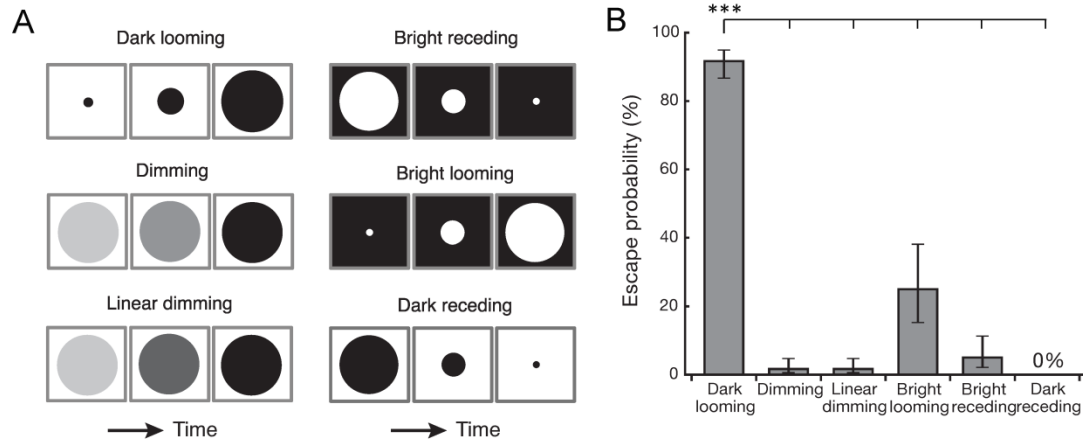


**Figure 2. A Dark Looming Disk is the Most Effective Stimulus in Driving Escapes. (A)** Schematics of the stimuli over time. **(B)** Escape probability of larvae in response to six stimuli above. Dark looming was the most effective in triggering escapes ( $n = 20$  larvae, GEE,  $p$ -value  $< 1 \times 10^{-7}$  for dark looming vs. all the others,  $p$ -value  $\leq 0.04$  for bright looming vs. all the others, multiple comparison corrected by Bonferroni-Holm). The dark receding stimulus did not trigger any escapes. Error bars indicate  $\pm$ S.E.

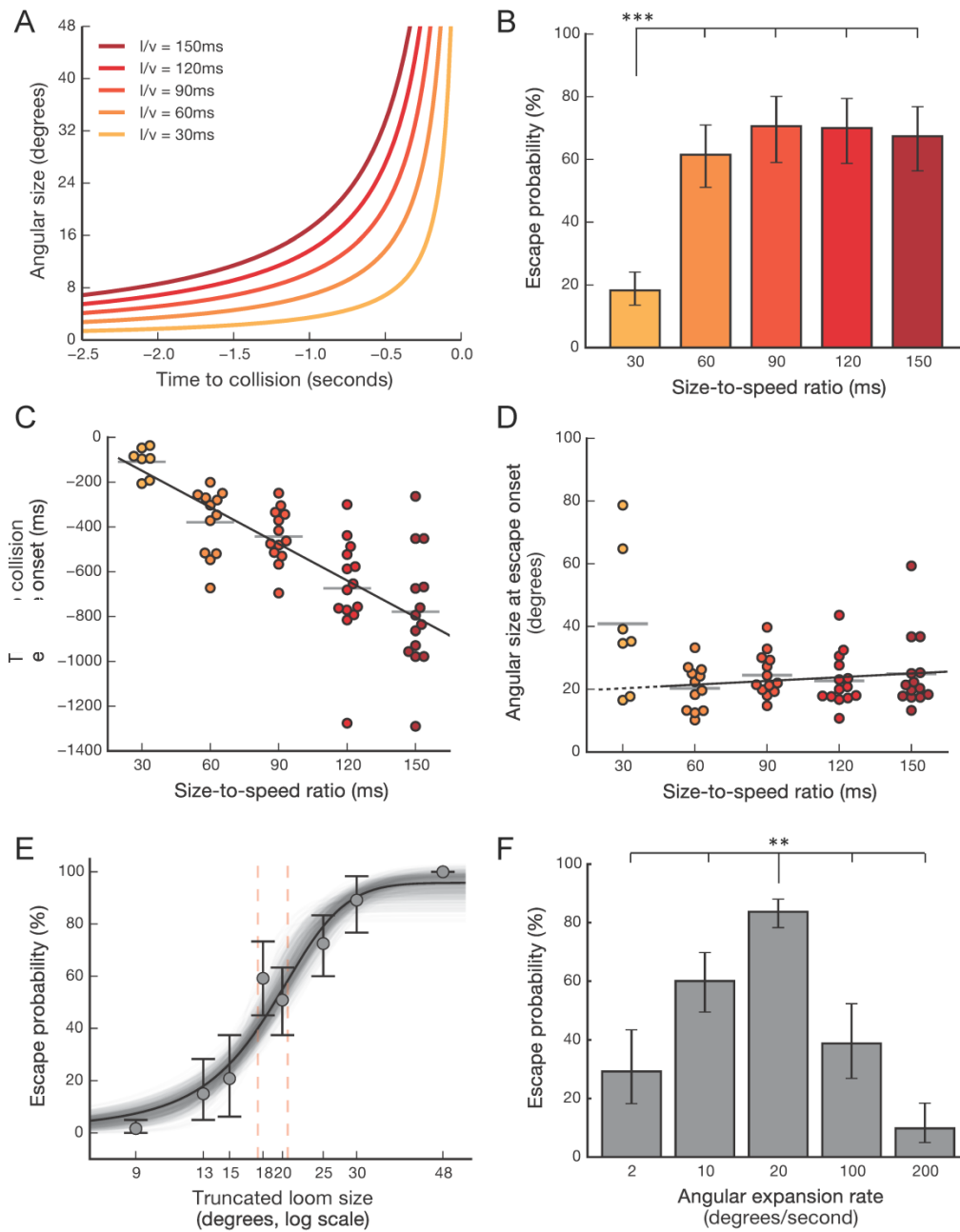


**Figure 3. Probability of Escapes Strongly Depends on the Stimulus Speed and a Threshold Angular Size.** (A) Expansion of angular size for constant approach speed looming stimuli in time from 2° to 48°. Time = 0 represents collision time, when the angular size reaches 180°.  $l$ : object's radius,  $v$ : approach speed. (B) Escape probability is consistently high for  $l/v$  values above 30 ms ( $n = 15$  larvae, GEE,  $p$ -value =  $9.32 \times 10^{-6}$  for  $l/v = 30$  ms vs. all the others, multiple comparison corrected by Bonferroni-Holm). Error bars indicate  $\pm$ S.E. (C) Remaining time to collision at escape onsets as a function of  $l/v$ . Same larvae as



for (B) (least-squares linear regression ( $y = -5.298x - 3.51$ ),  $p$ -value =  $1.4 \times 10^{-11}$ , from 60 responses across all  $l/v$  values) (D) Value of the stimulus angular size at a fixed neural delay preceding escape onset over  $l/v$  values from 60 ms to 150 ms:  $23.13^\circ$  average angular size ( $n = 15$  larvae, least-squares linear regression ( $y = 0.039x + 19.11$ ),  $p$ -value = 0.286). (E) Escape probability as a function of final angular size. Truncated looming stimuli were generated from the  $l/v = 60$  ms stimulus. The tuning curve was fitted by a least-square sigmoidal function. Bootstrap 95% confidence intervals computed to be  $17.5^\circ$  to  $20.7^\circ$  for the middle of the sigmoid which corresponds to point of maximal slope. Data points are mean probabilities across larvae ( $n = 20$  larvae). Error bars indicate 95% bootstraps. (F) Escape probability as a function of angular expansion rate. ( $n = 23$ , GEE,  $p$ -value =  $4.2 \times 10^{-3}$  for  $20^\circ/\text{s}$  vs  $10^\circ/\text{s}$ . For  $20^\circ/\text{s}$  vs. all the other speeds  $p$ -value  $< 0.0005$ , multiple comparisons were corrected by Bonferroni-Holm). Error bars indicate  $\pm$ S.E.

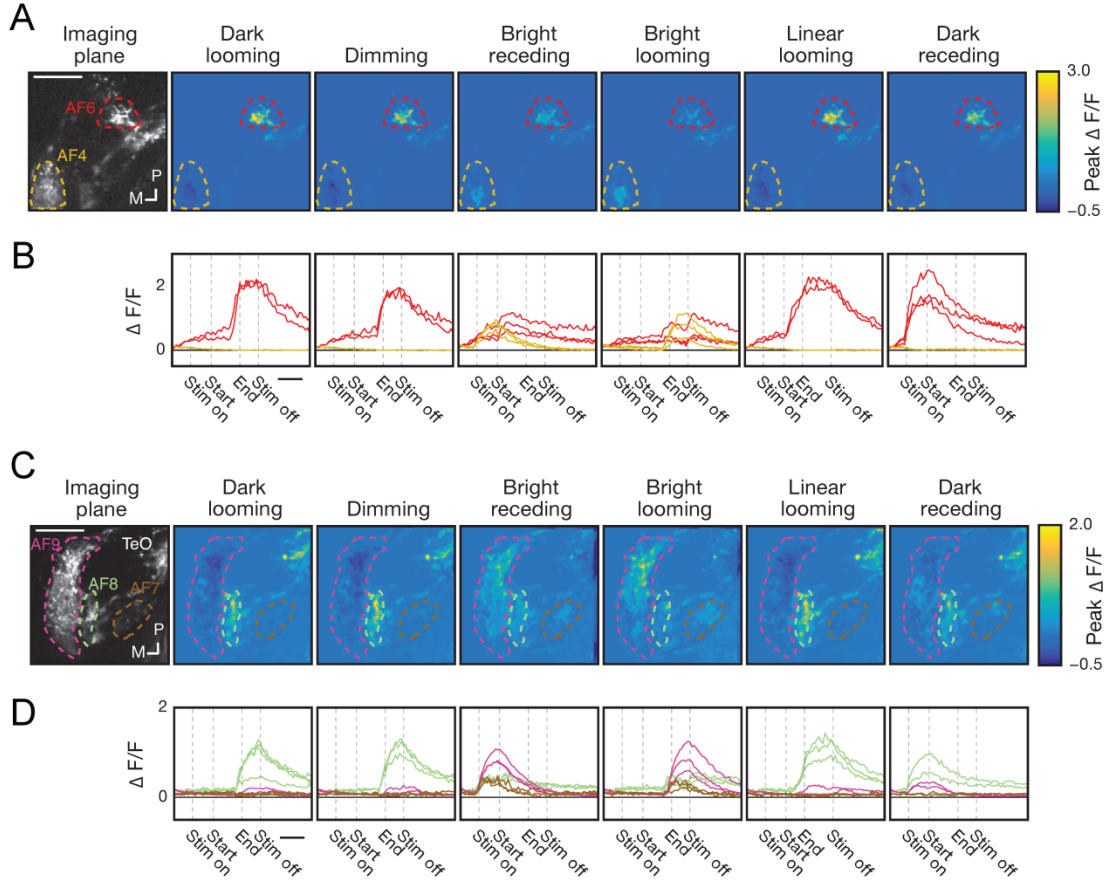


**Figure 4. RGC Axons That Project to AF6 and AF8 Respond to Looming and Dimming Stimuli.** (A) *Isl2b:Gal4, UAS:GCaMP6s* transgenic larvae were presented with a set of looming and control stimuli, and RGC axons in the plane containing AF6 and AF4 were imaged. The peak pixelwise stimulus response ( $\Delta F/F$ ) over the stimulus time window is plotted for each stimulus. Responses are averaged across all trials for a single fish. (B) Temporal dynamics of the AF6 responses to each stimulus as traces of individual trials. (C) Shows the same stimuli set as in (A), but in a more dorsal plane that includes AF7, AF8 and AF9. Responses are averaged across all trials for a single fish. (D) Temporal dynamics of AF8 and 9 responses are given per stimulus as traces of individual trials. The peak pixelwise stimulus responses ( $\Delta F/F$ ) are given as 95 percentile values. AF6: red, AF7: magenta, AF8: light green, AF9: orange colored dashed lines. In (B) and (D), scale bars = 3 seconds and black color traces indicate background. Scale bars = 30 $\mu$ m; TeO = Optic Tectum, P = posterior, M = medial.

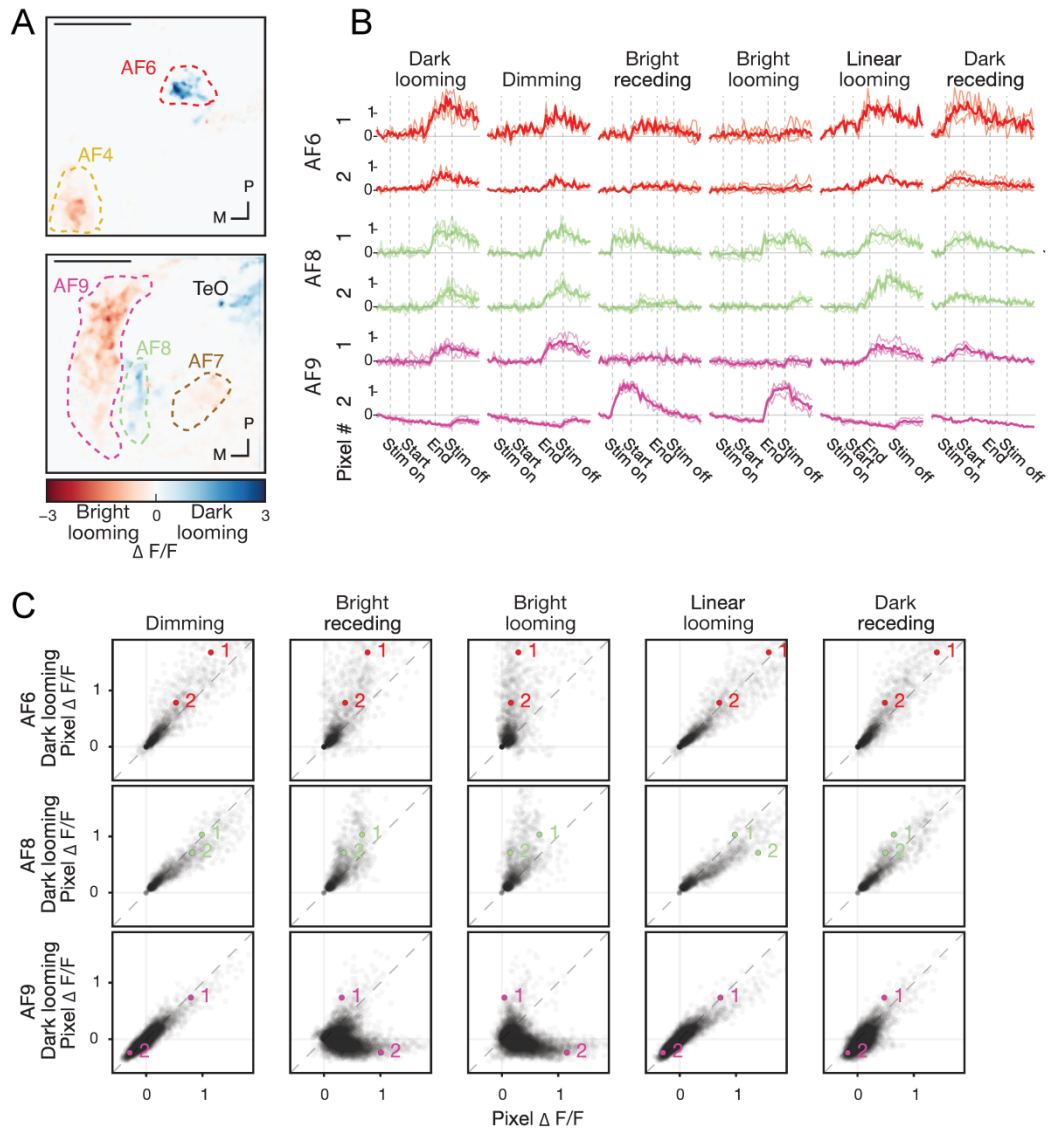


**Figure 5. Pixelwise Analysis of Responses to Looming vs. Control Stimuli Reveal Functional Specialization in extratectal AFs.** (A) Comparison of pixelwise responses to dark vs. bright looming stimulus. Each pixel's bright looming response is subtracted from its dark looming response. Pixels with positive values (larger response to dark looming) are blue, and negative values (larger response to bright looming) are red. (B)  $\Delta F/F$  traces of individual example pixels from corresponding AFs for each stimulus. Responses from individual trials are shown as colored traces and the mean is indicated by a bold colored trace. (C) Scatter plots comparing peak response for each pixel to looming dark vs. control stimuli. Pixels that are close to  $x = y$  line respond similarly for both compared stimuli ( $n = 4$  larvae). 95 percentile values were used as the pixel peak  $\Delta F/F$  values. Scale bars =  $30\mu\text{m}$ ; TeO = Optic Tectum, P = posterior, M = medial.

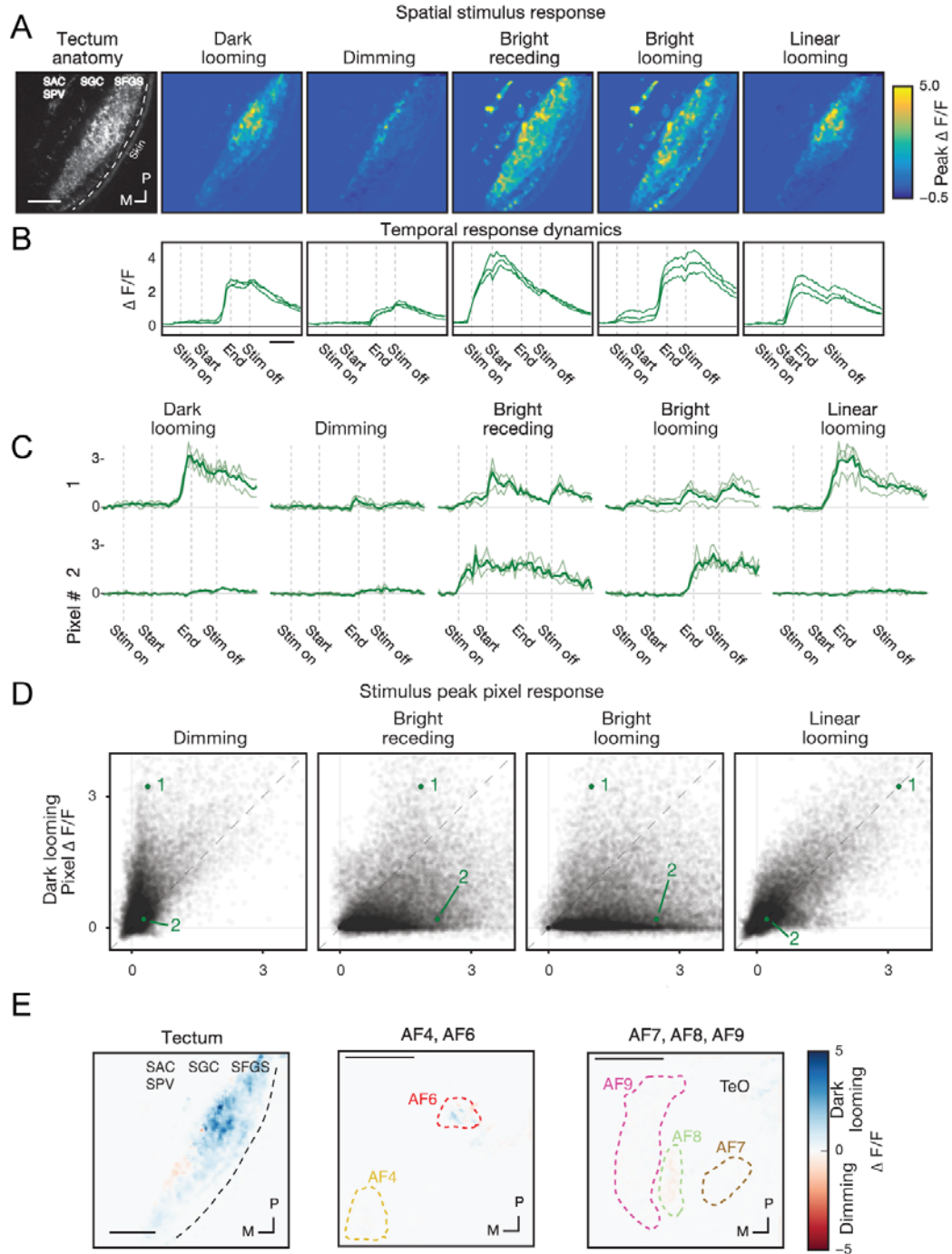


**Figure 6. Differential Activation of Tectal RGC Axons by Looming vs. Dimming.** (A) Looming dark and control stimuli are presented monocularly to 6 to 8 dpf *Isl2b:Gal4, UAS:GCaMP6s* transgenic larvae while imaging the response of RGC axons within the contralateral tectal neuropil. Baseline fluorescent image from the *Isl2b:Gal4, UAS:GCaMP6s* transgenic larva showing tectal anatomy (SO, stratum opticum; SFGS, stratum fibrosum et griseum superficiale; SGC, stratum griseum centrale; SAC, stratum

album centrale). The peak pixelwise stimulus response ( $\Delta F/F$ ) over the stimulus time window is plotted for each stimulus. Responses are averaged across all trials for a single fish. **(B)** Temporal dynamics of tectal neuropil responses are given per stimulus as traces of individual trials. Black colored trace indicates background. **(C)**  $\Delta F/F$  traces from individual example pixels for each stimulus. **(D)** Scatter plots comparing peak pixel responses for looming dark vs. control stimuli. Pixels that are close to the unity line ( $x = y$ ) respond similarly to both compared stimuli ( $n = 4$  larvae). **(E)** Comparison of pixelwise responses to dark looming vs. dimming stimulus. Each pixel's dimming response is subtracted from its dark looming response. Pixels with positive values (larger response to dark looming) are blue, and negative values (larger response to dimming) are red. 95 percentile values were used as the pixel peak  $\Delta F/F$  values. Scale bars = 30 $\mu$ m; TeO = Optic Tectum, P = posterior, M = medial.

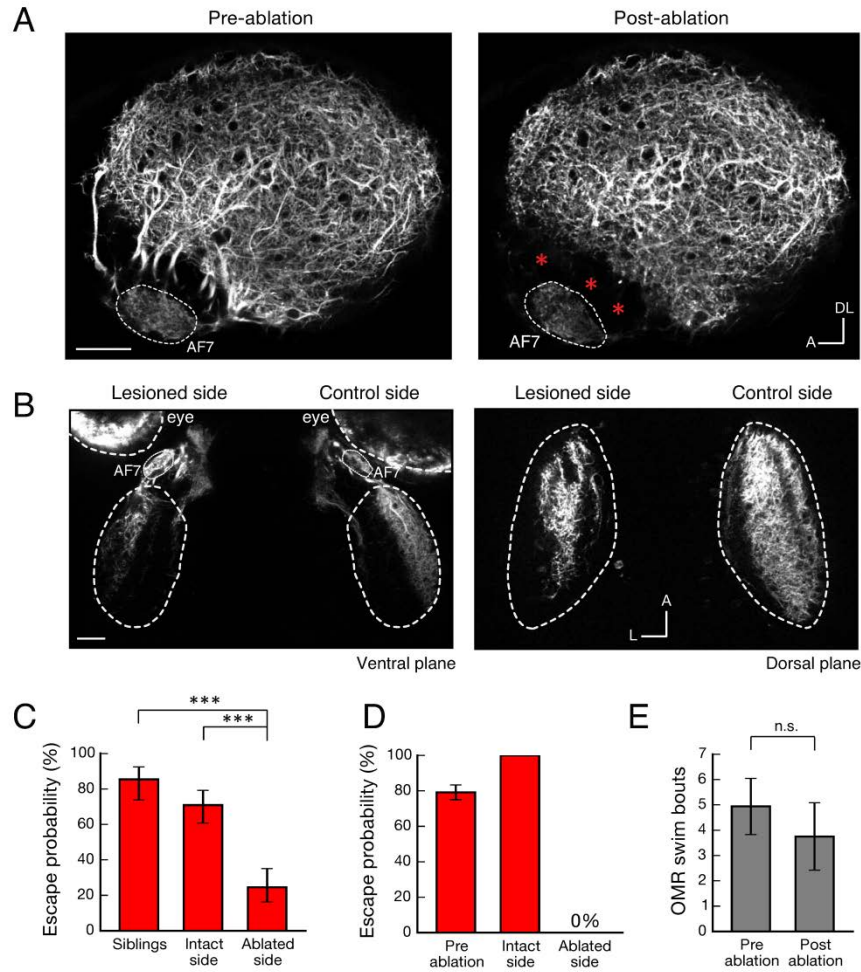


**Figure 7. Intact Tectal Neuropil is Necessary for the Looming-Evoked Escape Response.** (A) Side view of a 7 dpf *Ath5:Gal4, UAS:Dendra* transgenic larva with intact left tectal neuropil (left panel) and immediately following ablation of left tectal neuropil (right panel). (B) DiI injection of the same larva as in (A). DiI images are given in two example z planes (left panel = ventral; right panel = dorsal) to show the extent of lesions through tectal neuropil. (C) Escape probability in control larvae (transgenic siblings,  $n = 13$  larvae) and ablated larvae to the intact and ablated side ( $n = 12$  larvae, GEE,  $p$ -value =  $6.8 \times 10^{-6}$  for siblings control vs ablated side and  $p$ -value =  $9.2 \times 10^{-5}$  for intact side control vs ablated side) (D) Escape probability before and after ablations ( $n = 2$  larvae). Pre-ablation behavioral experiments were performed on the to-be-ablated side. No escape was observable to the ablated side. (E) Optomotor response triggered by moving gratings presented to the ablated side was unimpaired by tectum ablation ( $n = 5$  larvae, dependent t-test,  $p$ -value = 0.44). Intact side in ablated larvae was used as an intrinsic control for behavior experiments. Asterisks denote lesion sides. Error bars indicate  $\pm$ S.E.M. Scale bars = 30  $\mu$ m; A = anterior, L = lateral, DL = dorsa-lateral. Hatched white lines indicate tectal neuropil for each image in (A-B).

## Materials and methods

### Fish care and transgenic lines

Zebrafish were maintained and bred at 28° C on a 14/10 light/dark cycle. Embryos were raised in Danieau's solution (17 mM NaCl, 2 mM KCl, 0.12 mM MgSO<sub>4</sub>, 1.8 mM Ca(NO<sub>3</sub>)<sub>2</sub>, 1.5 mM HEPES). All animal procedures were in accordance with the guidelines of the institutional guidelines of the Max Planck Society and the local government (Regierung von Oberbayern). Wild type TL (*Tüpfel long-fin*) larvae were used for behavioral experiments, and unpigmented TLN larvae (*mitfa*<sup>-/-</sup>) were used for imaging.

The following transgenic lines were used: *Tg(Atoh7:Gal4-VP16)s1992t* (a.k.a. *Ath5:Gal4*), *Tg(Isl2b.2:Gal4-VP16)*, *Tg(UAS:Dendra-Kras)s1998t* and *Tg(UAS: GCaMP6s)*. Transgenic lines were kept in either TL or TLN background.

### Behavioral assays and data analysis

6-8 day-old TL larvae were used for behavioral experiments. Larvae were fed with baby powder (Sera Microns) at 5 dpf and embedded in 2.6% low melting point agarose (Invitrogen) 24h prior to the experiments. For embedding, the lid of a 35 mm Petri dish (Corning, Sigma-Aldrich) was used and larvae were positioned 2 - 3 mm away from the edge of the dish. After the agarose solidified, the dish was filled with Danieau's solution and agarose around the tail below the swim bladder was cut away using a scalpel, leaving the tail free to move. Embedded larvae were kept at 28° C in a chamber where behavioral experiments were conducted.

Visual stimuli were generated in Python using the VisionEgg psychophysics library<sup>101</sup>. Stimuli were displayed at 60 Hz on a 12 x 9 mm monochrome OLED screen (eMagin) spanning ~ 62° (horizontally) and ~ 50° (vertically) of the visual field. The screen was covered with three magenta Wratten filters (Edmund Optics) and positioned 10 mm from the larva. The stimuli were presented in the

center of the screen except for Figure 1C. An infrared light source illuminated the larvae from below, and tail movements were recorded from above with a high speed CMOS camera (Photonfocus) at 648 fps. Behavioral experiments were performed with the room lights on, and screen brightness at maximum. The luminance of the dark screen was  $0.07 \text{ cd/m}^2$  and that of the white screen was  $122.5 \text{ cd/m}^2$ .

Looming stimuli expanded from  $2^\circ$  to  $48^\circ$  unless otherwise stated. Expansion duration for  $l/v = 30, 60, 90, 120, 150 \text{ ms}$  was  $\sim 1.65, 3.3, 4.9, 6.5, 8 \text{ s}$  respectively. For the experiments testing behavioral responses to range of stimuli (Figures 1, 2, 3), stimuli were presented in a random order. In addition, to avoid habituation, intervals of at least 3 min separated successive trials.

To analyze behavior videos, we digitized the tail by assigning  $\sim 50$  points along the tail and extracted swim bouts as described previously<sup>88</sup>. In Figure 1D and Supplemental Video 5, the spontaneous swim video was flipped vertically before any analysis, so that the example escape and spontaneous swims would start in the same direction. In Figure 1D, tail angles were calculated by measuring the angles between the baseline vector and vectors along the digitized tail. In Figure 1E, tail bend angle was calculated by measuring the angle between two vectors: baseline vector and the vector from first point near the beginning of the tail to the mean position of three points at the end of the tail (to reduce noise). Tail beat frequencies were calculated as a ratio of tail flips per bout to detected bout duration. To distinguish spontaneous and escape swims, we first checked that the initial turn direction was away from the looming stimulus. Then we used two criteria to define escapes: maximum tail bend angle  $\geq 70^\circ$  or average tail beat frequency  $\leq 35 \text{ Hz}$  (see Results). Data were further compiled and visualized using Python.

For the experiments in Figure 2, the size-to-speed ratio was  $l/v = 60 \text{ ms}$ . Looming stimuli sometimes triggered more than one escape per trial, and in these cases only the first escape was analyzed. In Figure 3C-D, for calculation of escape onset timing, we detected the frame of first tail movement and subtracted a delay of 35 ms as a sum of the delays in central processing in visual information ( $\sim 25 \text{ ms}$ )



<sup>102,103</sup> and motor output ( $\sim 10$  ms) <sup>104</sup> from the escape onset as an approximation of total sensory delay. For computation of angular size threshold from the linear regression fit, we used the equation  $2 \times \tan^{-1}(1/\text{slope})$  <sup>71</sup>. In the absence of neural delay adjustment for the escape onset timing, the linear regression fit ( $y = -5.033x + 15.98$ ) gives an angular size threshold of  $22.5^\circ$ . Behavior data were averaged within larva first and then averaged as a population to calculate the escape probabilities.

### **Two-photon calcium imaging and data analysis**

Calcium imaging was performed using a movable objective two-photon microscope (Sutter Instruments) with a 40x water-immersion objective (Olympus). Excitation light was tuned to 920 nm (Chameleon Ultra, Coherent). Scanning and image acquisition were controlled using ScanImage software <sup>105</sup>. Time series were recorded with spatial resolution of 128x128 pixels (for extratectal AF imaging, see Figure 4) or 256 x 256 pixels (for tectal neuropil imaging, see Figure 5) at a frame rate of 3.62 Hz.

To prevent motion artifacts arising from movement in response to looming stimuli during imaging, most 6-8 dpf larvae were anaesthetized with 0.02% tricane (MS-222, tricaine methane-sulfonate; Sigma Aldrich) and then paralyzed by injection of alpha-bungarotoxin (4  $\mu$ l of 10 mg/ml; Invitrogen), 1  $\mu$ l Phenol Red and 1  $\mu$ l 5X Danieau's solution to the spinal cord. The tricaine was washed out prior to experiments. Larvae were embedded as for behavioral experiments, except that the agarose around the tail was not removed to prevent any movement artifacts. The imaging chamber was heated to  $28^\circ$  C. Stimuli were displayed on the same type of OLED screen as for behavior, also covered with three magenta filters.

The looming stimuli used for imaging consisted of five types, as for the behavior experiments (Figure 2A: dark looming, dimming, bright receding, dark receding and bright looming,  $l/v = 60$  ms). To prevent saturation of the photomultiplier tubes from green screen light that was able to pass through all three filters, we used a grey instead of white background for the dark looming stimulus, and changed all

other stimuli to match. The luminance of the grey screen was 19.75 cd/m<sup>2</sup>. We note that a grey/black looming stimulus was highly effective in triggering escapes in our behavior setup. Visual stimuli were presented three times each, in pseudorandom order, with intervals of 3-5 minutes between trials.

Calcium imaging analysis was done by custom-written Python-based codes. SIMA was used for motion correction<sup>106</sup>. For extratectal AF calcium imaging analysis, AFs were identified anatomically as in Supplemental Figure 2. For the tectal neuropil analysis, ROI covered all 4 retinorecipient zones (SO, SFGS, SGC, SAC/SPV). A Fast Fourier Transform (FFT) based automated alignment was performed to align across all trials for each fish (<http://www.lfd.uci.edu/~gohlke/code/imreg.py.html>). Minor filtering (median with a kernel size of 3, Gaussian with sigma = 0.2) was performed to reduce noise. Background subtraction linearized the luminosity over the slow axis of the microscope, which was then heavily filtered to extract the low frequency luminance changes affecting the whole image.  $\Delta F/F$  was calculated from the background subtracted image by subtracting the baseline from before the onset of visual stimulation from the response. Pixels corresponding to image background were filtered out by a threshold set by observation of the histogram of delta F values, and the threshold was set just to the right of the first peak of this distribution. Values above half of the threshold were linearly derated, and values below half of the threshold were discarded.

The peak  $\Delta F/F$  values were extracted using a 95th percentile filter. In Figure 4A 4C, and 6A, peak responses were taken over a time window of from just after stimulus start to after the stop of the stimulus but before its removal (~5 seconds) and were averaged over trials (for individual trials see Figure 6B) for a single fish and pseudocolored. In the scatter plots for pixel responses (Figure 5C, 5F, 6D), data from all larvae with very good pixel alignment across all trials ( $n = 4$  for each region) was plotted, using the maximum of each pixel's response during the same time window used above. The pixel analysis for all planes was performed at a resolution of 128x128 pixels. Individual pixel areas were 0.34, 0.57 and 1.44  $\mu\text{m}^2$  for AF6, AFs 7, 8 and 9, and the tectum, respectively. For the tectum, functional time-series were acquired at three depths. Stimuli were presented in a pseudorandom order unique to each plane in each

larva. Data from each plane were pooled across larvae to generate scatter plots for pixel activation for each stimulus.

### **Two-photon laser ablation**

Larvae were treated with 0.1 mM PTU (Sigma Aldrich) from 1 dpf on to prevent excessive tissue damage during ablations. A few hours prior to ablations, larvae were embedded completely in the center of a 35 mm Petri dish with an oblique angle to visualize the RGC axon bundles entering the tectal neuropil (see Figure 6A). Ablations were performed using a two-photon microscope (Femtonics, Hungary) with a laser system (Chameleon Ultra II, Coherent) in *Ath5:Gal4UAS:Dendra*, 7 dpf TLN larvae. A 20X water-immersion objective with a large back-aperture (Olympus, 1.0 NA) was used for ablations. Laser power after the objective was ~150 mW at 850 nm. Axons were ablated by scanning a focused pulsed laser beam for 1 s over a 62  $\mu\text{m}$  x 28  $\mu\text{m}$  rectangular area at three planes (ventral, middle and dorsal) within the tectal neuropil. Ablations were performed unilaterally (only in the left tectal neuropil) and for each plane, after scanning the entering axon bundles, 3-4 additional scans were performed randomly across the neuropil surface to lesion the neuropil (see Figure 7A). 24 hours after the ablations, an image stack of an ablated neuropil was acquired. After ablations, larvae were freed from the agarose and allowed to recover for 3-6 hours before being re-embedded for post-ablation behavioral experiments.

We waited 24 hours after embedding to test the escape behavior. For post-ablation behavior experiments, we used transgenic siblings of ablated larvae and subjected them to the same treatment as experimental larvae except laser ablations. If the ablated larvae did not perform any escapes to the looming stimuli when the intact side was facing the screen, they were excluded from the analysis (8 larvae out of 22). Control siblings that did not perform any escapes in response to the looming stimuli were also excluded from the analysis (3 larvae out of 17).

To test the ablated fish escape responses, we presented an exponentially looming stimulus at  $l/v = 60$  ms and a linearly looming stimulus  $20^\circ/\text{s}$  (Figure 7C-D) at least three times. To test OMR, we

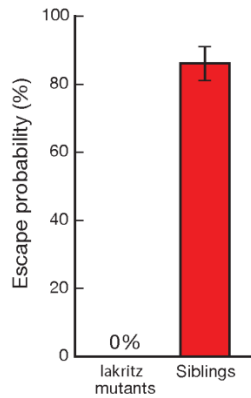
embedded 6 dpf larvae in the same manner as for escape behavioral experiments and waited 24 hours to test the pre-ablation OMR. Post-ablation larvae were re-embedded at 7 dpf and were allowed to recover for 24 hours. Embedded larvae were placed in the middle of an arena with a LCD screen (Miller Technologies), covering an area of 5.5 x 7.5 cm on the right side of the larvae. Gratings moving from caudal to rostral at speeds ranging from 16 - 29°/s were displayed to evoke a forward optomotor response. The same grating speeds were used before and after ablations. Stimulus presentation was controlled with a custom LabVIEW script, and tail movements were recorded at 250 fps using a high-speed camera (Pike F032B, Allied Vision Technologies) and StreamPix software (Norpix). Each stimulus was presented for 10 seconds. The number of OMR forward swim bouts was averaged for each larva from at least three trials (Figure 7E).

We used lipophilic dye labeling to assess the extent of the ablations. Ablated larvae at 8 dpf after post-ablation behavior experiments were fixed overnight at 4° C in 4% paraformaldehyde in PBS, pH7.4 and pressure-injected with 1% solution of DiI in chloroform between the lens and the retina as previously described<sup>107</sup>.

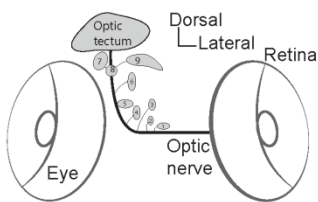
## Statistics

Statistical analysis was performed in R and Python. For analyses involving the measure of escape responses (where for each condition a fish is subjected to multiple trials and for each trial the response is binary, and thus can be thought of as Bernoulli trials) Generalized Estimating Equations (GEE) with a binomial link function were used, as in<sup>66</sup>. S.E.'s plotted were extracted from the GEE modeled population coefficient estimates. For other group comparisons, trials within each fish and condition were averaged and then pooled and analyzed with ANOVAs. Bootstrap 95% confidence interval error bars were calculated using SciPy module of Python. Multiple comparisons were corrected with Tukey HSD (ANOVA) or Bonferroni-Holm (all others) method when necessary. For all figures n.s. > 0.05; \* =  $p$ -value  $\leq$  0.05; \*\* =  $p$ -value  $\leq$  0.005; \*\*\* =  $p$ -value  $\leq$  0.0005.

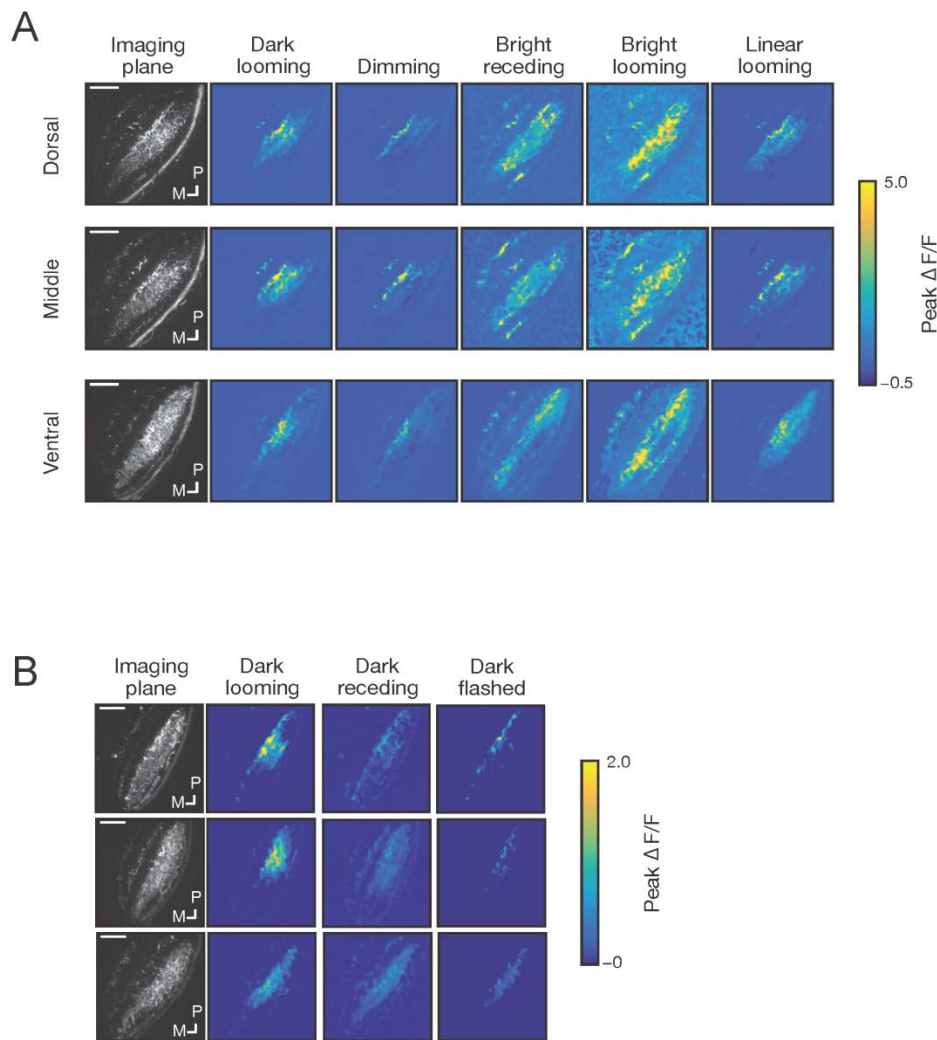
## Supplemental Figures



**Supplemental Figure 1. The Looming-Evoked Escape Response is Mediated by the Retina.** Escape probability in *lakritz* mutants lacking RGCs ( $n = 7$  larvae) and in heterozygotes control siblings ( $n = 12$  larvae). *Lakritz* mutants could not perform any escapes in response to looming stimulus.



**Supplemental Figure 2. Schematic Frontal View of the Larva Denoting AFs in the Midbrain and Forebrain.**



**Supplemental Figure 3. Spatial Pattern of Tectal Neuropil Responses to Looming vs. Control Stimuli From Individual Larvae, Related to Figure 6. (A)** Baseline fluorescent images (panel 1) and pseudocolored peak pixelwise stimulus responses ( $\Delta F/F$ ) from the three tectal planes imaged ( $n = 3$  larvae). Responses during the stimulus time window are averaged across all trials and plotted for each stimulus. The peak  $\Delta F/F$ 's are given as 95 percentile values. **(B)** Differential tectal neuropil responses to dark looming, dark receding and dark flashed stimulus ( $n = 3$  larvae). Scale bars =  $30\mu\text{m}$ ; P = posterior, M = medial.

## **Section 2 – Introduction to optogenetics and a motor control circuit**

The previous works have shown that psychophysics combined with two-photon calcium imaging can effectively find which brain regions are involved in processing a particular set of visual stimuli, and uncover crucial stimuli parameters. Ablations can show the sufficiency of circuit components at the level of nuclei, which provides a focus for more detailed investigation. However using this approach to follow the circuit further downstream towards the behavioral outputs becomes increasingly difficult. Single cell electroporation can be used to trace neurons from an involved area to downstream regions, such as the nucleus of the medial longitudinal fasciculus (nMLF), but the functional properties of the labeled neurons remain unknown.

Optogenetics offers the ability to more directly and flexibly investigate a circuit. The precise temporal and spatial resolution offered by optogenetics allows for detailed investigation, and importantly can show the sufficiency of a set of neurons to drive behavior. The ideal model circuit for optogenetic investigation should be near the motor output side, and easily drive behaviors. The nMLF is an interesting candidate circuit to explore, and is part of the reticulospinal system, projecting into the hindbrain and spinal cord. The nMLF plays a role in postural control and is involved in visually evoked behaviors.

# **Descending control of swim posture by a midbrain nucleus in zebrafish**

Tod R Thiele, **Joseph C Donovan**, Herwig Baier\*

Max Planck Institute of Neurobiology, Am Klopferspitz 18, 82152 Martinsried, Germany

\*Correspondence should be addressed to H.B. ([hbaier@neuro.mpg.de](mailto:hbaier@neuro.mpg.de))



## **Abstract**

The reticular formation in the brainstem controls motor output via axonal projections to the hindbrain and spinal cord. It remains unclear how individual groups of brainstem neurons contribute to specific motor functions. Here, we investigate the behavioral role of the nucleus of the medial longitudinal fasciculus (nMLF), a small group of reticulospinal neurons in the zebrafish midbrain. Calcium imaging revealed that nMLF activity is correlated with bouts of swimming. Optogenetic stimulation of neurons in the left or right nMLF activates the posterior hypaxial muscle and produces a graded ipsilateral tail deflection. Unilateral ablation of a subset of nMLF cells biases the tail position to the intact side during visually evoked swims, while sparing other locomotor maneuvers. We conclude that activity in the nMLF provides postural control of tail orientation and thus steers the direction of swimming. Our studies provide an example of fine-grained modularity of descending motor control in vertebrates.

## Introduction

Elucidating the neural architecture of sensorimotor circuits is fundamental to the broad goal of understanding the neural basis of behavior. Two opposing views concerning the functional organization of such circuits are that they operate in a "distributed vs. modular fashion". In the case of a distributed locomotor circuit, it is difficult to assign specific behavioral functions to individual neurons or even small groups of neurons given that global changes in circuit activity determine behavioral outputs. In a modular circuit design, the activity of discrete pools of neurons is dedicated to discrete kinematics, which are combined at the level of the musculature resulting in a complete behavioral program. Such neuronal modules could be used in varying combinations, giving rise to a diverse, seemingly continuous locomotor repertoire. Instead of being purely modular or distributed, it is likely that many behavioral circuits employ a mixture of these architectures.

Much of our knowledge of the organization of premotor circuitry has come from the investigation of invertebrate behaviors. Distributed neural coding schemes have been identified for the gill withdrawal reflex of *Aplysia californica*<sup>108</sup> and the local bending reflex in leech<sup>109</sup>. The discovery of "command neurons" underlying escape behavior, including the tail-flip response in crayfish, on the other hand, support an extreme version of the module hypothesis (Wiersma, 1947; Boyan et al., 1986). In addition to reflexive behaviors, studies in the nematode *C. elegans* have uncovered pools of forward and backward command neurons that promote opposing directions of rhythmic locomotion<sup>112</sup>.

In vertebrates, perhaps the best example of modular organization are the central pattern generators (CPGs) in the spinal cord. CPGs produce locomotion by coordinated, rhythmic activity of interneurons and motor neurons (Grillner, 2006; Kiehn, 2006; Tresch et al., 2002; Stein and Daniels-McQueen, 2002). Separate "unit CPGs" control antagonist limb movements, and the interaction between these circuit modules can be recombined to produce variations on a behavior such as changes in gait<sup>113</sup>. Additionally, an apparently modular organization has been identified in the descending reticulospinal system (RS) for 3D body orientation/orienting in lampreys, and for control of neck and back musculature in cats<sup>117,118</sup>.

The RS system in larval zebrafish is an attractive model for studies of descending motor control. There are relatively few RS neurons (about 150 on each side of the brain), many of which are individually identifiable from animal to animal (Kimmel et al., 1982). Functional studies of the RS system in zebrafish have been interpreted to support either modular<sup>123,124</sup> or distributed circuit organization (Gahtan et al., 2002). To further address this fundamental question, we investigated the behavioral role of the midbrain nucleus of the medial longitudinal fasciculus (nMLF). Neurons in the nMLF are the most rostral components of the RS system in larval zebrafish and possess dendrites that contact visual recipient regions as well as axonal projections that innervate circuits in the hindbrain and along the length of the spinal cord<sup>127</sup>. Activity in the nMLF has been broadly correlated with multiple sensory stimuli and behaviors, however its exact function remained undefined<sup>124,125,128,129</sup>. We show, by calcium imaging, that activity in nMLF cells is highly correlated with swimming behavior. Unilateral optogenetic activation evokes smooth ipsilateral steering movements, driven by posterior hypaxial musculature, whose amplitude increased roughly linearly with stimulation frequency. In agreement with these activation experiments, unilateral nMLF ablations biases the position of the tail during swims, while leaving other behaviors intact. Together these findings suggest that one central function of the nMLF is postural control of tail orientation during swimming and provide evidence for modular locomotor control emanating from the midbrain of a vertebrate.

## Results

### Reticulospinal neurons in the nMLF are labeled in the *Gal4<sup>s117It</sup>* transgenic line

To begin to dissect the behavioral role of the nMLF, we searched a library of Gal4 drivers generated by enhancer trapping for lines that allow us to genetically target cells in the nMLF<sup>119,122</sup>. This "shelf screen" identified the *Gal4<sup>s117It</sup>* line, which drives expression of UAS-linked transgenes in the midbrain tegmentum including many axons within the MLF (Figure 1A and 1B). Critical for optogenetic approaches, cell populations directly dorsal or ventral to the tegmentum in *Gal4<sup>s117It</sup>* are not labeled although other brain areas express the transgene (Figure S1). In the tegmentum, approximately 600

neurons are labeled in *Gal4<sup>s117It</sup>* with the vast majority localized to medial regions. Lateral portions of the expression pattern have sparser labeling and also contain a dense neuropil.

The nMLF is defined in zebrafish as a bilateral cluster of midbrain RS neurons, which are backfilled by neuronal tracers injected into the spinal cord <sup>121</sup>. Spinal cord backfills with a dextran-conjugated fluorescent dye revealed that *Gal4<sup>s117It</sup>* labels > 80% of neurons within the nMLF, including the four canonical large identified cells MeLr, MeLc, MeLm and MeM, as well as a population of smaller cells, most of which reside in the dorsal nMLF <sup>121</sup> (Figure 1A, 1C, S1, and Movie S1). The small nMLF cells, which we have named MeS (Mesencephalic Small), are more numerous and vary in position making individual identification by current methods challenging (Figure S1 and Movie S2). While most MeS cells are located in dorsolateral positions some of them could also be found ventrally including a pair of identifiable MeS neurons (named MeS1 and MeS2 here). These cells were positioned just lateral to MeLr and were also routinely backfilled with Texas Red dextran (Figure 1C and S1).

Antibody staining for choline acetyltransferase coupled with the *Gal4<sup>s117It</sup>* expression pattern revealed that the nMLF lies just rostral to the oculomotor nucleus (Figure 1D). This staining provided evidence that the nMLF is likely not homologous to the midbrain locomotor region (MLR), which has been described in other vertebrates. The MLR is thought to reside more rostrally, is partially cholinergic in non-mammalian vertebrates and has no direct spinal projections <sup>130,131</sup>.

### **Both MeS and MeL cells show distinct, cell-type specific projection patterns in hindbrain and spinal cord**

To label individual nMLF neurons we performed single cell electroporations of GFP-labeled cells with tetramethylrhodamine dextran in *Gal4<sup>s117It</sup>/UAS:GFP* fish. Our focus was on MeS cells, for which no morphological data existed. We recorded two distinct morphologies for the 15 individual MeS cells that were successfully labeled (Figure 2 and S2). One cell type possessed dendrites that project ventrally and also dendrites that project within the posterior commissure and cross the midline, ramifying in the neuropil of the contralateral nMLF (Figure 2B). Axons of these cells innervate the hindbrain and rostral

spinal cord ipsilaterally and terminate roughly halfway down the spinal cord (Figure 2E, 2G and S2; average termination: at the level of myotome  $11 \pm 4.3$ ). The second MeS cell type extends dendrites that run ventrally and axons that innervate the ipsilateral caudal hindbrain and rostral spinal cord (Figure 2C, 2F, 2G and S2; average termination: myotome  $7 \pm 3.1$ ).

The two MeLc neurons we labeled had similar dendritic patterns as previously described<sup>127</sup>, although their axons terminated more caudally than previously reported (Figure 2G; myotome 20 and 23, respectively). In addition, we labeled an MeLm neuron whose anatomy has not previously been described. This cell had elaborate ventral dendrites and an axon with extensive ipsilateral innervation in the hindbrain and rostral spinal cord and terminated in myotome 19 (Figure 2A, 2D, 2G and S2). This axon also contained a prominent contralateral collateral in the hindbrain (Figure 2D). In summary, our data extend previous observations of the connectional complexity of nMLF cells. Of particular note, all nMLF cells investigated showed extensive axon collaterals in the hindbrain (in addition to their terminal arbors in the spinal cord), suggesting that they may coordinate the activity of several premotor cell groups and participate in multiple behaviors.

### **Calcium imaging shows that nMLF cells are broadly and bilaterally active during behavior**

To image activity in the nMLF, we expressed the high-signal-to-noise, genetically encoded calcium sensor GCaMP6s<sup>132</sup> by crossing *Gal4<sup>s1171</sup>* fish to a newly constructed *Tg(UAS:GCaMP6s)mpn101* line. We performed two-photon calcium imaging while simultaneously monitoring tail kinematics during spontaneous behaviors with a high speed camera (Movie S3). Animals were head-embedded upright, such that similar populations of neurons in the left and right nMLF were present in the same z-plane. Fish exhibited a variety of spontaneous behaviors under our imaging conditions. During individual trials (20 sec and 40 sec long) we observed slow swims (tail beat frequencies of 18-25 Hz), asymmetric tail flips and struggles.

In accordance with previous imaging of the MeL neurons, we observed global activation of MeLc, MeLr and MeLm during swims, flips and struggling (Figure 3A, 3C and S3). We found that swims had the highest probability (98.7%) of evoking responses followed by flips, (78.2%) and struggles (58.3%)

(Figure 3D). During all behaviors, including single asymmetric tail flips we always observed activity in both the left and right nMLF (Figure 3A and 3C). In trials where multiple closely timed behaviors were present, we observed multiple activations in individual neurons that manifested as compound calcium responses (Figure 3C and S3). While we successfully recorded from each of the large MeL neurons, we could not reliably monitor activity in MeM neurons, as the high density of labeled neurons in medial regions hindered unambiguous identification of these cells.

Imaging of the MeS cells revealed that they possess similar response properties to the MeL neurons, with swims again producing the highest probability of responses (97.6%) followed by tail flips (80.7%) and struggles (50%) (Figure 3B and 3D). We observed two distinct populations of MeS neurons based on their response properties. The majority of cells, predominantly located in dorsal regions of the nMLF, had transient responses that mirrored the activity of the MeL cells (Figure 3B). Based on their location, these cells fall into the two morphological types described above. In all animals that were imaged, we also observed a very small number of neurons (3-4) in both the left and right ventral nMLF that had slow dynamics. These neurons ramped up activity during intervals between behaviors and had a pronounced decrease in activity following the onset of all behaviors (Figure 3C). In summary, neurons in the nMLF are bilaterally active during swim maneuvers, including those that have highly dissimilar kinematics.

### **Optogenetic activation of the nMLF causes smooth tail deflections**

To determine the behavioral consequences of nMLF activation, we generated fish in which *Gal4<sup>s1171t</sup>* drove expression of the light-activated cation channel Channelrhodopsin-2 (ChR2) <sup>133</sup>. For photostimulation experiments, animals were head-embedded in agarose with their tails unrestrained (Figure 4A). A vertically oriented optic fiber (10  $\mu$ m tip diameter) delivered 473 nm laser light into the fish's brain, while the tail was imaged at 250 Hz. Stimulation of the caudal midbrain in *Gal4<sup>s1171t</sup>/UAS:ChR2* transgenic fish larvae with a laterally moving fiber resulted in smooth tail deflections that closely followed the position of the fiber (Figure 4B and Movie S4, which provides a dramatic example of this behavior). Stationary fiber stimulation of a small region within 50  $\mu$ m of the

midline on either the left or right side produced a sustained ipsilateral tail deflection that lasted for the duration of the stimulus (Figure S4). Tail deflection amplitudes were equivalent for left and right stimulation sites, with both having a pivot point caudal to the swim bladder in the vicinity of myotome 6 (Figure 4A; Movie S4). Light-induced movements were not observed in *Gal4<sup>s117It</sup>/UAS:GFP* transgenic animals (Figure S4).

We identified the stimulation site within the *Gal4<sup>s117It</sup>* expression pattern using fish that expressed both ChR2 and the photoconvertible fluorescent protein Kaede<sup>134</sup>. Upon localizing a stimulation position that evoked ipsilateral tail deflections in *Gal4<sup>s117It</sup>/UAS:ChR2/UAS:Kaede* fish, the optic fiber was parked and the laser line switched to 405 nm to photoconvert Kaede at that position. In all 11 fish treated in this manner, a small converted region with a diameter of 10-50  $\mu\text{m}$ , or two mirror-symmetric regions for bilaterally treated fish, was observed (Figure 4C and Figure S5). Converted neurons localized to portions of the *Gal4<sup>s117It</sup>* expression pattern that overlap with laterally situated neurons of the nMLF. Cells in this region included all of the large MeL neurons and also the MeS cells (Figure 4D). From these stimulation and conversion experiments, we conclude that activity in a lateral subregion of the nMLF drives smooth tail deflections, which resemble postural 'steering' movements. These movements were striking for their reproducibility within and across animals and because they have not, to our knowledge, been previously observed in response to reticulospinal neuron stimulation.

### **Steering and swimming are triggered differentially by dosage and location of nMLF photo-activation**

To characterize the behavioral output of the nMLF, we stimulated 30 fish with three different stimulation frequencies (10 Hz, 20 Hz, 30 Hz) on both the left and right sides (Figure 5A). In nearly all fish (95%), 10 Hz stimulation resulted in a detectable ipsilateral steering movement in the tail (Figure 5D). In a minority of cases steering as well as swims or ipsilateral turns were present (13% and 1.6% respectively, Figure 5D). When stimulation frequency was increased to 20 Hz and then again to 30 Hz, we observed an increase in steer amplitude with a concomitant decrease in steer rise time (Figure 5B, 5C and S6). Stimulations at 20 Hz and 30 Hz always resulted in detectable steering movements. The

probability of eliciting swims that accompanied steering was similar for all conditions (10 Hz  $p=0.13$ , 20 Hz  $p=0.14$  & 30 Hz  $p=0.15$ , Figure 5D). When they occurred the tail beat frequency and duration of swims were not strongly dependent on stimulation frequency (Figure 5E and S6). These properties of the nMLF are different from those reported for the MLR, where increased activity produces a large increase in gait and swim frequencies in other vertebrates<sup>135,136</sup>. In contrast to swims, the probability of ipsilateral and contralateral turns increased with stimulation frequency, with ipsilateral turns being more common (Figure 5D). Turns consisted of either one large tail flip or multiple, laterally biased tail undulations. Increasing the light dose also resulted in a greater probability for trials where all three behaviors were present (steer, swim and turn) (Figure 5D).

To determine if more medial regions of the nMLF produce ChR2-driven behavior we positioned the optic fiber above the midline, equidistant to verified left and right stimulation sites. For the majority of medial stimulation trials, we could not detect a change in tail kinematics (17 of 20 fish) (Figure 5A, 5B and S6). These results suggest that, when stimulated in isolation, medial regions of the nMLF are not directly involved in moving the tail. We next determined which tail kinematics are produced when the nMLF is bilaterally activated. In these experiments we used a large-diameter (105  $\mu\text{m}$ ) optic fiber to excite the entire nMLF region. Here, stimulation using 20 Hz or 30 Hz pulses was capable of producing long bouts of swimming that often lasted the duration of illumination (Figure 5F). However, for the majority of fish stimulated in this fashion, uncoordinated movements were elicited (8 of 12). When long bouts of swimming were present, tail beat frequencies were similar to those for unilateral stimulation ( $20.5 \pm 2.8$  Hz), however bout durations far exceeded the length of swims observed in freely swimming or head-restrained fish (Budick and O'Malley, 2000; Portugues and Engert, 2011).

### **Both MeL and MeS neuronal populations contribute to steering behavior**

Our Kaede conversion experiments determined that the region within the lateral nMLF where steering is evoked contains the MeL neurons as well as MeS neurons. To resolve the relative contributions of these two populations of neurons to steering, we measured ChR2 evoked steering in *Gal4<sup>s171t</sup>/UAS:GFP/UAS:ChR2* animals before and after cell-targeted two-photon ablations (Figure 6A).



To isolate steering behavior, relatively low stimulation parameters were used to reduce the likelihood of evoking swims or turns. Unilateral ablation of both MeL and MeS neurons (6-8 dorsal MeS neurons, MeS1, MeS2, MeLc, MeLr and MeLm) dramatically reduced steering on the ipsilateral side while leaving contralateral steering intact (Figure 6B). Targeting just the MeS cells produced a similar reduction, whereas removal of the MeL cells had an intermediate effect (Figure 6C). From these ablation results, we conclude that both neuron types contribute to steering, with a larger contribution coming from the MeS population.

### **The nMLF is required for maintaining the direction of forward swims during optomotor behavior**

Neurons in the nMLF are active when stimuli that drive forward optomotor behavior are presented<sup>124</sup>. To determine the nMLF's function in this visually guided behavior we performed optogenetic and lesion experiments using a head-fixed optomotor preparation (Figure 7A). In this assay, caudal-to-rostral moving gratings presented on vertically oriented LCD screens elicited forward swims, whereas rotating gratings produced tail flips toward the direction of rotation. Unilateral ChR2 activation of the nMLF introduced an ipsilateral bias to swims evoked by forward moving gratings presented to both eyes (Figure 7B and 7C). This increase in tail angle was most prominent during the first few tail oscillations. In line with these activation experiments, unilateral ablation of neurons in the lateral nMLF (6-8 dorsal MeS neurons, MeS1, MeS2, MeLc, MeLr and MeLm) caused forward swims to be biased toward the intact side (Figure 7D-G, Movie S5 and S6). In three animals we observed a striking tail deflection toward the intact side prior to the onset of tail oscillations (Figure 7F and Movie S6). These deflections resembled steering movements evoked by unilateral ChR2 stimulation. Ablations to isolate the behavioral contribution of the MeL and MeS cell types only uncovered a significant effect on swimming tail angle when MeS neurons were removed (Figure 7H). Bilateral nMLF ablations did not alter tail orientation during swims (Figure S7). Strikingly, unilateral nMLF ablations only affected forward swims, having no detectable effect on the amplitude of turns evoked by ipsiversive or contraversive OMR stimuli (Figure 7D, 7G and 7H). Bout frequency and bout duration for all three OMR behaviors were unaffected by unilateral removal of nMLF neurons (Figure S7), underpinning the specificity of our ablations.

## Posterior hypaxial musculature drives steering movements

Given the unique and stereotyped steering produced by unilateral nMLF stimulation, we hypothesized that a particular muscle (or group of muscles) may underlie these movements. We took advantage of background muscle expression in *Gal4<sup>s1171t</sup>* to conduct ChR2 muscle activation experiments, as well as calcium imaging, in muscle groups following unilateral nMLF stimulation. We found that ipsilateral stimulation of the posterior hypaxial muscles<sup>137</sup>, a muscle group with previously unknown function, produced robust tail deflections that resembled unilateral activation of the nMLF (Figure 8A). Activation of medial trunk hypaxial muscles (THM) produced only modest tail deflections (Figure 8A). Kaede conversion experiments confirmed the identity of these muscle groups (Figure 8B and 8C). To demonstrate a functional connection between the nMLF and PHM, we imaged muscle activity using GCaMP6s before and after unilateral ChR2 stimulation of the nMLF. Here, we observed robust activity in the ipsilateral PHM and only modest activity in the THM (Figure 8D). The configuration of our optical setup did not allow for muscle imaging during nMLF stimulation. Stimulation of sites just caudal to the nMLF did not evoke muscle activity (Figure S8). Based on the position of the PHM, we expect its motor unit to be located in the hindbrain, in close proximity to axon collaterals from nMLF neurons.

## Discussion

The functional organization of the premotor brainstem is an area of intense investigation. Here, we sought to characterize the organization of descending motor commands emanating from the nMLF, the most rostral component of the larval zebrafish RS system. Previous results have shown that the nMLF is broadly active during a variety of behaviors including swimming, escape, optomotor responses and prey capture<sup>124,125,128,129</sup>. Using a combination of calcium imaging, optogenetic activation and laser ablations we showed that a central function of the nMLF is to provide postural positioning of the tail during forward swims, likely via activation of the posterior hypaxial musculature. Furthermore, our results indicate that this function is primarily carried out by the MeS neuron population, with contributions from

MeL cells. This function is likely to be carried out in concert with separate descending motor commands for rhythmic tail oscillations during swimming<sup>138,139</sup>.

From a library of Gal4 enhancer trap lines<sup>119,140</sup>, we identified the line *Gal4<sup>s117It</sup>*, which drives expression in the midbrain tegmentum. Retrograde tracing from spinal cord revealed that the vast majority of nMLF neurons are labeled in *Gal4<sup>s117It</sup>*, including the large MeL and MeM neurons, as well as the smaller MeS neurons. MeS neurons fall into two broad types based on their dendritic morphology, and have ipsilaterally innervating axons that terminate at the level of the caudal hindbrain and rostral spinal cord. MeL and MeM axons, on the other hand, project all the way to the caudal spinal cord. Collateral arbors from both MeL and MeS axons are found in the hindbrain, near the attachment site of the posterior hypaxial musculature and the probable location of the associated motor pool. Consistent with a functional connection between nMLF neurons and this muscle, their optogenetic activation each produced very similar tail deflections.

As a first step toward understanding how these neurons contribute to behavior, we used *Gal4<sup>s117It</sup>* to drive expression of GCaMP6s<sup>132</sup> and monitored population activity in the nMLF during spontaneous behaviors. Imaging revealed that neurons in nMLF are broadly active during slow swims, tail flips and struggles. We found that swims had the highest probability of evoking calcium responses, followed by tail flips and struggles. In addition, we observed that nMLF neurons on both sides were synchronously active during all behaviors including highly asymmetric tail flips. Our results agree with previous imaging results<sup>129</sup> and extend them to a greater number of neurons and the MeS population.

While our imaging data suggested that the nMLF carried out an apparently nonspecific function during locomotor maneuvers, the optogenetic activation experiments indicated a greater functional differentiation within the nucleus. Unilateral activation of the nMLF with ChR2 elicited smooth ipsilateral steering movements in > 95% of the animals tested. Higher light doses drove larger tail bends, often followed by full-blown swim bouts. Bilateral stimulation of the nMLF typically evoked uncoordinated movements, but was also capable of producing robust symmetric swimming. A potential neural basis for stimulus dependent recruitment of steering and swims is soma size of nMLF neurons.

MeS neurons, which we have shown to be primarily responsible for steering evoked by low optical stimulation doses, are likely to reach threshold faster than the large MeL neurons given their compactness. Under this model, the larger MeL neurons would only reach threshold with higher stimulation and thus their activity may underlie the swim kinematics we observed with high frequency stimulation. This hypothesis should become further testable with improved methods for optical or genetic targeting of individual cells.

Our optogenetic results are at least partially consistent with electrical stimulation experiments in goldfish<sup>141,142</sup>, another cyprinid teleost. Here, unilateral injection of current in the vicinity of the nMLF evoked ipsilateral turns, whereas bilateral stimulation evoked swims. These earlier studies did not report isolated tail bends resulting from nMLF stimulation. A caveat of electrical stimulation is its limited spatial resolution; excitation of neurons outside the target site may confound interpretations of the circuitry underlying evoked behaviors. Furthermore, the close proximity of the nMLF to descending and ascending fibers in the MLF makes precise electrical targeting of the nMLF especially challenging. The specificity of optogenetic approaches compared to electrical stimulation techniques could explain the observed differences.

In loss-of-function experiments, we removed nMLF neurons using cell-targeted two-photon laser ablations and assessed behavior using a head-fixed optomotor assay. Previous imaging in fully embedded animals showed that both the MeL and MeS neuronal populations are tightly tuned for forward moving gratings that evoke swims and are mostly unresponsive to laterally moving gratings that promote turns<sup>124</sup>. In line with these findings, nMLF ablations specifically affected OMR forward swims while leaving turns intact. Unilateral ablation of either the left or right nMLF caused swims to be biased to the intact side, however did not have an effect on the number of swim bouts per trial or the duration of bouts. Furthermore, in several fish, we observed a pronounced deflection of the tail to the intact side prior to the onset of swimming. This result indicates that activity in at least part of the nMLF precedes the initiation of locomotion. A potential source of this activity is the slow MeS neurons whose activity increases prior to the onset of locomotion.

Our results suggest that neurons in the left and right nMLF activate trunk musculature equally when fish swim straight and asymmetrically when fish swim with a biased trajectory. This model is consistent with previous findings where ablation of nMLF neurons reduced prey capture behavior by increasing the yaw angle between the head and the tail during capture swims <sup>128</sup>. In light of the present results, it is likely that these altered capture swim kinematics result from a reduction in postural steering control by the nMLF.

Orientation of the body in three dimensions is critical for successful navigation of the environment. Studies in various organisms have revealed neural strategies for transforming sensory inputs into appropriate body orientation adjustments <sup>143,144</sup>. In the lamprey, unequal RS activation of spinal cord networks controls roll, pitch and turn orienting movements <sup>145–148</sup>. The steering mechanism we describe here is likely to act in concert with RS neuron modulation of spinal cord circuits to generate biased swims. The behavioral role we have identified for the nMLF has the distinct signature of postural control. Given the positioning of the nMLF, these circuits could function similarly to those in the mammalian ventral tegmental field that underlie postural control during ambulation <sup>149,150</sup>.

Our results are most consistent with a large degree of functional specialization of premotor circuits. Recent studies of the RS system in larval zebrafish have also supported such a modular architecture. Investigation of the vSPNs (ventromedial Spinal Projection Neurons), has provided strong evidence that these neurons are solely responsible for large tail deflections during turn behaviors. Imaging of the entire RS system while presenting OMR stimuli found that the vSPNs comprise a small population of neurons that preferentially respond to turn-inducing stimuli <sup>124</sup>. Turns in response to OMR stimuli manifest as a series of tail oscillations where the first undulation cycle is highly biased to one side. Ablation of these vSPNs was shown to completely eliminate OMR turning while leaving swims intact <sup>124</sup>. Subsequent studies have shown that vSPNs are also necessary for phototactic turning, spontaneous turns and turns evoked by dark flashes <sup>123</sup>. In the absence of the vSPNs, there is an increase in swim bouts, suggesting that in ablated animals turn events were transformed into additional swims bouts. The simplest explanation for this result is that activity in the vSPNs adds a lateral bias on top of an independent

oscillatory motor pattern <sup>123</sup>. In this model, the activity of a yet to be identified population of swim-inducing neurons, perhaps in the caudal hindbrain (Arrenberg et al., 2009), combined with the activity of the vSPN turn module results in the complete turn motor program.

Locomotor patterns have been proposed to result from the linear combination of muscle synergies <sup>151,152</sup>. Under this scheme, dedicated modules – as opposed to distributed neural circuits – are responsible for commanding discrete groups of muscles <sup>153</sup>. In the context of zebrafish behavior, specific motor components appear to be driven by distinct clusters of neurons, including the speed of the escape-associated C-bend <sup>126,154,155</sup>, spontaneous and stimulus-evoked turning <sup>123,124</sup>, forward swimming <sup>138,139</sup> and ballistic eye movements <sup>156</sup>. We have shown here that activity in a small population of anatomically defined midbrain neurons is necessary and sufficient for controlling swim orientation as part of the optomotor response. Together, these data support a framework of modular neuronal control underlying vertebrate locomotion.

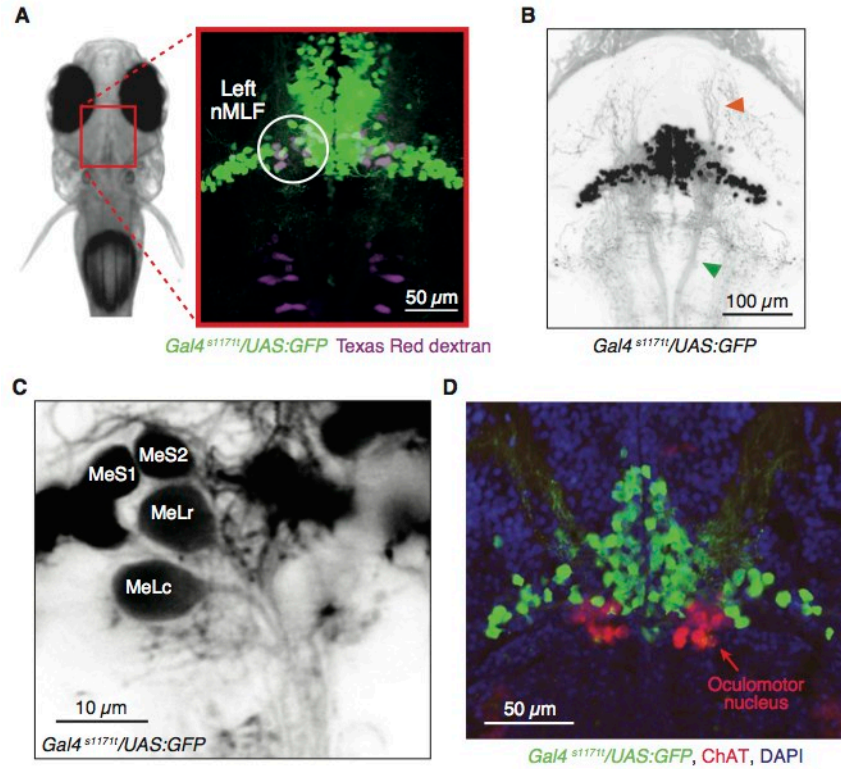


**Figure 1. Enhancer trap line *Gal4<sup>s117It</sup>* drives expression in the nMLF.**

**A.** Confocal projection of the midbrain in a 6-day-old *Gal4<sup>s117It</sup>/UAS:GFP* fish. Optical sections (100 $\mu$ m) were collapsed to yield a maximum intensity projection. Reticulospinal neurons were backfilled from the spinal cord with Texas Red dextran. Right panel is an expanded view of the nMLF region indicated by the red box in the left panel. Green cells are GFP-labeled by *Gal4<sup>s117It</sup>*. Magenta cells are RS neurons in the rostral hindbrain and midbrain, labeled by Texas Red. White or pale magenta cells within the white circle are left nMLF neurons, which are double-labeled. **B.** Confocal projection of a slice (80  $\mu$ m) of the GFP dorsal expression in *Gal4<sup>s117It</sup>/UAS:GFP*. The axon tract of the MLF (green arrowhead) and dendrites exiting the nMLF (orange arrowhead) are highlighted. **C.** Two-photon image of a single plane highlighting four identified nMLF neurons, MeLr and MeLc, plus the newly identified MeS1 and MeS2. **D.** Confocal image projection of a cryostat section (25  $\mu$ m) from *Gal4<sup>s117It</sup>/UAS:GFP* stained with antibodies to GFP (green) and ChAT (red). Cell nuclei are labeled with a DNA dye (blue). See also Figure S1.

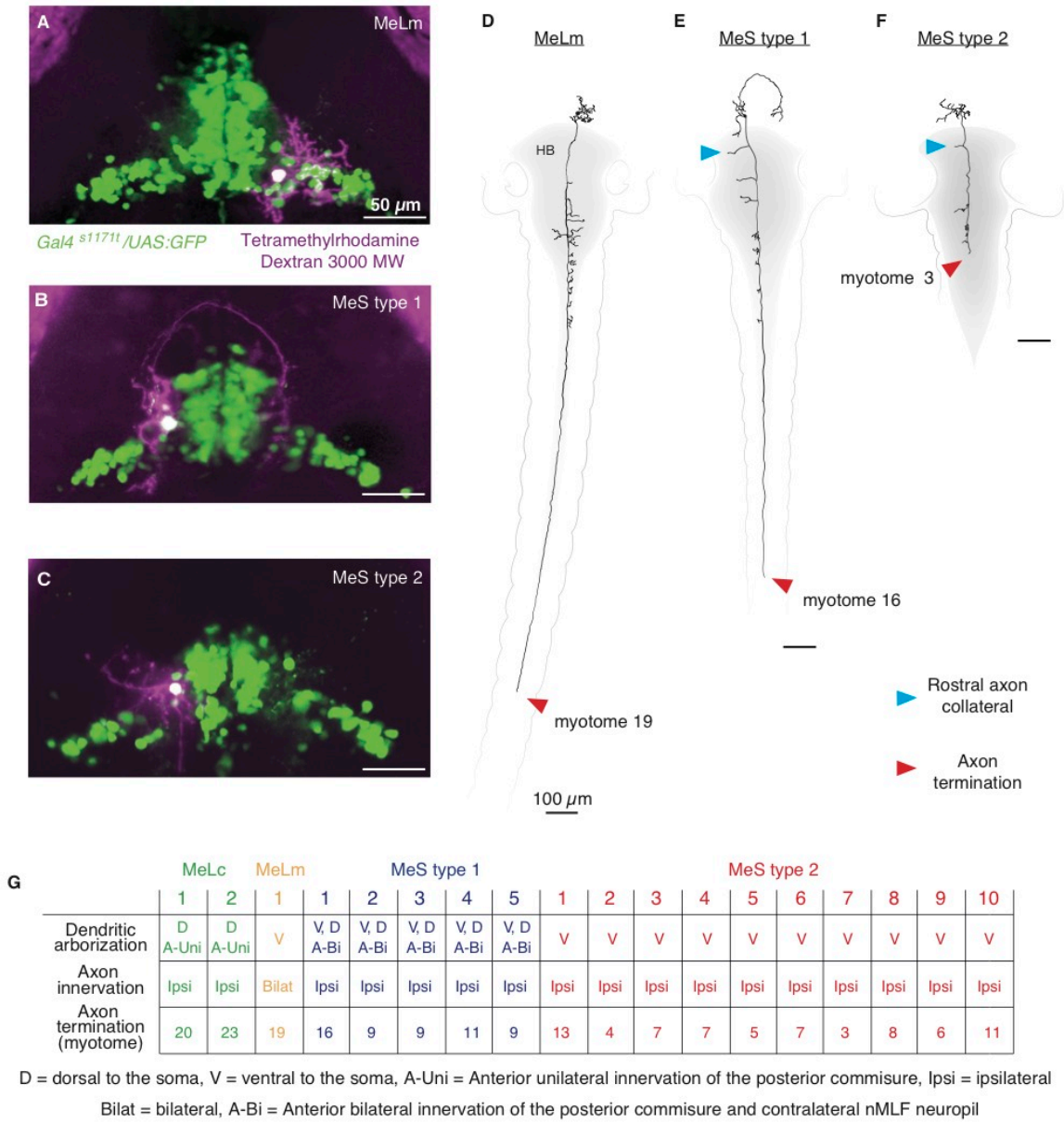


**Figure 2. MeS neuron morphologies revealed by single-cell electroporations.**

**A-C.** Examples of confocal image projections of the midbrain in 6-day-old *Gal4<sup>s117It</sup>/UAS:GFP* fish. MeLm (**A**), MeS type 1 (**B**) and MeS type 2 (**C**) are shown. Cells were electroporated with tetramethylrhodamine (TMR) dextran (magenta). GFP (green) is driven by *Gal4<sup>s117It</sup>*. TMR is brighter than GFP in cellular processes. The dendrites therefore appear magenta. The somas of electroporated cells are double-labeled by GFP and TMR and appear as white. **D-F.** Drawings of the nMLF cells in **A-C** showing their axonal projections. The corresponding photomicrographs are provided in Figure S2. Axon termination points are indicated by red arrowheads. Rostral collaterals in the hindbrain are indicated by blue arrowheads. **G.** Summary table for all electroporations performed. See also Figure S2.



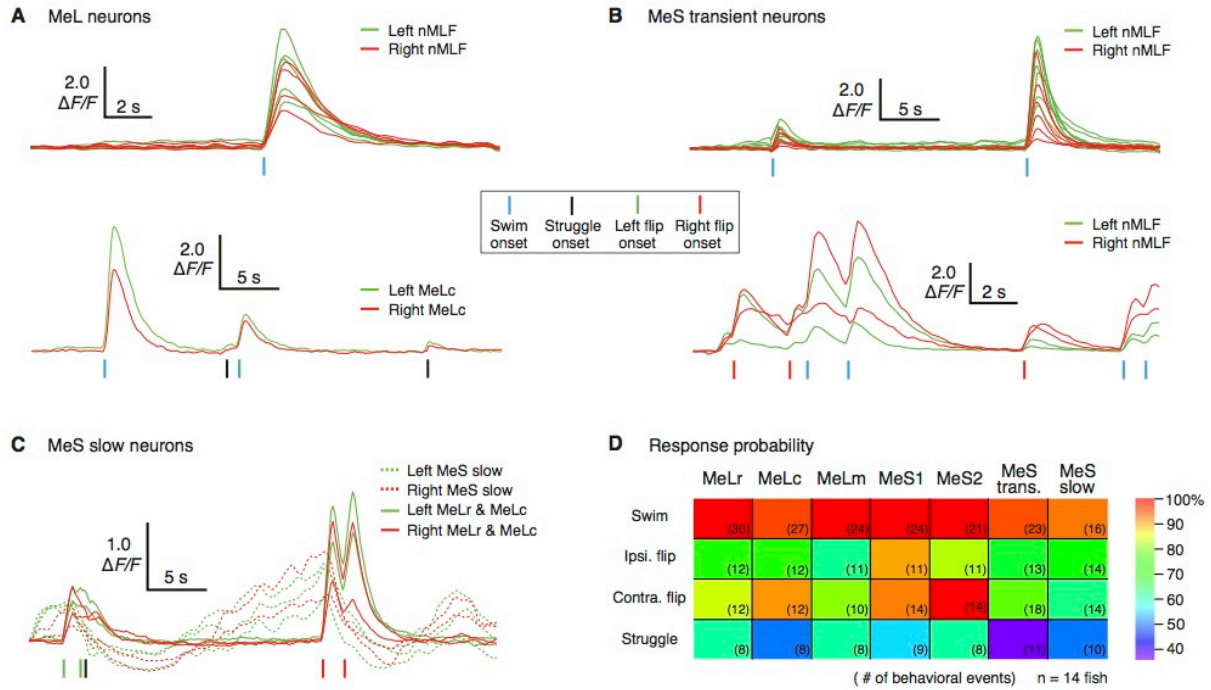


**Figure 3. Calcium imaging of nMLF activity during spontaneous behavioral bouts.**

Fish larvae (6dpf) with genotype *Gal4<sup>s117It</sup>/UAS:GCaMP6s* were used. **A.** Examples of calcium responses in MeL neurons, accompanying a single swim (upper panel) and to swims and struggles (lower panel). **B.** Examples of calcium responses in MeS neurons that display transient responses to swims (upper panel) and swims and tail flips (lower panels). **C.** Calcium responses in MeS neurons that have slow response properties and turn off at the onset of tail flips. Responses in MeLc and MeLr neurons during tail flips are also shown. **D.** Summary table indicating the probability of calcium responses across neurons and spontaneous behaviors. Probability is represented by the color scale to the right of the table. Calcium traces were low-pass filtered for display purposes. Activity in nMLF cells is highly correlated ( $> 0.9$ ) with swims and less correlated ( $0.4 - 0.9$ ) with tail flips and struggles. See also Figure S3.

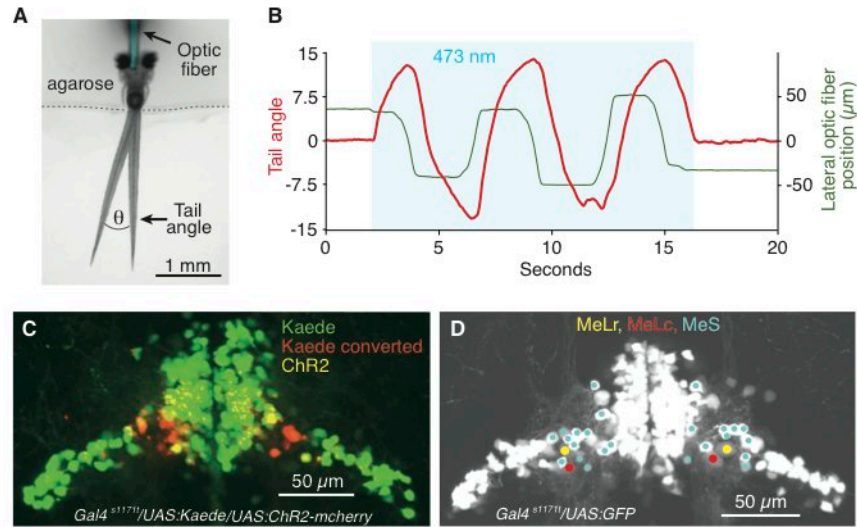


**Figure 4. ChR2 stimulation of nMLF neurons and their localization using photoconversion.**

**A.** Dorsal view of the experimental setup used for ChR2 experiments. Two different tail positions are shown to illustrate the tail angle measurement used below and in subsequent figures. Optic fiber is pseudocolored for clarity. **B.** Change in tail angle (red) in a *Gal4<sup>s1171t</sup>/UAS:ChR2* fish, elicited by nMLF stimulation with a laterally moving optic fiber (green; 10 $\mu\text{m}$  fiber diameter, continuous beam 0.8 mW/mm<sup>2</sup>). Blue shaded region depicts the epoch of ChR2 stimulation. **C.** Confocal image projection of the midbrain in a *Gal4<sup>s1171t</sup>/UAS:ChR2/UAS:Kaede* fish, which underwent bilateral Kaede conversions at sites that produced left and right steering, respectively. **D.** Confocal image projection, detailing the positions of two large MeL and the MeS neurons in the lateral nMLF. See also Figures S4 and S5.

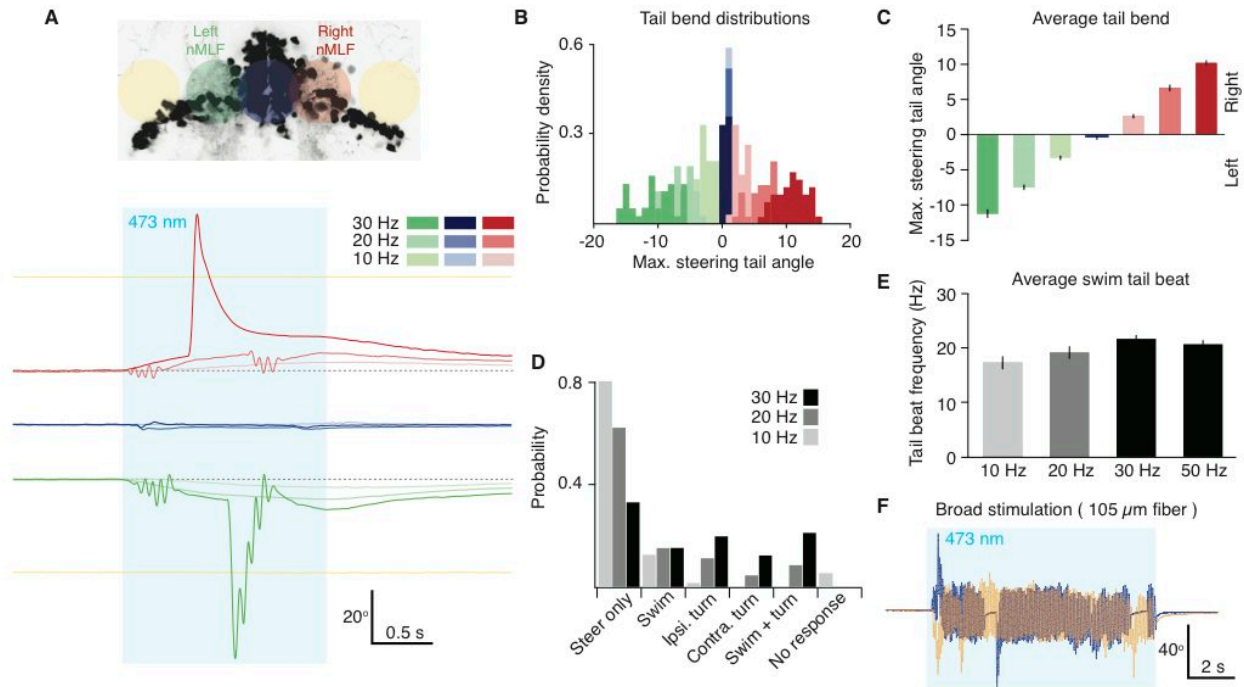


**Figure 5. Behavioral effects of ChR2 stimulation depend on light dose and fiber location.**

**A.** (Top) Schematic of five stimulation sites within the midbrain expression pattern of *Gal4<sup>sl171t</sup>*. (Bottom) Traces depict tail angle as a function of time in a single fish at five stimulus locations with 10 Hz, 20 Hz and 30 Hz light pulses (10 ms pulse duration, 1 mW/mm<sup>2</sup>). Blue shaded region depicts the epoch of ChR2 stimulation. **B.** Probability density histogram for maximum tail angles at left, middle and right stimulation sites ( $n \geq 30$  for left and right positions,  $n \geq 20$  middle; color code is the same as in A). **C.** Mean values for maximum tail angle at left, middle and right stimulation locations (effect of frequency and location:  $P < 0.01$ ; color code is the same as in A). **D.** Probability of observing different tail kinematics at each stimulation frequency. Left and right trials were combined. **E.** Tail beat frequencies for swim bouts at each stimulation frequency (effect of frequency:  $P < 0.05$ ;  $n \geq 9$ ). **F.** Two trials (blue and yellow) where long swimming bouts were evoked by bilateral stimulation with a large (105  $\mu$ m) optic fiber ( $n = 2$ ; 20 Hz pulse frequency).  $n$  values indicate number of fish. Error bars indicate s.e.m. See also Figure S6.

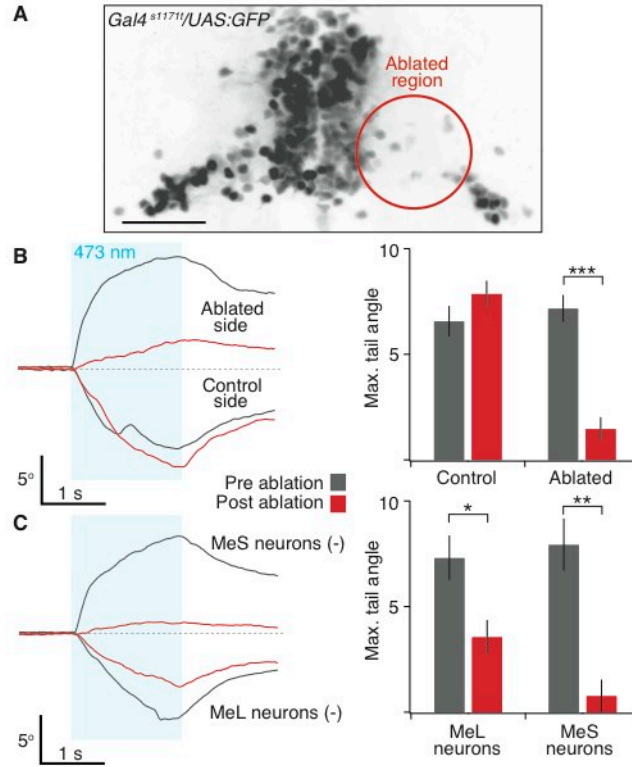


**Figure 6. Contributions of large MeL neurons and MeS neurons to steering.**

**A.** Two-photon image projection of the midbrain in a *Gal4<sup>1171t</sup>/UAS:GFP* fish, in which the lateral region of the right nMLF was ablated 12 h prior. Scale bar, 50  $\mu$ m. **B.** (left) Tail angle as a function of time after stimulating left (bottom traces) and right (top traces) ChR2 sites before and after lateral right nMLF ablation. (right) Reduction in tail angle is observed on the ablated side ( $n = 14$ , paired t-test,  $P < 10^{-5}$ ;  $t(13) = 6.91$ ), but not on the control side ( $n = 14$ , paired t-test,  $P = 0.12$ ;  $t(13) = 1.62$ ). **C.** (left) Tail angle as a function of time for left and right ChR2 stimulation sites before and after ablation of large MeL neurons on the left side (bottom traces) and MeS on the right side (top traces). (right) Reduction in tail angle is observed for MeL ablations ( $n = 7$ , paired t-test,  $P < 0.02$ ;  $t(6) = -3.49$ ) and superficial MeS ablations ( $n = 7$ , paired t-test,  $P < 0.001$ ;  $t(6) = -5.91$ ).  $n$  values indicate number of fish. Error bars indicate s.e.m.

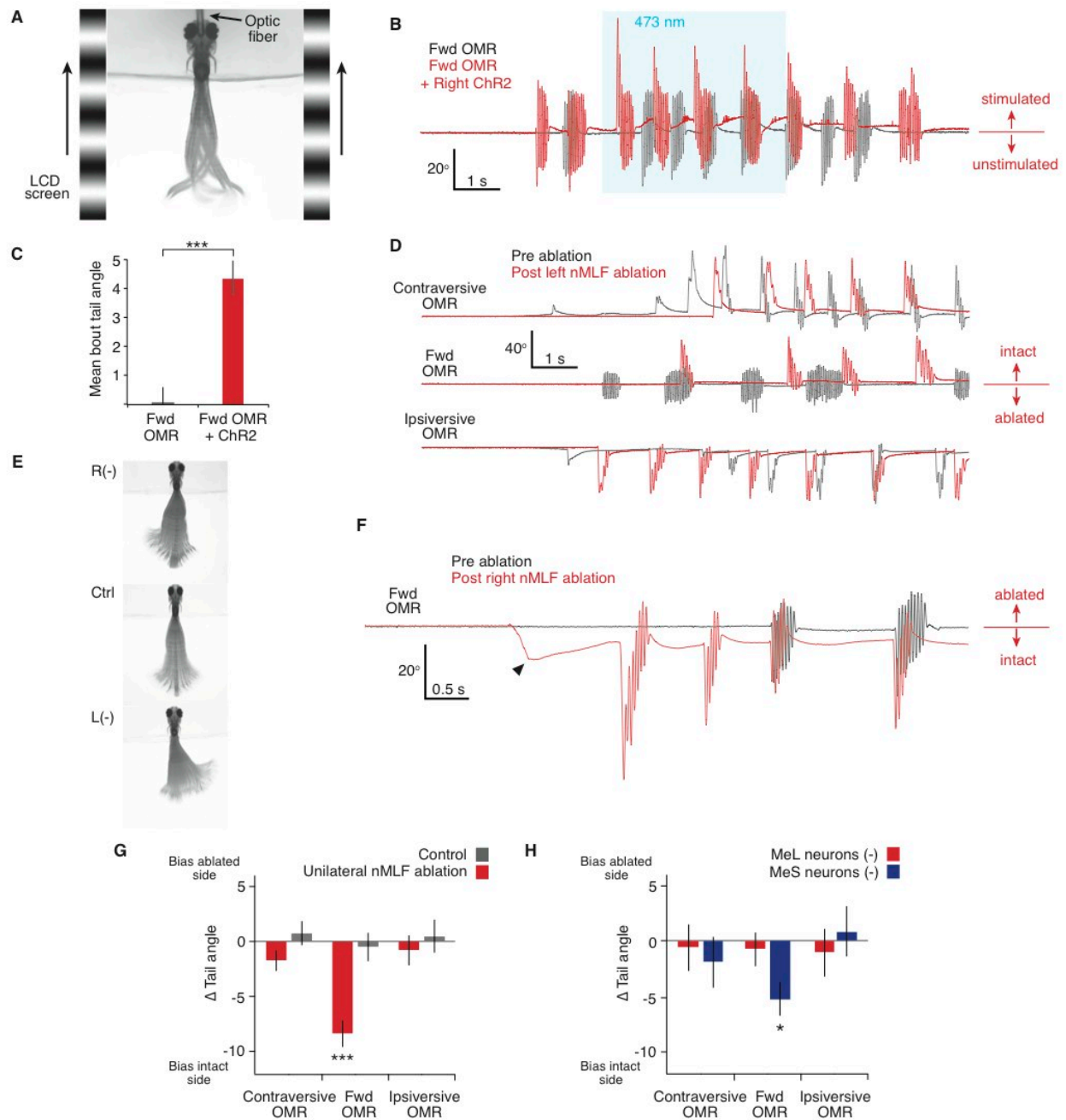


**Figure 7. Role of lateral nMLF neurons in the optomotor response.**

**A.** Schematic of the optomotor assay. Animal is head-embedded in agarose with the tail free. Two LCD screens on each side of the fish display caudal to rostral moving gratings for forward OMR stimulation. A third screen (not shown) is added in front of the animal to create rotating gratings for contraversive and ipsiversive OMR stimulation. **B.** Change in tail angle in a *Gal4<sup>s117It</sup>/UAS:ChR2* fish elicited by continuous forward OMR stimulation (black) or by both OMR stimulation and ChR2 activation of the right nMLF (red). Blue shaded region depicts the epoch of ChR2 stimulation. **C.** Increase in tail angle during forward

OMR swim bouts induced by Chr2 stimulation ( $n = 21$ ;  $P < 10^{-6}$ ;  $t(20) = -5.26$ ). **D.** Change in tail angle in a *Gal4<sup>s1171</sup>/UAS:GFP* fish evoked by three different OMR stimuli before (black) and after (red) ablation of lateral neurons in the left nMLF. All traces are from the same fish. **E.** Projection of video frames displaying tail position of three fish (right ablated, control and left ablated) for an entire forward OMR trial. **F.** Change in tail angle evoked by a forward OMR stimulus before (grey) and after (red) ablation of lateral neurons in the right nMLF. Black arrowhead denotes a left tail deflection that precedes swimming. Traces are from the same fish. **G.** In ablated fish (red bars) swims are biased toward the intact side for forward OMR ( $n = 31$ ; paired t-test,  $P < 10^{-6}$ ;  $t(30) = 6.96$ ). Turns evoked by contraversive ( $n = 28$ ;  $P = 0.076$ ;  $t(27) = 1.84$ ) or ipsiversive ( $n = 28$ ;  $P = 0.55$ ;  $t(27) = 0.59$ ) grating stimuli are unchanged. In control fish (grey bars), no biases were observed for forward ( $n = 10$ ;  $P = 0.70$ ;  $t(9) = 0.39$ ), contraversive ( $n = 8$ ;  $P = 0.52$ ;  $t(7) = -0.67$ ) or ipsiversive ( $n = 8$ ;  $P = 0.86$ ;  $t(7) = -0.17$ ) stimuli. **H.** Unilateral superficial small neuron ablations (blue bars) generated a bias in OMR forward swims toward the intact side ( $n = 13$ ; paired t-test,  $P < 0.02$ ;  $t(12) = 2.82$ ). Responses to contraversive ( $n = 11$ ;  $P = 0.63$ ;  $t(10) = 0.48$ ) or ipsiversive ( $n = 11$ ;  $P = 0.88$ ;  $t(10) = -0.14$ ) stimuli were unchanged. Unilateral MeL neuron ablations (red bars) did not affect forward swims ( $n = 8$ ;  $P = 0.62$ ;  $t(7) = 0.51$ ), or turns to contraversive ( $n = 8$ ;  $P = 0.97$ ;  $t(7) = 0.03$ ) or ipsiversive ( $n = 8$ ;  $P = 0.62$ ;  $t(7) = 0.51$ ) stimuli.  $n$  values indicate number of fish. Error bars indicate s.e.m. See also Figure S7.



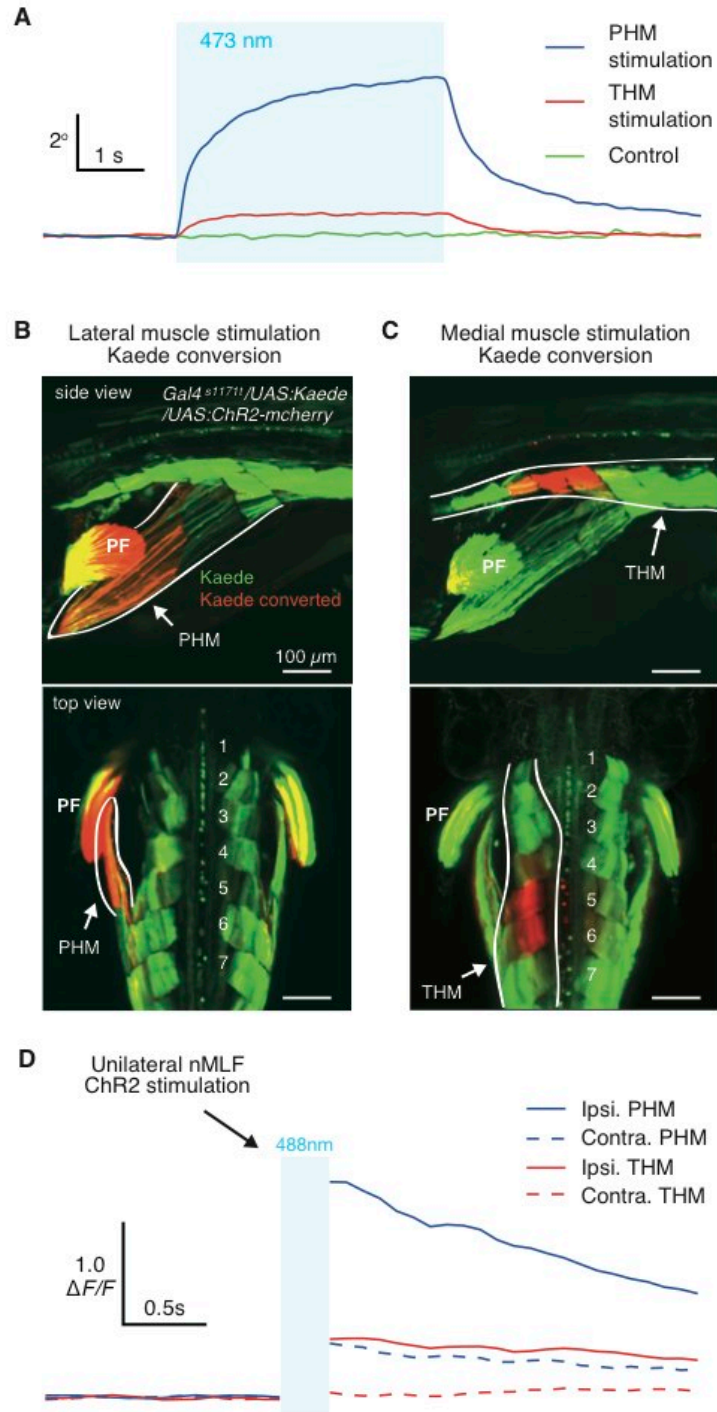


**Figure 8. Specific muscle activation generates tail deflections.**

**A.** Change in tail angle in *Gal4<sup>s1171</sup>/UAS:ChR2* fish elicited by ipsilateral hypaxial muscle with a stationary vertically oriented optic fiber (105μm fiber diameter, continuous beam 2 mW/mm<sup>2</sup>). Blue shaded region depicts the epoch of ChR2 stimulation. The blue trace represents the average change in tail angle when lateral muscle regions in the vicinity of myotomes 4-6 were stimulated ( $n = 6$ ). The red

trace represents the average change in tail angle when muscle regions just lateral to the midline were stimulated ( $n = 6$ ). The green trace represents the average change in tail angle in *Gal4<sup>s1171t</sup>/UAS:GFP* fish ( $n = 3$ ). **B.** Confocal image projection from the side and top of a *Gal4<sup>s1171t</sup>/UAS:ChR2/UAS:Kaede* fish that underwent Kaede conversion at a lateral muscle site, which produced a substantial tail deflection angle. This conversion labeled the posterior hypaxial muscle group (PHM) outlined in white. **C.** Confocal image projection from the side and top of a *Gal4<sup>s1171t</sup>/UAS:ChR2/UAS:Kaede* fish that underwent Kaede conversion at a medial muscle site, which produced a small, but detectable tail deflection. This conversion labeled the trunk hypaxial muscle group (THM) outlined in white. **D.** Average calcium responses in ipsilateral PHM (blue), ipsilateral THM (red), contralateral PHM (blue dash) and contralateral THM (red dash) following unilateral nMLF optical stimulation in *Gal4<sup>s1171t</sup>/UAS:ChR2/UAS:GCaMP6* fish ( $n = 5$ ). Blue shaded region depicts a 200 ms epoch of ChR2 stimulation. ChR2 was stimulated using the minimum laser power required to produce a tail deflection.  $n$  values indicate number of fish. PF denotes pectoral fin. See also Figure S8.



## Materials and methods

### Zebrafish lines

Zebrafish were raised and bred at 28°C on a 14 h light / 10 h dark cycle using standard techniques<sup>157</sup>. All animal procedures conformed to the guidelines of the University of California, San Francisco and the Max Planck Society. Transgenic lines were made in the TLN background, which is based on the Tüpfel long-fin (TL) wildtype strain carrying mutations in *mitfa* (*nacre*, *N*). We used *Tg(UAS-E1b:Kaede)s1999t*, *Tg(UAS:ChR2(H134R)-mCherry)s1986t*, *Tg(UAS:GFP)mpn100*, *Tg(UAS:GCaMP6s)mpn101*, and *Et(-0.6hsp70l:Gal4-VP16)<sup>s1171t</sup>*. The *Gal4<sup>s1171t</sup>* line was established from a Tol2 enhancer-trap screen (Scott et al., 2007). Linker-mediated cloning established that *Gal4<sup>s1171t</sup>* is inserted in the first intron of the *sim1a* gene (T. Thiele, unpublished result). *Tg(UAS:GCaMP6s)mpn101* was constructed by first cutting the GCaMP6s open reading frame out of *pGP-CMVGCaMP6s* (Addgene no. 40753) and cloning it into a *pTol2-14xUAS* vector. This construct was then injected with transposase mRNA into one-cell-stage *Gal4<sup>s1171t</sup>* embryos. Transgenic lines were maintained in either the TL or the TLN background. Designations of mutant and transgenic lines adhered to nomenclature rules set according to <http://zfin.org>.

### Immunohistochemistry, backfills and confocal imaging

*Gal4<sup>s1171t</sup>/UAS:GFP* larvae (5dpf) were fixed in 4% PFA and processed for antibody staining according to published protocols<sup>158</sup>. A mouse anti-GFP antibody (GTX13970, Genetex) was used at a concentration of 1:1000 and a goat anti-choline acetyltransferase antibody (AB144p, Millipore) was used at a concentration of 1:200. Alexa dye conjugated secondary antibodies (Invitrogen) were used at 1:1000 dilutions. Backfills were performed as described previously<sup>128</sup>. Briefly, a 50% (w/v) solution of Texas Red dextran (10,000 MW, Invitrogen) was pressure injected into the spinal cord of 5-7dpf larvae anesthetized with 0.02% tricaine in Danieau's solution. Confocal imaging was performed on either a Zeiss LSM700 or LSM780 microscope. Image processing was done using FIJI<sup>159</sup>.

## Electroporations

*Gal4<sup>s117It</sup>/UAS:GFP* fish (5dpf) were embedded in 2% low melting point agarose (Invitrogen) and immersed in extracellular physiological saline containing 0.02% tricaine. Patch pipettes (8-9 MΩ) were filled with intracellular saline containing 15% tetramethylrhodamine dextran (3000 MW). For MeS labeling, small GFP-positive somas dorsal to the MeL neurons were visually targeted using a 40x water immersion objective (Olympus, 1.0 NA). Upon cell contact, light suction was applied, and a voltage train (1.5 second duration, 150 Hz, 1.5 ms pulse width, 2-7 volts) was applied using an Axon Axioprotector (Molecular Devices). Cell morphologies were then imaged on a Zeiss LSM780 confocal microscope.

## Calcium imaging

*nMLF: Gal4<sup>s117It</sup>/UAS:GCaMP6s* zebrafish (6dpf) were head-embedded in 2% low melting point agarose (Invitrogen). Agarose around the tail was dissected away using a scalpel blade. Fish were allowed to recover from the mounting procedure for several hours. Calcium responses were imaged using a customized moveable objective microscope (MOM, Sutter Instruments) and a 20x objective (Olympus XLUMP, 0.95NA). Scan control and image acquisition were controlled using ScanImage software<sup>160</sup>. GCaMP6s was excited by 920 nm light (Chameleon Ultra, Coherent). Scan rates were 5.92 frames/second (256 x 256 pixels). Tail kinematics were simultaneously imaged at 100 Hz using an infrared ring light and an IR sensitive high speed CMOS camera (Photonfocus, MV1-D1312L-160-CL-12). Frame acquisition was controlled using StreamPix software (Norpix Inc). Data streams were synched using a custom Python script. Tail kinematics were scored manually and confirmed by independent observers. Data were analyzed using Igor Pro software (Wavemetrics). A threshold of 0.2  $\Delta F/F$  was used to define a calcium response.

*Hypaxial muscle: Gal4<sup>s117It</sup>/UAS:GCaMP6s/UAS:ChR2(H134R)-mCherry* larval zebrafish (6dpf) were head-embedded in 2% low melting point agarose. Imaging was performed using a water immersion objective (10x, 0.3NA) on a LSM780 Zeiss confocal microscope, controlled with ZEN software. Scan

rates were 10 frames/second (128 x 128 pixels). Muscles were imaged using an Argon 488 nm laser with 0.9% power before and after unilateral nMLF stimulation. The nMLF was stimulated using a region bleaching scan mode with 40-50% laser power for 200 ms. The minimum laser power required to produce a repeatable tail deflection was used. Muscles were not imaged during the stimulation period.

## **ChR2 stimulation**

*Gal4<sup>s1171</sup>/UAS:ChR2(H134R)-mCherry* larval zebrafish (7dpf) were head-embedded in 2% low melting point agarose. Agarose around the tail was dissected away using a scalpel blade. Fish were allowed to recover from the mounting procedure for several hours. Laser light (473 nm) was delivered to the fish's head, using low numerical aperture multimode optic fibers (10  $\mu$ m or 105  $\mu$ m; HPSC10 or AFS105/125Y, Thorlabs). Optic fibers were prepared as described previously<sup>138</sup>. The position of the optic fiber was controlled using a micromanipulator (MC1000e, Siskiyou Corporation). A 473 nm direct diode laser (LuxX 80mW, Omicron) and 405 nm direct diode laser (LuxX 60mW, Omicron) were mounted within a laser beam combiner (Lighthub, Omicron) and coupled to the optic fiber. Light intensities were controlled by sending an analog voltage signal to the laser. Light intensities between 0.5 and 2 mW/mm<sup>2</sup> measured at the fiber tip were used for ChR2 activation. Tail kinematics were imaged at 250 frames per second (390x390 pixels) using a high-speed camera (Pike F032B, Allied Vision Technologies) and StreamPix software (Norpix Inc). The camera was coupled to a boom-mounted stereomicroscope (SMZ800, Nikon) with a C-mount adapter. Stimulation and imaging were synchronized using custom scripts written in LabVIEW. Muscle stimulation experiments were conducted in the same manner except a 105  $\mu$ m diameter fiber was used.

For Kaede conversion experiments, the laser line was switched to 405 nm (1.8 mW) for 2 min. The light dosage for conversion experiments was therefore 60-90 times greater (intensity x duration) than that used for ChR2 experiments. Given this large difference in light exposure and the increased scattering at

405nm, our conversion experiments are likely to be an upperbound size estimate for ChR2 stimulation sites (Arrenberg et al., 2009).

### **Neuronal ablations**

Neurons were located by position and GFP expression in *Gal4<sup>1171</sup>/UAS:GFP* fish. Imaging and ablations were performed using the same two-photon microscope used for calcium imaging. Neurons were killed by scanning a focused 850 nm femtosecond pulsed laser beam for ~200 ms over a ~1  $\mu\text{m}$  square in the center of soma. Laser power after the objective was ~270 mW/mm<sup>2</sup>. Behaviors were assessed before ablations and 8-12 hours after surgery. For complete unilateral nMLF ablations, we targeted all visible MeS and MeL neurons (6-8 dorsal MeS neurons, MeS1, MeS2, MeLc, MeLr and MeLm in each animal). For MeS-only ablations, we targeted 6-8 neurons MeS neurons and MeS1 and MeS2. For MeL-only ablations, we targeted MeLc, MeLr and MeLm. The completeness of ablations was determined by imaging the ablated brain region after behavioral experiments. Data from animals with incomplete ablations were discarded.

### **Optomotor assay**

Fish larvae (7-8dpf) were head-embedded in the same manner as for ChR2 stimulation except they were allowed to recover from mounting for 8-12 hours. We found this time-delay improved the responsiveness of mounted larvae to visual stimulation. The experimental arena and control software used for the optomotor assay were described previously<sup>156</sup>. Briefly, fish were placed in the middle of an arena surrounded by three LCD screens (5.5 x 7.5 cm), one in front of the fish and one on each side. Caudal-to-rostral drifting gratings were displayed on the two side screens to evoke a forward optomotor response. Rotating gratings were displayed on all three screens to evoke turn responses. Fish tail kinematics were imaged at 250 frames per second (390x390 pixels) using a high-speed camera (Pike F032B, Allied Vision Technologies) and StreamPix software (Norpix Inc). Grating presentation and speed were controlled using a custom script written in LabVIEW. At the start of an experiment, an ideal grating speed was

determined for each fish. These speeds ranged from 16-28°/second for forward gratings and 20-30°/second for rotating gratings. The same grating speeds were used before and after ablations. In the text ipsiversive refers to gratings rotating toward the ablation site whereas contraversive refers to gratings drifting away from the ablation site.

## **Data analysis**

Tail motions were tracked using custom software written in Python. Tail tracking software used OpenCV to load videos and then implemented a tracking algorithm, which returns a series of midpoints along the tail in each frame. The algorithm is seeded by a user-selected point near the base of the zebrafish larvae tail and then iterates towards the end of the tail. At each point, the tail's lateral midpoint was located by taking a cross-section of the tail and convolving with a function representing the luminosity of a prototypical tail cross-section. The maximum of this convolution was used as the tail midpoint. This procedure is then repeated along the length of the tail returning ~40 points for each video frame. Tail angle was calculated by measuring the angle between the first midpoint near the tail base and the mean position of three midpoints at the end of the tail (to reduce noise). The detected tail midpoints were normalized to correct for small variations in the baseline position of the tail. Another custom Python script was used to segment the tracked tail movements into separate behavioral bouts. The bout detection algorithm operates by comparing the smoothed absolute value of the first derivative of the tail angle over time to a threshold. Data were further compiled and visualized using Igor Pro (Wavemetrics).

## **Statistics**

Statistical analysis was performed in Python using the following libraries: Pandas for data structures, Scipy and Statsmodels for statistics. Welch's *t*-test was used for pairwise comparisons. The family wise error rate was controlled with the Bonferroni correction. Normality and homoscedasticity were inspected visually (Q-Q plots) and using tests: Shapiro-Wilk for normality, and Bartlett's and Levene's for equality of variance. Individual tests were as follows: Steer angles (Figure 5C) ANOVA, tail beat frequency

(Figure 5E) Box Cox transform and ANOVA, steer rise time (Figure S6) linear regression, swim duration (Figure S6) Box Cox transform and ANOVA, ablations (Figure 6, 7 and S7) paired *t*-test.

## **Acknowledgements**

We thank T. Xiao for generating the *UAS:GFP* line, E. Kuehn for generating the *UAS:GCaMP6s* line, A. Arrenberg and F. Kubo for technical assistance with the optogenetic stimulation and OMR experimental setups, S. Faumont for assistance with data analysis, W. Staub and A. Tran for animal care, A. Barker, J. Semmelhack, E. Robles, and D. Foerster for critical reading of the manuscript. H. Hguyen and R. Schorner contributed an illustration to Figure 2. This work was initiated at the University of California, San Francisco, and completed at the Max Planck Institute of Neurobiology. Support was provided by the Max Planck Society and grants from the NIH (F32NS064797 TRT; EY12406 & EY13855 HB) and a Grass Foundation fellowship to TRT.

## Supplementary Figures

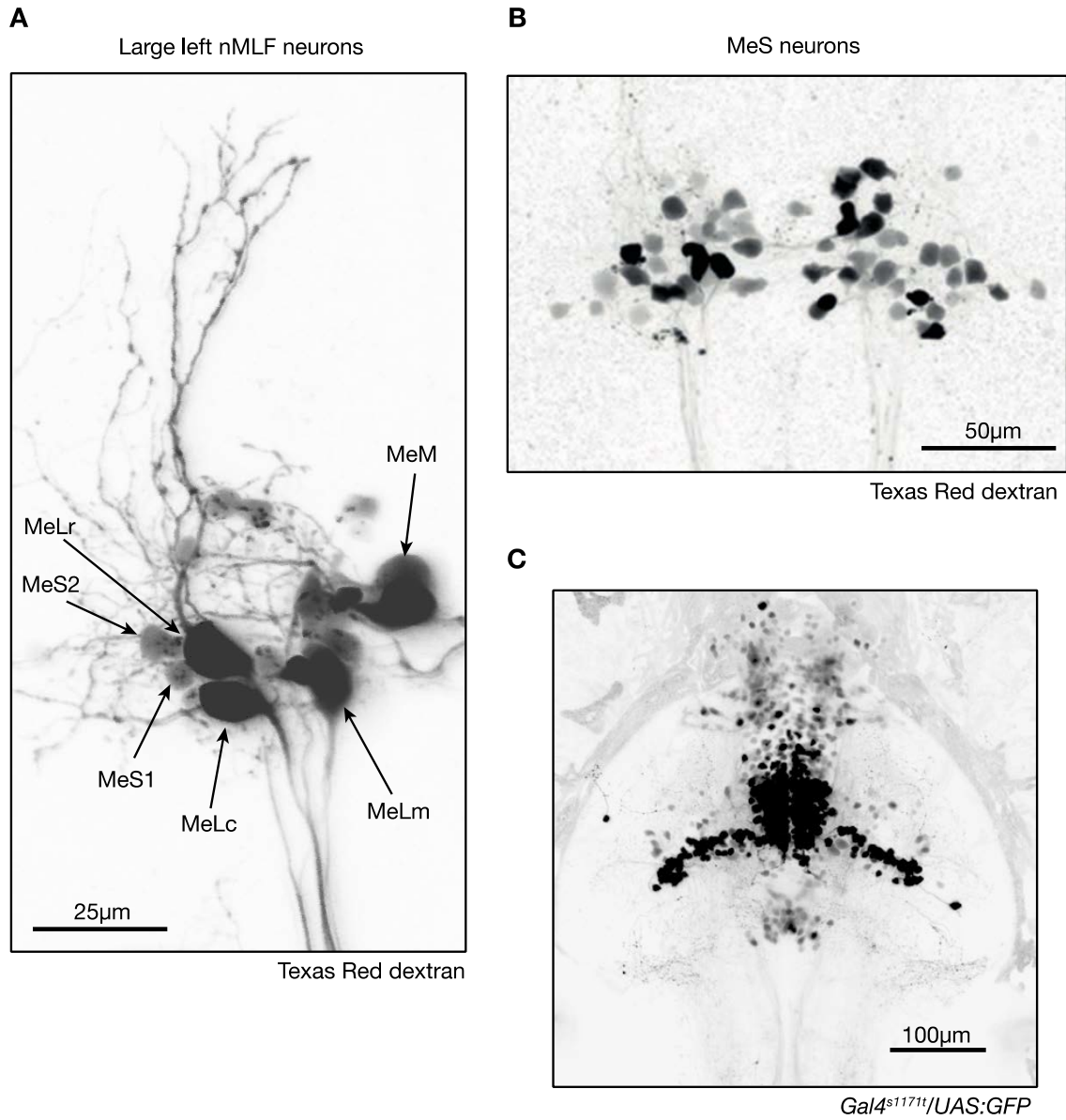


**Figure S1. Anatomy of the nMLF revealed by spinal cord backfills (related to Figure 1).**

**A.** Confocal image projection (80 μm) of several nMLF neurons backfilled from the spinal cord with Texas Red dextran. In this labeling, the large identified neurons MeLc, MeLr, MeLm and MeM are prominently labeled. The identity of each cell is indicated. In addition, the newly identified smaller MeS1 and MeS2 cells are indicated. **B.** Two-photon image projection (80 μm) of a different nMLF backfill in which many MeS neurons are labeled as defined by their small soma diameter. **C.** Confocal image projection (220 μm) displaying both dorsal and ventral expression patterns in *Gal4<sup>s1171t</sup>/UAS:GFP*.

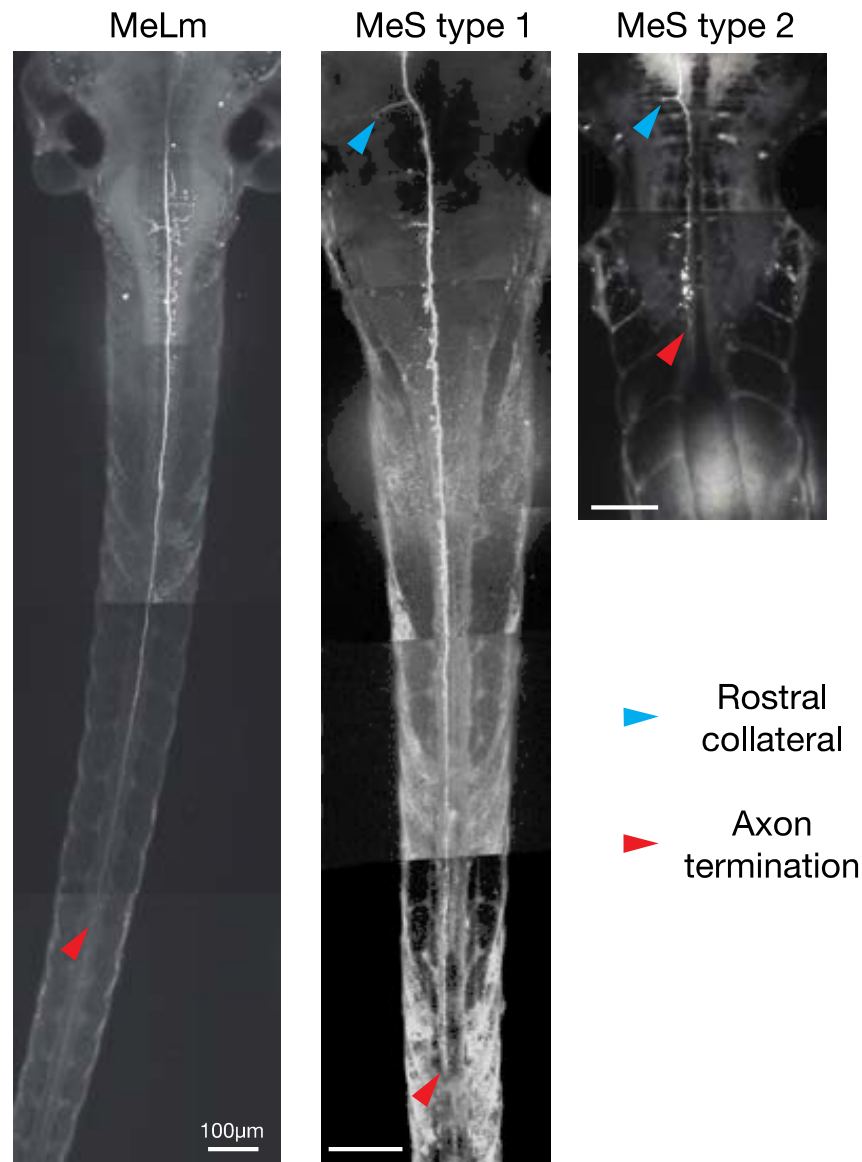
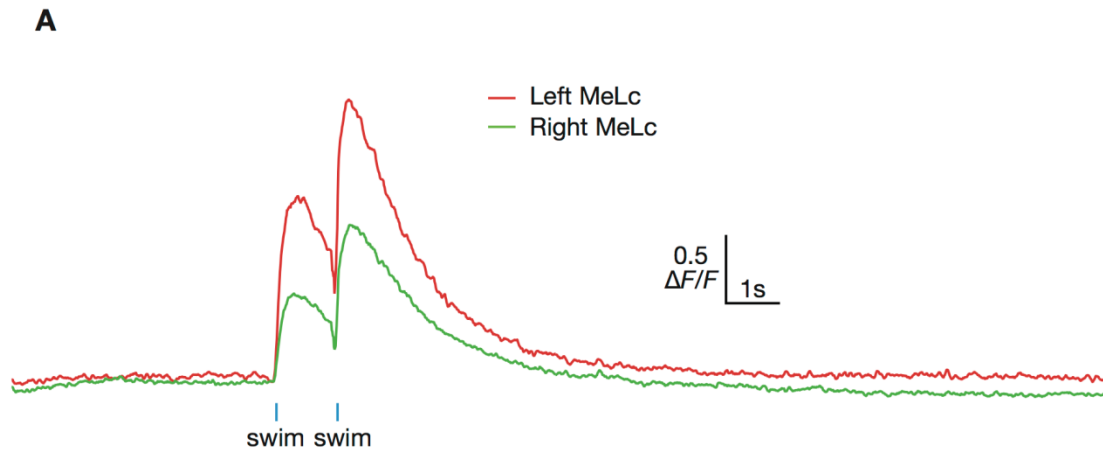


**Figure S2. MeLm and MeS axon morphologies revealed by single-cell electroporations (related to Figure 2).**

Single cell axon morphologies for a MeLm, MeS type 1 and MeS type 2 neuron. GFP expressing neurons in the region of the nMLF were targeted for electroporation in *Gal4<sup>S17H</sup>/UAS:GFP* fish. Cells were electroporated with tetramethylrhodamine dextran 3,000 MW. These images were used for the axon tracing illustrations in Figure 2D-F.





**B**

	Swim	Ipsilateral tail flip	Contralateral tail flip	Struggle
MeLr	30 / 30	9 / 12	10 / 12	5 / 8
MeLc	26 / 27	9 / 12	11 / 12	4 / 8
MeLm	24 / 24	7 / 11	8 / 10	5 / 8
MeS1	24 / 24	10 / 11	13 / 14	5 / 9
MeS2	21 / 21	9 / 11	14 / 14	5 / 8
MeS trans	22 / 23	9 / 13	14 / 18	4 / 11
MeS slow	15 / 16	10 / 14	9 / 14	5 / 10

responses / behavioral events    n=14 fish

**Figure S3. Calcium Imaging (related to Figure 3).**

**A.** Calcium responses in left and right MeLc neurons accompanying multiple swim bouts. Calcium traces were low-pass filtered for display purposes. **B.** Summary table of MeL and MeS calcium responses across spontaneous behaviors.

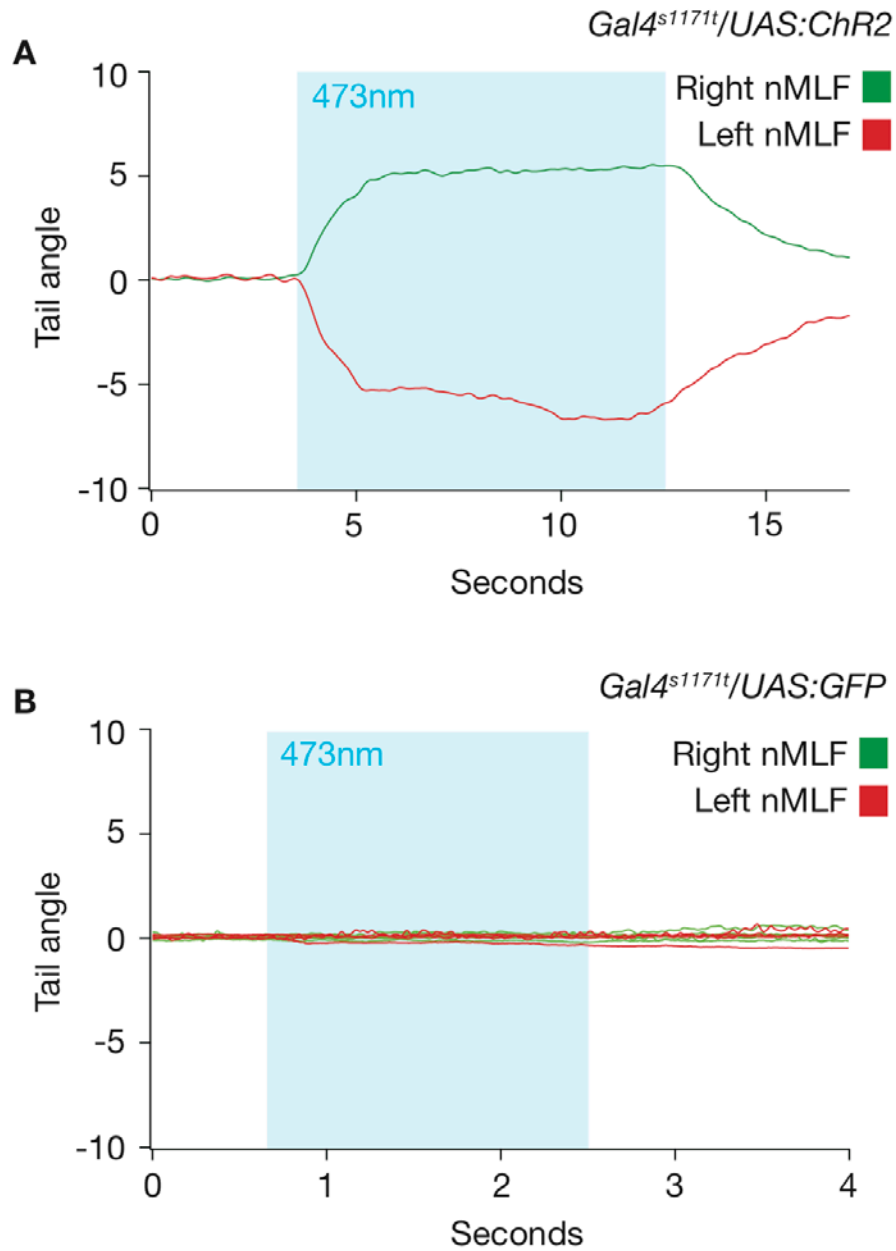


**Figure S4. Stationary fiber stimulation and control responses (related to Figure 4).**

**A.** Tail angle changes in a *Gal4<sup>s1171t</sup>/UAS:ChR2* fish elicited by left or right midbrain stimulation with a stationary optic fiber (blue shaded region, 10  $\mu$ m optic fiber, 10 ms pulses, 20 Hz, 1 mW/mm<sup>2</sup>; traces are from a single fish). **B.** Tail angle changes in *Gal4<sup>s1171t</sup>/UAS:GFP* control fish elicited by left or right midbrain stimulation with a stationary optic fiber ( $n = 8$  fish; 20 Hz, 10 ms pulse width, 1 mW/mm<sup>2</sup>).

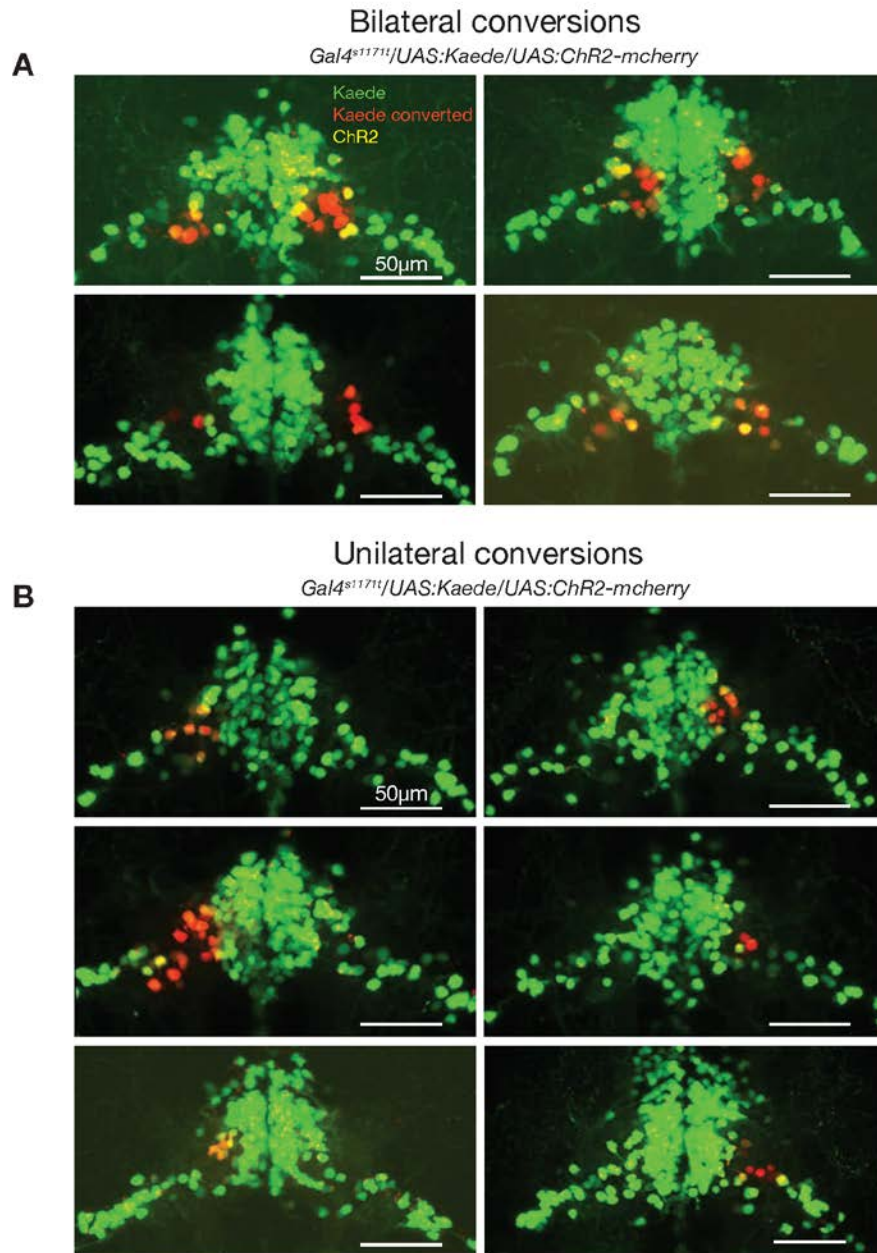


**Figure S5. Kaede photoconversions (related to Figure 4).**

**A.** Confocal image projections (80  $\mu\text{m}$ ) for four *Gal4<sup>s1171t</sup>/UAS:ChR2/UAS:GFP* fish that underwent bilateral Kaede conversion at sites that evoked tail deflections. **B.** Confocal image projections (80  $\mu\text{m}$ ) for six *Gal4<sup>s1171t</sup>/UAS:ChR2/UAS:GFP* fish that underwent unilateral Kaede conversion at a site that evoked an ipsilateral tail deflection.

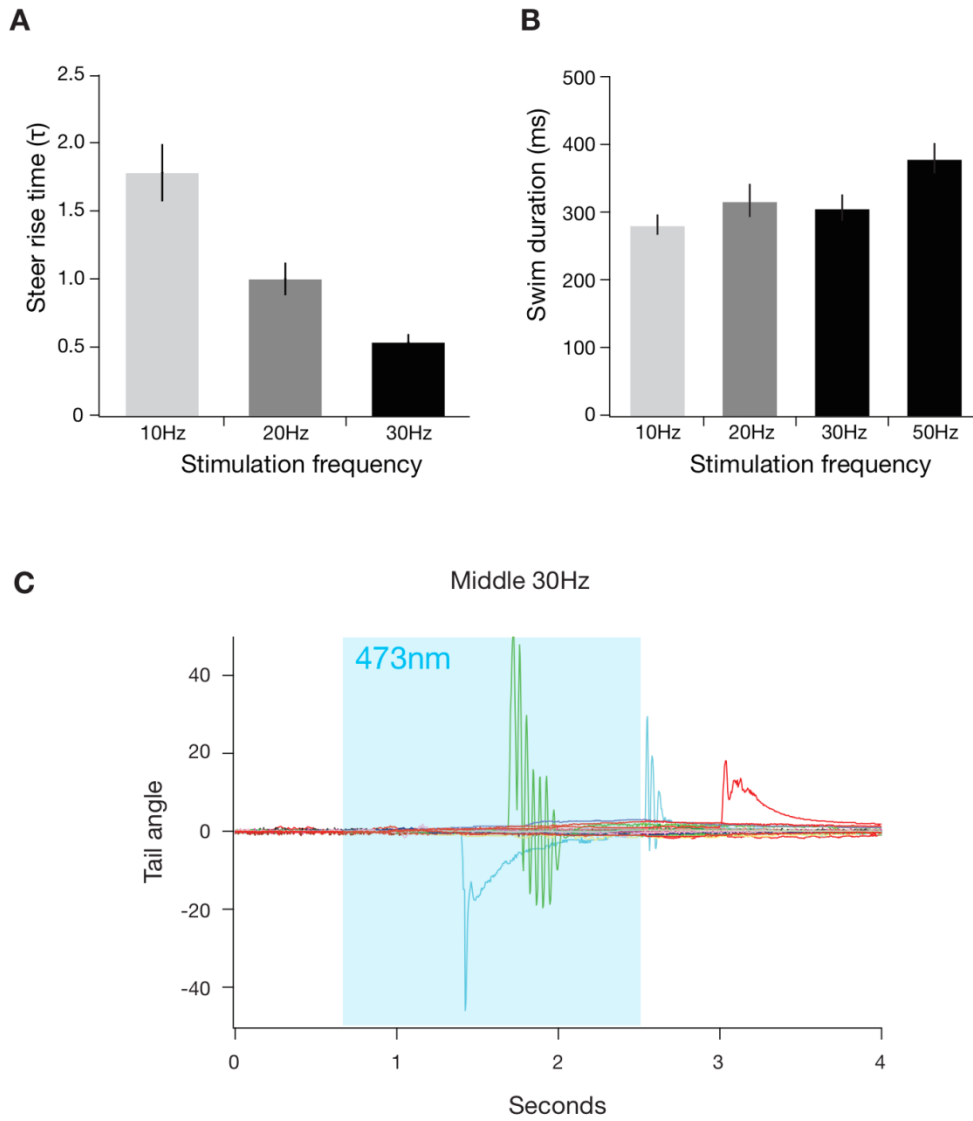


**Figure S6. ChR2 stimulation of the nMLF in *Gal4<sup>Δ171</sup>/UAS:ChR2* fish**

(related to Figure 5).

**A.** Effect of light pulse frequency on steer rise time: Tail bends occur sooner for larger light doses ( $P < 10^{-5}$ ). **B.** Swim bout duration is not affected by light dose ( $P = 0.052$ ). Error bars indicate s.e.m. **C.** Changes in tail angle elicited by stimulation equidistant from the left and right stimulation sites ( $n = 20$  fish; 10  $\mu\text{m}$  optic fiber, 10 ms pulses, 30 Hz, 2  $\text{mW}/\text{mm}^2$ ).

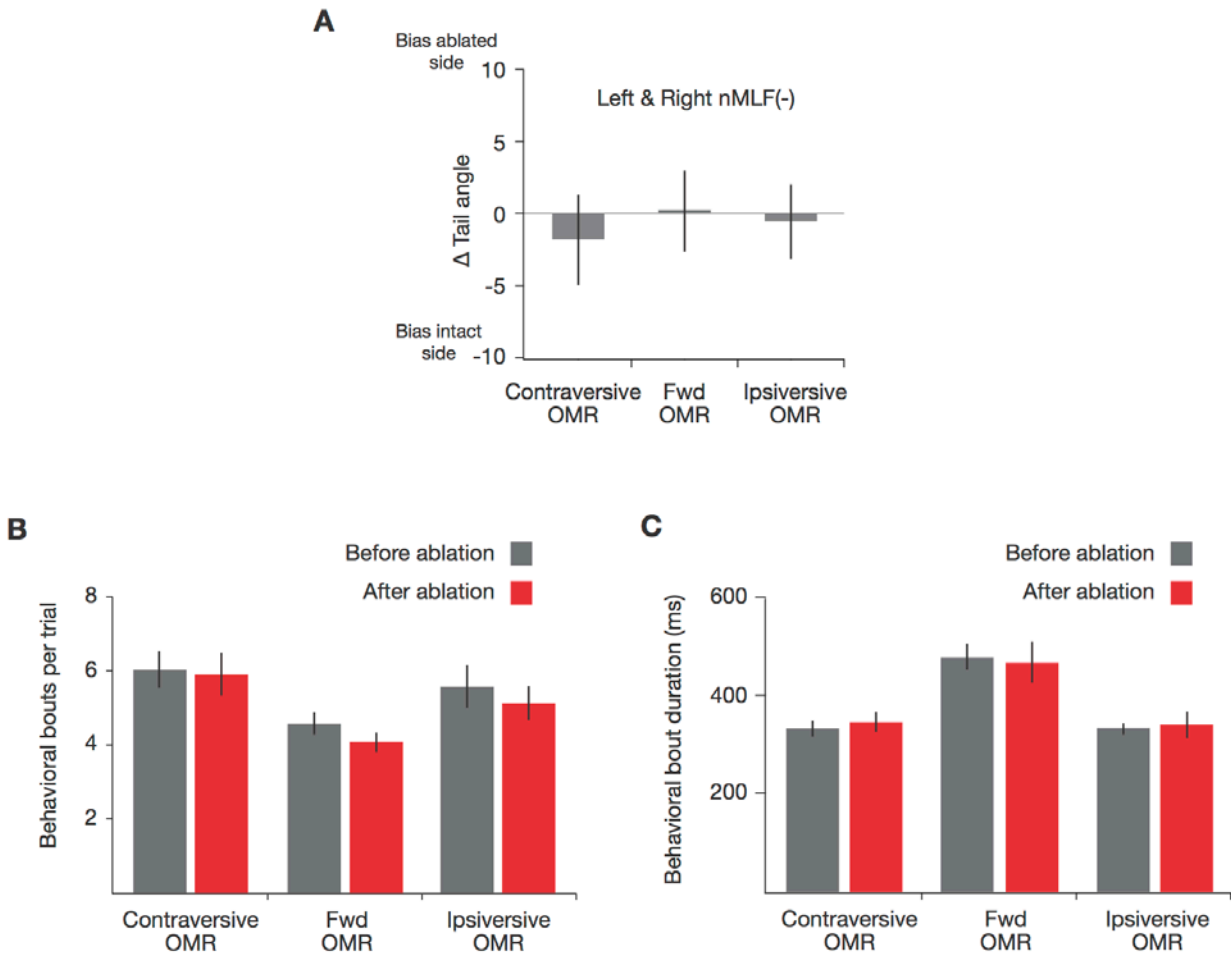


**Figure S7. Effects of nMLF ablation on OMR behavior (related to Figure 7).**

**A.** Bilateral ablations of both MeL and MeS neurons. No change in tail bias was seen for forward ( $n = 7$ ;  $P = 0.97$ ;  $t(6) = 0.03$ ), right ( $n = 7$ ;  $P = 0.84$ ;  $t(6) = -0.21$ ) or left ( $n = 7$ ;  $P = 0.59$ ;  $t(6) = -0.58$ ) stimuli. **B.** Ablation effects on the frequency of behavioral bouts. Contraversive OMR ( $n = 15$ ;  $P = 0.55$ ;  $t(14) = -0.61$ ), forward OMR ( $n = 17$ ;  $P = 0.77$ ;  $t(16) = 0.29$ ), ipsiversive OMR ( $n = 15$ ;  $P = 0.78$ ;  $t(14) = -0.28$ ) were unaffected. **C.** Ablation effects on the duration of individual behavioral bouts. Contraversive OMR ( $n = 15$ ;  $P = 0.85$ ;  $t(14) = 0.85$ ), forward OMR ( $n = 17$ ;  $P = 0.08$ ;  $t(16) = 1.78$ ), Ipsiversive OMR ( $n = 15$ ;  $P = 0.40$ ;  $t(14) = 0.41$ ) were all unaffected.  $n$  values indicate number of fish. Error bars indicate s.e.m.

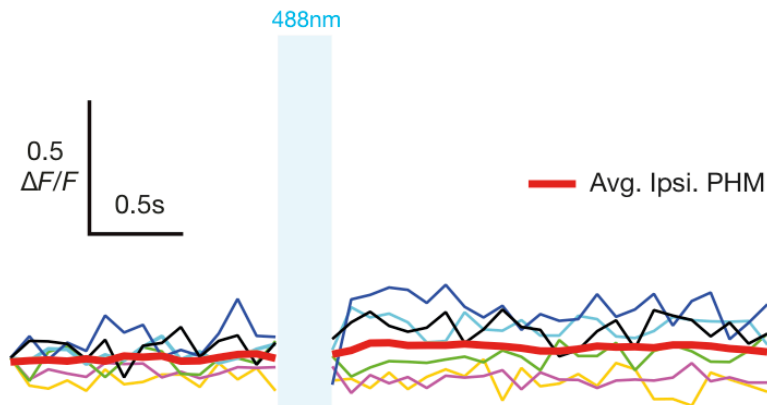


**Figure S8. Muscle calcium responses are dependent on nMLF optical activation (related to Figure 8).**

Individual calcium responses in ipsilateral PHM, following unilateral stimulation 100 $\mu$ m caudal to the ipsilateral nMLF in *Gal4<sup>s117It</sup>/UAS:ChR2* fish ( $n = 6$  fish, average response in red). Blue shaded region depicts a 200 ms epoch of ChR2 stimulation.

## **Section 3 – Optical circuit exploration using shaped three-dimensional light fields**

This work used calcium imaging and optogenetics independently to investigate a motor nucleus, demonstrated its involvement in behavior, and quantified several cell types within the nMLF. This work is a step towards understanding the functional role of neurons within a behavioral circuit. Extracting functional information from the circuit at the level of individual neurons is troublesome when using broad optogenetic activation and calcium imaging in different individuals.

Coupling imaging with simultaneous optogenetic stimulation allows for better circuit dissection, especially within each specimen, and increasing the specificity of the optogenetic activations allows for more precise discovery of how individual cells contribute to the network state. To increase the specificity of optogenetics, the optimal approach is to more selectively shape light – which is more flexible and powerful than using improved genetic targeting, since it allows for different patterns to be activated within each specimen. Simpler approaches to shaping light, such as using a digital micromirror device (as in a projector), are fairly straightforward to implement, however suffer from poor efficiency, generally do not have single neuron specificity (unless field of view is sacrificed), and most limiting, produce only two-dimensional patterns, whereas neuronal circuits are spread throughout three dimensions.

Another approach, which benefits from the two-photon effect for increased axial resolution, is scanned two-photon activation<sup>161</sup>. However scanned activation is more sensitive to the channel kinematics regarding current integration in the neuron, since not all channels in the targeted neuron are being activated simultaneously, and in our hands it seemed to be quite dependent on the expression levels of the optogenetic actuator and not reliable across neurons. Additionally, since this technique can only activate a single neuron at a time, activating multiple neurons must be done in series, limiting the number that can be activated.

The solution we have chosen to implement is computer-generated holography. This is a complex but extremely powerful technique, as it allows for the generation of complex three-dimensional patterns. Combining it with the two-photon effect achieves the resolution required to activate targeted neurons individually.



# **Linking neural circuits to behavior by 3D cell resolution optogenetics and multiplane network imaging**

Marco dal Maschio\*, **Joseph Donovan\***, Thomas Helmbrecht, and Herwig Baier<sup>#</sup>

Department Genes – Circuits – Behavior, Max Planck Institute of Neurobiology, 82152 Martinsried,  
Germany

**\*Equal contributions**

<sup>#</sup>Corresponding author, e-mail: [hbaier@neuro.mpg.de](mailto:hbaier@neuro.mpg.de)

## Abstract

Understanding how individual cells in the brain interact to process information and generate behavior remains a major challenge for neuroscience. We developed a precise light shaping system, based on two-photon computer-generated holography (2P-CGH) to independently target multiple single neurons in the zebrafish brain. Our optical configuration enabled simultaneous 3D photostimulation of up to eight channelrhodopsin (ChR2)-expressing cells, while monitoring GCaMP6s signals in hundreds of neurons in different planes at four volumes per second. Using an iterative selection procedure, we identified neurons in the midbrain that are crucial for driving a quantifiable motor output. The morphologies of these neurons could subsequently be reconstructed following 2P photo-activation of co-expressed paGFP. An analysis framework, based on dimensionality reduction and regression models, was designed to causally link neuronal activity to motor outcome and to characterize the brain-wide network dynamics. Together, this powerful toolkit allows circuit investigation at the resolution of individual neurons, changing the scale and depth at which questions about the cellular basis of behavior can be answered.

## Introduction

Neuronal networks process sensory information and generate behavior by means of dynamic interactions among synaptically connected cells. Disentangling the contributions of individual neurons and their connections to circuit function is a central goal for neuroscience<sup>162,163</sup>. Technical advances have enabled functional imaging from large populations of neurons, allowing parameters of stimuli and behavior to be correlated with the activity of individual neurons<sup>164,165,166,167,168</sup>. This approach is useful to localize neurons active during a particular task; however, imaging alone provides only correlative information, which is insufficient to directly relate a neuron's firing to activity driven in other neurons or to downstream behavioral output<sup>169,170</sup>.

To better explore causal relationships between circuit dynamics and motor output, we set out to develop a suite of non-invasive, optical methods combining targeted activation of cells with interrogation and analysis of brain activity during behavior. Optogenetics, through the use of light-gated ion channels, enables photostimulation to drive cells of interest in the living brain. Technical proofs of concept for combining targeted optogenetics with genetically encoded optical sensors have been reported<sup>171,172,173</sup>. Here we have developed this approach further and demonstrate its potential for circuit exploration in the genetically and optically accessible zebrafish system. Previous work has identified several circuits of moderate complexity that produce robust and quantifiable behaviors in head-restrained fish larvae<sup>166,174,175,168</sup>. In the current study, we focus on the nMLF, a midbrain nucleus of the reticular formation positioned ventral to the tectum. The nMLF was previously shown to play an active role in controlling tail posture<sup>174</sup> and in the engagement of particular swim patterns<sup>176,168</sup>. We used the nMLF circuit for a proof of principle to show how 3D optogenetics, volumetric imaging, and behavioral recording can be simultaneously combined to identify critical circuit-driving components.

## Results

### Hardware configuration

To achieve precise targeting for optogenetic stimulation, we adopted a 2P-CGH approach<sup>177,178</sup> using a liquid-crystal Spatial Light Modulator (SLM) to engineer the phase of the light wavefront and precisely render photostimulation patterns in the sample volume. The photostimulation path is supplied by a pulsed infrared (IR) source tuned to 920-950 nm for the 2P activation of ChR2<sup>161</sup> and is coupled to a standard galvo-galvo 2P imaging system (Fig. 1a). The imaging path includes an electro-tunable lens to remotely offset the imaging plane<sup>179</sup>. A high-speed camera is used to record the motor behavior of a head-restrained fish larva and an additional camera for calibration (Supplementary Fig. 1, for details, see online methods).

We developed a procedure for precise 3D registration of the two light paths. A multiplane iterative Gerchberg-Saxton algorithm<sup>180</sup> was implemented in order to render precise 3D light distributions in the sample volume, taking into account parameters from the optical system and registration. This protocol typically achieves alignment of approximately one  $\mu\text{m}$  between the imaging and photostimulation beams ( $0.9 \pm 0.3 \mu\text{m}$ , mean  $\pm$  sd) and can address a volume of  $160 \times 160 \times 250 \mu\text{m}^3$ .

To test the 3D precision of this approach in a live brain, we photo-activated paGFP<sup>181</sup> in multiple individual neurons in a densely packed population (Fig. 1b). The stimulation profile for each target cell was chosen to be  $6 \mu\text{m}$ , closely matching the typical cell diameter in this region ( $6.9 \pm 0.9 \mu\text{m}$ ). Targeted neurons were successfully visualized with paGFP, with minimal off-target fluorescent signal in neighboring cells (Fig. 1c; Supplementary Fig. 2).

### Protocol design for simultaneous 2P imaging and 2P photostimulation

We devised a protocol to photostimulate single neurons expressing an optogenetic actuator, while simultaneously recording the induced network activity using a genetically encoded calcium indicator.

Ideally, the activation spectra of actuator and sensor molecules should not overlap. Previous studies have combined imaging of GCaMP variants at 920 nm with red-shifted actuators<sup>172,173</sup>, such as C1V1<sup>182</sup>, ReachR<sup>183</sup>, or Chrimson<sup>184</sup>, excited at 1020-1060 nm. However, the activation spectra of these actuators have a blue “shoulder”<sup>185,186</sup>, which, when combined with imaging GCaMP, can lead to unintended activation and poses restrictions on the choice of imaging parameters<sup>172,173</sup> (see Discussion for details). We therefore adopted a strategy with an inverted excitation scheme based on ChR2 activation at 920 nm (near its absorption maximum) and GCaMP6s imaging at 1020 nm. This is possible because the action spectrum of GCaMP extends to wavelengths >1000 nm<sup>187,188,189</sup> (Supplementary Fig. 3a). We reasoned that the low ChR2 activation probability at 1020 nm<sup>190</sup> and its shorter off kinetics<sup>182,190</sup> would effectively reduce the risk of inadvertently altering membrane potential during imaging.

To verify that our imaging at 1020 nm does not activate ChR2, we measured activity in neurons of transgenic zebrafish expressing GCaMP6s with and without ChR2 across laser power levels ranging from 14 mW to 40 mW. The number of spontaneous transients was very similar for both genotypes, even at power significantly above what we used for imaging (0.85 vs 0.63 events per minute, respectively; Supplementary Fig. 3b). Imaging at 920 nm, in contrast, leads to more transients when ChR2 is co-expressed (1.9 vs. 0.81 events per minute, respectively).

We also investigated if stimulation at 920 nm could adversely impact GCaMP6s imaging through indicator photobleaching or phototoxicity. Using laser power densities ranging from 0.05 to 5 mW/ $\mu\text{m}^2$ , we found that GCaMP6s fluorescence level decreased by less than 4% right after the photostimulation event (Supplementary Fig. 3c). Furthermore, baseline fluorescence was similar before and after repeated photostimulations ( $2 \pm 1.5\%$ ; five stimulations over 60 seconds), confirming the photostability of GCaMP6s. However, the stimulation light did cause detectable contamination in the recorded signal during the photostimulation phase with a non-linear relationship to stimulation intensity (Supplementary Fig. 3d). Therefore, especially at high stimulation powers, we adopted a line-by-line subtraction

procedure to filter out the stimulation artifact when contamination of the GCaMP signal was significant (see Methods; Supplementary Fig. 3e).

### **Photostimulation with single-neuron precision in the zebrafish brain**

To test the precision of photostimulation, we targeted midbrain neurons expressing ChR2 with 920 nm activation while simultaneously imaging GCaMP6s at 1020 nm (Fig. 1d,e). When ChR2-positive neurons were stimulated, with typical power densities ranging from 0.1 to 0.5 mW/ $\mu\text{m}^2$ , we detected strong calcium transients in 97% of trials (581 trials across 6 fish). As expected, the temporal dynamics of each induced event were similar to spontaneous events (Fig. 1d; Supplementary Fig. 4a,b), and their amplitudes were correlated with the expression level of ChR2 (Supplementary Fig. 4c). Targeting the 920 nm photostimulation beam at neurons expressing GCaMP6s, but not ChR2, did not result in any detectable responses.

To measure spatial resolution of our 2P-CGH protocol, we shifted the targeted volume laterally or axially, while recording responses from a small population of cells co-expressing ChR2 and GCaMP6s. Calcium transients were detected only in the targeted cells in the vast majority of trials (Supplementary Fig. 5a). The induced  $\Delta F/F$  rapidly decreased with increasing distance from the targeted cell (Supplementary Fig. 5b,c): outside a volume approximately 8  $\mu\text{m}$  wide and 10  $\mu\text{m}$  high, the detected responses had less than half the amplitude of those at the center of the target. Together, these experiments demonstrate that photostimulation can be restricted to the dimensions of single cells *in vivo*.

### **Simultaneous 3D optogenetics and multiplane imaging**

To maximize the potential of 3D optogenetic activation for the investigation of circuits, we coupled it to fast volumetric functional imaging. An electrically tunable lens (ETL)<sup>179</sup> was placed close to a plane conjugated to the back focal plane of the objective, to remotely shift the imaging plane within few milliseconds, independently of the photostimulation patterns. Our acquisition protocol (Fig. 2a) allows for recording of GCaMP6s signals in 5 different planes covering a volume of 80 x 160 x 32  $\mu\text{m}^3$  at a rate of 4

volumes per second. The measured settling time for the ETL to accomplish an 8  $\mu\text{m}$  z-step was  $6.1 \pm 1.2$  ms (Supplementary Fig. 1b). As a proof of principle of the 3D stimulation capability, we show that targeted cells in different planes can be independently and selectively stimulated, showing responses locked to the stimulation timing, with minimal activation of non-targeted cells (Fig. 2 c,d). We also confirmed that, with our chosen parameters, inadvertent activation of neurites near the cell soma does not induce somatic calcium responses in the targeted cell (Supplementary Fig. 6).

### **Using 3D optogenetics to explore behavior**

The nMLF is a midbrain nucleus which receives inputs from visual areas and projects axons to the spinal cord<sup>175</sup>. In initial experiments, we showed that broad unilateral photostimulation of the nMLF with an optic fiber induces a tail deflection towards the activated side, as has been previously reported<sup>174</sup> (Supplementary Fig. 7a,b). Using the versatility of our approach, we asked which subsets of neurons could drive this motor output. Initially, we mapped the circuit coarsely by photostimulating slightly overlapping regions, 18  $\mu\text{m}$  in diameter ( $0.2 \text{ mW}/\mu\text{m}^2$ ), which were located at different distances from the midline (Fig. 3a). From the recorded behavioral data, we extracted the spatiotemporal kinematics of the tail with a computerized tracking routine<sup>191</sup>, to quantify tail steering events (Fig. 3b,c) and distinguish these from other motor patterns. We found that activation of a region in the center of the nMLF (region B of Fig. 3a) resulted in the largest tail deflection angles (Fig. 3b). The typical behavioral pattern during a 2 second stimulation consisted of a tail deflection ( $3.4 \pm 2.2$  degrees/s), followed by a slower relaxation phase ( $1.7 \pm 0.9$  degrees/s) after the stimulation (Fig. 3c). Activation periods shorter than two seconds elicited progressively smaller bending amplitudes, with a minimal duration of 200 ms necessary to cause a detectable change in tail position (Supplementary Fig. 8). The same stimulation protocol applied in control fish expressing only a fluorescent marker did not result in tail deflections (Fig 3b).

## **Identifying groups of behaviorally relevant neurons**

The number of possible activation patterns, consisting of different combinations of targeted neurons, scales up rapidly with the number of neurons in the circuit (see also Discussion). We developed an iterative procedure to straightforwardly isolate a minimal subset of neurons that are sufficient to drive the behavioral outcome. Starting from the coarse stimulation patterns detailed above, we focused on those that induced significant tail bending. We then probed subsets targeting one less neuron than the current set and selected the one subset with the greatest average magnitude of bending events. This procedure was repeated until the subset was insufficient to elicit behavior. For the example exploration in Fig. 3d, starting from the original set, this procedure quickly arrived at a critical subset of three neurons.

## **Morphological characterization of functionally identified neurons**

To assist in the mapping of these behaviorally relevant neurons across different specimens, and as a step towards a circuit wiring diagram, we show the possibility to reconstruct the morphologies of identified neurons using paGFP photoactivation. We co-expressed ChR2 and paGFP in the nMLF and targeted two-photon excitation at 750 nm to label selected single neurons identified during the behavior characterization (Fig. 3e,f). Tracings of several neurons in different fish were merged in one reference map to find commonalities in their morphologies and connectivity patterns (Fig. 3g). To further enhance this approach, the addition of a nuclear localized calcium indicator can provide complementary functional information, enabling 2P optogenetics, 2P imaging, and 2P paGFP photoactivation all within the same cell (Supplementary Fig. 9).

## **Exploration of network dynamics supporting behavior**

Next we leveraged our approach to investigate the induced network dynamics of the nMLF circuit driving behavior. After identifying a small subset of behaviorally relevant neurons as described, we recorded the activity of the surrounding network by multiplane imaging. We imaged a five plane volume including the nMLF, while photostimulating the identified neurons with 2P-CGH for two seconds (Fig.



4a). This allowed the recording of 486 neurons while tracking behavior (Fig. 4b). Consistently across different stimulation trials and fish, a subset of neurons showed activity profiles locked to the stimulation and/or correlated with tail bending (Fig. 4c, Supplementary Fig. 10). A different set of neurons showed activity associated with large amplitude tail oscillations, which occurred with low probability (Fig. 4c, trial 3).

To visualize the relevant temporal components of the circuit activity, we adopted an analytical framework based on dimensionality reduction by independent component analysis (ICA). This approach projects common activity patterns across the circuit into few components. In the representative example given in Fig. 4, the ICA captured more than 40% of the variance in the network dynamics within a three-dimensional representation (Fig. 4d). The first component (IC1) captured the phasic increase in activity induced by photostimulation and the onset of tail bending. The other two components were generally associated with swimming (IC2) or with slower, perhaps adaptive, integrative or preparatory, changes in circuit state (IC3).

This compact description of circuit dynamics can also be used to evaluate the relative contribution of individual neurons towards each IC (Fig. 4e). For IC1 (“tail steering”), the corresponding map shows that most neurons are localized on one side of the fish, ipsilateral to the stimulation. For IC2 (“swimming”) and IC3 the patterns of activity are broader and extend to the contralateral circuit. The “center of mass” for each IC was quantified using a laterality index, showing a significant lateralization for IC1 (Fig 4e). This characteristic pattern was consistent across trials and several fish (n=30 trials in 3 fish; Supplementary Figs. 10a, 11a, and 12). Trials with a different stimulation pattern or with the pattern shifted to a different axial plane failed to induce tail movements (Supplementary Fig. 11b).

In some of the fish tested, this method identified a small subpopulation of cells, contralateral to the stimulation targets, that showed a negative weight for IC1. Focusing on these cells, we realized that after the onset of the stimulation, while the cells on the ipsilateral side took  $1.7 \pm 0.4$  s (mean  $\pm$  s.d.) to

reach the  $\Delta F/F$  maximum, this population of contralateral cells, after a delay of  $1.6 \pm 0.5$  s (mean  $\pm$  s.d.), reached a negative peak in  $2.2 \pm 0.6$  s (mean  $\pm$  s.d.) followed by a gradual return to baseline levels (Supplementary Fig. 13). We interpret this kind of activity as a suppression of ongoing activity induced by the stimulation on the ipsilateral side of the circuit.

### **Linking network dynamics to behavior**

Understanding behavior requires spatiotemporal features of network activity be related to specific behavioral parameters. A clustering procedure applied to the kinematic parameters of induced tail movements (Fig. 5a,b; see Methods for details) revealed that the behavioral outcome fell into two distinct classes: one representing the trials in which a tail deflection of varying amplitude was observed, the other in which large amplitude swimming bouts also occurred (Supplementary Fig. 14). We adopted a logistic model to evaluate the relationship between network states and behavior outcomes. This model assigns a weight to each neuron, which relates that neuron's activity to a specific behavioral class. Regularization is used to find sparse components and reduce overfitting (see Methods). This analysis reveals the specific tuning of the different cells in the network (Fig. 5b) and suggests that induced neuronal dynamics can be reliably related to the behavioral outcome.

Next, we focused on the first behavioral cluster (tail bending events without swims) and employed a regularized linear regression to model the tail angle at each instant based on the current neuronal activity recorded in the circuit (Fig. 5c). This simplified model predicts the tail angles, and pinpoints the few neurons that have the greatest contribution to this behavioral outcome (Fig. 5d). The resulting behavior map shows an ipsilateral cluster of cells with increased activity when the tail is deflected ipsilaterally (in red) and a second population, mostly contralateral, which decreases activity during tail steering (in green). Maps such as these can serve as the starting point for further exploration of the circuit, either by experimental probing or computational modeling, to examine the differential involvement of individual circuit components on behavioral parameters.

## Imaging of long-range neural activity

How do other brain regions respond to the activity initiated in the nMLF? In addition to investigating local functional dynamics, our configuration was used to detect induced GCaMP6s signals across the whole brain in a zebrafish larva. To record photostimulation-linked activity at a distance, we imaged a 550  $\mu\text{m}$  field of view at 4Hz. Up to 9 planes, separated by a z-step of 8-10  $\mu\text{m}$ , were sequentially recorded. This volume contains almost the entire midbrain and hindbrain of the larva. A pixel-wise regression analysis<sup>164</sup> was used to identify cells activated upon stimulation leading to behavior. This approach revealed a focus of behavior-linked activity within and near the stimulus site (Fig. 6a), as expected, but also another “hotspot” in the hindbrain localized 250-300  $\mu\text{m}$  caudally and 60-70  $\mu\text{m}$  dorsally to the nMLF (Fig. 6a). Most responsive cells showed an activity pattern that was in phase with the photostimulation. However some cells, especially on the contralateral side, present activity profiles out of phase, with a more prominent component near the end of stimulation - corresponding to the relaxation of the tail (Fig. 6c). The optimal regression for these cells included a temporal shift for the fitting functions of 1.6-1.9 s after the onset of the photostimulation. Thus our combined approach enables following the activity induced by only a few neurons, through the whole brain, to uncover spatiotemporal network relationships underlying behavior.

## Discussion

Here we present a suite of optical methods and analytical approaches for a comprehensive interrogation of neuronal circuits in the brain of a behaving animal. Optogenetic activation in 3D is achieved by phase modulation of the light wavefront with 2P-CGH, enabling parallel and independent photostimulation of multiple cells expressing ChR2<sup>192,178,93</sup>. We extended this approach in four directions: First, we designed a novel protocol for all-optical interrogation of the circuits, combining ChR2 photostimulation with activity recording using GCaMP6s. This enabled stimulation and recording of network dynamics, associated with a behavioral output, at the scale of single cells. Second, we showed

how 2P-CGH can be combined with a volumetric imaging approach based on an electro-tunable lens to retrieve functional signals in distant regions and axial planes distinct from those of the stimulation sites. Third, we devised an exploratory strategy to identify behaviorally-relevant neuronal subsets and to deal with the "combinatorial explosion" that accompanies multi-neuron activation experiments. This let us establish causality between defined optogenetic activation patterns and induced motor behavior. Using this iterative selection procedure, we found that as few as three cells in the nMLF of the midbrain tegmentum could drive a simple motor behavior, the steering of the tail. Fourth, we outlined a flexible computational analysis strategy to relate the neuronal activity patterns to specific aspects of the induced behavior, which helps to form testable hypotheses about circuit mechanisms.

Two-photon activation of ChR2<sup>194,161,190</sup> and C1V1<sup>190</sup> have been previously achieved with fast raster or spiral scanning along the contours of the cell body<sup>194,172,190,161,168</sup>. Here we adopted an alternative approach. Using 2P-CGH<sup>178,177,195,196</sup>, we achieved parallel activation of ChR2 molecules through multiple 2D-extended illumination shapes in a 3D volume to maximize simultaneous membrane currents<sup>161,178</sup>. With 2P-CGH, excitation profiles can be tailored to the actual sizes of the targeted cells, chosen from a heterogeneous neuronal population. It is also worth considering photostimulation efficiency; while scanning schemes sum up the currents of opsins activated sequentially, 2P-CGH achieves simultaneous activation and is therefore less sensitive to the off-kinetics of the particular actuator used.

By engineering the illumination profile to match the diameter of the targeted cells, we have achieved parallel activation of up to eight neurons even in densely packed regions of the zebrafish brain (typical cell body size is 6-7  $\mu\text{m}$ ; inter-cell membrane gaps are 1-3  $\mu\text{m}$ ). We further demonstrate that, by combining 2P-CGH with volumetric imaging, it is possible to investigate how induced signals propagate through extended brain networks. Several approaches have been proposed for volumetric GCaMP imaging<sup>197,179,198,199,200</sup>. We selected a configuration based on an electrically tunable lens<sup>179</sup>, because it is straightforward to implement in an already existing optical path and provides a temporal resolution of a few milliseconds.

We searched systematically for an actuator/sensor pair for which spectral crosstalk would be minimal and identified a scheme that could be further expanded in the future to include a red-shifted calcium sensor to target two different neuron populations. However, we note that the currently available red-emitting indicators produce substantially weaker signals than GCaMP6s<sup>188,201,189</sup>. Moreover, they may induce undesirable fluorescence increases when excited with light in the blue-UV range<sup>201,202,99</sup> and have been reported to show a secondary absorption component in the band typically used for 2P ChR2 activation<sup>189</sup> (Supplementary Fig. 15).

Unintended activation of the optogenetic actuator is a critical concern for this type of experiment. Theoretically, using a red-shifted opsin variant would therefore be advantageous. However, the common red-shifted actuators, such as C1V1<sup>204,182,190</sup>, ReachR<sup>183</sup> and Chrimson<sup>184</sup>, have a significant shoulder in the blue range<sup>185</sup> of the spectrum and therefore cannot easily be combined with GCaMP6s and other tools<sup>182,184,205,172,173</sup>. By using ChR2 together with a longer GCaMP6s imaging wavelength we were able to avoid activating this shoulder.

Even ignoring differences in activation power and timing, selecting just five neurons from an ensemble of 50 produces millions of potential combinations. To navigate this combinatorial explosion, we used a simple exploratory strategy. First, we identified a relatively large group of neurons in the nMLF that, when activated, evoked tail steering. We then picked overlapping subsets from among the initial population to determine if their activation was sufficient for the behavior. This procedure was repeated with fewer and fewer cells. In the case of tail bending, this iterative subtraction strategy quickly converged on a small subset of neurons that were sufficient to drive the behavioral outcome. Such detailed characterization is not feasible with traditional photostimulation approaches<sup>166,174,206,207,208</sup>.

Our approach allowed us to identify large ensembles of cells associated with active control of tail position. To handle the complexity of this data set we used dimensionality reduction and regularized regression algorithms. Dimensionality reduction extracts simplified activity patterns from the network, based purely on the relationships between neurons' activities. We were encouraged to find that a small

number of components captured the most relevant features of network dynamics and behavioral output. This was complemented by regularized regression models to quantify the contributions of individual neurons. Neurons within a local circuit may often be correlated, which poses a challenge for regression models; however, the combination of ICA and regression effectively solves this problem (see also methods).

The methods presented here capture correlative and causative relationships between neural networks and behavior in an individual brain. Although the broader circuit architecture of the zebrafish brain is stereotyped<sup>165</sup>, number and position of single neurons are intrinsically variable among animals. Therefore, in order to draw general conclusions, it is useful to obtain additional information about the neurons identified by functional imaging. Our modular approach has allowed us to visualize the morphologies of these cells by photoactivation of co-expressed paGFP<sup>181</sup>. This procedure could, in the future, be repeated across many specimens, selecting specific sets of functional components and aligning them in a standard reference brain<sup>209</sup>. Information about transmitter phenotype, gene expression and, eventually, connectivity can then be added to incrementally build up a function-based wiring diagram.

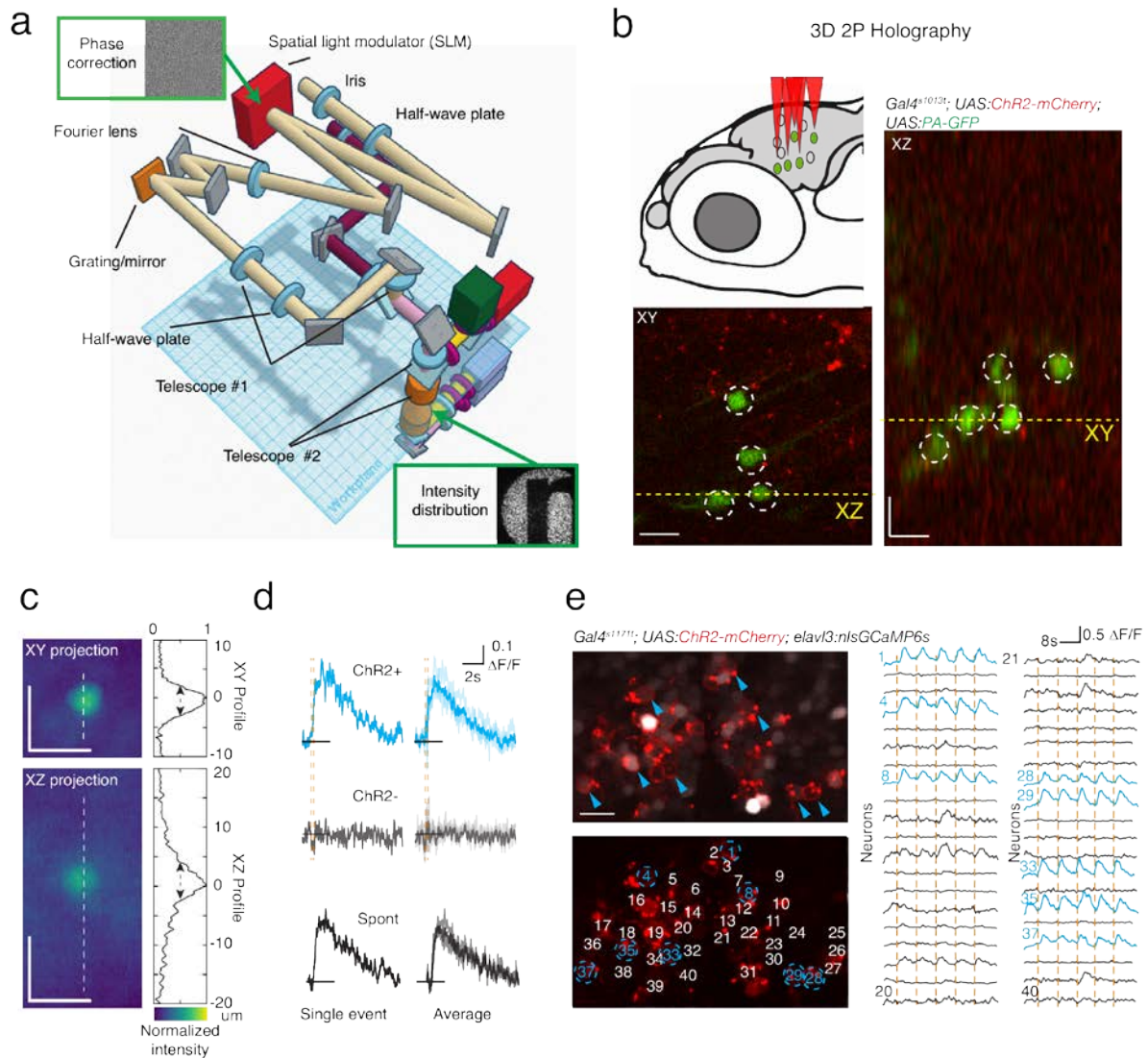


**Figure 1. Parallel two-photon optogenetic photostimulation and activity readout**

(a) The optical layout uses a spatial light modulator (SLM, red) as the core element of the photostimulation path (light brown) to impose a phase modulation pattern, enabling precise photostimulation. The photostimulation path is driven by a dedicated Ti:Sapphire laser, and includes a beam expander, iris, and half-wave plate to condition the beam to the window size and the polarization preference of the SLM. The phase modulated beam is combined with the imaging path (purple path) by a polarizing beam splitter after the galvo-galvo scanhead and is relayed to the back focal plane of the objective by means of two telescopes. The objective transforms the phase pattern, computed by means of

an FFT-based algorithm, into the designed intensity distribution at the sample (bottom green inset, institute logo). **(b)** Parallel two-photon activation of paGFP *in vivo* using a three-dimensional excitation pattern with a random distribution of circular ROIs (3  $\mu\text{m}$  radius). The photoconversion foci are generated in optic tectum at the depth of 120-150  $\mu\text{m}$ , in a zebrafish larvae expressing mCherry and paGFP (*Gal4s1013t*, *UAS:ChR2(H134R)-mCherry*, *UAS:paGFP*). **(c)** Axial and lateral average projections of a paGFP photoconversion volume obtained *in vivo* with a target pattern 6  $\mu\text{m}$  in diameter. The paGFP profiles, photoconverted at 750 nm with a power of 0.25 mW/ $\mu\text{m}^2$  at the sample, closely match the typical cell diameter (FWHM:  $5.84 \pm 0.56 \mu\text{m}$  laterally and  $7.86 \pm 1.2 \mu\text{m}$  axially). **(d)** Somatic GCaMP6s signals induced by 200 ms photostimulation at 920 nm, while imaging at 1020 nm. Cells expressing ChR2 and GCaMP6s show stimulation-induced calcium increases (blue traces) while cells expressing only GCaMP6s (gray traces) do not. Activation events in targeted neurons show similar response dynamics to spontaneously occurring events (black traces). **(e)** Parallel neuronal stimulation *in vivo*. A small network of neurons is imaged during repeated simultaneous photostimulation of eight targeted neurons (in blue). Photostimulations are indicated by orange vertical lines, and the traces for photostimulated neurons are in blue. Scale bars are 10  $\mu\text{m}$ .



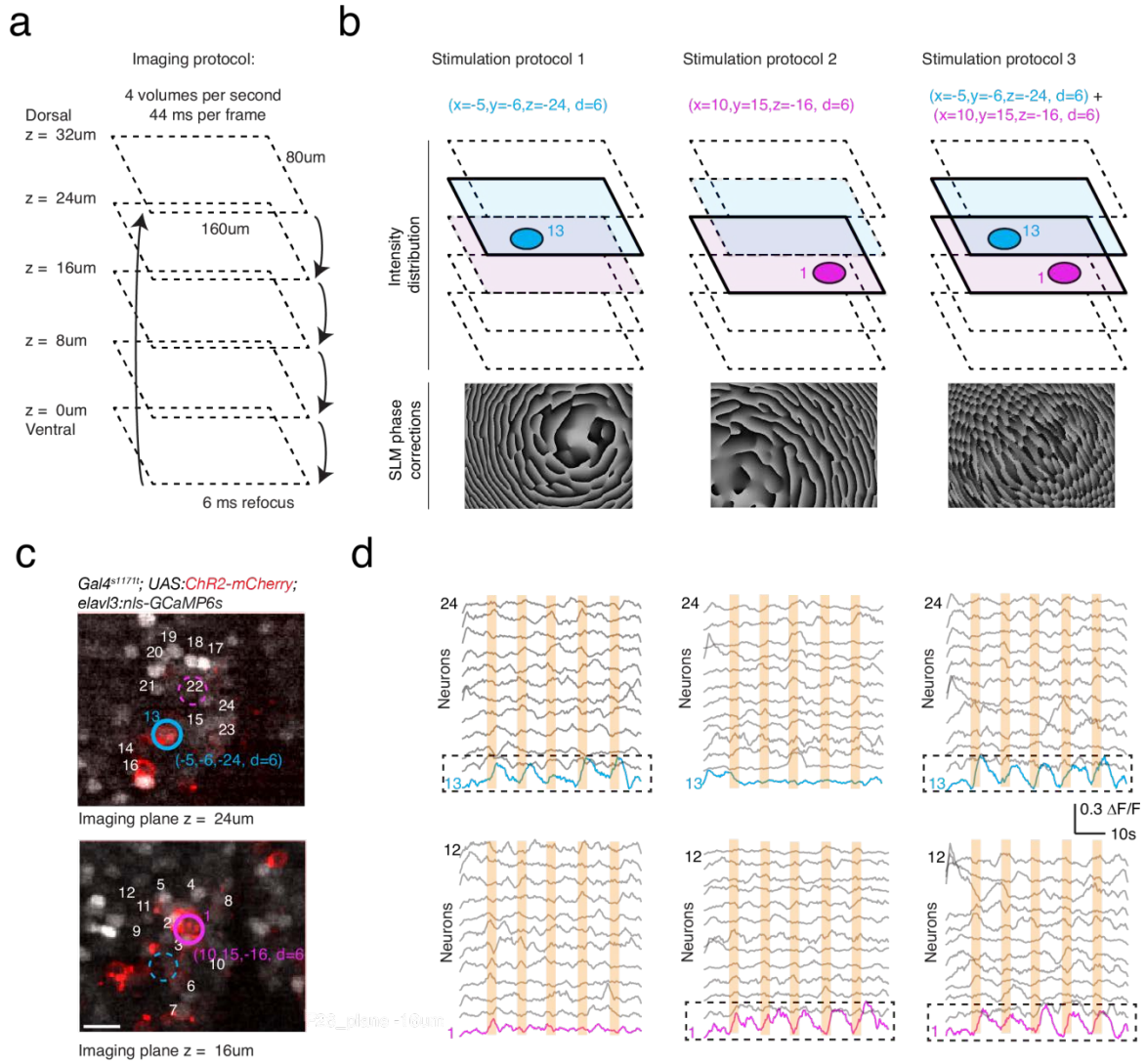


**Figure 2. In vivo three dimensional parallel, cell resolution photo-stimulation and calcium imaging.**

**(a)** Multiplane imaging protocol. An electrically tunable lens is used to switch rapidly between five imaging planes separated by 8 μm and to record GCaMP6s signals across a volume of 160x80x32 μm<sup>3</sup> four times per second. **(b)** Design of three-dimensional photostimulation protocols. On the basis of an acquired Z-stack, three different 3D photostimulation patterns are designed to target 6 μm stimulation spots either independently or simultaneously to two ChR2 expressing neurons localized in different planes (cell #1, purple, in the ventral plane at z = 16 μm; cell #13, blue, in the dorsal plane at z = 24 μm). The corresponding phase correction patterns are calculated based on the photostimulation targets, and

superimposed on the light wavefront by means of the spatial light modulator. **(c)** A view of the two planes selected for photostimulation from a fish expressing pan-neuronal nuclear localized calcium indicator (nls-GCaMP6s) and ChR2 + mCherry fusion protein. ROIs indicate the cells selected for the stimulation. Scale bar is 10  $\mu\text{m}$ . **(d)** The recorded activity from a subset of cells in the imaged planes. Matching the photostimulation protocol applied, only the targeted cells show an activity profile locked to the stimulus timing, with minimal cross activation of the surrounding cells.

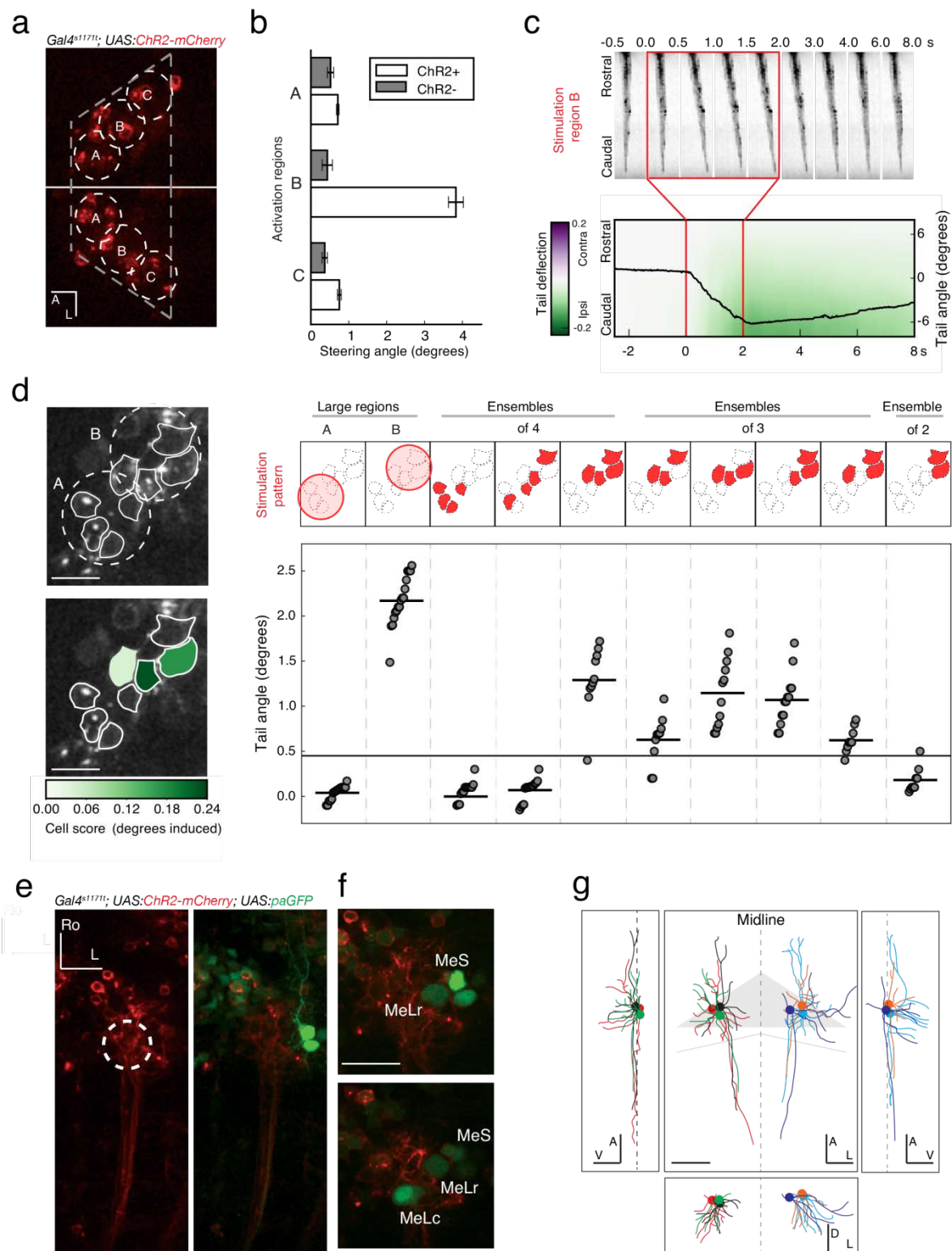


**Figure 3. Characterization of the behavior relevant neurons**

**(a)** Probing the neuronal substrates driving a motor outcome. Circular and slightly overlapping photostimulation regions 18  $\mu\text{m}$  in diameter were targeted bilaterally in fish expressing ChR2-mCherry in the nMLF for an initial characterization of the circuit substrates inducing tail steering. **(b)** Comparison of the maximum tail steering angle induced by 2P photostimulation of the different regions. The difference in steering angle is only significant for Pos B (p-value < 0.001, Welch's t-test, Bonferonni corrected, n = 15 trials across 6 fish). **(c)** Kinematics of the tail configuration induced by the photostimulation. When region B is targeted, slow ipsilateral deflection in the tail is detected followed by relaxation to the baseline level at the end of stimulation. The angle between the base of the tail and the caudal tip of the tail is shown as a black line, overlaid onto a heatmap which shows the relative offset along the tail. **(d)** Behavior-based identification of individual neurons driving the steering outcome. From the regions used for initial mapping, smaller subsets are iteratively selected by means of a score based on the induced motor outcome until minimal subsets of neurons are identified that drive behavior above a threshold set at five standard deviations from baseline (black line). A regression model is used to calculate a cell behavioral score, which estimates the contribution of each cell to the steering outcome. **(e)** Morphological reconstruction by paGFP photoactivation. Identified cells with the highest behavioral scores during behavior trials were targeted to highlight their structure and connectivity pattern. **(f)** Circuit landmarks can also be highlighted by paGFP photoactivation, such as specific cells in the circuit. **(g)** Neurons registered from five fish based on distance from midline, the dorsal extent of the nMLF and the distance from the midbrain-hindbrain boundary. Rostral-caudal axis is aligned according to the average axonal direction. Scale bars are 10  $\mu\text{m}$ , error bars are SEM.

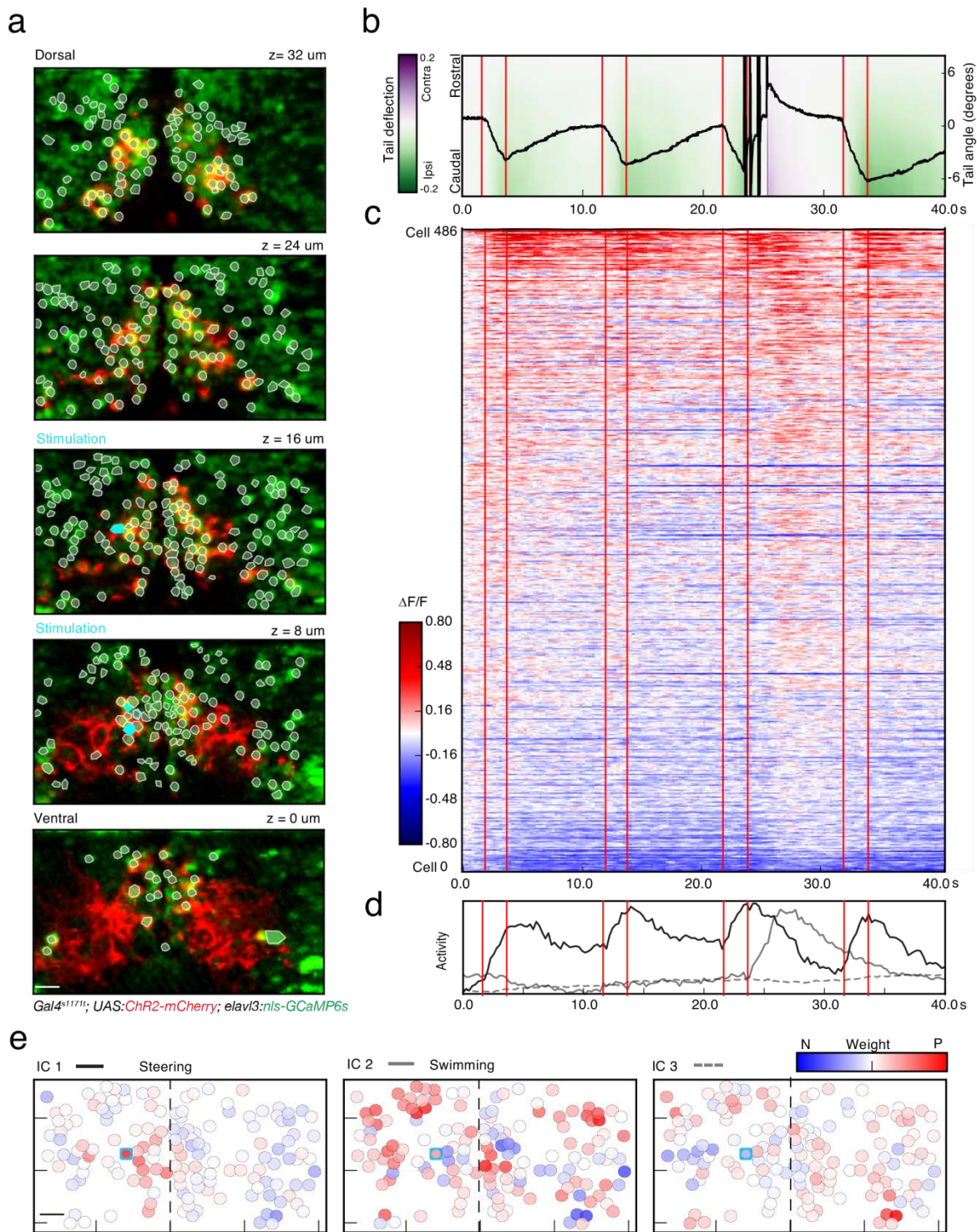


**Figure 4. Simultaneous targeted stimulation with functional neuronal activity and behavior recording**

**(a)** Volumetric recording of the activity of 486 cells during stimulation induced behavior. Planes imaged in the midbrain of fish expressing ChR2-mcherry (red) and nlsGCamp6s (green). ROIs corresponding to the cell bodies selected for the analysis are highlighted in white, and units selected for the photostimulation are shown in cyan. **(b)** Kinematics of the tail during stimulation. An excerpt showing the temporal evolution of the tail angle during the four repetitions of photostimulation (red lines indicate stimulation onset and offset). **(c)** Raster plot showing the activity for the recorded population, temporally aligned with the behavior shown in **b**. A small subset of neurons show a reliable activity pattern temporally locked to the stimulation and tail steering. A larger number of neurons show an activity increase corresponding to the larger amplitude swim after the third stimulation. **(d)** Representation of common patterns in population activity by independent component analysis. The first three components of the representation are shown. **(e)** The circuit maps for the plane at  $z = 16\mu\text{m}$  with the weight assigned on the basis of the first three independent components. For IC2 and IC3, laterality indices were  $0.142 \pm 0.115$  and  $0.006 \pm 0.21$  (mean  $\pm$  s.e.m, p-value 0.08), indicating slight, if any, ipsilateral bias. IC1, on the other hand, is significantly lateralized ( $0.354 \pm 0.145$ , p-value 0.04). Scale bar is  $10\mu\text{m}$ .



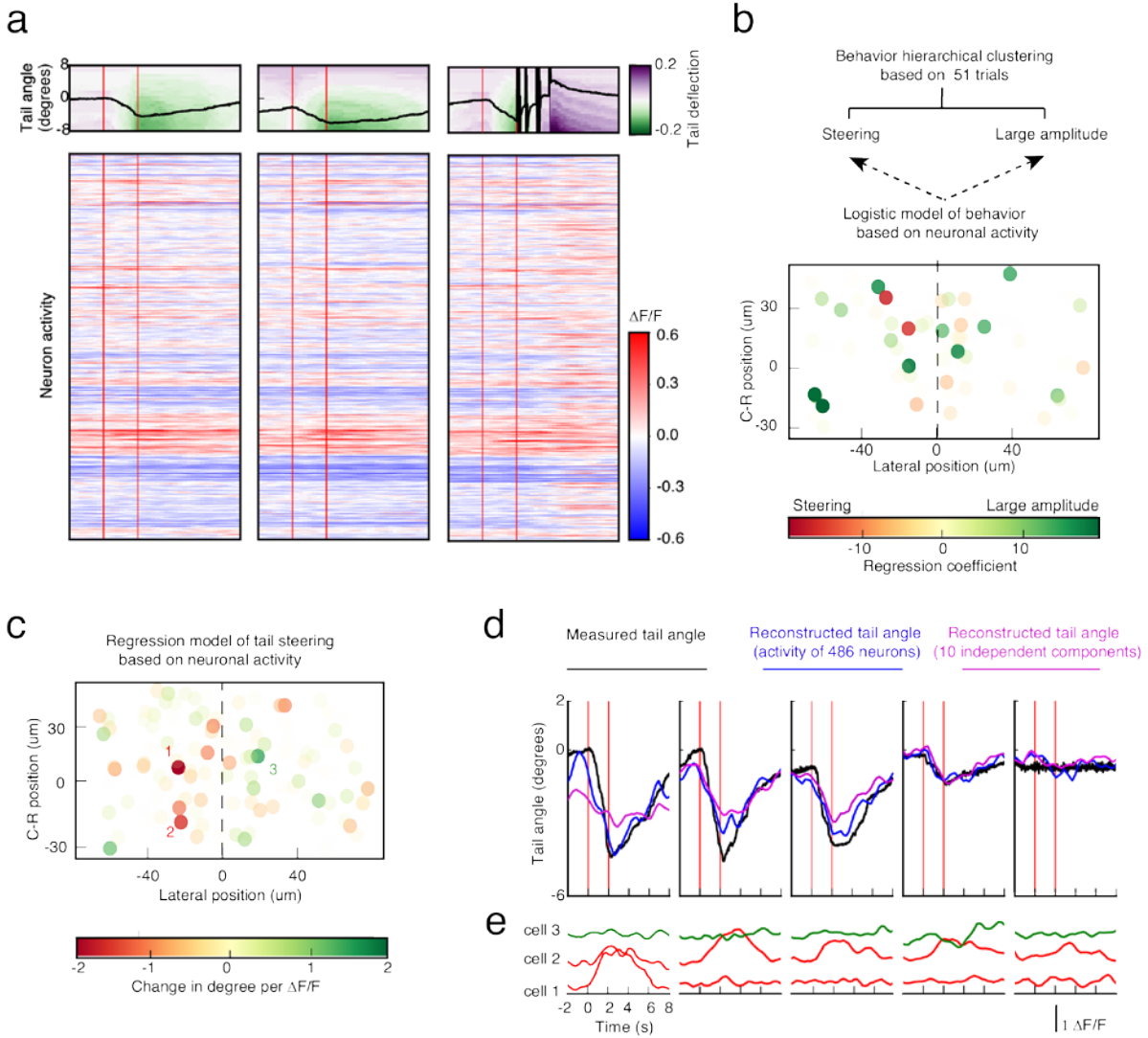


**Figure 5. Analysis of the behavior outcome by means of regression models.**

**(a)** Hierarchical clustering, based on the tail angle, was used to analyze the behavioral patterns. Two main groups, steering/subthreshold behavior and larger swim bursts, were identified. For these sample trials  $\Delta F/F$  profiles are shown for the 486 cells recorded. **(b)** Logistic regression based on neuronal responses. Spatial distribution of the components from a regularized logistic regression which predicts the type of bout based on neuronal activity pattern. A projection of all five planes imaged is showing the cells more active during large amplitudes swims (green) and those more active during steering outcome (red). **(c)** Regularized linear regressions of the steering outcome. A model based on neuron activity is

used to predict tail steering angle (black) at each time point. This presents statistical issues related to the large number of components compared to trials, and the correlated activity of the components (R-squared = .85). A second model is shown, based on a reduced space of only 10 components from ICA, which doesn't suffer from the same statistical limitations, and still manages to performs well (R-squared = .74).

**(d)** Spatial distribution of components for the steering regression. This map shows the neurons with non-null regression components according to their relative weight in the model based. The coefficient units (colorbar) encode the predicted change in degrees for the tail orientation accounted for by a unitary change in  $\Delta F/F$ . **(e)** Selected neurons identified by the regression can be examined, showing different patterns of activity relating to behavioral parameters.



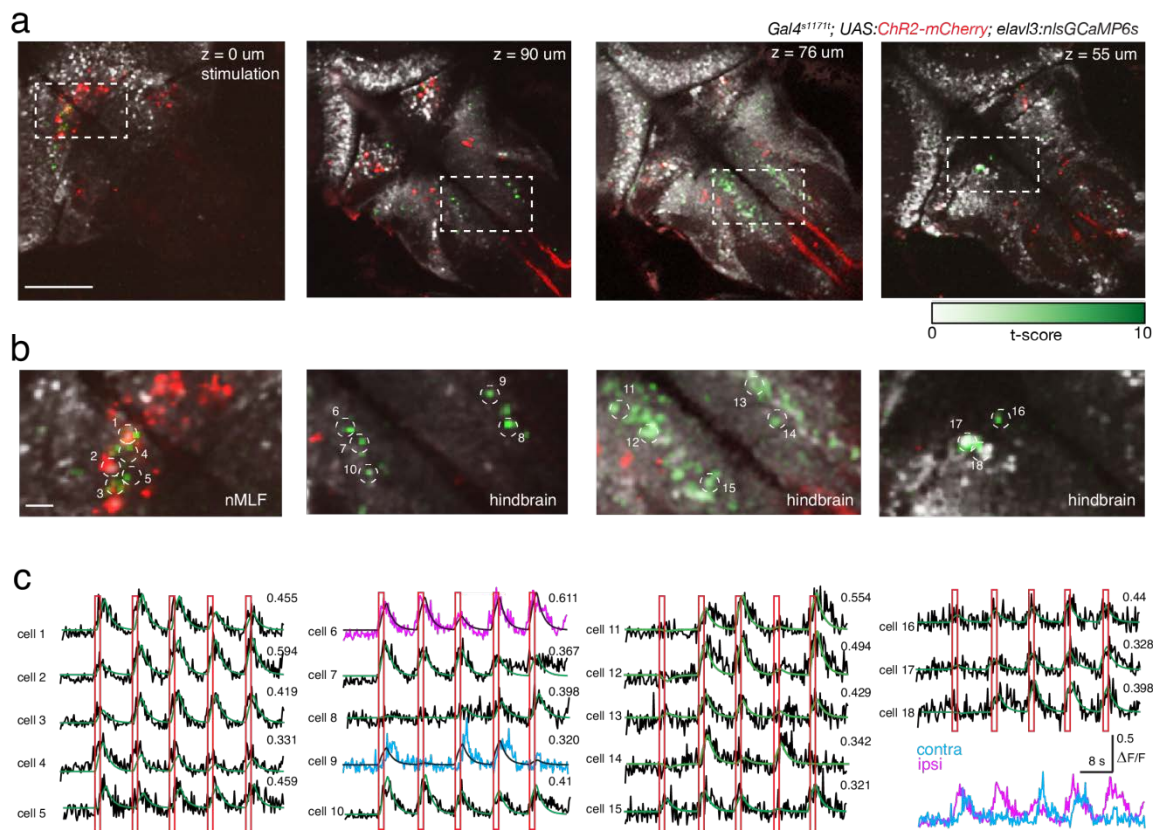


**Figure 6. Whole brain imaging of the activity associated to steering behavior**

**(a)** Brain-wide activity induced by stimulation of the nMLF. From functional recordings acquired at different planes while keeping the photostimulation target in the region of the nMLF, a pixel-wise regression model pinpoints those pixels with a response profile matching with the one predicted from the stimulation protocol. The pixel-wise t-statistic from different trials acquired at the same plane and leading to tail steering outcome were averaged together to generate maps of the regions across the brain active in association with the steering behavior (highlighted in green). In red the ChR2-mCherry expression pattern is shown, and in grey the GCaMP average projection. Scale bar is 100  $\mu\text{m}$ . **(b)** Zoomed view of the high t-statistic regions. Activation of neurons in the nMLF region, leads to a lateral activity component in the same midbrain region but to bilateral activity foci in the hindbrain region in planes located at a different level with respect to the nMLF. Scale bar is 10  $\mu\text{m}$ . **(c)** Response exemplars. For the ROIs in panel B, the

response profiles are shown for the different planes along with the model prediction and the coefficient of determination resulting from the regression procedure. In pink and cerulean are shown two response profiles whose maximal  $R^2$  are obtained when a temporal shift is introduced between their respective models of response.

## **Materials and methods**

### **Hardware for imaging pathway**

The optical setup is based on a standard galvo-galvo scanning commercial 2P microscope (Femtonics 3DRC, Femtonics, Tuzlo, Hungary) combining two independent Ti:Sapphire sources (Chameleon Ultra II, Coherent), one for imaging and the other for photostimulation. The fluorescence collection path includes a DM670HP dichroic mirror, an IR blocking filter and a 563HP mirror splitting the fluorescence light toward two GaAsP detectors (Hamamatsu H10770PA-40) equipped with EM525/50 and EM590/60 emission filters, respectively.

In addition to the standard imaging configuration, an electrically tunable lens (ETL, Optotune, EL-10-30-Ci-VIS-LD-MV) was inserted along the imaging path before the galvo mirrors, to enable fast z-plane refocusing. The ETL achieved a 75  $\mu\text{m}$  z-travel range at the sample, when coupled with a 20x LUMPLAN Olympus (NA 0.9, WD 2.2mm) objective (used for most experiments), or 125  $\mu\text{m}$  with a 16x CFI70 Nikon objective (NA 0.75). Supplementary figure 1b shows the switching time for the ETL, which was sufficiently fast to enable multiplane volumetric imaging.

### **Hardware for 3D-2P-CGH Photostimulation**

For the holographic path, following Pockel's cell intensity modulation, the beam was deflected by a flippable mirror towards the phase modulation section. The phase modulation approach uses a spatial light modulator (SLM, Hamamatsu, X10468-07) and is designed according to the standard 4f configuration, including (in order): a 4x beam expander to fill the optical window of the SLM, a half-wave plate to match the polarization orientation required by the SLM, and the SLM device itself, working in a pure phase modulation scheme. A 400mm lens conjugates the SLM plane, where the phase modulation is imposed, to the first Fourier plane where the amplitude modulation is rendered. At this plane, either a blazed grating (600lp/mm) close to normal orientation (for temporal focusing) or a mirror (used for most experiments) can be combined with a zero order block (constructed from foil on a glass

slide) to suppress the residual light component not effectively modulated by the SLM. The obtained amplitude distribution is relayed to the sample plane by means of two telescopes in a cascade, resulting in a total magnification factor of about 1/220. The first telescope, comprising a 200mm and a 100mm lens, conjugates the Fourier plane to the back focal plane of the tube lens and includes an half wave-plate to control the direction of polarization of the photostimulation beam downstream of the SLM. The second telescope is comprised of the tube lens and the objective.

To combine the imaging and phase modulation path, a polarizing beam splitter or, alternatively, a dichroic mirror, was used. The focal planes of each pathway were independently adjusted depending on the experimental requirements. This was done adjusting the tunable lens and/or axially shifting the phase modulation pattern of the SLM. With this layout for the phase modulation path, a volume of 180 x 180 x 350  $\mu\text{m}^3$  could be effectively addressed using the 20x objective and 200 x 200 x 400  $\mu\text{m}^3$  for the 16x objective.

### **Hardware for 1P fiber photostimulation**

In experiments with 2P imaging of GCaMP and fiber based visible light photostimulation, 473nm or 638nm modulated laser diodes were coupled to a 200 or 50  $\mu\text{m}$  core multimode fiber. The fiber tip was inserted in the 2.2 mm cleft between the objective lens and the sample, and the fiber was positioned to target the desired region. In such experiments, interference from stray photostimulation light was minimized by means of a temporal interleaving scheme. Therefore, the photostimulation laser was pulsed, with its phase locked to the galvo scanning frequency, resulting in microsecond photostimulation pulses only during flyback time of the galvo scanners.

### **Hardware for behavioral recording**

To record the behavior, the tail was illuminated with a high power IR LED (850nm, Thorlabs) placed approximately 10 cm from the fish's position. A high-speed IR sensitive camera (Photonfocus MV1-D1312 or Thorlabs DCC1545M CMOS) was used to acquire at 300 frames per second.

## **Software Interface for 3D-2P-CGH Photostimulation**

A Python based software system was created to control the SLM and to interface with the proprietary software controlling the microscope system (MES, Femtonics Ltd.). Code is available on request under a GPL open-source license, and an easy to use demo application of the algorithm is provided (Labview, suitable for Windows systems). The core of the system is a server module (holobase.py – see diagram in Supplementary Fig. 1c) which is in charge of all the procedures required for the generation of the calibrated light distribution including camera acquisition, calibration, SLM look up table (LUT) and flatness correction, Z control, and pattern computation.

Different client applications can interface with the server. One client application is hooked into the MES software (holoclient.py) and used to launch the calibration procedure. A simple client provides a script interface for quick control of multiplane patterns (holomultiZ.py). Another client is a graphical user interface (GUI – holoGUI.py), which was the primary point of interaction for the user. This interface allows the user to load TIF stacks acquired on the imaging system. Temporal and power parameters can be configured and a polygonal selection tool is used to select the desired illumination patterns at the different planes of the z-stack. The patterns are compactly stored in a scalable vector graphics (SVG) based format, exchanged with the server, and are mapped onto the holographic system's coordinates by the calibration. For communication between the clients and server, messages are passed with the ZMQ library (zeromq.org) and Google protocol buffers (developers.google.com/protocol-buffers/) are used to provide language-neutral data storage.

## **Phase computation for multiplane photostimulation patterns**

In order to engineer the desired light distribution at the sample, a multiplane Gerchberg-Saxton (mGS) algorithm was implemented<sup>1</sup> in Python. With this iterative procedure based on Discrete Fourier Transforms, the phase modulation required for multiplane photostimulation patterns are computed from the superposition of multiple complex 2D fields, one for each different plane along the propagation

direction  $z$ . For each loop through the algorithm execution, the phase of each 2D field computed at different planes is corrected with a lens-type modulation corresponding to its axial offset. This correction is applied twice, once with a negative profile during the forward propagation of the wavefront, and once with a positive profile after the backward propagation of the wavefront before the mixing step. Below is pseudocode corresponding to the basic core of the loop, where  $i$  refers to the imaginary unit,  $\text{abs}$  is the absolute value,  $\exp$  is the exponential function,  $\text{angle}$  returns the argument of complex numbers, and  $\#$  denotes comment lines.

### **Pseudocode for holographic computation**

function mGS (target\_amplitudes, target\_Zs, wavelength, iterations):

    #input arguments:

    #target\_amplitudes      # list of target patterns at different planes

    #target\_Zs              # list of target Z levels (axial displacements from focal plane

    #wavelength            # wavelength the laser is operating at

    #iterations             # number of iterations

    initial\_distribution\_am   # a random distribution of real numbers to initialize amplitude

    unified\_slm\_phase        # a random distribution of real numbers to initialize the field

    for iterations:

        slm\_fields = empty list #list of distributions of real numbers corresponding to the phase

            maps computed

        for each target\_amplitude plane in target\_amplitudes:

            # a phase mask which acts as a lens is computed from the axial offset for this

            plane

```

lens = compute_lens(target_Z, wavelength)

# computing the slm field for this plane, by applying a lens to unified_slm_phase
slm_field = initial_distribution_am * exp(i * (unified_slm_phase - lens))

# propagating forward
target_field = 2Dfft(slm_field)

# substituting the computed amplitude of the field with target_amplitude for this
plane
target_field = abs(target_amplitude) * exp(i * angle(target_field))

# propagating backward
slm_field = inverse_2Dfft(target_field)

# taking the phase information and shifting it
slm_phase = (angle(slm_field) + lens)

# substituting the computed phase
slm_field = initial_distribution_am * exp(i * slm_phase)

append slm_field to slm_fields

# mixing the fields at the slm plane
unified_slm_phase = angle(sum(slm_fields)) % (2 * pi)

return unified_slm_phase

```

We complemented this algorithm with corrections to reduce the difference in intensity of shapes generated in different positions due to the inherent inhomogeneous diffraction efficiency of SLM devices.

## Calibration procedures

At the beginning of an experimental session, a calibration routine is run involving four sequential steps: 1. Mapping of the working range of the electrically tunable lens to obtain a z-shift vs voltage relation; 2. Identification of the optimal look up table (LUT) for the SLM, to map a  $2\pi$  phase stroke onto the SLM's 8 bit modulation values; 3. XY registration, to map the coordinate system of the imaging beam to the patterns generated by the phase modulation system; 4. Z registration, to map how axial shifts by phase modulation relate to z-offsets (in microns) in the sample volume. To calibrate the ETL, ten command voltages, covering the full travel range, are sequentially applied. At each voltage, the corresponding offset along z of the imaging beam is measured by moving the objective to find the shift in focus. A third order polynomial is applied on these samples, to generate a function mapping desired offset into a voltage command.

In the second step, which calibrates the look up table (LUT) for the SLM values by finding the optimal linear scaling factor, two phases are used. In the first coarse phase, amplitude patterns using 8 different scaling factors for the LUT (ranging from 128 to 255 for this 8-bit SLM) are used. The pattern that minimizes zero and second order components is selected. The second step, centered around the previous optimum, evaluates a finely-spaced set of 6 values and the best value is selected. Following this, XY spatial registration begins. The galvo mirrors are used to sequentially steer the imaging beam to a series of points. At each point the calibration camera captures an image, and the beam center is automatically detected. Next, a series of phase modulation patterns corresponding to points are played, and also automatically captured and quantified. Based on the points captured from the two different paths, the optimal affine transformation between the two coordinate systems is calculated. This transformation is applied to all following holographic patterns. The maximal spatial discrepancy accepted between the imaging and photostimulation beams is one  $\mu\text{m}$  and is typically reached with a couple of runs of the calibration procedure. In the last step, for the registration along the axial (Z) dimension, a similar approach is used. The holographic system plays a series of patterns, with phase modulations that



correspond to different axial offsets. For each pattern, the objective position required to optimally focus the holographic pattern is measured. A low-order polynomial is fit onto the measured values, to provide a transformation between a desired axial (Z) position, and the required ‘lens’ for the computation of the phase modulation pattern.

### **GCaMP data processing**

For all acquisitions which included behavior tracking and photostimulation standard raster scanning was used, at 4 volumes or frames per second (for multiplane or single plane recordings, respectively). For some timing sensitive measurements, for instance in characterization of the protocol, a quick random access linescan was used at 300-500 Hz with 8-10 pixels per cell. To correct for offsets in the image background/baseline in some recording, a region outside of the expression pattern is selected, and the average intensity of this background region is subtracted.

With the adopted sensor-actuator pair the fluorescence imaging signal can be contaminated by photostimulation, however this can be effectively subtracted by a post-processing algorithm. Consider that during photostimulation the stimulation light intensity is constant, thus the contamination artifact equally affects all pixels, whether the pixels are ‘silent’ and only contain the artifact, or if there are also underlying changes in GCaMP fluorescence from neuronal activity. The algorithm automatically selects a subset of inactive pixels across the different lines of the imaging field of view, and uses percentile filtering on these inactive pixels to detect the level of the stimulation artifacts for each line. This can then be subtracted, resulting in a nearly contamination free signal at the scale of the normal GCaMP activity transients.

These data were further processed with custom Python routines. First for volumetric imaging, the raw data series was split into sub-streams, one for each plane imaged. This was followed by rigid-body image registration to correct for drift and motion. Next the data is temporally filtered with a .25 second rolling

average window, to reduce noise. As is usual for such data,  $\Delta F/F$  is used for normalization, using a baseline measured towards the start of imaging.

### **Resolution characterization**

For measuring the lateral resolution of ChR2 stimulation, a single circular region of interest, 6  $\mu\text{m}$  in diameter, was moved sequentially across a subset of neurons expressing ChR2 and GCaMP6s. The activity of all sampled cells was recorded at 300 Hz by linescan with stimulation epochs lasting for 200 ms. For the axial (Z) resolution, the relative displacement between the imaging and the photostimulation planes was achieved either by controlling the z level computed in the phase correction or by moving the objective in a different plane and refocusing with the tunable lens on the reference plane. To score the activity change, the maximum  $\Delta F/F$  relative to the targeted cell was computed for each pixel. This was fit with an exponential model based on the distance from the target cell. For the data comparing spontaneous and ChR2 induced GCaMP responses, both GCaMP6s and nls-GCaMP6s were evaluated. The time to peak and half-decay of the signal were used as the basis for a comparison of the temporal dynamics.

### **Analysis details**

To extract common patterns in network activity, a dimensionality reduction approach was applied, using Independent Component Analysis (ICA) from the Python scikit-learn library. From the component weights maps are generated associating each neuron's contribution to the different components. This representation of circuit state for each trial was robust across different dimensionality reduction methods (Supplementary Fig. 16). Imaging data over large fields of view (about  $500 \times 500 \mu\text{m}^2$ ) were analyzed using a pixel-wise regression-based identification of activity components. For every trial, a regressor for each stimulation period was created, and convolved with a single exponential kernel to model nlsGCaMP6s, with  $\text{tauoff} = 2.3 \text{ s}$ , which was set by optimizing the coefficient of determination  $R^2$ . Regressors were fit to the data using a linear regression, along with a constant term. From the resulting set

of coefficients, the t-statistic was calculated for each pixel, and averaged across all trials that induced tail steering.

### **Behavior processing**

The tail position in recorded behavior data was extracted using an automated Python-based algorithm, which maps ~30 points along the tail. A heatmap of the tail position, is used to show the lateral deflection of each point along the tail, relative to the overall tail length. To quantify the tail movement using a single parameter, the tail deflection angle is calculated, which is the angle from the base of the tail to the most caudal points of the tail. A median or Gaussian filter with a size of a few milliseconds was applied to reduce high-frequency noise. A threshold for significant tail steering was set to a tail deflection angle beyond 5 standard deviations from the baseline. In order to assign a behavior score to the photostimulated neurons on the basis of the deflection angle (Fig 3d), a linear regression model was used.

### **Behavior models**

To discriminate between steering events and swimming bouts across different trials, a hierarchical clustering procedure was adopted based on the Fourier power spectrum of the tail deflection angle. Using a logistic model, we characterize the contribution of the neurons differentially associated to the two classified behavioral outcomes. The regression used the Python scikit-learn library, and used elastic net regularization to reduce overfitting and produce a sparser fit. For each neuron, the coefficients of the resulting model were used to generate a map showing the impact on the behavior. For the analysis of the impact of neuron activity in the magnitude of the steering outcome, a linear regression method was used, also regularized with elastic net to reduce overfitting (also see Supplementary Fig. 17).

### **Statistical details**

All tests performed were two-sided. Data distributions were checked, when applicable, for normality with a quantile plot. For statistics involving multiple fish, the mean value for each fish was used for test

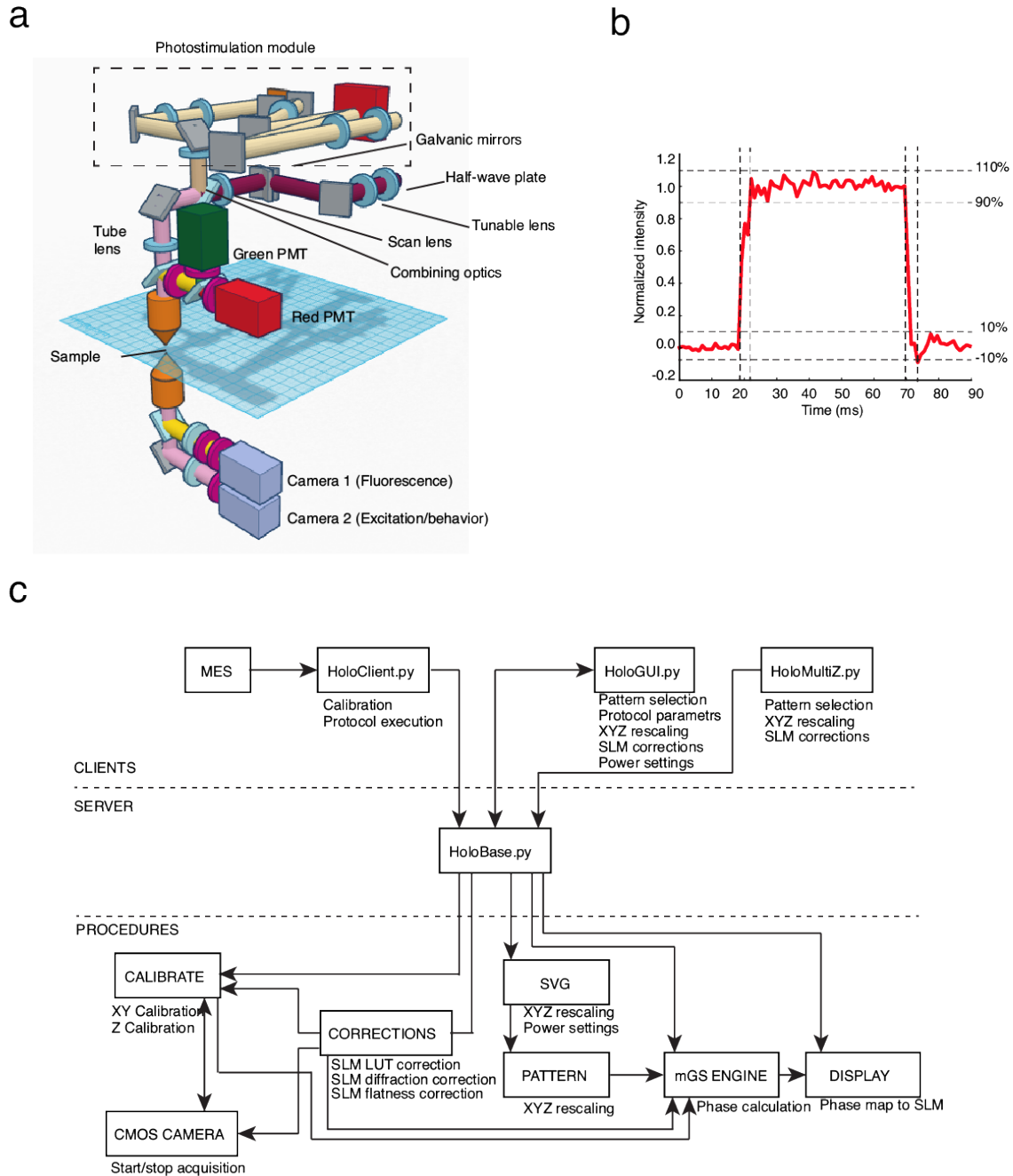
comparisons, as pooling individual trials together from multiple fish violates the assumption of independent measurements. Fish with stronger and more complete expression patterns (covering as many cells as possible) were preferentially selected for experimentation, since behavioral circuit mapping is infeasible with sparse or weak expression. Behavioral trials with two or more spontaneous swimming bouts in the 60 seconds preceding experimental trials were excluded. Imaging trials with a Z-drift greater than 2  $\mu\text{m}$  were excluded. XY shifts before and after stimulation protocols were checked following registration (described earlier in methods), and trials with shifts exceeding 2  $\mu\text{m}$  were discarded. A pre-analysis to determine sample size was not performed, as this work is focused on highlighting useful applications of a cutting-edge approach.

### **Fish procedures**

Fish were raised in accordance with an animal protocol approved by the Max Planck Society and the regional government (Regierung von Oberbayern), at 28°C on a 14h light/10h dark cycle using standard procedures. Zebrafish larvae 5-7 days post-fertilization were used from Gal4s1013t/UAS:ChR2(H134R)-mCherry/UAS:PAGFP line to test the system, Gal4s1171t/UAS:ChR2(H134R)-mCherry and Gal4s1171t/UAS:ChR2(H134R)-mCherry/UAS:PAGFP lines for circuit mapping experiments, Gal4s1171t/UAS:GCaMP6s as a ChR2 negative control Gal4s1171t/UAS:ChR2(H134R)-mCherry/UAS:GCaMP6s, elavl3:GCaMP5G x Gal4s1171t/UAS:ChR2(H134R)-mCherry, elavl3:nlsGCaMP6s x Gal4s1171t/UAS:ChR2(H134R)-mCherry, and elavl3:nlsGCaMP6s-P2A-PAGFP x Gal4s1171t/UAS:ChR2(H134R)-mCherry lines were used in experiments combining photostimulation and calcium imaging. 5-7 dpf larvae were embedded in 1.5-2% low-melting-point agarose and the agarose surrounding the tail was carefully removed using a scalpel blade to free the tail. Fish were allowed to recover for four hours before starting the experimental sessions.

### **Acknowledgments**

The authors would like to acknowledge members of the Baier lab for insightful discussions. In particular, Miguel Antonio Fernandes for providing carriers of Gal4s1171t, UAS:ChR2(H134R)-mCherry and UAS:GCaMP6s, and Dominique Foerster that generated eval:nlsGCaMP6s and eval:nlsGCaMP6s-p2a-paGFP. We also thank Gergely Katona and associates (Femtonics Ltd.) for help in the integration of messaging and callbacks for calibration and hardware commands into the MES microscope software. We would like to acknowledge Andrea Antonini and Tommaso Fellin for providing the ultrathin fluorescent layers used for the initial characterization of the system. Funding was provided by the Max Planck Society and the Center for Integrated Protein Science (CIPSM).

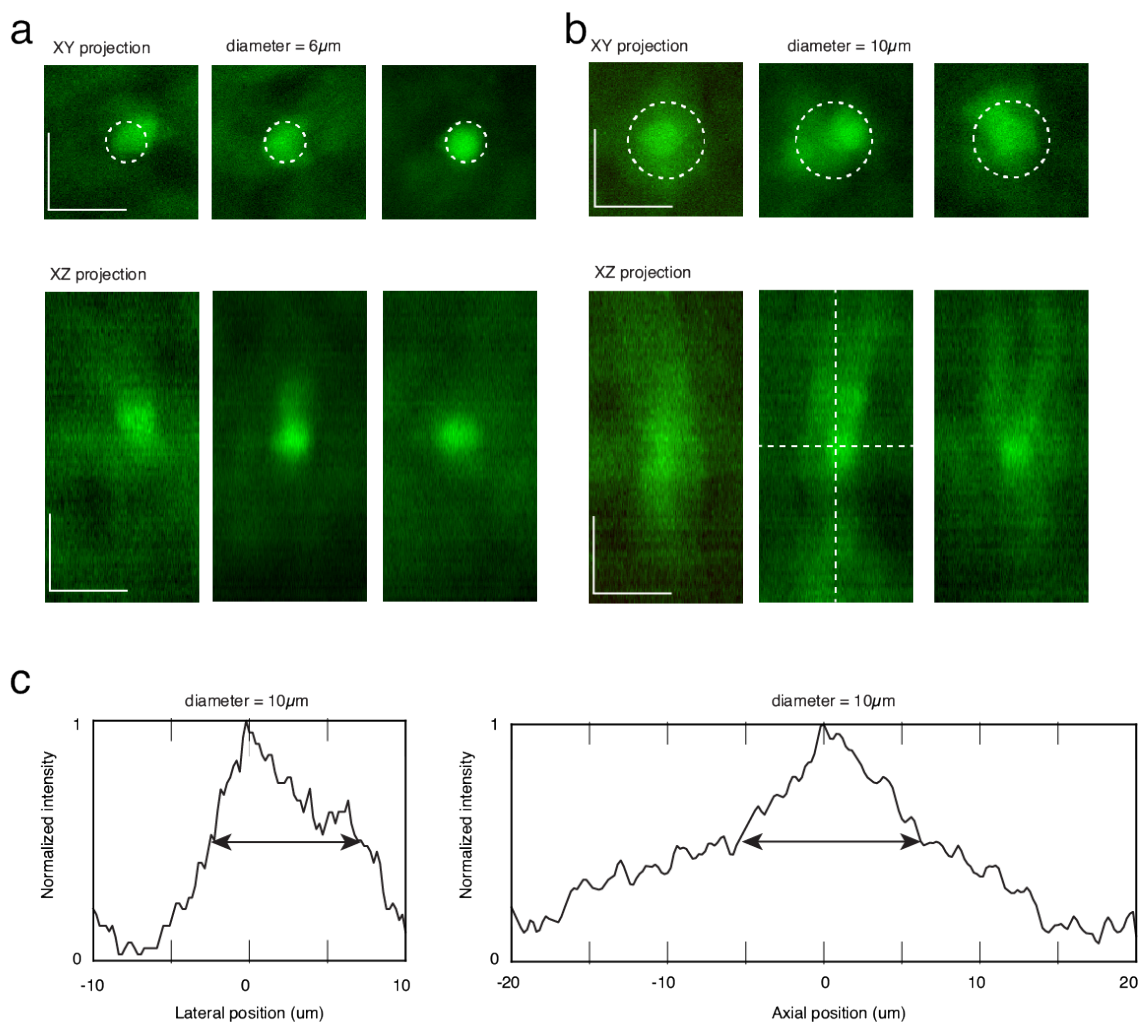


Related to figure 1

### Supplementary Fig. 1 Hardware and software configuration

**(a)** The module for 3D-2P-Computer Generated Holography (*tan optical path*) is integrated in a commercial 2P setup equipped with a galvo-galvo scanhead, two GaAsP photomultiplier tubes and an electrically tunable lens (ETL) for the remote control of the imaging plane independently from the

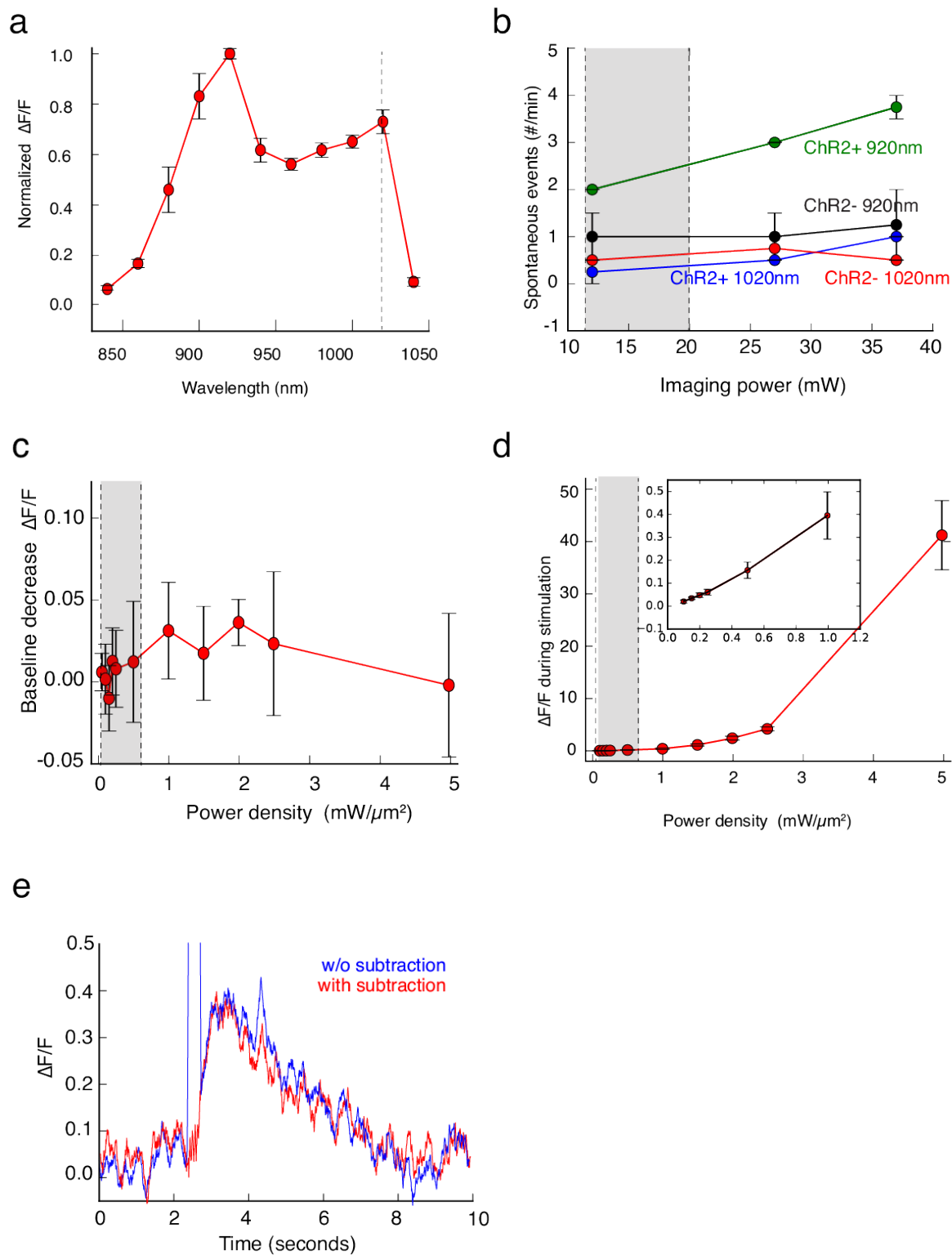
objective position. The two paths are combined downstream the scanlens by means of a polarizing beam splitter (a dichroic mirror can also be used if the wavelengths are sufficiently separated). Two additional arms under the objective are included, one with a camera for the alignment of the two optical paths and acquisition of the photostimulation profiles, and the other, equipped with fast IR CMOS, for tracking the fish behavior. **(b)** Settling time measurement of the ETL for an 8  $\mu\text{m}$  transition. Using 1KHz line scan recording, the ETL is used to shift the excitation focus in and out of an ultrathin fluorescent layer. The measured rise times (10% and 90%) were  $3.1 \pm 1.4$  ms, and the fall time  $4.2 \pm 2.2$  ms. Average total settling time (0 to 100%) was  $6.2 \pm 0.9$  ms. **(c)** Schematic of the software architecture. The server-client structure of the control system is shown along with the main functions required for the functionality of the software interface, as described in the method session.



### Supplementary Fig. 2 paGFP photoactivation precision and repeatability

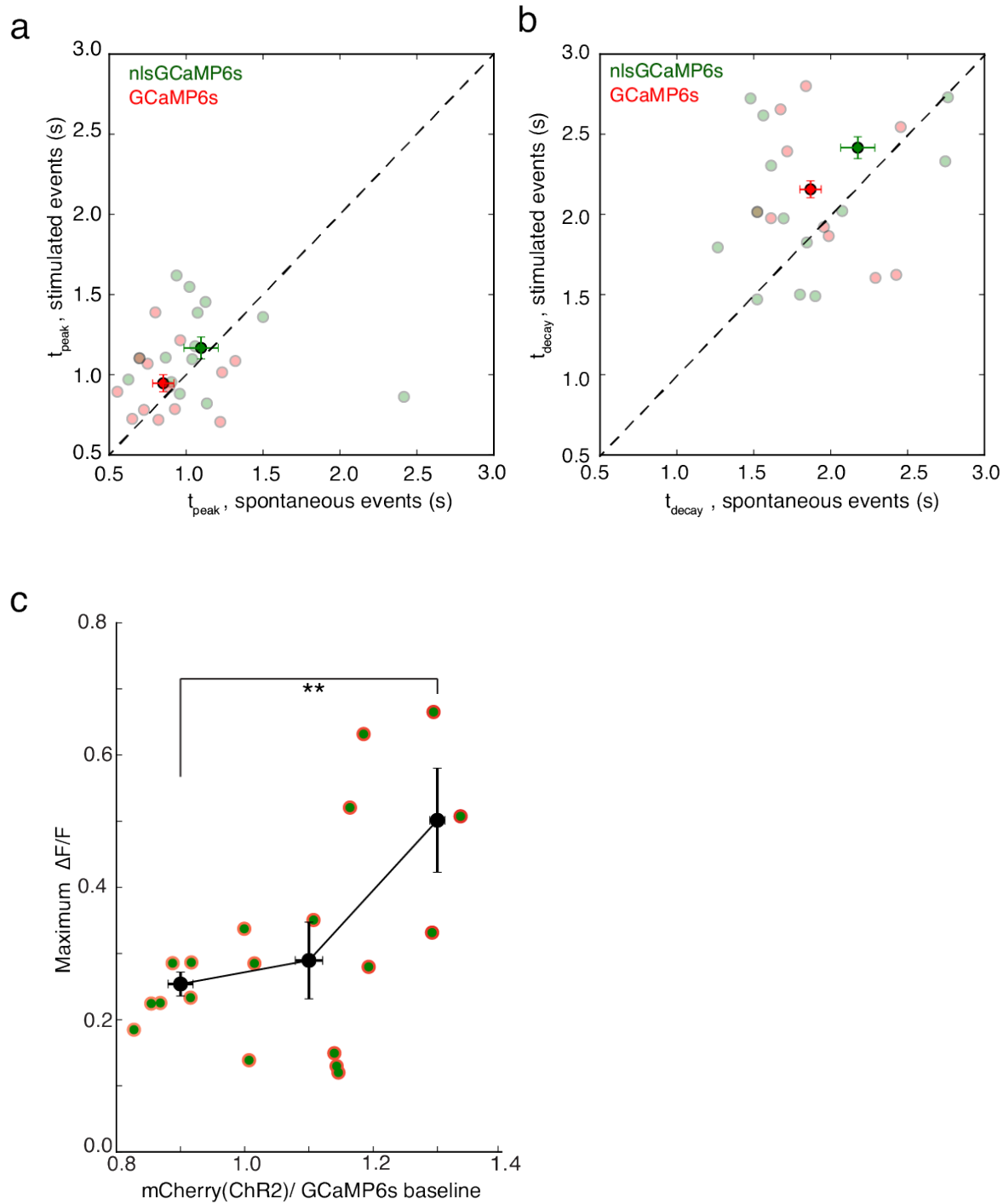
(a) Profiles for paGFP photoactivation obtained in non-anesthetized fish using a circular excitation with a 6  $\mu\text{m}$  diameter, from three different trials done at 750 nm with  $0.25 \text{ mW}/\mu\text{m}^2$  at the sample. (b) The same as (a) but with a circular photostimulation pattern 10  $\mu\text{m}$  in diameter. (c) Quantification of intensity profiles for the photoactivation pattern with 10  $\mu\text{m}$  diameter. Lateral FWHM was  $10.9 \pm 1.4 \mu\text{m}$  and the axial FWHM was  $13.5 \pm 2.2 \mu\text{m}$  respectively. Scale bars are 10  $\mu\text{m}$ .





**Supplementary Fig. 3 Characterization of the optogenetic actuator and sensor pair**

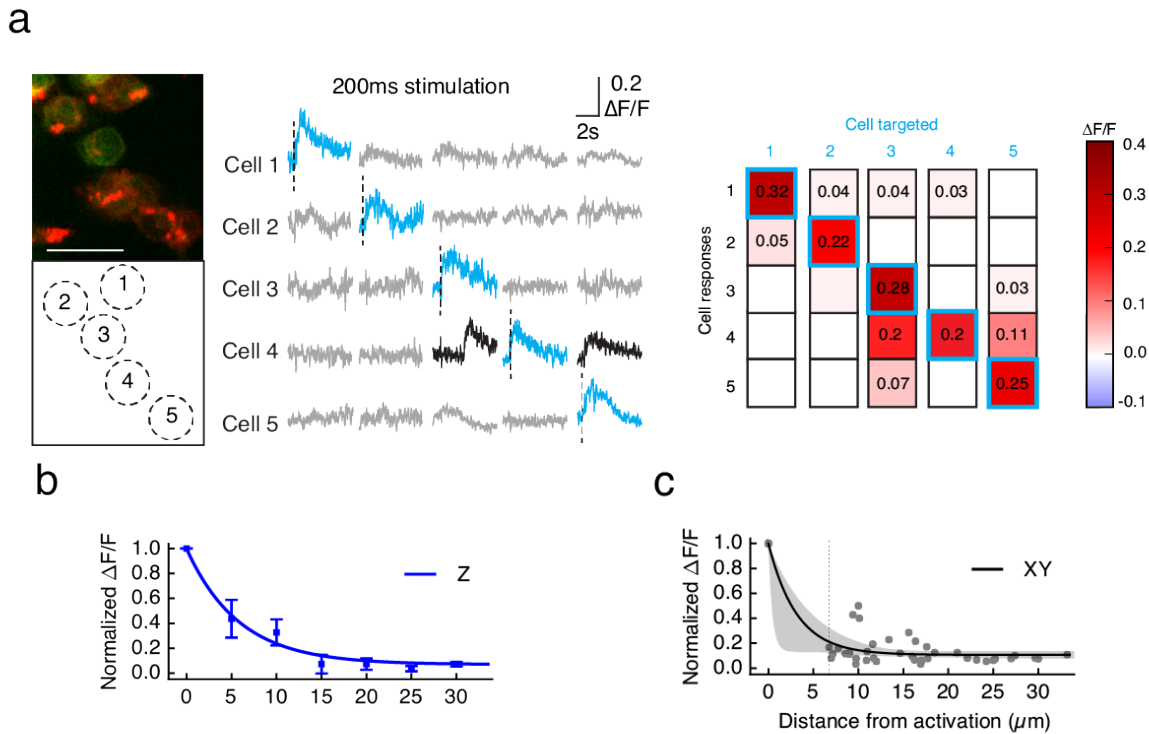
**(a)** Action spectrum for GCaMP6s measured in the zebrafish optic tectum during a repeated visual stimulation protocol consisting of light flashes each 500 ms long. GCaMP6s responses were acquired at different wavelengths with a constant excitation power at the sample of 9mW, and are normalized with respect to the peak at 920 nm. **(b)** Excitability of neurons due to imaging light. Comparison of the spontaneous GCaMP events detected from individual cells at two different imaging wavelengths, 920 and 1020 nm. In grey the excitation power typically used in this work is highlighted. **(c)** GCaMP6s baseline fluctuation following photostimulation. GCaMP fluorescence (excited at 1020 nm) for different photostimulation power densities, after 2 second long stimulation at 920 nm, showed minimal change with respect to the baseline acquired before the onset of the stimulation. In grey the excitation power typically used in this work is highlighted. **(d)** Effect of the ChR2 photostimulation on the detected signal from GCaMP. Absorption of GCaMP at the wavelength used for ChR2 activation leads to a contamination component in the signal detected. The contribution of this component in terms of  $\Delta F/F$  increases non-linearly with the stimulation power. **(e)** A comparison between GCaMP responses before and after subtraction of the contamination components, using the algorithm presented in the methods section. The stimulation artifact is removed, with only minor perturbation to the signal.



**Supplementary Fig. 4 Characterization of induced GCaMP responses**

**(a)** GCaMP onset temporal dynamics. Comparison of the time to the peak (0 to 100%) for GCaMP responses recorded from photostimulated versus spontaneous activity events in the same cells. No

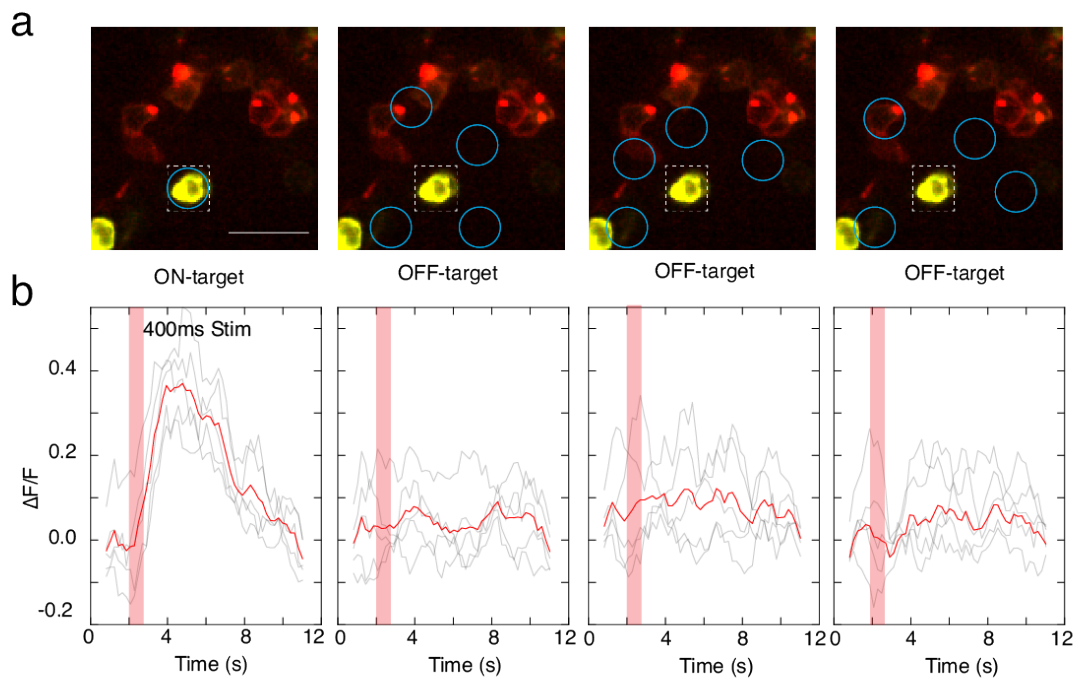
significant difference was found between the stimulated and spontaneous conditions (p-value=0.35, t-test). **(b)** Comparison of the decay time (to reach 50%) for GCaMP responses recorded. No significant difference was found between the two conditions (p-value=0.16, t-test). **(c)** Neurons expressing both GCaMP and ChR2 were imaged at 1020 nm with 9 mW while being stimulated at 920nm with  $0.11\text{mW}/\mu\text{m}^2$ . The maximum recorded amplitudes are plotted in relation to the ratio between the fluorescence level of ChR2\_mcherry and GCaMP's baseline fluorescence. Data were grouped into three bins, black indicates averages and S.E.M. (p-value=0.021, t-test).



**Supplementary Fig. 5 Spatial resolution of photostimulation**

**(a)** Spatial selectivity in the photostimulation. A small population of neurons co-expressing ChR2\_mCherry and GCaMP6s were sequentially targeted with a circular photostimulation pattern  $6\mu\text{m}$  in diameter for 200 ms and the response recorded from all the cells in the field of view. In most trials only the targeted cell shows induced activity, as indicated in the table with peak  $\Delta F/F$  values. **(b)** Axial

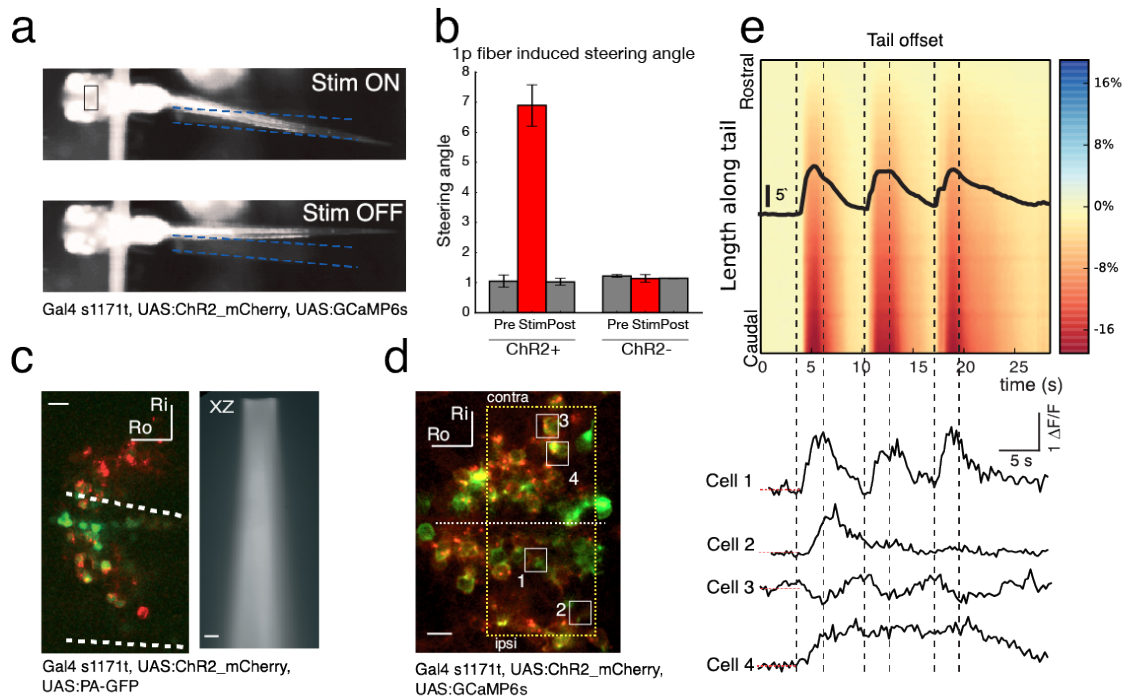
photostimulation resolution. The target pattern was shifted axially from the imaging plane, either with the electrically tunable lens or by ‘lensing’ the holographic pattern. The induced  $\Delta F/F$  recorded with GCaMP6s is shown, normalized to the activity when the target is at the imaged plane. Fit is an exponential model (blue line). **(c)** Lateral photostimulation resolution. A single targeted cell is photostimulated while nearby neurons in the same imaging plane are recorded. Each grey dot corresponds to one non-targeted cell, with  $\Delta F/F$  normalized relative to the targeted cell. The thin dashed grey line shows the minimum distance between cells observed. An exponential fit is shown (black line) with 95% confidence interval (bootstrap, shown in grey).



**Supplementary Fig. 6 Further characterization of photostimulation resolution**

**(a)** To further test for the possibility that photostimulation unintendedly could activate out of target neurons, we characterized the impact of multiple off-target stimulations. A neuron expressing GCaMP6s and ChR2 was imaged during several stimulation patterns with  $0.21 \text{ mW}/\mu\text{m}^2$ . **(b)** Induced activation. When the recorded cell is stimulated (ON-target) there is a reliable and detectable increase in GCaMP

signal. Patterns with multiple stimulation regions that are OFF-target fail to induce a response, and eventual responses are significantly lower than the ON-target activations (0.04, t-test). Red bars indicate the stimulation epochs.

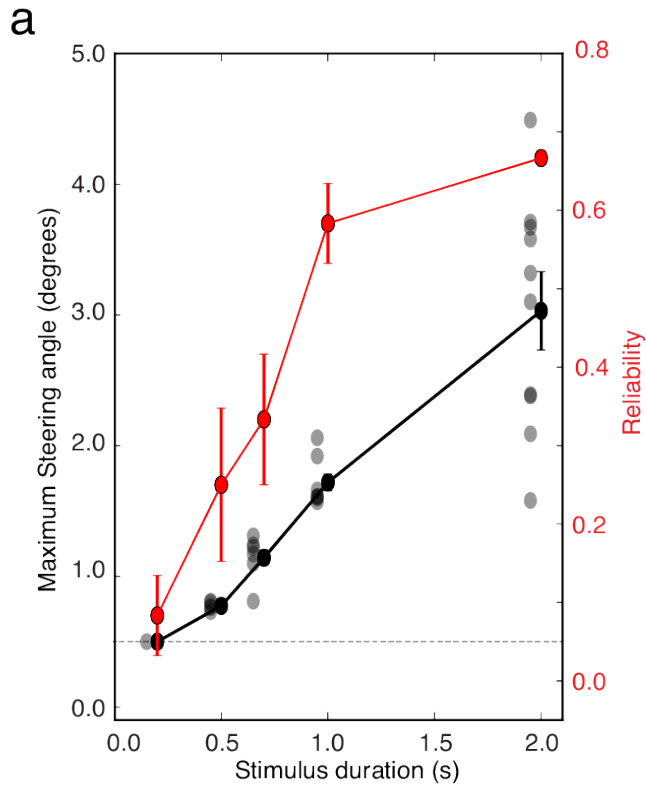


*Related to figure 3*

### Supplementary Fig. 7 Optic fiber induced behavior with imaging

**(a)** Fiber based optogenetic testing of the motor outcome. An optic fiber with a core diameter of 200  $\mu\text{m}$  is placed close to fish in order to target the nMLF region on one side of the fish midbrain (in blue). A 2 second stimulation pulse at 473 nm leads to tail steering toward the side ipsilateral to the stimulation. **(b)** Optogenetic stimulation in fish not expressing ChR2 does not result in any change of the tail profile with respect to the baseline. **(c)** Post-investigation paGFP photoactivation profile. In fish expressing ChR2\_mCherry and paGFP, after assessment of the magnitude of the motor outcome, the

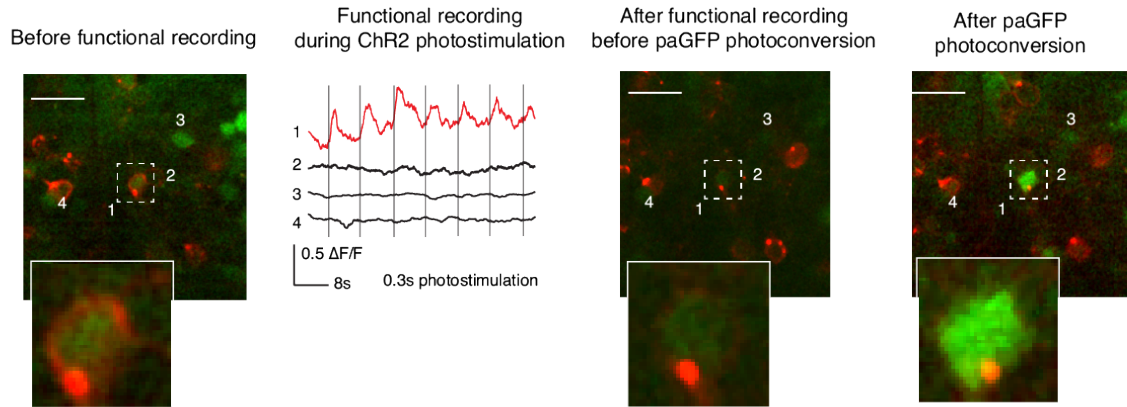
photostimulation source is switched to 405 nm to photoconvert paGFP molecules in the region previously targeted for ChR2 activation with a 50  $\mu\text{m}$  fiber. The fiber activation profile is broad, as shown in the right panel by the illumination side profile in fluorescein. **(d)** Combining 2p imaging and fiber-based optogenetics. Advancing from previous independent imaging and stimulation<sup>210</sup>, optic fiber illumination can be combined with 2p calcium imaging through syncing stimulation timing to the imaging flyback time. The activity from four selected cells during activation is shown. **(e)** Characterization of the tail kinematics during stimulation. A colormap shows the lateral offset along the tail, with a black line showing the tail steering angle. Dotted lines indicate stimulation onsets and offsets. The concurrent activity for the four selected cells from (d) is shown below. Note the peculiar dynamics for the cell #3 with respect to the stimulation protocol and behavior. All scale bars are 10  $\mu\text{m}$ .



**Supplementary Fig. 8 Impact of stimulus duration on behavior**

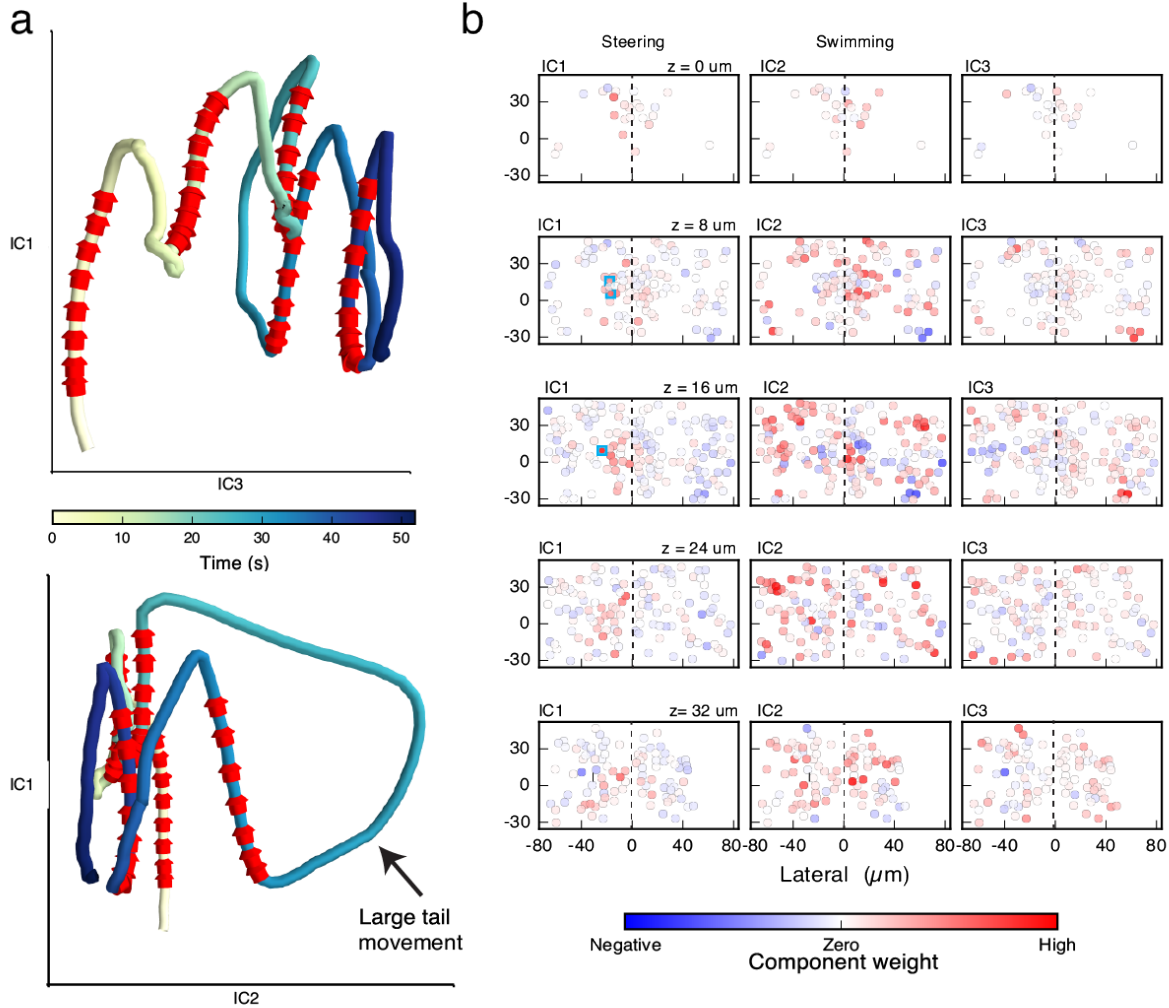
**(a)** The maximum tail steering angle induced by targeted 2P-CGH stimulation increases with longer stimulus durations. The shortest pulse length tested (200 ms) leads rarely to detectable motor outcome, while 2 second stimulation leads to significant tail steering in 68% of trials.





**Supplementary Fig. 9 Extension of the experimental protocols by two-photon paGFP photoactivation**

(a) Demonstration of the combination of selective 2P ChR2 stimulation and GCaMP imaging with targeted 2P paGFP photoconversion. In transgenic fish expressing ChR2-mCherry, nlsGCaMP6s, and paGFP, neurons of interest, selected based on activity during behavior, can be photoactivated for analysis of the circuit. In the example presented, a ChR2, nls-GCaMP6s, and paGFP-positive neuron (cell 1) is first targeted for 3D-2P-CGH 300 ms stimulation of ChR2 at 920 nm. Simultaneous recording of GCaMP at 1020 nm reveals that the targeted photostimulation reliably induces activity. Following recording and stimulation, this cell is targeted for photoactivation of paGFP at 750nm, resulting in a strong increase in the emitted signal. The resolution achievable in the paGFP photoconversion protocol, as shown for the conversion profile in figure 1 and supplementary figure 3, allows for single cell specificity.

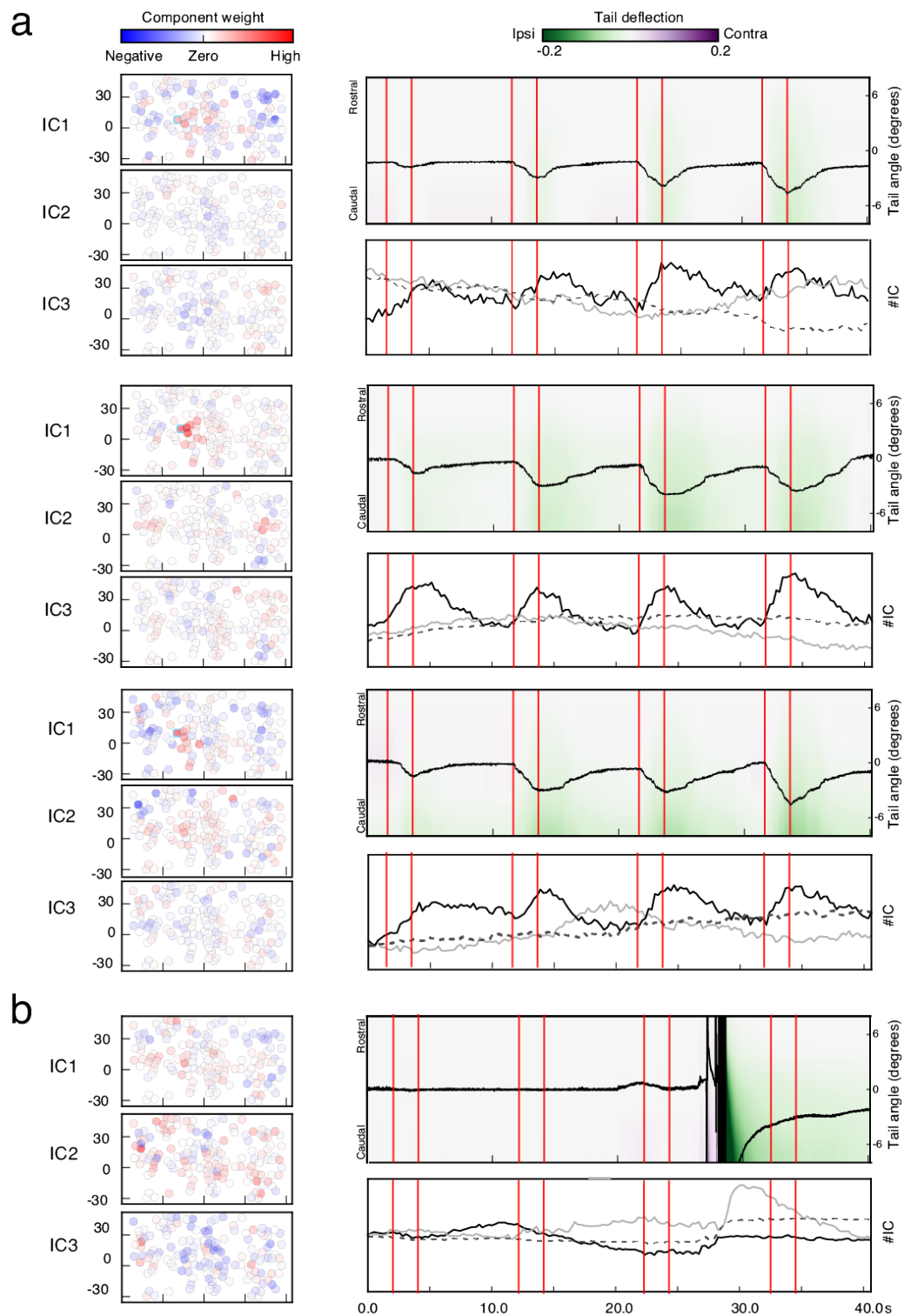


*Related to figure 4*

### Supplementary Fig. 10 Dimensionality reduction compactly captures circuit dynamics

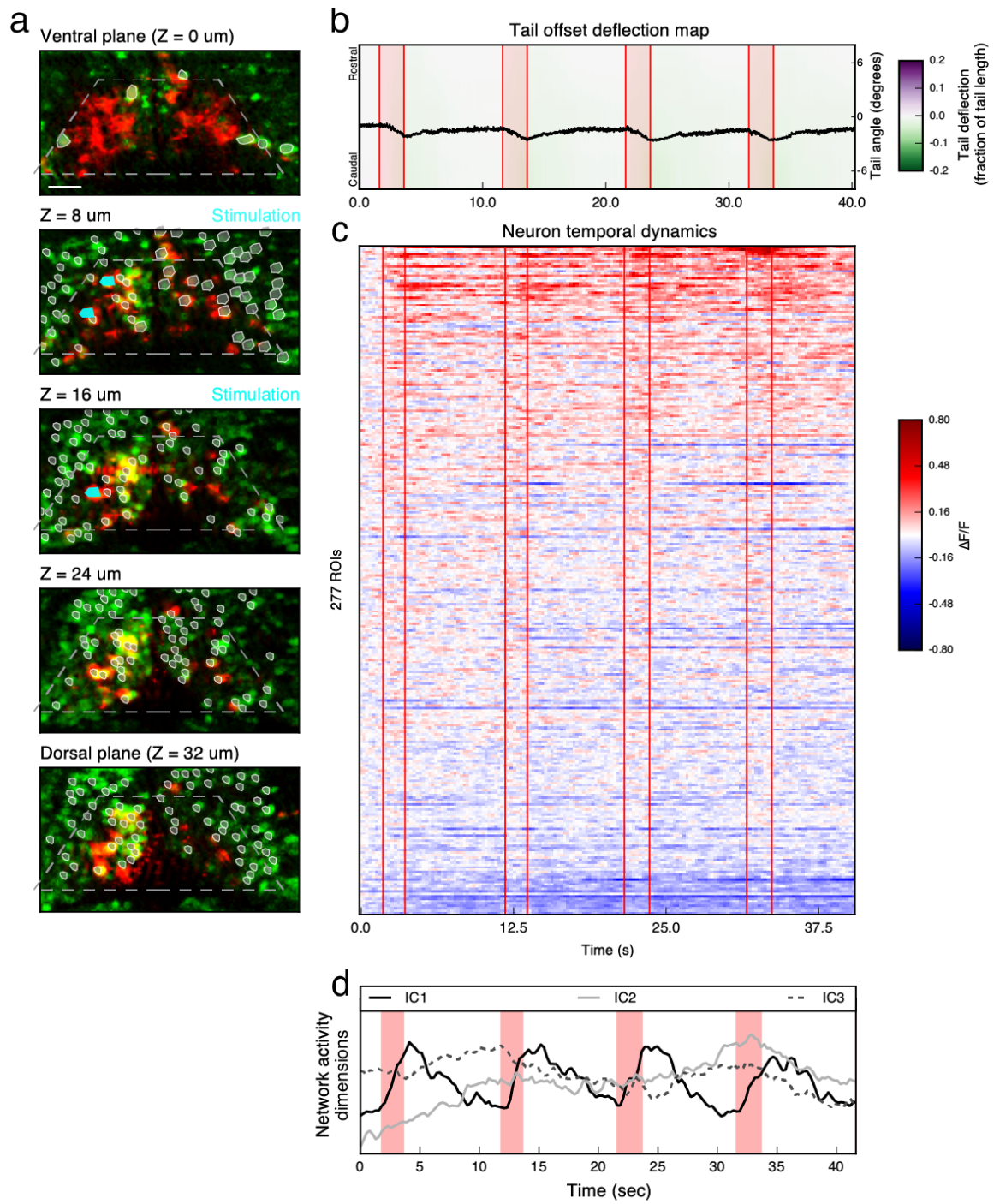
**(a)** The network activity of approximately 500 neurons is projected into a simplified three dimensional space obtained by independent component analysis. A heatmap shows the temporal evolution of the network state, with stimulation indicated by red arrows. Each stimulation shifts the circuit into a different state, with a return towards baseline following the end of stimulation. Notably, the large swim bursts corresponds to a markedly different network state than the trials with only steering. **(b)** Spatial patterns of the network activity components at each imaged plane. The relative weights of cells in the independent

component representation are used to spatially visualize common activity modes across the circuit. IC1, capturing steering and dynamics temporally locked to activation, shows a focused and lateralized pattern near the stimulation. IC2 (large swimming bout) and IC3 (slow circuit dynamics), have a broader and more bilateral distribution.



**Supplementary Fig. 11 Additional example trials**

**(a)** Additional stimulation trials from the fish shown in figure 4. The induced tail steering angle is shown, along with independent components representing network activity. The stimulation pattern is the same as in figure 4, and reliably induces tail steering, with varying amplitude. The weights of dimensional reduction components are shown, and in all trials a consistent focus of activity can be seen for IC1. The other principal components don't show a focus of activity, and aren't lateralized. **(b)** The photostimulation pattern used has the same geometric profile as in (a), but was shifted 30  $\mu\text{m}$  dorsal, and failed to induce the characteristic activity pattern or tail steering behavior. The only activity component identified resulted in association to a spontaneous swimming bout not temporally synchronized to stimulation.

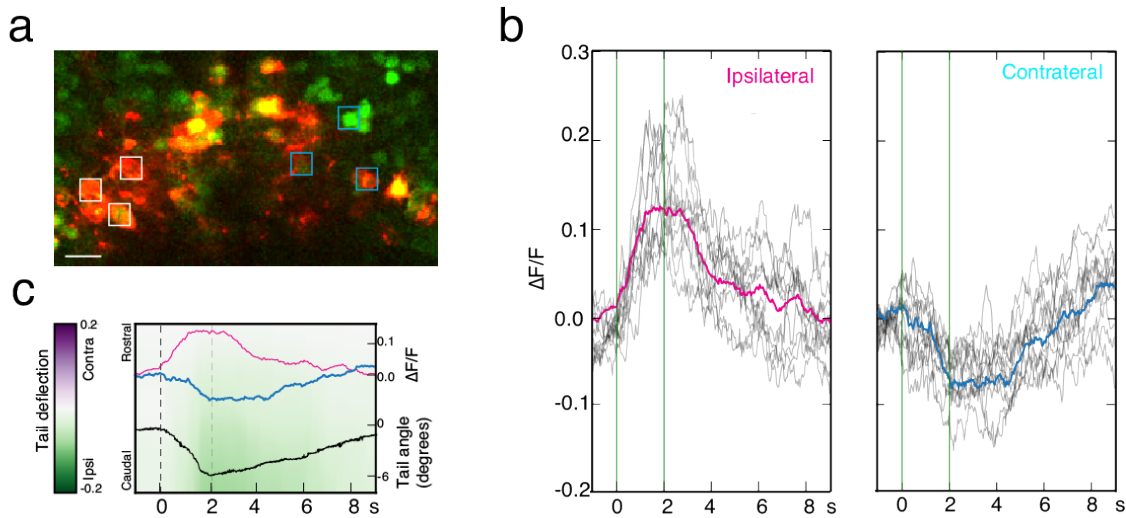


**Supplementary Fig. 12 Example of investigation protocol in an additional larva**

**(a)** Volumetric recording of the activity of hundreds of neurons during stimulation induced behavior.

Planes imaged in the midbrain of fish expressing ChR2-mcherry (red) and nls-GCamp6s (green). ROIs

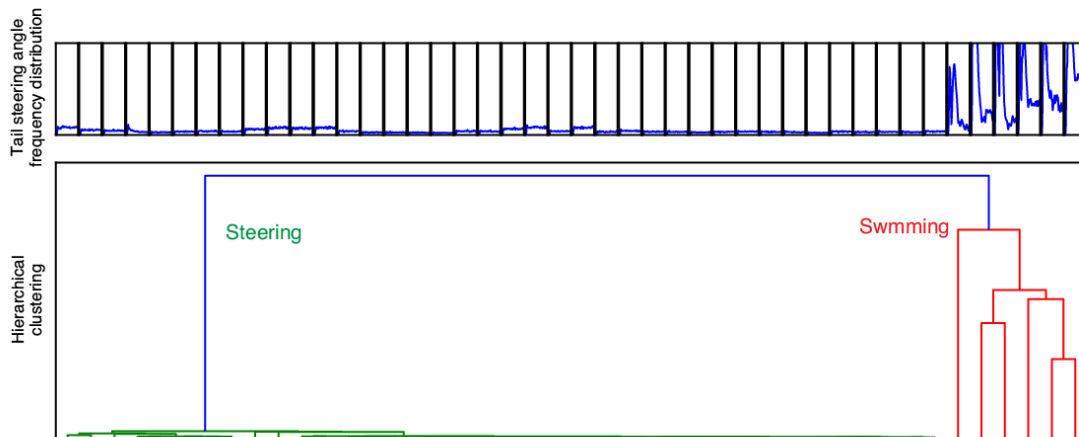
corresponding to the cell bodies selected for the analysis are highlighted in white, and units selected for the photostimulation are shown in blue. **(b)** Kinematics of the tail during stimulation. An excerpt showing the temporal evolution of the tail angle during the four repetitions of photostimulation (red lines indicate stimulation onset and offset). **(c)** Raster plot showing the activity for the recorded population, temporally aligned with the behavior shown in **(b)** Similar to the example in figure 4, a small subset of neurons show a reliable activity pattern temporally locked to the stimulation and tail steering. **(d)** Representation of common patterns in population activity by independent component analysis. The first component captures the stimulation induced network activity that corresponds to the steering behavior. Scale bar is 10  $\mu\text{m}$ .



**Supplementary Fig. 13 Different local dynamics induced in the nMLF**

**(a)** Two different activity patterns in the nMLF during the induced steering outcome can be detected, when comparing the side ipsilateral to stimulation versus the contralateral side. **B, (c)** While in the region ipsilateral to the stimulation an increase in calcium level is detected (white outlines in (a), gray lines single trials, pink trace is mean), an activity decrease in some contralateral neurons was detected that was temporally synchronized with the stimulation and induced steering (blue outlines in (a), grey lines single trials, blue trace is mean).

a

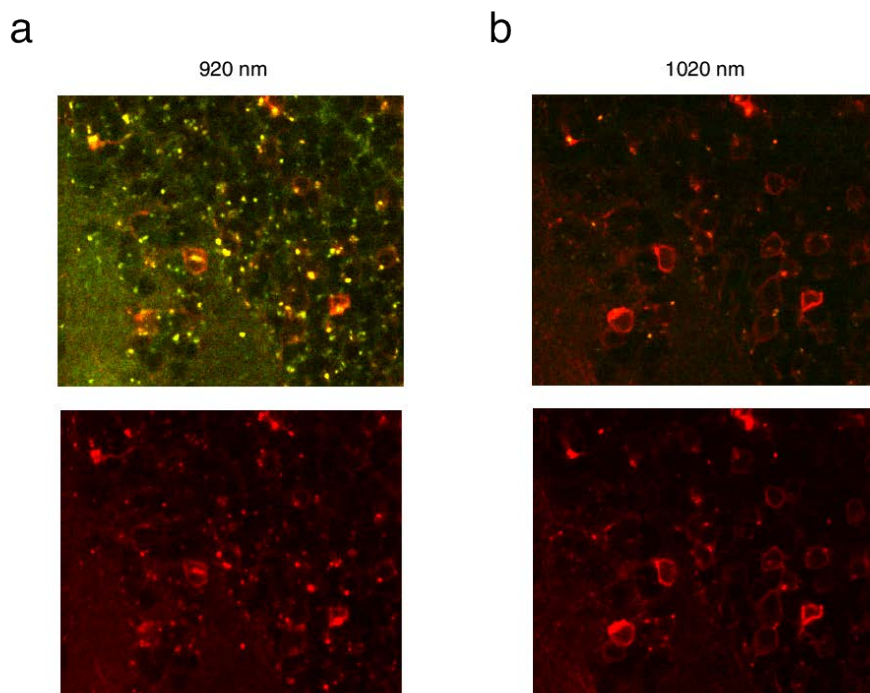


*Related to figure 6*

### Supplementary Fig. 14 Hierarchical behavior clustering

(a) A range of the frequency power spectrum of tail steering angles, obtained using a Fourier transform (FFT), during 44 trials from the example fish used in figure 4 and 5. To separate behavior patterns, we adopted a hierarchical clustering approach, based on the distance between each trials' frequency distribution. As shown in the dendrogram, this approach split trials into two distinct clusters, one corresponding to the trials with swimming, and the other to the tail steering response.

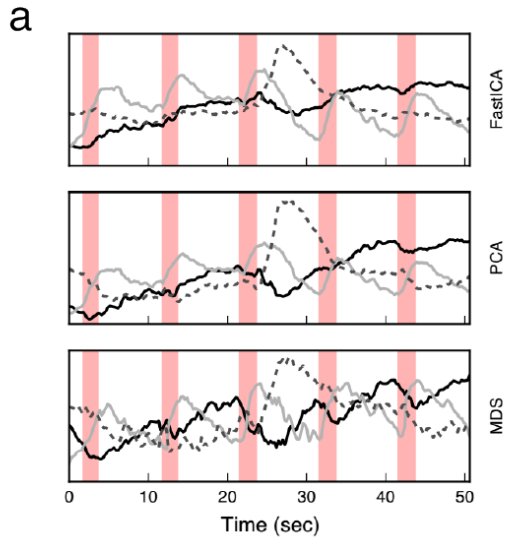




*Related to discussion*

**Supplementary Fig. 15 jRGeco spectral properties.**

Fish expressing jRGeco (elev12jR-GECO1.a) were imaged at two different wavelengths. jRGeco fluorescence emission is characterized by two components<sup>189</sup>: short-wavelength (500-550 nm in green) and long-wavelength (560-650 nm in red). The top panel corresponds to the merged short and long wavelength channels, and the bottom panel shows the long-wavelength signal. **(a)** jRGeco excited at 920 nm result in broadband emission and shows fairly strong signal originated from “puncta”, especially in the short-wavelength channel. Images were acquired with 33 mW at the sample. **(b)** jRGeco imaged at 1020 nm emits prevalently in the long-wavelength band. Images were acquired with 24 mW at the sample. From the perspective of combining jRGeco imaging with Chr2 2P photostimulation, the complex emission of the indicator has to be considered in terms of the contamination of the signal detected in the long-wavelength band upon excitation of Chr2 at 920nm.

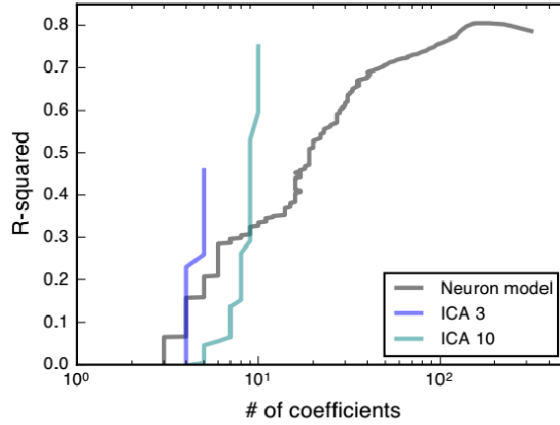


*Related to online methods*

### **Supplementary Fig. 16 Comparison of dimensionality reduction methods**

**(a)** Comparison of dimensionality reduction methods on the same data shown in figure 4. The two methods capture a quite similar representation of the network, where one component captures the stimulation induced activation, and another component captures the activity associated with the large swim. MDS, a manifold non-linear dimensional reduction technique, also finds qualitatively similar components.

a



### Supplementary Fig. 17 Steering regression

(a) For the regression on tail steering angle, shown in Fig. 6 c and d, we quantify the influence of the number of coefficients on the performance of the regression. The regression involves a regularization step, detailed in the methods, which drives the model towards a low number of components. By adjusting the parameters of the regularization, we can effectively adjust the number of components included in the model.

## Section 4 – Conclusion and outlook

Precise holographic optogenetics, combined with simultaneous imaging and behavior is a powerful tool for circuit exploration. Investigations, such as shown in the first three papers in this thesis, can be extended by such an approach, to the level of individual neurons within these circuits.

There are several challenges remaining. Optogenetic actuators have variable expression levels across neurons. Our system has control over power level, but the relationship between expression and power level is non-linear and will vary with the intrinsic properties of each neuron. It would be quite useful to have an automatic normalization routine that calibrates the power delivered to each neuron to account for its expression level and excitability, possibly using the imaged responses to activation as a guide.

Another impediment is navigating the combinatorial explosion of possible stimulation patterns. Using behavior to guide stimulation is effective, as shown in the paper, and it would also be possible to use previously imaged activity to guide stimulation. This requires rapid processing of imaging data - ideally the data from one trial of imaging/stimulation is processed in time to help select the next round of stimulation. There are several practical issues, for instance matching stimulation, imaging data, and behavior together for analysis and accounting for sample movement over time, though all are quite solvable with sufficient technical effort. Closed-loop stimulation – that is using imaging data to immediately trigger stimulation - is an interesting possibility but achieving a useful latency is onerous and with calcium sensors the best latency possible is around one hundred milliseconds.

A complex and more abstract issue is aligning functional circuit elements across specimens. Increasing the data collected within each specimen makes it more feasible to align the functional roles of each neuron across individuals - a puzzle is easier when the puzzle pieces are bigger. Additionally, increasing the combinations of techniques used in each specimen can lessen the challenge. For instance, by adding photoactivation and morphological tracing, neurons can be aligned based both on functional

properties, projection patterns, as well as their impact on the circuit when stimulated. Computational and statistical approaches will be developed to optimally process and combine information across these various sources, to better understand the functional distributions of neurons within the circuits and across individuals.

What is the ultimate goal of circuit investigation, as demonstrated in the preceding paper? One possibility to replay recorded activity patterns<sup>211</sup>. With current tools the temporal resolution of both recording and playback will be limited, which may be an important parameter for many circuits. Even if playback is achieved with improved tools, what is learned? It is an impressive technical demonstration, but doesn't advance understanding. Furthermore, as an activity pattern is played back, the activated neurons will drive other neurons in the circuit, but the drive from the activated neurons will start to overlap with the stimulation patterns for any circuit that has local connections, resulting in the desired pattern not being properly recreated. This could be potentially solved by having a model of the interactions between functional components in the circuit, which leads us in the direction of a better solution.

Through the use of modeling, which can be based on previous knowledge, imaging, and behavior, stimulations can be targeted to extract the maximal information from the circuit during each stimulation trial. A model would capture interactions between functional circuit elements, and could be a 'meta' model, which optimizes the stimulation patterns within a specimen during investigation, but also slowly – across the course of many specimens – could learn common details of the circuit mechanism. Ultimately, such approaches will be very effective tools to extract functional understanding from circuits, limited mainly by the models scientists can conceive to capture the functional complex of circuits.

## References

1. Ewert, J. P. The neural basis of visually guided behavior. *Sci. Am.* **230**, 34–42 (1974).
2. Sanes, J. R. & Masland, R. H. The types of retinal ganglion cells: current status and implications for neuronal classification. *Annu. Rev. Neurosci.* **38**, 221–246 (2015).
3. Baden, T. *et al.* The functional diversity of retinal ganglion cells in the mouse. *Nature* **529**, 345–350 (2016).
4. Pnevmatikakis, E. A. *et al.* Simultaneous Denoising, Deconvolution, and Demixing of Calcium Imaging Data. *Neuron* **89**, 285–299 (2016).
5. Kobak, D. *et al.* Demixed principal component analysis of neural population data. *eLife* **5**, (2016).
6. Freeman, J. Open source tools for large-scale neuroscience. *Curr. Opin. Neurobiol.* **32**, 156–163 (2015).
7. Looger, L. L. & Griesbeck, O. Genetically encoded neural activity indicators. *Curr. Opin. Neurobiol.* **22**, 18–23 (2012).
8. Deisseroth, K. Optogenetics: 10 years of microbial opsins in neuroscience. *Nat. Neurosci.* **18**, 1213–1225 (2015).
9. Jarrell, T. A. *et al.* The Connectome of a Decision-Making Neural Network. *Science* **337**, 437–444 (2012).
10. Kato, S. *et al.* Global Brain Dynamics Embed the Motor Command Sequence of *Caenorhabditis elegans*. *Cell* **163**, 656–669 (2015).
11. Scott, E. K. & Baier, H. The cellular architecture of the larval zebrafish tectum, as revealed by gal4 enhancer trap lines. *Front. Neural Circuits* **3**, 13 (2009).
12. Scott, E. K. *et al.* Targeting neural circuitry in zebrafish using GAL4 enhancer trapping. *Nat. Methods* **4**, 323–326 (2007).
13. Suster, M. L., Sumiyama, K. & Kawakami, K. Transposon-mediated BAC transgenesis in zebrafish and mice. *BMC Genomics* **10**, 477 (2009).

14. Portugues, R. & Engert, F. The neural basis of visual behaviors in the larval zebrafish. *Curr. Opin. Neurobiol.* **19**, 644–647 (2009).
15. Budick, S. A. & O'Malley, D. M. Locomotor repertoire of the larval zebrafish: swimming, turning and prey capture. *J. Exp. Biol.* **203**, 2565–79 (2000).
16. Helmchen, F. & Denk, W. Deep tissue two-photon microscopy. *Nat. Methods* **2**, 932–940 (2005).
17. Ewert, J. P. *et al.* Neural modulation of visuomotor functions underlying prey-catching behaviour in anurans: perception, attention, motor performance, learning. *Comp. Biochem. Physiol. A. Mol. Integr. Physiol.* **128**, 417–61 (2001).
18. Olberg, R. M., Worthington, A. H. & Venator, K. R. Prey pursuit and interception in dragonflies. *J. Comp. Physiol. [A]* **186**, 155–62 (2000).
19. Simmons, P. J., Rind, F. C. & Santer, R. D. Escapes with and without preparation: the neuroethology of visual startle in locusts. *J. Insect Physiol.* **56**, 876–83 (2010).
20. Yilmaz, M. & Meister, M. Rapid innate defensive responses of mice to looming visual stimuli. *Curr. Biol. CB* **23**, 2011–5 (2013).
21. Borla, M. A., Palecek, B., Budick, S. & O'Malley, D. M. Prey capture by larval zebrafish: evidence for fine axial motor control. *Brain. Behav. Evol.* **60**, 207–29 (2002).
22. McElligott, M. B. & O'Malley, D. M. Prey tracking by larval zebrafish: axial kinematics and visual control. *Brain. Behav. Evol.* **66**, 177–96 (2005).
23. Gahtan, E., Tanger, P. & Baier, H. Visual prey capture in larval zebrafish is controlled by identified reticulospinal neurons downstream of the tectum. *J. Neurosci. Off. J. Soc. Neurosci.* **25**, 9294–303 (2005).
24. Patterson, B. W., Abraham, A. O., MacIver, M. A. & McLean, D. L. Visually guided gradation of prey capture movements in larval zebrafish. *J. Exp. Biol.* **216**, 3071–83 (2013).
25. Bianco, I. H., Kampff, A. R. & Engert, F. Prey capture behavior evoked by simple visual stimuli in larval zebrafish. *Front. Syst. Neurosci.* **5**, 101 (2011).

26. Trivedi, C. A. & Bollmann, J. H. Visually driven chaining of elementary swim patterns into a goal-directed motor sequence: a virtual reality study of zebrafish prey capture. *Front. Neural Circuits* **7**, 86 (2013).
27. Lettvin, J. Y., Maturana, H. R., McCulloch, W. S. & Pitts, W. H. What the frog's eye tells the frog's brain. *Proc. Inst. RADIO Eng.* **47**, 1940–1951 (1959).
28. Chen, S.-K., Badea, T. C. & Hattar, S. Photoentrainment and pupillary light reflex are mediated by distinct populations of ipRGCs. *Nature* **476**, 92–5 (2011).
29. Dhande, O. S. *et al.* Genetic dissection of retinal inputs to brainstem nuclei controlling image stabilization. *J. Neurosci. Off. J. Soc. Neurosci.* **33**, 17797–813 (2013).
30. Simpson, J. I. The accessory optic system. *Annu. Rev. Neurosci.* **7**, 13–41 (1984).
31. Burrill, J. D. & Easter, S. S. Development of the retinofugal projections in the embryonic and larval zebrafish (*Brachydanio rerio*). *J. Comp. Neurol.* **346**, 583–600 (1994).
32. Muto, A., Ohkura, M., Abe, G., Nakai, J. & Kawakami, K. Real-time visualization of neuronal activity during perception. *Curr. Biol. CB* **23**, 307–11 (2013).
33. Gabriel, J. P., Trivedi, C. A., Maurer, C. M., Ryu, S. & Bollmann, J. H. Layer-specific targeting of direction-selective neurons in the zebrafish optic tectum. *Neuron* **76**, 1147–60 (2012).
34. Nikolaou, N. *et al.* Parametric functional maps of visual inputs to the tectum. *Neuron* **76**, 317–24 (2012).
35. Xiao, T. & Baier, H. Lamina-specific axonal projections in the zebrafish tectum require the type IV collagen Draqnet. *Nat. Neurosci.* **10**, 1529–37 (2007).
36. Robles, E., Laurell, E. & Baier, H. The Retinal Projectome Reveals Brain-Area-Specific Visual Representations Generated by Ganglion Cell Diversity. *Curr. Biol.* (2014).  
doi:10.1016/j.cub.2014.07.080
37. Roeser, T. & Baier, H. Visuomotor behaviors in larval zebrafish after GFP-guided laser ablation of the optic tectum. *J. Neurosci. Off. J. Soc. Neurosci.* **23**, 3726–34 (2003).



38. Thiele, T. R., Donovan, J. C. & Baier, H. Descending Control of Swim Posture by a Midbrain Nucleus in Zebrafish. *10.1016/j.neuron.2014.04.018* (2014). doi:10.1016/j.neuron.2014.04.018
39. Levick, W. R. Receptive fields and trigger features of ganglion cells in the visual streak of the rabbits retina. *J. Physiol.* **188**, 285–307 (1967).
40. Zhang, Y., Kim, I.-J., Sanes, J. R. & Meister, M. The most numerous ganglion cell type of the mouse retina is a selective feature detector. *Proc. Natl. Acad. Sci. U. S. A.* **109**, E2391–8 (2012).
41. van Wyk, M., Taylor, W. R. & Vaney, D. I. Local edge detectors: a substrate for fine spatial vision at low temporal frequencies in rabbit retina. *J. Neurosci. Off. J. Soc. Neurosci.* **26**, 13250–63 (2006).
42. Russell, T. L. & Werblin, F. S. Retinal synaptic pathways underlying the response of the rabbit local edge detector. *J. Neurophysiol.* **103**, 2757–69 (2010).
43. Berry, M. J., Brivanlou, I. H., Jordan, T. A. & Meister, M. Anticipation of moving stimuli by the retina. *Nature* **398**, 334–8 (1999).
44. Leonardo, A. & Meister, M. Nonlinear dynamics support a linear population code in a retinal target-tracking circuit. *J. Neurosci. Off. J. Soc. Neurosci.* **33**, 16971–82 (2013).
45. Springer, A. D. & Mednick, A. S. Topography of the retinal projection to the superficial pretectal parvicellular nucleus of goldfish: a cobaltous-lysine study. *J. Comp. Neurol.* **237**, 239–50 (1985).
46. Schnitzlein, H. N. The habenula and the dorsal thalamus of some teleosts. *J. Comp. Neurol.* **118**, 225–267 (1962).
47. Northcutt, R. G. & Butler, A. B. Retinofugal pathways in the lingnose gar *Lepisosteus osseus* (linnaeus). *J. Comp. Neurol.* **166**, 1–15 (1976).
48. du Lac, S. & Knudsen, E. I. Neural maps of head movement vector and speed in the optic tectum of the barn owl. *J. Neurophysiol.* **63**, 131–46 (1990).
49. Bergeron, A., Matsuo, S. & Guitton, D. Superior colliculus encodes distance to target, not saccade amplitude, in multi-step gaze shifts. *Nat. Neurosci.* **6**, 404–13 (2003).

50. Del Bene, F. *et al.* Filtering of visual information in the tectum by an identified neural circuit. *Science* **330**, 669–73 (2010).
51. Shires, J., Joshi, S. & Basso, M. A. Shedding new light on the role of the basal ganglia-superior colliculus pathway in eye movements. *Curr. Opin. Neurobiol.* **20**, 717–25 (2010).
52. Knudsen, E. I. Control from below: the role of a midbrain network in spatial attention. *Eur. J. Neurosci.* **33**, 1961–72 (2011).
53. Marín, G. *et al.* A cholinergic gating mechanism controlled by competitive interactions in the optic tectum of the pigeon. *J. Neurosci. Off. J. Soc. Neurosci.* **27**, 8112–21 (2007).
54. Severi, K. E. *et al.* Neural Control and Modulation of Swimming Speed in the Larval Zebrafish. *10.1016/j.neuron.2014.06.032* (2014). doi:10.1016/j.neuron.2014.06.032
55. Arrenberg, A. B., Del Bene, F. & Baier, H. Optical control of zebrafish behavior with halorhodopsin. *Proc. Natl. Acad. Sci. U. S. A.* **106**, 17968–73 (2009).
56. Kimura, Y. *et al.* Hindbrain V2a neurons in the excitation of spinal locomotor circuits during zebrafish swimming. *Curr. Biol. CB* **23**, 843–9 (2013).
57. Scudder, C. A., Kaneko, C. S. & Fuchs, A. F. The brainstem burst generator for saccadic eye movements: a modern synthesis. *Exp. Brain Res.* **142**, 439–62 (2002).
58. Straw, A. D. Vision egg: an open-source library for realtime visual stimulus generation. *Front. Neuroinformatics* **2**, 4 (2008).
59. Pedregosa, F. *et al.* Scikit-learn : Machine Learning in Python. *J. Mach. Learn. Res.* **12**, 2825–2830 (2011).
60. Chang, C.-C. & Lin, C.-J. LIBSVM : A Library for Support Vector Machines. *ACM Trans. Intell. Syst. Technol.* **2**, 27:1–27:27 (2011).
61. Kohavi, R. A study of cross-validation and bootstrap for accuracy estimation and model selection. *IJCAI95 Proc. 14th Int. Jt. Conf. Artif. Intell.* **2**, 1137–1143 (1995).
62. Robles, E., Filosa, A. & Baier, H. Precise lamination of retinal axons generates multiple parallel input pathways in the tectum. *J. Neurosci. Off. J. Soc. Neurosci.* **33**, 5027–39 (2013).

63. Schiff, W., Caviness, J. A. & Gibson, J. J. Persistent fear responses in rhesus monkeys to the optical stimulus of 'looming'. *Science* **136**, 982–3 (1962).
64. Sun, H. & Frost, B. J. Computation of different optical variables of looming objects in pigeon nucleus rotundus neurons. *Nat. Neurosci.* **1**, 296–303 (1998).
65. King, J. G., Lettvin, J. Y. & Gruberg, E. D. Selective, unilateral, reversible loss of behavioral responses to looming stimuli after injection of tetrodotoxin of cadmium chloride into the frog optic nerve. *Brain Res.* **841**, 20–6 (1999).
66. Preuss, T., Osei-Bonsu, P. E., Weiss, S. A., Wang, C. & Faber, D. S. Neural representation of object approach in a decision-making motor circuit. *J. Neurosci. Off. J. Soc. Neurosci.* **26**, 3454–64 (2006).
67. Holmqvist, M. H. A visually elicited escape response in the fly that does not use the giant fiber pathway. *Vis. Neurosci.* **11**, 1149–61
68. Fotowat, H. & Gabbiani, F. Relationship between the phases of sensory and motor activity during a looming-evoked multistage escape behavior. *J. Neurosci. Off. J. Soc. Neurosci.* **27**, 10047–59 (2007).
69. Ball, W. & Tronick, E. Infant responses to impending collision: optical and real. *Science* **171**, 818–20 (1971).
70. Hatsopoulos, N., Gabbiani, F. & Laurent, G. Elementary computation of object approach by wide-field visual neuron. *Science* **270**, 1000–1003 (1995).
71. Gabbiani, F., Krapp, H. G. & Laurent, G. Computation of object approach by a wide-field, motion-sensitive neuron. *J. Neurosci. Off. J. Soc. Neurosci.* **19**, 1122–41 (1999).
72. de Vries, S. E. J. & Clandinin, T. R. Loom-sensitive neurons link computation to action in the *Drosophila* visual system. *Curr. Biol. CB* **22**, 353–62 (2012).
73. Nakagawa, H. & Hongjian, K. Collision-sensitive neurons in the optic tectum of the bullfrog, *Rana catesbeiana*. *J. Neurophysiol.* **104**, 2487–99 (2010).
74. Fotowat, H., Fayyazuddin, A., Bellen, H. J. & Gabbiani, F. A novel neuronal pathway for visually guided escape in *Drosophila melanogaster*. *J. Neurophysiol.* **102**, 875–85 (2009).

75. Yamamoto, K., Nakata, M. & Nakagawa, H. Input and output characteristics of collision avoidance behavior in the frog *Rana catesbeiana*. *Brain. Behav. Evol.* **62**, 201–11 (2003).
76. Münch, T. A. *et al.* Approach sensitivity in the retina processed by a multifunctional neural circuit. *Nat. Neurosci.* **12**, 1308–16 (2009).
77. Yilmaz, M. & Meister, M. Rapid innate defensive responses of mice to looming visual stimuli. *Curr. Biol. CB* **23**, 2011–5 (2013).
78. Budick, S. A. & O'Malley, D. M. Locomotor repertoire of the larval zebrafish: swimming, turning and prey capture. *J. Exp. Biol.* **203**, 2565–2579 (2000).
79. Burgess, H. A. & Granato, M. Modulation of locomotor activity in larval zebrafish during light adaptation. *J. Exp. Biol.* **210**, 2526–2539 (2007).
80. Sankrithi, N. S. & O'Malley, D. M. Activation of a multisensory, multifunctional nucleus in the zebrafish midbrain during diverse locomotor behaviors. *Neuroscience* **166**, 970–993 (2010).
81. Liu, Y. C. & Hale, M. E. Alternative forms of axial startle behaviors in fishes. *Zoology* **117**, 36–47 (2014).
82. Kohashi, T. & Oda, Y. Initiation of Mauthner- or non-Mauthner-mediated fast escape evoked by different modes of sensory input. *J. Neurosci. Off. J. Soc. Neurosci.* **28**, 10641–10653 (2008).
83. Liu, Y. C., Bailey, I. & Hale, M. E. Alternative startle motor patterns and behaviors in the larval zebrafish (*Danio rerio*). *J. Comp. Physiol. A Neuroethol. Sens. Neural. Behav. Physiol.* **198**, 11–24 (2012).
84. Roberts, A. Pineal eye and behaviour in *Xenopus* tadpoles. *Nature* **273**, 774–5 (1978).
85. Fernandes, A. M. *et al.* Deep brain photoreceptors control light-seeking behavior in zebrafish larvae. *Curr. Biol. CB* **22**, 2042–7 (2012).
86. Kay, J. N., Finger-Baier, K. C., Roeser, T., Staub, W. & Baier, H. Retinal ganglion cell genesis requires *lakritz*, a zebrafish atonal homolog. *Neuron* **30**, 725–736 (2001).
87. Takeuchi, Y., Hori, M. & Oda, Y. Lateralized kinematics of predation behavior in a Lake Tanganyika scale-eating cichlid fish. *PloS One* **7**, e29272 (2012).

88. Semmelhack, J. L. *et al.* A dedicated visual pathway for prey detection in larval zebrafish. *eLife* **3**, (2014).
89. von Reyn, C. R. *et al.* A spike-timing mechanism for action selection. *Nat. Neurosci.* **17**, 962–70 (2014).
90. Burrill, J. D. & Easter, S. S. Development of the retinofugal projections in the embryonic and larval zebrafish (*Brachydanio rerio*). *J. Comp. Neurol.* **346**, 583–600 (1994).
91. Robles, E., Laurell, E. & Baier, H. The Retinal Projectome Reveals Brain-Area-Specific Visual Representations Generated by Ganglion Cell Diversity. *Curr. Biol.* **24**, 2085–2096 (2014).
92. Nikolaou, N. *et al.* Parametric functional maps of visual inputs to the tectum. *Neuron* **76**, 317–324 (2012).
93. Robles, E., Filosa, A. & Baier, H. Precise lamination of retinal axons generates multiple parallel input pathways in the tectum. *J. Neurosci. Off. J. Soc. Neurosci.* **33**, 5027–5039 (2013).
94. Roeser, T. & Baier, H. Visuomotor behaviors in larval zebrafish after GFP-guided laser ablation of the optic tectum. *J. Neurosci. Off. J. Soc. Neurosci.* **23**, 3726–3734 (2003).
95. Dill, L. M. The Escape Response of the Zebra Danio (*Brachydanio Rerio*) I. the Stimulus for Escape. *Anita Behav* 711–722 (1974). doi:10.1016/S0003-3472(74)80022-9
96. Ishikane, H., Gangi, M., Honda, S. & Tachibana, M. Synchronized retinal oscillations encode essential information for escape behavior in frogs. *Nat. Neurosci.* **8**, 1087–95 (2005).
97. Sahibzada, N., Dean, P. & Redgrave, P. Movements resembling orientation or avoidance elicited by electrical stimulation of the superior colliculus in rats. *J. Neurosci. Off. J. Soc. Neurosci.* **6**, 723–33 (1986).
98. Sparks, D. L. & Nelson, J. S. Sensory and motor maps in the mammalian superior colliculus. *Trends Neurosci.* **10**, 312–317 (1987).
99. Gahtan, E., Tanger, P. & Baier, H. Visual prey capture in larval zebrafish is controlled by identified reticulospinal neurons downstream of the tectum. *J. Neurosci. Off. J. Soc. Neurosci.* **25**, 9294–9303 (2005).

100. O'Malley, D. M., Kao, Y. H. & Fetcho, J. R. Imaging the functional organization of zebrafish hindbrain segments during escape behaviors. *Neuron* **17**, 1145–55 (1996).
101. Straw, A. D. Vision egg: an open-source library for realtime visual stimulus generation. *Front. Neuroinformatics* **2**, 4 (2008).
102. Zottoli, S. J., Hordes, A. R. & Faber, D. S. Localization of optic tectal input to the ventral dendrite of the goldfish Mauthner cell. *Brain Res.* **401**, 113–121 (1987).
103. Canfield, J. G. Temporal constraints on visually directed C-start responses: behavioral and physiological correlates. *Brain. Behav. Evol.* **61**, 148–58 (2003).
104. Zottoli, S. J. Correlation of the startle reflex and Mauthner cell auditory responses in unrestrained goldfish. *J. Exp. Biol.* **66**, 243–254 (1977).
105. Pologruto, T. A., Sabatini, B. L. & Svoboda, K. ScanImage: flexible software for operating laser scanning microscopes. *Biomed. Eng. Online* **2**, 13 (2003).
106. Kaifosh, P., Zaremba, J. D., Danielson, N. B. & Losonczy, A. SIMA: Python software for analysis of dynamic fluorescence imaging data. *Front. Neuroinformatics* **8**, 80 (2014).
107. Ben Fredj, N. *et al.* Synaptic activity and activity-dependent competition regulates axon arbor maturation, growth arrest, and territory in the retinotectal projection. *J. Neurosci. Off. J. Soc. Neurosci.* **30**, 10939–51 (2010).
108. Wu, J. Y., Cohen, L. B. & Falk, C. X. Neuronal activity during different behaviors in *Aplysia*: a distributed organization? *Science* **263**, 820–823 (1994).
109. Lockery, S. R. & Kristan, W. B. J. Distributed processing of sensory information in the leech. II. Identification of interneurons contributing to the local bending reflex. *J. Neurosci. Off. J. Soc. Neurosci.* **10**, 1816–1829 (1990).
110. Wiersma, C. A. G. Giant nerve fiber system of the crayfish; a contribution to comparative physiology of synapse. *J. Neurophysiol.* **10**, 23–38 (1947).
111. Boyan, G. S., Ashman, S. & Ball, E. E. Initiation and modulation of flight by a single giant interneurone in the cercal system of the locust. *Naturwissenschaften* **73**, 272–274 (1986).

112. Chalfie, M. *et al.* The neural circuit for touch sensitivity in *Caenorhabditis elegans*. *J. Neurosci. Off. J. Soc. Neurosci.* **5**, 956–964 (1985).
113. Grillner, S. Biological pattern generation: the cellular and computational logic of networks in motion. *Neuron* **52**, 751–766 (2006).
114. Stein, P. S. G. & Daniels-McQueen, S. Modular organization of turtle spinal interneurons during normal and deletion fictive rostral scratching. *J. Neurosci. Off. J. Soc. Neurosci.* **22**, 6800–6809 (2002).
115. Kiehn, O. Locomotor circuits in the mammalian spinal cord. *Annu. Rev. Neurosci.* **29**, 279–306 (2006).
116. Tresch, M. C., Saltiel, P., d’Avella, A. & Bizzi, E. Coordination and localization in spinal motor systems. *Brain Res. Brain Res. Rev.* **40**, 66–79 (2002).
117. Pavlova, E. L. & Deliagina, T. G. Responses of reticulospinal neurons in intact lamprey to pitch tilt. *J. Neurophysiol.* **88**, 1136–1146 (2002).
118. Peterson, B. W., Pitts, N. G. & Fukushima, K. Reticulospinal connections with limb and axial motoneurons. *Exp. Brain Res.* **36**, 1–20 (1979).
119. Baier, H. & Scott, E. K. Genetic and optical targeting of neural circuits and behavior--zebrafish in the spotlight. *Curr. Opin. Neurobiol.* **19**, 553–560 (2009).
120. Friedrich, R. W., Genoud, C. & Wanner, A. A. Analyzing the structure and function of neuronal circuits in zebrafish. *Front. Neural Circuits* **7**, 71 (2013).
121. Kimmel, C. B., Powell, S. L. & Metcalfe, W. K. Brain neurons which project to the spinal cord in young larvae of the zebrafish. *J. Comp. Neurol.* **205**, 112–127 (1982).
122. Scott, E. K. *et al.* Targeting neural circuitry in zebrafish using GAL4 enhancer trapping. *Nat. Methods* **4**, 323–326 (2007).
123. Huang, K.-H., Ahrens, M. B., Dunn, T. W. & Engert, F. Spinal projection neurons control turning behaviors in zebrafish. *Curr. Biol. CB* **23**, 1566–1573 (2013).

124. Orger, M. B., Kampff, A. R., Severi, K. E., Bollmann, J. H. & Engert, F. Control of visually guided behavior by distinct populations of spinal projection neurons. *Nat. Neurosci.* **11**, 327–333 (2008).
125. Gahtan, E., Sankrithi, N., Campos, J. B. & O'Malley, D. M. Evidence for a widespread brain stem escape network in larval zebrafish. *J. Neurophysiol.* **87**, 608–614 (2002).
126. Liu, K. S. & Fetcho, J. R. Laser ablations reveal functional relationships of segmental hindbrain neurons in zebrafish. *Neuron* **23**, 325–335 (1999).
127. Gahtan, E. & O'Malley, D. M. Visually guided injection of identified reticulospinal neurons in zebrafish: a survey of spinal arborization patterns. *J. Comp. Neurol.* **459**, 186–200 (2003).
128. Gahtan, E., Tanger, P. & Baier, H. Visual prey capture in larval zebrafish is controlled by identified reticulospinal neurons downstream of the tectum. *J. Neurosci. Off. J. Soc. Neurosci.* **25**, 9294–9303 (2005).
129. Sankrithi, N. S. & O'Malley, D. M. Activation of a multisensory, multifunctional nucleus in the zebrafish midbrain during diverse locomotor behaviors. *Neuroscience* **166**, 970–993 (2010).
130. Dubuc, R. *et al.* Initiation of locomotion in lampreys. *Brain Res. Rev.* **57**, 172–182 (2008).
131. Thankachan, S., Fuller, P. M. & Lu, J. Movement- and behavioral state-dependent activity of pontine reticulospinal neurons. *Neuroscience* **221**, 125–139 (2012).
132. Chen, T.-W. *et al.* Ultrasensitive fluorescent proteins for imaging neuronal activity. *Nature* **499**, 295–300 (2013).
133. Boyden, E. S., Zhang, F., Bamberg, E., Nagel, G. & Deisseroth, K. Millisecond-timescale, genetically targeted optical control of neural activity. *Nat. Neurosci.* **8**, 1263–1268 (2005).
134. Ando, R., Hama, H., Yamamoto-Hino, M., Mizuno, H. & Miyawaki, A. An optical marker based on the UV-induced green-to-red photoconversion of a fluorescent protein. *Proc. Natl. Acad. Sci. U. S. A.* **99**, 12651–12656 (2002).
135. Shik, M. L., Severin, F. V. & Orlovskii, G. N. [Control of walking and running by means of electric stimulation of the midbrain]. *Biofizika* **11**, 659–666 (1966).



136. Sirota, M. G., Di Prisco, G. V. & Dubuc, R. Stimulation of the mesencephalic locomotor region elicits controlled swimming in semi-intact lampreys. *Eur. J. Neurosci.* **12**, 4081–4092 (2000).
137. Haines, L. *et al.* Met and Hgf signaling controls hypaxial muscle and lateral line development in the zebrafish. *Dev. Camb. Engl.* **131**, 4857–4869 (2004).
138. Arrenberg, A. B., Del Bene, F. & Baier, H. Optical control of zebrafish behavior with halorhodopsin. *Proc. Natl. Acad. Sci. U. S. A.* **106**, 17968–17973 (2009).
139. Kimura, Y. *et al.* Hindbrain V2a Neurons in the Excitation of Spinal Locomotor Circuits during Zebrafish Swimming. *Curr. Biol. CB* (2013). doi:10.1016/j.cub.2013.03.066
140. Scott, E. K. *et al.* Targeting neural circuitry in zebrafish using GAL4 enhancer trapping. *Nat. Methods* **4**, 323–326 (2007).
141. Uematsu, K. *et al.* Central mechanisms underlying fish swimming. *Brain. Behav. Evol.* **69**, 142–150 (2007).
142. Kobayashi, N., Yoshida, M., Matsumoto, N. & Uematsu, K. Artificial control of swimming in goldfish by brain stimulation: confirmation of the midbrain nuclei as the swimming center. *Neurosci. Lett.* **452**, 42–46 (2009).
143. Deliagina, T. G. & Orlovsky, G. N. Comparative neurobiology of postural control. *Curr. Opin. Neurobiol.* **12**, 652–657 (2002).
144. Deliagina, T. G., Arshavsky, Y. I. & Orlovsky, G. N. Control of spatial orientation in a mollusc. *Nature* **393**, 172–175 (1998).
145. Deliagina, T. G., Zelenin, P. V., Fagerstedt, P., Grillner, S. & Orlovsky, G. N. Activity of reticulospinal neurons during locomotion in the freely behaving lamprey. *J. Neurophysiol.* **83**, 853–863 (2000).
146. Grillner, S. & Wallén, P. Cellular bases of a vertebrate locomotor system-steering, intersegmental and segmental co-ordination and sensory control. *Brain Res. Brain Res. Rev.* **40**, 92–106 (2002).
147. Wannier, T., Deliagina, T. G., Orlovsky, G. N. & Grillner, S. Differential effects of the reticulospinal system on locomotion in lamprey. *J. Neurophysiol.* **80**, 103–112 (1998).

148. Zelenin, P. V., Pavlova, E. L., Grillner, S., Orlovsky, G. N. & Deliagina, T. G. Comparison of the motor effects of individual vestibulo- and reticulospinal neurons on dorsal and ventral myotomes in lamprey. *J. Neurophysiol.* **90**, 3161–3167 (2003).
149. Iwahara, T., Wall, P. T., Garcia-Rill, E. & Skinner, R. D. Stimulation-induced setting of postural muscle tone in the decerebrate rat. *Brain Res.* **557**, 331–335 (1991).
150. Mori, S. Integration of posture and locomotion in acute decerebrate cats and in awake, freely moving cats. *Prog. Neurobiol.* **28**, 161–195 (1987).
151. Bizzi, E., Cheung, V. C. K., d’Avella, A., Saltiel, P. & Tresch, M. Combining modules for movement. *Brain Res. Rev.* **57**, 125–133 (2008).
152. Roh, J., Cheung, V. C. K. & Bizzi, E. Modules in the brain stem and spinal cord underlying motor behaviors. *J. Neurophysiol.* **106**, 1363–1378 (2011).
153. Briggman, K. L. & Kristan, W. B. Multifunctional pattern-generating circuits. *Annu. Rev. Neurosci.* **31**, 271–294 (2008).
154. O’Malley, D. M., Kao, Y. H. & Fetcho, J. R. Imaging the functional organization of zebrafish hindbrain segments during escape behaviors. *Neuron* **17**, 1145–1155 (1996).
155. Prugh, J. I., Kimmel, C. B. & Metcalfe, W. K. Noninvasive recording of the Mauthner neurone action potential in larval zebrafish. *J. Exp. Biol.* **101**, 83–92 (1982).
156. Schoonheim, P. J., Arrenberg, A. B., Del Bene, F. & Baier, H. Optogenetic localization and genetic perturbation of saccade-generating neurons in zebrafish. *J. Neurosci. Off. J. Soc. Neurosci.* **30**, 7111–7120 (2010).
157. Westerfield, M. *The Zebrafish Book: A Guide for the Laboratory Use of Zebrafish*. (Inst of Neuro Science, 1994).
158. Xiao, T. & Baier, H. Lamina-specific axonal projections in the zebrafish tectum require the type IV collagen Draqnet. *Nat. Neurosci.* **10**, 1529–1537 (2007).
159. Schindelin, J. *et al.* Fiji: an open-source platform for biological-image analysis. *Nat. Methods* **9**, 676–682 (2012).

160. Pologruto, T. A., Sabatini, B. L. & Svoboda, K. ScanImage: flexible software for operating laser scanning microscopes. *Biomed. Eng. Online* **2**, 13 (2003).
161. Rickgauer, J. P. & Tank, D. W. Two-photon excitation of channelrhodopsin-2 at saturation. *Proc. Natl. Acad. Sci. U. S. A.* **106**, 15025–15030 (2009).
162. Kiehn, O. Decoding the organization of spinal circuits that control locomotion. *Nat. Rev. Neurosci.* **17**, 224–238 (2016).
163. Olsen, S. R. & Wilson, R. I. Cracking neural circuits in a tiny brain: new approaches for understanding the neural circuitry of *Drosophila*. *Trends Neurosci.* **31**, 512–520 (2008).
164. Miri, A., Daie, K., Burdine, R. D., Aksay, E. & Tank, D. W. Regression-Based Identification of Behavior-Encoding Neurons During Large-Scale Optical Imaging of Neural Activity at Cellular Resolution. *J. Neurophysiol.* **105**, 964–980 (2011).
165. Portugues, R., Feierstein, C. E., Engert, F. & Orger, M. B. Whole-brain activity maps reveal stereotyped, distributed networks for visuomotor behavior. *Neuron* **81**, 1328–1343 (2014).
166. Kubo, F. *et al.* Functional Architecture of an Optic Flow-Responsive Area that Drives Horizontal Eye Movements in Zebrafish. *Neuron* **81**, 1344–1359 (2014).
167. Ahrens, M. B. *et al.* Brain-wide neuronal dynamics during motor adaptation in zebrafish. *Nature* **485**, 471–477 (2012).
168. Dunn, T. W. *et al.* Brain-wide mapping of neural activity controlling zebrafish exploratory locomotion. *eLife* **5**, e12741 (2016).
169. Weichwald, S. *et al.* Causal interpretation rules for encoding and decoding models in neuroimaging. *NeuroImage* **110**, 48–59 (2015).
170. Grosenick, L., Marshel, J. H. & Deisseroth, K. Closed-Loop and Activity-Guided Optogenetic Control. *Neuron* **86**, 106–139 (2015).
171. Szabo, V., Ventalon, C., De Sars, V., Bradley, J. & Emiliani, V. Spatially selective holographic photoactivation and functional fluorescence imaging in freely behaving mice with a fiberscope. *Neuron* **84**, 1157–1169 (2014).

172. Packer, A. M., Russell, L. E., Dagleish, H. W. P. & Häusser, M. Simultaneous all-optical manipulation and recording of neural circuit activity with cellular resolution in vivo. *Nat. Methods* **12**, 140–146 (2015).
173. Rickgauer, J. P., Deisseroth, K. & Tank, D. W. Simultaneous cellular-resolution optical perturbation and imaging of place cell firing fields. *Nat. Neurosci.* **17**, 1816–1824 (2014).
174. Thiele, T. R., Donovan, J. C. & Baier, H. Descending control of swim posture by a midbrain nucleus in zebrafish. *Neuron* **83**, 679–691 (2014).
175. Gahtan, E., Tanger, P. & Baier, H. Visual Prey Capture in Larval Zebrafish Is Controlled by Identified Reticulospinal Neurons Downstream of the Tectum. *J. Neurosci.* **25**, 9294–9303 (2005).
176. Severi, K. E. *et al.* Neural control and modulation of swimming speed in the larval zebrafish. *Neuron* **83**, 692–707 (2014).
177. Maschio, M. D. in *Novel Approaches for Single Molecule Activation and Detection* (eds. Benfenati, F., Fabrizio, E. D. & Torre, V.) 7–26 (Springer Berlin Heidelberg, 2014).
178. Oron, D., Papagiakoumou, E., Anselmi, F. & Emiliani, V. Two-photon optogenetics. *Prog. Brain Res.* **196**, 119–143 (2012).
179. Grewe, B. F., Voigt, F. F., van 't Hoff, M. & Helmchen, F. Fast two-layer two-photon imaging of neuronal cell populations using an electrically tunable lens. *Biomed. Opt. Express* **2**, 2035–2046 (2011).
180. Sinclair, G. *et al.* Interactive application in holographic optical tweezers of a multi-plane Gerchberg-Saxton algorithm for three-dimensional light shaping. *Opt. Express* **12**, 1665–1670 (2004).
181. Patterson, G. H. & Lippincott-Schwartz, J. A photoactivatable GFP for selective photolabeling of proteins and cells. *Science* **297**, 1873–1877 (2002).
182. Yizhar, O. *et al.* Neocortical excitation/inhibition balance in information processing and social dysfunction. *Nature* **477**, 171–178 (2011).

183. Lin, J. Y., Knutsen, P. M., Muller, A., Kleinfeld, D. & Tsien, R. Y. ReaChR: A red-shifted variant of channelrhodopsin enables deep transcranial optogenetic excitation. *Nat. Neurosci.* **16**, 1499–1508 (2013).
184. Klapoetke, N. C. *et al.* Independent optical excitation of distinct neural populations. *Nat. Methods* **11**, 338–346 (2014).
185. Paluch-Siegler, S. *et al.* All-optical bidirectional neural interfacing using hybrid multiphoton holographic optogenetic stimulation. *Neurophotonics* **2**, 031208 (2015).
186. Prigge, M. *et al.* Color-tuned Channelrhodopsins for Multiwavelength Optogenetics. *J. Biol. Chem.* **287**, 31804–31812 (2012).
187. Akerboom, J. *et al.* Optimization of a GCaMP Calcium Indicator for Neural Activity Imaging. *J. Neurosci.* **32**, 13819–13840 (2012).
188. Inoue, M. *et al.* Rational design of a high-affinity, fast, red calcium indicator R-CaMP2. *Nat. Methods* **12**, 64–70 (2015).
189. Dana, H. *et al.* Sensitive red protein calcium indicators for imaging neural activity. *eLife* **5**, e12727 (2016).
190. Prakash, R. *et al.* Two-photon optogenetic toolbox for fast inhibition, excitation and bistable modulation. *Nat. Methods* **9**, 1171–1179 (2012).
191. Semmelhack, J. L. *et al.* A dedicated visual pathway for prey detection in larval zebrafish. *eLife* **3**, (2014).
192. Golan, L., Reutsky, I., Farah, N. & Shoham, S. Design and characteristics of holographic neural photo-stimulation systems. *J. Neural Eng.* **6**, 066004 (2009).
193. Packer, A. M. *et al.* Two-photon optogenetics of dendritic spines and neural circuits. *Nat. Methods* **9**, 1202–1205 (2012).
194. Zhu, P. *et al.* Optogenetic Dissection of Neuronal Circuits in Zebrafish using Viral Gene Transfer and the Tet System. *Front. Neural Circuits* **3**, (2009).

195. Vaziri, A. & Emiliani, V. Reshaping the optical dimension in optogenetics. *Curr. Opin. Neurobiol.* **22**, 128–137 (2012).
196. Dal Maschio, M. *et al.* in *Cellular Imaging Techniques for Neuroscience and Beyond* (ed. Wouterlood, F. G.) 101–120 (Academic Press, 2012).
197. Botcherby, E. J. *et al.* Aberration-free three-dimensional multiphoton imaging of neuronal activity at kHz rates. *Proc. Natl. Acad. Sci. U. S. A.* **109**, 2919–2924 (2012).
198. Dal Maschio, M., De Stasi, A. M., Benfenati, F. & Fellin, T. Three-dimensional in vivo scanning microscopy with inertia-free focus control. *Opt. Lett.* **36**, 3503 (2011).
199. Yang, W. *et al.* Simultaneous Multi-plane Imaging of Neural Circuits. *Neuron* **89**, 269–284 (2016).
200. Duemani Reddy, G., Kelleher, K., Fink, R. & Saggau, P. Three-dimensional random access multiphoton microscopy for functional imaging of neuronal activity. *Nat. Neurosci.* **11**, 713–720 (2008).
201. Shen, Y., Lai, T. & Campbell, R. E. Red fluorescent proteins (RFPs) and RFP-based biosensors for neuronal imaging applications. *Neurophotonics* **2**, 031203–031203 (2015).
202. Akerboom, J. *et al.* Genetically encoded calcium indicators for multi-color neural activity imaging and combination with optogenetics. *Front. Mol. Neurosci.* **6**, (2013).
203. Wu, J. *et al.* Improved Orange and Red Ca<sup>2+</sup> Indicators and Photophysical Considerations for Optogenetic Applications. *ACS Chem. Neurosci.* **4**, 963–972 (2013).
204. Mattis, J. *et al.* Principles for applying optogenetic tools derived from direct comparative analysis of microbial opsins. *Nat. Methods* **9**, 159–172 (2012).
205. Erbguth, K., Prigge, M., Schneider, F., Hegemann, P. & Gottschalk, A. Bimodal Activation of Different Neuron Classes with the Spectrally Red-Shifted Channelrhodopsin Chimera C1V1 in *Caenorhabditis elegans*. *PLoS ONE* **7**, e46827 (2012).
206. Schoonheim, P. J., Arrenberg, A. B., Bene, F. D. & Baier, H. Optogenetic Localization and Genetic Perturbation of Saccade-Generating Neurons in Zebrafish. *J. Neurosci.* **30**, 7111–7120 (2010).

207. Aravanis, A. M. *et al.* An optical neural interface: in vivo control of rodent motor cortex with integrated fiberoptic and optogenetic technology. *J. Neural Eng.* **4**, S143 (2007).
208. Gradinaru, V. *et al.* Targeting and Readout Strategies for Fast Optical Neural Control In Vitro and In Vivo. *J. Neurosci.* **27**, 14231–14238 (2007).
209. Randlett, O. *et al.* Whole-brain activity mapping onto a zebrafish brain atlas. *Nat. Methods* **12**, 1039–1046 (2015).
210. Thiele, T. R., Donovan, J. C. & Baier, H. Descending control of swim posture by a midbrain nucleus in zebrafish. *Neuron* **83**, 679–691 (2014).
211. Packer, A. M., Roska, B. & Häusser, M. Targeting neurons and photons for optogenetics. *Nat. Neurosci.* **16**, 805–815 (2013).

## Publishing Agreement

It is the policy of the University to encourage the distribution of all theses, dissertations, and manuscripts. Copies of all UCSF theses, dissertations, and manuscripts will be routed to the library via the Graduate Division. The library will make all theses, dissertations, and manuscripts accessible to the public and will preserve these to the best of their abilities, in perpetuity.

I hereby grant permission to the Graduate Division of the University of California, San Francisco to release copies of my thesis, dissertation, or manuscript to the Campus Library to provide access and preservation, in whole or in part, in perpetuity.

Author Signature  Date 15 / 05 / 2016

(This final page must be signed and dated and should be numbered.)